

Alma Mater Studiorum - Università di Bologna

DOTTORATO DI RICERCA IN
DATA SCIENCE AND COMPUTATION

Ciclo 35

Settore Concorsuale: 03/D1 - CHIMICA E TECNOLOGIE FARMACEUTICHE,
TOSSICOLOGICHE E NUTRACEUTICO - ALIMENTARI

Settore Scientifico Disciplinare: CHIM/08 - CHIMICA FARMACEUTICA

**EXPLORING RHOGTPases: A COMPUTATIONAL STUDY OF
PROTEIN-PROTEIN INTERACTIONS AND DRUG DESIGN**

Presentata da: Maria Antonietta La Serra

Coordinatore Dottorato

Daniele Bonacorsi

Supervisore

Marco De Vivo

Esame finale anno 2024

Table of Contents

Acknowledgments	1
Abstract	3
Chapter 1. RHOGTPases: Physiology and Pathology	4
1.1. Aim of the thesis	4
1.2. The RHOGTPases family	4
1.2.1 The conserved structure of RHOGTPases	5
1.2.2 The fine regulation of RHOGTPases activity	8
1.2.3 RHOGTPases regulate vital cellular processes	12
1.3. The CDC42 subfamily	18
1.3.1. CDC42	18
1.3.2. RHOQ	24
1.3.3. RHOJ	25
1.4. Therapeutic Relevance of the CDC42/PAK interaction	26
1.5. Targeting CDC42/PAK signaling: <i>the state of art</i>	32
1.5.1. CDC42 family inhibitors	32
1.5.2. PAK inhibitors	33
1.6. Investigation of protein-protein interactions to uncover druggable interaction	35
Chapter 2. Theory and Methods	38
2.1. Molecular Docking	38
2.2. Molecular Dynamics Simulations	41
2.2.1. Force field	41
2.2.2. Non-bonded interactions computation	46

2.2.3. MD simulation procedures	48
2.2.3.1 Minimization	49
2.2.3.2 Equilibration	50
2.2.3.3 MD production	51
2.3 Data collection and structural analysis from MD Simulations	52
2.4. MM/GBSA Calculations	55
2.6. Alchemical Free Energy Calculations	59
Chapter 3. Structure-based design of CDC42 effector interaction inhibitors	62
3.1. Approaching the CDC42/PAK signaling blockade	62
3.2. Investigation of a drug-binding pocket present in GTP-bound RHOJ and CDC42	64
3.3. Identification of a CDC42-RHOJ effector interaction <i>hit compound</i> inhibitor	73
3.4. Hit-to-lead optimization	76
3.5. ARN22089 binding mode analysis	81
3.6. ARN22089 <i>in vitro</i> and <i>in vivo</i> studies	83
3.7. Discovery and optimization of follow-up inhibitors	84
3.8. ARN25062 and ARN24928 binding mode analysis	87
3.9. MD simulation details	91
Chapter 4. Alchemical Free Energy Calculations for protein–protein interface studies	94
4.1. CDC42/PAK interaction as test case for free energy calculations	94
4.2. CDC42/PAK1 Homology Modeling and Systems set-up	95
4.3. MD simulations of CDC42/PAK1 complexes	98

4.4. Alchemical free energy calculations based on sidechain transformation	103
4.5. Improving alchemical free energy calculations results	106
4.5.1. Tuning the mapping scheme for T35S and F28Y	106
4.5.1.1. T35S mutation	106
4.5.1.2. F28Y mutation	109
4.5.2. Right Pick of the Initial Conformation for Y32F and V33N	112
4.5.2.1. Y32F mutation	112
4.5.2.2. V33N mutation	114
4.5.3. Structural analysis as keystone for alchemical free energy calculations	115
4.6. Free energy methods results comparison	119
4.7. Computational details	119
4.7.1. MD simulations	119
4.7.2. Alchemical Free Energy calculations	120
4.7.3. MM/GBSA calculations	123
Chapter 5. Alchemical Free Energy Calculations to predict key residues at the RHOA/ROCK1 interface	124
5.1. The RHOA/ROCK1 signaling is central for diverse cellular functions	124
5.2. Therapeutic Relevance of the RHOA/ROCK1 interaction	128
5.3. Blocking RHOA/ROCK1 signaling: the state of art	134
5.3.1. ROCK inhibitors	134
5.3.2. RHOA inhibitors	138
5.4. Systems set-up	141
5.5. Classical MD simulations	144
5.5.1. Apo form RHOA MD simulation	144

5.5.2. ROCK1-bound form RHOA MD simulation	147
5.5.3. Computational details	152
5.6. Alchemical Free Energy Calculations for the RHOA/ROCK1 system	153
5.6.1. RHOA mutants selection	153
5.6.2. Computational details and preliminary results	156
Chapter 6. Conclusions and Future Perspectives	162
Bibliography	167

Acknowledgments

It feels like just yesterday that I arrived at IIT, carrying a huge backpack of fears and questions. That morning, to welcome me, Jacopo, Elisa, Sebastian and Matteo, the very first traveling companions on this intense journey. Thank you for all the laughs, discussions and time spent together.

Jacopo, your working advices have been invaluable as they have been the countless moments we spent in front of a couple of beers, sharing jokes and delving into the intricacies and the complexities of our innermost thoughts.

A special thank is reserved to everyone who has been by my side throughout these years and to all the *comp people* with whom I shared my daily life in the office, and not only — Mattia, Sara, Federico, Pietro, Laura, Jacopo, Elisa and her gentle and reassuring gaze, Inacrist, Adam, Jissy, Sebastián, Federica, Matilde, Jo, David, Luigi, Gianfranco, Alessia, Stefano, Giorgia, Alice, and Manuel, my incredible and kind PhD partner who profoundly experienced with me both the highs and lows of this demanding intense path. Thank you all for being part of this journey!

Federica, regardless the small amount of time, thank you for reminding me of the importance being always brave and proactive, no matter what. Grateful to have found a friend. It is not the amount of time spent, but rather the quality of that time we spent and spend together that fed and feeds our relationship.

Of course, I would like to express my sincere gratitude to Dr. Pietro Vidossich, who always has a trick up his sleeve to solve every problem! Thank you for your invaluable help and support. Your expertise and insightful feedbacks have significantly contributed to this research work.

However, the greatest acknowledgment goes to Dr. Marco De Vivo, without whom none of this would have been possible. Thank you for recognizing in me, that time in that small study room at the University of Calabria, something that has pushed me this far. Thank you for your time and your teachings. The path was challenging at times, but your invaluable guidance made a significant difference for me. I will forever hold a profound sense of gratitude towards you.

I also thank Dr. Dal Peraro and his group for having kindly hosted me during my time in Lausanne. I loved the city and the experience!

Lastly, but certainly not least, I want to express my immense gratitude to the fundamental columns of my life, my family and Rosario. No words will be enough to adequately thank you for always accompanying me. Your unwavering support, encouragement, and constant belief in me have been inestimable pillars that sustained me during my doctoral journey, and beyond. By dedicating this thesis to you, I aim to give you back all the love I have been fortunate to receive from you.

Abstract

The CDC42 RHOGTPases subfamily (RHOJ, RHOQ, CDC42) is often overexpressed but rarely mutated in cancer. These GTPases play a critical role in governing both the invasiveness of tumor cells into nearby tissues and the ability of endothelial cells to establish blood vessels within tumors. A key pathway involves the interaction between CDC42 proteins and the serine/threonine kinase PAK, which activates downstream signaling. This interaction is a crucial juncture, initiating and transmitting signaling downstream, ultimately influencing cellular behavior and disease progression. Recognizing the importance of this interaction, computer-aided drug design has been utilized to identify a new class of inhibitor compounds specifically targeting the CDC42 subfamily. This strategic approach aimed to interfere in this critical pathway and potentially impede cancer progression. Moreover, the study utilized alchemical free energy calculations to quantitatively and accurately evaluate the effect of mutations at the protein–protein interface, using the CDC42/PAK interaction as a test case. The study demonstrated an excellent agreement between computed and experimental data on binding affinity. A meticulous analysis of the sidechain conformations of the mutated residues was crucial in enhancing the accuracy of the computed estimates, effectively addressing limitations associated with sampling. This study underscored the advantage of integrating alchemical free energy calculations into the design of experimental mutagenesis studies, highlighting the potential for this approach to significantly contribute to understand the complex protein interactions and guide drug development strategies. In accordance with these findings, the study extended the analysis to the RHOA/ROCK1 interface, which is also heavily implicated in cancer. Preliminary results from alchemical free energy calculations on RHOA mutants lay the foundation for utilizing this methodology to identify hotspot residues crucial for the interaction between these two proteins. Ultimately, this method has the potential to facilitate the exploration of new targetable interactions, contributing to the development of novel tailored therapeutics.

Chapter 1. RHOGTPases: Physiology and Pathology

1.1. Aim of the thesis

The aim of this thesis is to study, characterize and target the deregulated RHOGTPases signaling associated to diverse pathological conditions, including cancer. After an overview encompassing the general structure, regulation, and functional aspects of the RHOGTPases family, the thesis will specifically focus on the CDC42 subfamily (RHOJ, RHOQ, CDC42). Subsequently, following a description of the physiological roles of CDC42 proteins in cellular biology, the discussion will proceed covering specific events associated with the pathological progression of cancer influenced by CDC42 proteins. Indeed, CDC42 proteins are often overexpressed and/or upregulated in cancer, exerting control over both the ability of tumor cells to proliferate and invade surrounding tissues as well as the ability of endothelial cells to vascularize tumors. These pathological processes are predominantly accomplished through the activation of the downstream effector proteins PAK. Moreover, the use of computational methods able to predict key residues involved in the recognition mechanism, facilitating the identification of druggable interactions, will be explored. Finally, the study will also explore the significance of the RHOA/ROCK signaling pathway and its relevance in cancer, particularly focusing on the relative protein-protein interaction.

1.2. The RHOGTPases family

RHOGTPases are monomeric low molecular weight (~21 kDa) signaling proteins, which belong to the Small GTP-binding proteins family (also called *Ras superfamily*)¹⁻⁷. From the discovery of the first Rho gene in the abdominal ganglia of *Aplysia* in the 1985, up to date 20 RHOGTPases have been identified in mammals, divided into eight subfamilies (Figure 1)^{4,8,9}.

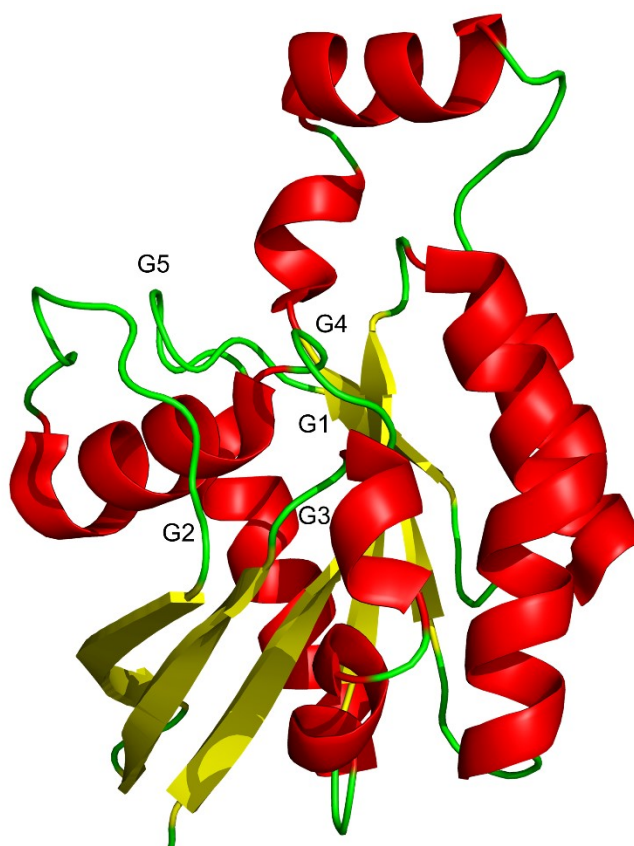


Figure 2. RHO GTPases structural representation. The GCP-bound CDC42 (PDB code 2ODB, 2.4 Å resolution) is reported. The protein is shown in red, yellow and green cartoon representation for the helices, the strands and the polypeptide loops, respectively. The non-hydrolyzable GCP nucleotide and Mg^{2+} are not shown. Conserved motifs around the nucleotide binding site are labelled as G1, G2, G3, G4 and G5.

The G1 glycine-rich loop motif GxxxxGK[S,T] is found in all the Ras-related proteins and also in other nucleotide-binding proteins, such as ATPases and kinases, where it is crucial for the Mg^{2+} and phosphates' nucleotide binding^{4,12-17}. Structurally, the loop enfolds around the GTP's phosphates allowing the main chain nitrogen atoms of the loop to tightly interact with the negatively charged β - and γ -phosphate oxygens of the GTP. Notably, the strongly conserved lysine residue of the G1 loop directly interacts with those phosphates and it is crucial in the GTP catalysis, where it participates to the coordination of a water molecule during its nucleophilic attack at the γ -

phosphate^{11,12,14,15,17–19}. Remarkably, also the threonine of the G1 glycine-rich loop motif GxxxxGK[S,T] is a highly conserved residue. In detail, the threonine hydroxyl group participates to the coordination of the Mg²⁺ ion in the active site and forms additional contacts with the β-phosphate oxygen^{10,13}. In agreement, mutations of the corresponding Ser17 of the GxxxxGK[S,T] motif in the homolog Ras showed to have reduced affinity for GTP²⁰. Also the G2 loop contains a conserved threonine which is found in all the Ras superfamily members, as well as in the Gα subunits of heterotrimeric G proteins¹⁶. Likewise, the conserved threonine is responsible for the Mg²⁺ binding and it is crucial for sensing the presence of the GTP γ-phosphate. Indeed, the specific threonine interactions at the catalytic site with the Mg²⁺ ion and γ-phosphate suggest its key role in modulating the crucial conformational transition of the protein, from the GTP-bound to the GDP-bound state. Specifically, the removal of the γ-phosphate from the nucleotide triggers modifications in the interactions network at the nucleotide site that involve the threonine residue, resulting in a rearrangement of the protein into a different GDP-bound conformation^{10–14,16,17,21–23}. Mutations of Thr35 in RAS consistently perturb the conformational state shifting the equilibrium towards the inactive state^{11,24}. Being the Mg²⁺ ion coordinated by the threonine residues from the G1 and G2 loops, oxygen atoms from the β- and γ-phosphates of the GTP and two water molecules, is important to underline that the G3 loop motif DXXG contains a conserved aspartate, which keeps in place one of the two Mg²⁺ coordinating waters^{10,12,16}. Moreover, the glycine residue of the G3 loop motif is conserved as part of the DXXG motif in all guanine-nucleotide-binding proteins and forms a hydrogen bond with the GTP γ-phosphate. Importantly, the conserved glycine is recognized to be a player in the triggering process that leads to the conformational change after the nucleotide hydrolysis^{4,10–12,21}.

The nucleotide binding is characterized by contacts that involve not only the Mg²⁺ ion and phosphate groups, but also the guanine base. Indeed, the guanine base is recognized by the G4 and G5 loops. The G4 loop contains a consensus sequence NKXD whose observed variations in the RHO family are [N,T,C][K,Q]XD. The conserved aspartate directly interacts with the nucleotide through a bifurcated hydrogen bond with the NH and NH₂ groups of the guanine base and with the side chain of a strictly conserved serine (e.g. Ser158 in CDC42). In accordance, mutation of the corresponding Asp119 in

Ras decreases the affinity for guanosine^{10–14,17,21,25,26}. Additionally, the lysine/glutamine residue from the loop motif makes hydrophobic interactions by stacking along the plane of the base, but also interacts with the nucleotide ribose and residues from the G1 loop^{4,10,12,21}. Finally, the G5 loop motif contains a consensus sequence SAK whose observed variations in the RHO family are S[A,S,V][K,L,R,F,V]. The conserved alanine in the G5 loop directly binds the nucleotide through a strong hydrogen bond with O6 atom of the guanine base and seems to be highly conserved for steric purposes. Indeed, its substitution by a larger residue would lead to steric hindrance, disrupting the hydrogen bond and probably decreasing the association with the nucleotide^{4,10–13,17}. Furthermore, RHOGTPases have also a flexible carboxyl-terminal region, which contains a post-translational lipid modifications site (CAAX motif, where C: cysteine, A: aliphatic and X: any amino acid) and an adjacent polybasic region responsible for homodimer formation and for the proper subcellular localization^{4,10,27,28}.

1.2.2 The fine regulation of RHOGTPases activity

The GTP- and GDP- bound states define two different structural conformations, which mainly differ at the so-called *switch regions*. Specifically, the switch I region is a loop that connects the α 1 helix and the β 2 strand, while the switch II region is formed by the α 2 helix and part of the G3 loop. Only the GTP-bound active conformation has the proper structural arrangement to interact with effector proteins and, thus, transmit the signal downstream^{1–3,6,7,10,11}. Accordingly, RHOGTPases are considered molecular switches that cycle between two functional states: the GTP-bound active state and the GDP-bound inactive state¹. The equilibrium between the functional states is regulated by other interacting proteins namely i) the guanine nucleotide exchange factors (GEFs), ii) the GTPase-activating proteins (GAPs), and iii) the guanine nucleotide dissociation inhibitors (GDIs)^{1,6} (Figure 3).

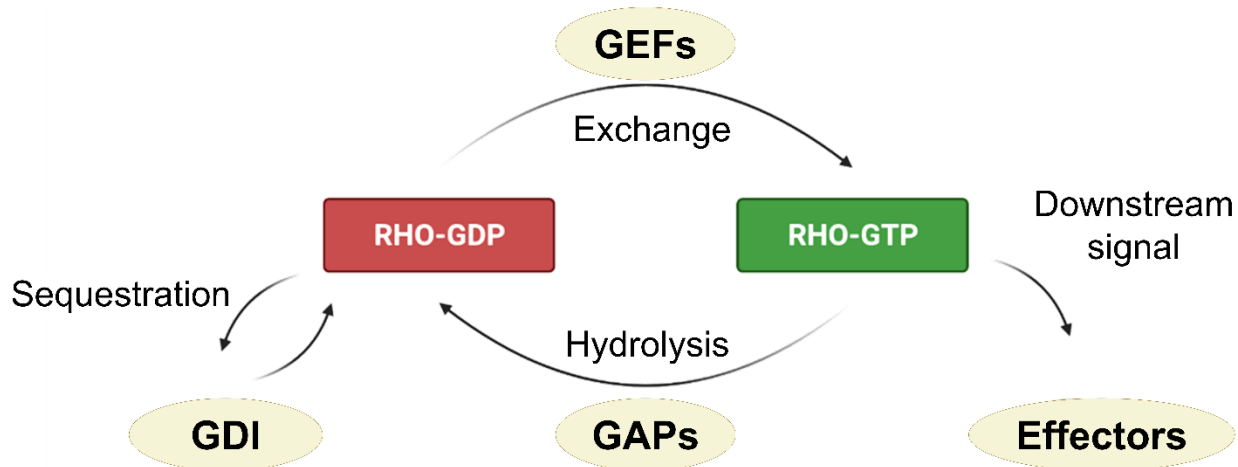


Figure 3. RHO GTPases regulation cycle. RHO GTPases cycle between the GTP-bound active and GDP-bound inactive functional states. The inactive state is bound and activated by the guanine nucleotide exchange factors GEFs. Once activated, RHO GTPases are able to interact with diverse effectors transmitting the signal downstream. To quench the signal, the GTPase-activating proteins GAPs enhance GTP hydrolysis to deactivate RHO GTPases. To balance and regulate the overall RHO GTPases activation, the GDP-bound inactive form is held in the cytosol by the guanine nucleotide dissociation inhibitors GDIs.

Firstly, RHO GTPases activation requires the GDP dissociation from the protein followed by the subsequent GTP binding. Because of the high GDP/GTP affinity for the protein, such process is intrinsically slow and it is accelerated by the guanine nucleotide–exchange factors (GEFs), which promote RHO activity by enhancing the exchange of GDP for GTP^{4,6,11,13,29}. Structural analysis of small G protein-GEF complexes has shown that different families of GEFs are not structurally related, but are instead conserved within a given subfamily. Accordingly, RHO-GEFs could contain either two structural domains the Dbl-homology (DH) domain and the adjacent pleckstrin-homology (PH) domain or an unrelated DOCK-homology domain. In spite of these structural differences, GEF activity is thought to be accomplished by a common multistep process in which GEF primarily binds to the GDP-bound RHO GTPase and, then, induce the dissociation of the nucleotide. To achieve this goal, GEFs interact with the switch regions of RHO GTPases and insert residues close to the G1 loop and the Mg²⁺ binding site inducing structural rearrangements, which, in turn, reduce the nucleotide affinity. Given the largely higher

GTP cellular concentrations respect to the GDP, the resulting nucleotide-free protein binds to the predominant GTP nucleotide, leading to the protein activation. Indeed, the GTP binding induce consequently the proper conformational rearrangements suitable for the interaction with effectors, allowing the transmission of the signal downstream.

The actual GTP hydrolysis reaction performed by RHOGTPases is intrinsically very slow and would not be appropriate for most of the biological signal transduction processes. Accordingly, once the signaling has been accomplished, the GTPase-activating proteins GAPs stimulate the intrinsic GTPase activity by enhancing the GTP hydrolysis. The structure of the Ras-RasGAP complex in presence of aluminium fluoride was crucial to understand the mechanism of reaction carried out by GAPs. As for the GEFs mechanism, also the activity of GAPs is a multistep process in which a water molecule needs to be positioned and polarized optimally for an in-line nucleophilic attack to the γ -phosphate. Accordingly, GAPs stabilize a conserved glutamine from the switch II, which acts as a catalytic base and it is responsible for the attacking water coordination. Importantly, an arginine from GAPs, called *arginine finger*, stabilizes the transition state into the phosphate-binding site by neutralizing negative charge at the γ -phosphate. Reported GAPs-RHOGTPases complexes X-Ray structures confirm the described mechanism. Notably, an arginine found in the α -subunits of large G proteins acts the same role of the *arginine finger* provided by GAPs. The combined activity of GEFs and GAPs results in a highly regulated and efficient RHOGTPases activity. Remarkably, in absence of GEFs the RHOGTPases signaling would be transduced too slowly as well as in absence of GAPs the active state would improperly be maintained.

Together with the key regulation acted by GEFs and GAPs, a complementary degree of control for the RHOGTPases is achieved by a third class of protein: the GDP dissociation inhibitors (GDIs). In detail, GDIs sequester the GDP-bound RHOGTPases in the cytosol, preventing the dissociation of GDP and the GTPase activation by GEFs. Additionally, GDIs also regulate the cycling of RHOGTPases between the cytosol and the membranes through the binding of the post-translationally modified motifs at the RHOGTPase C-terminus. When released, RHOGTPases are thus able to insert into the lipid bilayer of the plasma membrane through their C-terminus, where they will be activated by GEFs^{9,11,13,30}.

As mentioned above, the most important aspect of the fine RHOGTPase regulation is that the GTP- and GDP- bound functional states define two different structural conformations, differing in the switch regions. Importantly, only the GTP-bound active conformation interacts with downstream effector proteins^{1-4,6,10,11}. From several experimental evidences, it is possible to define some structural features that characterize the active and the inactive conformations. In particular, in the GTP-bound active conformation switch regions are located close to the nucleotide and it is possible to evidence two conserved hydrogen bonds between two of the γ -phosphate oxygens and the main chain NH groups of the conserved threonine and glycine from the G2 and G3 loop, respectively. Relevantly, the recognized conformational change triggered by the GTP hydrolysis is known as *loaded-spring mechanism* and involves the breakage of these two described bonds after the release of the γ -phosphate. The result of this interaction network rearrangement allows the switch regions to relax into the GDP-bound conformation^{11,13}.

Another distinguishing feature of the protein conformational state is the orientation of the sidechain of a fully conserved tyrosine within the RHOGTPases family that is located on the switch I (e.g. Tyr32 in CDC42). Indeed, the tyrosine ring flips inside, toward the GTP γ -phosphate in the active state, while points outward towards the solvent in the GDP-bound conformation^{4,10,31}. Conversely, the GDP-bound state is characterized by an intramolecular contact between a highly conserved phenylalanine in the switch I (e.g. Phe37 in CDC42) and a usually aliphatic residue located on the α 1 helix (e.g. Ile21 in CDC42)^{32,33}. Finally, in the GTP-bound active conformation the presence of the γ -phosphate allows the switch regions to be kept in place in the structural shape suitable for the interaction with downstream effectors by influencing the Mg^{2+} coordination in the active site. Indeed, an oxygen atom from the γ -phosphate of the GTP participates to the tight magnesium ion coordination, which is completed by the contacts with an oxygen atom from the β -phosphate of the GTP, the two conserved threonine from the G1 and G2 loops and two water molecules.

1.2.3 RHOGTPases regulate vital cellular processes

RHOGTPases control a wide variety of signal transduction pathways that consecutively regulate numerous aspects of the cellular life (Figure 4). The major function of RHOGTPases is to regulate the polymerization, the assembly and organization of the actin and microtubule cytoskeleton^{1,6,7,9}. The modulation of the actin filaments operated by the RHOGTPases mainly regards well-defined signaling pathways related to the activity of lamellipodia and filopodia. Lamellipodia and filopodia are important cellular protrusions composed by actin filaments employed by cells for migration and probing processes, respectively. The functional maintenance of both lamellipodia and filopodia is strictly correlated to the modulation of the actin polymerization and organization directed by the RHOGTPases. In detail, the actin polymerization is largely regulated by the factor Arp2/3 that is indirectly activated by the RHOGTPases CDC42 and RAC through the upstream direct binding to members of the Wiskott-Aldrich syndrome protein (WASP) and Wiskott-Aldrich syndrome protein family verprolin-homologous protein (WAVE) families, respectively. Furthermore, RHOGTPases drive the control of the actin polymerization through the interaction with members of the formin family. Indeed, RHOGTPases stimulate actin polymerization through the interaction with the mammalian diaphanous-related formins *mDia*¹.

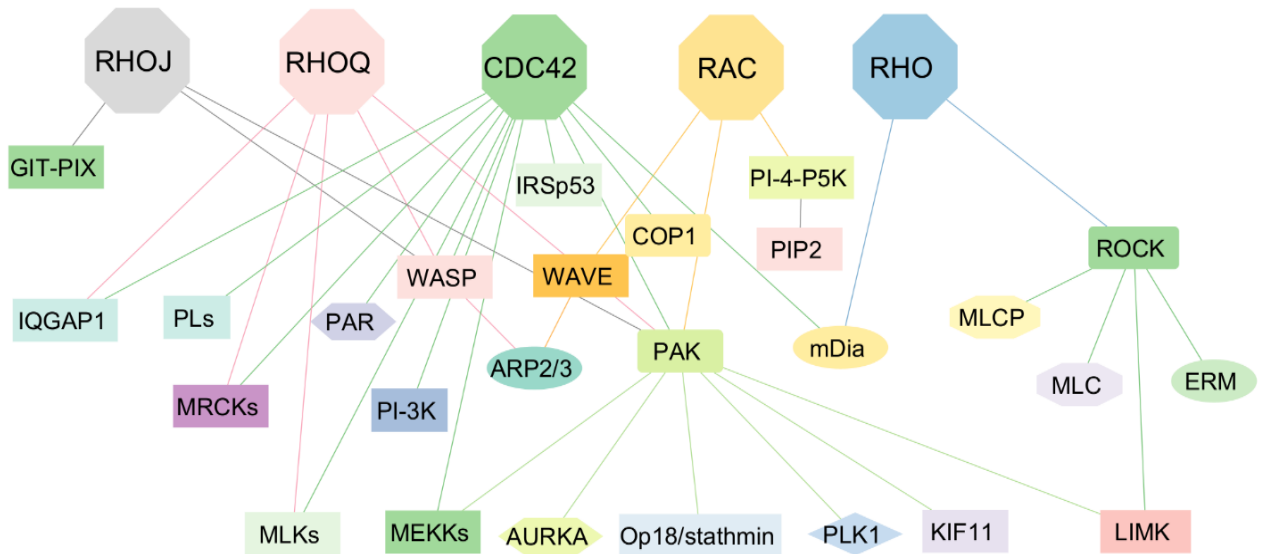


Figure 4. RHO GTPases signalling networks summary. RHO GTPases govern diverse signal transduction pathways, sequentially modulating numerous aspects of cellular existence. The image illustrates mostly of the interactions depicted in this thesis, providing a visual representation of the interplays described.

In conjunction with the actin polymerization, the organization of the polymerized actin filaments is also critical as it is decisive for the cytoskeleton to acquire the proper spatial organization to correctly accomplish its functions. Accordingly, the control of the cytoskeleton is also central for cell morphogenesis that, in turn, is linked to the tuning of the cell polarity and to the appropriate establishment of extracellular interactions. Indeed, the development of the cell shape is strongly dependent on the establishment of the appropriate intracellular asymmetric polarity that concerns the arrangement of subcellular components, such as plasma membrane proteins, protein complexes and cytoskeletal components. Remarkably, transient or stable cell polarity allows cells to accomplish their specialized functions^{34–40}. Over years, genetic studies pointed out the so-called PAR complex as one of the most important molecular contributors for the acquirement of the cell polarity^{35,41–43}. In detail, the PAR complex is made up of PAR6, PAR3 and aPKC⁴⁴. The complex is held together by interactions, which involve the first PDZ domain of PAR3 with the single PDZ domain of PAR6 and contacts between the N-terminal domains of PAR6 and aPKC. Summarizing, PAR6 mediates the connection between PAR3 and

aPKC. Interestingly, members of the RHOGTPases CDC42 and RAC subfamilies have been found to contribute to the establishment of the correct cell polarity thanks to their influence on these key player proteins^{45,46}. Indeed, although the precise process is not completely outlined, CDC42 directly targets PAR6 and seems to induce downstream events resulting in the regulation of the aPKC activity and of the overall cell polarity^{44,47-50}. Together with cell polarity, the regulation of extracellular interactions, such as cell-substratum and cell-cell adhesion, is also fundamental for cell morphogenesis. Remarkably, RHOGTPases members from the RHO, RAC and CDC42 subfamilies are found to be involved in the assembly and organization of both focal adhesions and tight and adherens junctions^{1,2,51-54}.

RHOGTPases are also fundamental in the coordination of the microtubule cytoskeleton, which determines the intracellular organization and distribution of organelles and directs the intracellular transport. Indeed, RHOGTPases critically drive the microtubule dynamics by influencing the activity of microtubule plus end-binding proteins. The Op18/stathmin family proteins represent an example of the upstream regulation operated by RHOGTPases. In depth, the Op18/stathmin proteins are regulating proteins that essentially inhibit the microtubule polymerization and whose phosphorylation leads to its inactivation. Interestingly, the CDC42-RAC dependent effector kinase PAK mediates the Op18/stathmin phosphorylation with consequent microtubule polymerization.

The fine cytoskeleton regulation operated by the RHOGTPases is also fundamental for the cellular movement, which is central in diverse physiological events comprising embryogenesis, wound healing, immune response and tissue regeneration^{1,2,55-60}. Cell migration is a multistep process that starts with the determination of the direction of motion followed by the extension of protrusions that are subsequently stabilized by sticking to the extracellular matrix (ECM). Once anchored, migrating cells contract themselves to move forward. Finally, the rear adhesions are disassembled and cells retract their tails^{6,9,61,62}. Notably, each of this single step is mediated by the specific RHOGTPases activity⁵⁹. Firstly, the directional movement is determined by soluble or matrix-associated signals resulting in the generation of filopodia coordinated by CDC42². As partly discussed above, filopodia are membrane protrusions at the leading edge composed by compactly bundled parallel actin filaments employed by

cells for probing the extracellular environment^{4,59,63–66}. Importantly, CDC42 regulates the formation of filopodia by stimulating actin polymerization through the activation of the members of the Wiskott–Aldrich Syndrome protein (WASP) and formin (mDia) families^{6,54,59,67–70}. Next, the lamellipodia, larger actin filaments-based membrane protrusions, are assembled at the leading edge of the migrating cell under the CDC42 and RAC proteins control. Indeed, CDC42 and RAC proteins regulate the lamellipodia development through the triggering of the downstream effectors WASP and WAVE, which leads to the activation of the Arp2/3 complex, stimulating the actin nucleation and polymerization processes^{2,4,6,71}. Additionally, RAC proteins bind and active the effector phosphatidylinositol 4-phosphate 5-kinase (PI-4-P5K) that, sequentially, trigger the downstream phosphatidylinositol 4,5-bisphosphate (PIP2). Particularly, PIP2 is involved in the release of capping proteins, promoting the filament assembly in migrating cells⁷². Furthermore, the RHO-mediated activation of the downstream effectors mDia also promote actin filament formation^{54,59}.

Next, the actin rich membrane extensions produced by the migrating cell are held to the extracellular matrix (ECM) through the formation of new adhesion. Subsequently, the sticking to the ECM induces the integrin-dependent activation of RAC and CDC42 that promote cell spreading^{59,62,73}. RAC promotes the assembly of nascent cell-ECM adhesion structures, called focal complexes, through the activation of downstream effectors from the serine/threonine p21-activated kinases (PAK) family, resulting in increased membrane protrusions and actin polymerization^{2,74}. While the migrating cell moves towards the settled direction, the RHOGTPases RHO stimulate the development of the focal complexes into more stable and larger cell-ECM adhesion arrangements, called focal adhesions^{6,52,74–77}. Focal adhesions provide a strategic anchorage between the migrating cell and the ECM required to pilot the cell over the adhesions. Despite the stabilization at the leading edge guided by the novel connections, the overall cell migration depends also from the traction forces determined by the cell contraction.

Remarkably, the RHOGTPases CDC42 and RHO regulate actomyosin cell contractility through the Myotonic dystrophy kinase-related CDC42-binding kinases (MRCKs) and the Rho-associated protein kinase (ROCK) signaling, respectively^{78,79}. Although ROCK phosphorylates diverse downstream substrates, the phosphorylation of

the myosin light chain (MLC) is one of the primary RHO-ROCK signaling pathways. Indeed, the phosphorylation of the regulatory MLC of myosin II induces its interaction with the actin, which thereby activates the myosin ATPase resulting in enhanced cell contractility. Additionally, ROCK phosphorylates the myosin light chain phosphatase (MLCP), which negatively regulates actomyosin-based contractility by dephosphorylating the MLC. The resulting process increases myosin activity and cell contractility^{51,59,62,80,81}. Despite the predominant contribution of RHO/ROCK signaling to cell contractility, CDC42 promotes actin stress fiber contractility through the activation of its effectors MRCK1 and MRCK2 (Myotonic dystrophy-related Cdc42-binding kinases 1 and 2). Specifically, the CDC42/MRCK signaling cooperates with ROCKs to enhance myosin phosphorylation and cell migration^{78,79,82}.

Overall, the resulting actomyosin contractility provides to the cell the needed tension to advance in its migration. The concluding stage of the cell migration process is represented by the disassembly of the former adhesions at the rear of moving cells and their tail retraction^{62,83}. Remarkably, RHOGTPases RHO are again key factors in the contraction at the rear of moving cells^{62,84,85}. Furthermore, other less characterized RHOGTPases contribute to the migration process. In detail, the RHOGTPase RHOJ has been found to regulate the endothelial cell migration by modulating the actomyosin contractility, but also the focal adhesion disassembly^{86,87}. Accordingly, RHOJ interacts with the GIT-PIX complex, a regulator of focal adhesion disassembly. Further studies showed that the RHOGTPase RHOD controls cytoskeleton-related events, such as the cell adhesion and migration⁸⁸. Lastly, in hematopoietic cells lack of the RHOGTPase RHOH results in defective T cell receptor (TCR) complex signaling, migration and adhesion⁸⁹. Overall, cell migration exemplify a functional interplay between the RHOGTPases of separated but interconnected cytoskeleton events embracing cell polarization, membrane protrusions formation, adhesions establishment, cell contraction and tail retraction. The importance of the RHOGTPases in the regulation of cell contractility is also outlined in the context of the vascular smooth muscle cells, which modulate blood flow by contracting and distending, with regards to the received information and stimulation. Predominantly, the RHOGTPase RHO subfamily is found to own a crucial role in those processes^{2,90-92}.

RHOGTPases play another key role in the regulation of the cell cycle progression^{2,6,7,93,94}. In detail, RHOGTPases pilot the activity of cyclin-dependent kinases and the organization of the microtubule and actin cytoskeletons during the phases G1 and M, respectively.

The G1 phase is primarily regulated by the cyclin-dependent kinases Cdk4/Cdk6 and Cdk2, which are in turn activated and inhibited by the cyclins D and E and by the INK4A and Cip/Kip proteins. Briefly, the G1 phase progression depends on the cellular levels of cyclins and the Cdk inhibitors. RHOGTPases mediate extracellular signals that regulate those levels^{1,95}. During the mitotic phase M, the RHO/ROCK and CDC42/mDia3 signaling pathways are required to allocate centrosomes and to regulate microtubules attachment to kinetochores, respectively^{1,96,97}. Also, the RAC/CDC42 effector PAK6 regulates mitosis by modulating the kinesin-5 Eg5, found to be essential for mitotic spindle assembly⁹⁸⁻¹⁰⁰. Finally, cytokinesis is the concluding step of the cell cycle during which a single cell origins the two daughter cells. The contraction of actomyosin filaments is the major driving force of this separation. Notably, RHOGTPases are key regulators of this process, which act through the modulation of the ROCK, citron kinase and mDia signaling. In detail, studies showed that ROCK signaling has a general positive role as a promoter of cell proliferation in mammalian cells as well as in *Xenopus embryos*^{80,81,101-104}, where it phosphorylate several proteins at the cleavage furrow¹⁰². Accordingly, the inhibition of the RHOGTPases RHO and CDC42 blocks cell cytokinesis^{2,101,105}.

Being the cytoskeleton arrangement indispensable for the vesicle trafficking, it is not surprising that RHOGTPases also contribute to diverse vesicle transport-related events^{4,54,106-111}. Consistently, RHOGTPases are also implicated in phagocytosis^{4,109}. However, along with their cytoskeletal effects, RHOGTPases influence other various signaling pathways among which gene expression^{1,6,112,113}. In this regard, one of the recognized RHOGTPases functions concerns the regulation of the serum response element SRE. In depth, SRE is found in many promoters of genes encoding components of the cytoskeleton and it is modulated by the serum response factor (SRF) which is in turn affected by RHOGTPases^{1,114,115}. Interestingly, RHOGTPases also influence gene expression via signal transduction pathways not engaging the actin cytoskeleton^{1,116,117}. Additionally, RHOGTPases are involved in the regulation of enzymatic activities, mainly

involved in lipid metabolism and ROS generation^{2,118–121}. Last but not least, RHOGTPases contributes to the control of essential processes involved in neuronal morphology, survival and death^{5,95,122–124}. To conclude, RHOGTPases are central contributors in a wide variety of biochemical and biological processes pointing them as high-ranking targets to investigate.

1.3. The CDC42 subfamily

The CDC42 subfamily is a three-member cluster within the broader RHOGTPases family. Specifically, the CDC42 family is composed by CDC42 (Cell Division Cycle 42), RHOQ (or TC10) and RHOJ (or TC10-like, TCL).

1.3.1. CDC42

CDC42 is a 191 residues long protein of 21 kDa whose gene is positioned on the chromosome 1p36.1¹²⁵. This small G protein was firstly discovered in the *Saccharomyces cerevisiae* yeast¹²⁶, where it was found to regulate cytoskeleton-related functions¹²⁷ linked to the establishment of cell polarity and to the assembly of budding and mating projections¹²⁸. Next, further studies in *Caenorhabditis elegans* and *Drosophila* showed that CDC42 was required during the embryonic morphogenesis for establishing and maintaining the proper cellular polarity^{129–131}. Finally, CDC42 was identified as the human homolog of the yeast protein in 1990¹³². Nowadays, CDC42 is one of the best-characterized member of the RHOGTPases family. Consistently with the RHOGTPases functional role in the regulation of the cytoskeleton architecture, CDC42 is decisive for the actin filaments polymerization and organization. Indeed, the modulation of actin structures is pivotal for diverse functions that balance cell homeostasis, such as morphogenesis. Cell morphogenesis is a combination of signaling processes that allow cells to acquire their appropriate shape by organizing themselves into functional structures to ultimately develop complex tissues and organs. Cell polarity is a dominant factor in the overall process⁵⁷.

Cell polarity concerns the asymmetric organization of cellular and structural components and it is indispensable for the cellular biology. Accordingly, cell polarity

coordinates the execution of specialized functions involved in cell division and migration³⁴, cell development^{36,133}, neuronal communication³⁷, transport of molecules across epithelia³⁹, lymphocyte homing^{40,134}, and further key processes. One of the first indications of involvement of CDC42 in cell polarity modulation was found in the yeast *Saccharomyces cerevisiae*^{128,135}. Next, additional studies have revealed that CDC42 forms a stable binding with the so-called heterotrimeric *PAR complex*, which comprises PAR6, PAR3 and the atypical protein kinase C aPKC^{42,45,48,50,136}. Notably, from the pioneer discovery of PAR genes in *Caenorhabditis elegans* embryos⁴¹, studies have pointed out PAR complex as one of the most important molecular contributors for the acquirement of the cell polarity^{35,42,43,137,138}. PAR complex is associated by intermolecular contacts, which encompass the first PDZ domain of PAR3 with the single PDZ domain of PAR6¹³⁹ and the N-terminal domains of PAR6 and aPKC. Structurally, PAR6 intermediates the association between PAR3 and aPKC. CDC42 directly targets the CDC42/RAC interactive binding motif (CRIB) on PAR6 inducing a conformational transition in the effector, which in turn modulates the basal aPKC activity^{44,47–50,140–142}. Accordingly, once stimulated, aPKC is able to activate a large number of downstream substrates involved in cell polarity regulation^{49,142–145}. Importantly, cell polarity, even if transient, is fundamental for the cells to accomplish their function and to maintain homeostasis¹⁴⁶. Epithelial cells morphogenesis exemplifies the importance of cell polarization in cellular biology. Indeed, epithelia perform a variety of functions in embryonic and adult tissues, such as protection, secretion, absorption, excretion, filtration, diffusion, and sensory reception¹⁴⁷. To be able to perform these functions, epithelial cells develop a functional and structural polar arrangement with apical and basolateral domains^{1,148,149}. Interestingly, CDC42 is involved in the establishment of apical-basal polarity during epithelial morphogenesis^{150,151}. Relevantly, gene-targeting studies in mice highlighted how the CDC42 deficiency is associated to polarity anomalies in pancreas, skin and nervous system^{140,152–155}. As result of its leading role, CDC42 represent the core of the cell polarity regulation.

Together with cell polarity, cell migration is also necessary for tissues and organs development and conservation. Cell migration is an extremely integrated multistep process that occurs during embryogenesis and in adult tissues. Indeed, cell migration is

the driving force during gastrulation to develop the ectoderm, endoderm and mesoderm embryonic layers, but also during the following organogenesis, where cells migrate to their correspondent sites^{57,156,157}. In adult organisms, cell migration assists the preservation of the homeostatic state participating to diverse processes such as tissue renewal and repair, and immune response^{156–159}. To occur, cell migration requires precise cytoskeletal rearrangements, which are strongly mediated by CDC42¹⁶⁰. As previously discussed, cell migration is a combined process that requires the early polarization of the migrating cell, the assembly of filopodial and lamellipodial extensions, the arrangement of cell-ECM adhesions and the final cell contraction to drive the cell forwards. CDC42 is necessary for cell migration and, in detail, for the filopodia formation, essential chemotactic sensors for guiding cells during migration^{62,65,161,162}. In depth, CDC42 stimulates the formation of filopodia by interacting and activating members of the Wiscott-Aldrich syndrome proteins (WASPs) family that, in turn, bind to the highly conserved Arp2/3 complex through one of its seven subunits, p21-Arc^{163–168}. The proposed action mode for CDC42 is to induce a conformational change in WASP relieving the autoinhibitory domain located at its C-terminal region that successively associates with the Arp2/3 complex through the its VCA domain (verprolin-homology, cofilin-homology and acidic region), promoting actin polymerization^{169–171}. Additionally, CDC42 contributes to the filopodia formation through the binding and the activation of the formins mDia^{59,68,172}. An alternative pathway to expand filopodia is achieved by triggering the CDC42 effector insulin-receptor substrate p53 (IRSp53). IRSp53 is an adaptor protein, which binds and bends membrane through its Bin/Amphiphysin/Rvs (BAR) domain^{54,63}. This large scaffolding protein exists in an autoinhibited state in which its domain SH3, which acts as a recruiter of actin cytoskeleton effectors, is hampered by the IRSp53-CRIB motif. The binding of CDC42 to the CRIB domain induce a conformational rearrangement that activates IRSp53 that, finally, can promote downstream effectors activities. The best-described pathway involves the activation of the downstream substrate MENA, an Ena/VASP (enabled/vasodilator-stimulated phosphoprotein) family member, and WAVE2 (WASP Family Verprolin-homologous Protein 2)^{173–175}. Accordingly, in lens of mice specific deletion of CDC42 leads to decreased filopodia formation and lens epithelial invagination as results of the IRSp53 activation lacking¹⁷⁶.

Last, but not least, CDC42/PAK signaling generates filopodia protrusions. In detail, studies show the noteworthy involvement of PAK1 and PAK4^{7,177,178}. Specifically, CDC42/PAK signaling controls filopodia formation by stimulating the activity of the LIM kinase (LIMK), substrate of PAK, which consecutively phosphorylates and inhibits the actin-binding protein ADF/cofilin. Since the ADF/cofilin primary function is to sever and disassemble actin filaments, its inhibition results in an increased actin polymerization^{1,54,179}. Noteworthy, in Alzheimer the PAK/LIMK disproportion is one of the causes for developing the disease^{164,180}. In addition, PAK5 induces filopodia formation in neuroblastoma cells, leading to neurite outgrowth¹⁸¹. Being central for cell migration, it is not surprising that targeted deletion of CDC42 in diverse tissues, as well as in the immune system, is associated to different cytoskeleton anomalies^{140,176,182,183}.

Cell migration is directly connected with the ability of cells to assembly adhesions with the extracellular environment. Importantly, CDC42 regulates the formation and the activity of cadherins, Ca²⁺ dependent cell-cell adhesions¹⁸⁴. In depth, CDC42 regulates cell-cell adhesions by modulating the activity of the scaffolding protein effector IQGAP1 (Isoleucine-Glutamine-Motif containing GTPase-activating protein 1)¹⁸⁵. Indeed, in a weak adhesive state IQGAP1 interacts with the cytoplasmic domain of E-cadherin and the N-terminal domain of the β -catenin. This direct interaction prevent the binding between α - and β - catenins. Notably, the primary function of the α -catenin is to link cadherins to the actin cytoskeleton¹⁸⁶⁻¹⁹⁰. CDC42 positively regulates the cadherin-mediated cell-cell adhesions by interacting with IQGAP1 and suppressing the inhibitory action of IQGAP1. This results in a stabilized cadherin-catenins complex with strong adhesive activity¹⁸⁸. Accordingly, CDC42 is required for maintaining the cell-cell and cell-substratum adhesions in MDCK cells (Madin-Darby canine kidney)¹⁹¹. Furthermore, the fine cellular adhesion regulation is accomplished by the CDC42/PAK signaling. Indeed, CDC42/PAK1¹⁹² and CDC42/PAK4¹⁹³ signaling is found to be involved in the reorganization of stress fibers and focal adhesions. Additionally, CDC42/PAK1 signaling mediates cell spreading⁷³. Consistently, morphological changes and modifications of cell adhesion induced by PAK activity play a direct role in oncogenic transformation, as amply discussed in the paragraph 1.4¹⁶⁴. Consistent with its focal role, gene-targeting studies in

mice showed the association between CDC42 deficiency and cell adhesion anomalies in liver¹⁹⁴, blood^{195,196} and nervous system^{140,154}.

CDC42 is also involved in the coordination of microtubules. Specifically, CDC42 regulates the *microtubule organizing center* (MTOC), cellular structure that allows microtubule nucleation^{1,2,197,198}. Additionally, CDC42/PAK signaling mediates the Op18/stathmin phosphorylation with consequent inhibition and activation of the microtubule polymerization². The ability of CDC42 to control microtubules' activity is strictly connected with its role in mitosis¹. Indeed, to correctly accomplish mitosis, cells require a complex bipolar microtubule-based structure, called *mitotic spindle*, which accurately coordinates the segregation of chromosomes during cell division^{199–201}. Accordingly, the correct bi-oriented alignment of chromosomes²⁰² during metaphase and their correct segregation during anaphase are crucial events for a proper cell division. The overall process is carried out by interactions between kinetochores and microtubules. Notably, CDC42 regulate microtubules attachment to kinetochores by stabilizing the bi-orientated microtubules attachment for the appropriate chromosome alignment and the following segregation. Accordingly, inhibition of CDC42 activity is associated to the failure of the mitotic spindle to bind chromosomes in the proper bipolar orientation at the metaphase plate. Deeply, during mitosis CDC42 acts through the modulation of its effector mDia3⁹⁷. Afterwards, further RNA interference (RNAi) studies confirmed the key role of CDC42 in mitosis and revealed the contribution of the GEF Ect2 and the GAP MgcRacGAP proteins in the modulation of the CDC42 activity²⁰³. Likewise, other studies showed that the CDC42/PAR6 signaling is involved in the orientation of the mitotic spindle during cell division^{129,150}. Finally, also CDC42/PAK1 and CDC42/PAK6 signaling are involved in the mitotic progression by regulating the activity of the PAK substrates PLK1 (Polo-like kinase 1)²⁰⁴, Aurora-A kinases^{205–207} and the kinesin-5 Eg5^{98–100}, respectively.

CDC42 regulates also other phases of the cell cycle progression. Indeed, studies demonstrated the role of CDC42 in the modulation of the G1 phase progression and in the associated DNA synthesis stimulation⁹³. As discussed in the previous paragraph, RHOGTPases are involved in the regulation of the cyclin-dependent kinases Cdk4/Cdk6 and Cdk2, balanced by activators (cyclins D and E) and the inhibitors (INK4A and Cip/Kip). Specifically, CDC42 regulates the expression of the cyclins D²⁰⁸ and E²⁰⁹.

Interestingly, CDC42 modulation of the cyclin D expression is fundamental in bone remodeling. Precisely, osteoclast-specific CDC42 deletion in mice led to osteopetrosis and reduced bone resorption, as a consequence of an altered cyclin D expression²¹⁰. Consistently, CDC42/PAK2 signaling has been recently found to be involved in osteoclastogenesis²¹¹.

CDC42 is additionally implicated in vesicle trafficking^{212,213} and gene expression^{112,115}. Indeed, CDC42 is connected with Golgi activity^{214,215} and endocytic²¹⁶, exocytic^{108,217} and phagocytic^{2,109} processes. Specifically, CDC42 binds the γ -subunit of the coatamer complex (COP1) through a dilysine motif present in its C-terminal domain²¹⁸. Accordingly, in NIH-3T3 cell lines a modified mutant at the dilysine motif showed a reduction in intracellular trafficking activity²¹⁸. CDC42 influences also gene expression. One recognized route is the one that involves the activation of the serum response factor (SRF), which is a transcription factor able to modulate the expression of genes encoding structural and regulatory effectors of actin dynamics^{115,219}. CDC42 also activates NF κ B (Nuclear factor-kappaB), a transcription factor that plays critical roles in inflammation, immunity, cell proliferation, differentiation, and survival^{112,220}. A well-recognized pathway that activates NF κ B is the CDC42/PAK signaling²⁰⁵.

Furthermore, CDC42 triggers the JNK (c-Jun N-terminal kinase) pathway, a conserved group within the mitogen-activated protein (MAP) kinases family, which regulates the activity of several transcription factors involved in cell growth, differentiation, survival and apoptosis^{116,117}. Specifically, CDC42 mediates the JNK activation through its direct upstream interaction with the JNK activators MEKK1, MEKK4, MLK2 and MLK3^{221,222}. Notably, the CDC42 effector PAK can also directly phosphorylate and activate MEKK1^{140,223,224}. Remarkably, heart-specific deletion of CDC42 in mice heart induces enhanced growth effects as a result of the inability to activate JNK signaling. Accordingly, reduced expression of CDC42-targeting microRNA-133 was detected in both mouse and human models of cardiac hypertrophy^{140,225}. Narrow JNK signaling was also uncovered in mice liver where hepatocyte-specific CDC42 deletion resulted in delayed liver regeneration after partial hepatectomy²²⁶.

Concluding, CDC42 is a leading contributor in various essential pathways that regulate the dynamic organization of the cytoskeleton as well as vital physiologic processes such as cell proliferation, motility, polarity, cytokinesis, membrane trafficking and cell growth. Ultimate, CDC42 also binds effector proteins involved in lipid metabolism, such as PI-3-kinase (phosphoinositide 3-kinase) and the phospholipase D and C (PLD, PLC). Being pivotal in cell biology, it is not surprising that alterations in CDC42 activity are associated to cancer and disease development, as deeply discussed in the following paragraph 1.3.

1.3.2. RHOQ

RHOQ (or TC10, from the name of the human teratocarcinoma (TC) cDNA library used to identify the protein) is the less characterized member of the CDC42 subfamily. In agreement with the high conservation within the RHOGTPases family, RHOQ is structurally similar to CDC42 with a percentage of identity of ~66%. After the initial discovery of RHOQ in 1990²²⁷, studies have better characterized this small G protein. Neudauer et al. demonstrated for the first time the involvement of RHOQ in cytoskeleton regulation and its capability to produce peripheral protrusions, as CDC42²²⁸. Interestingly, RHOQ is able to bind mostly of the CDC42 effectors, specifically PAK1, PAK2 and PAK3, IQGAP1, MRCK1 and MRCK2, N-WASP, MLK2 and MSE55, but does not interact significantly with MLK3, WASP and ACK-1. Additionally, RHOQ is also able to activate the JNK signaling^{228,229}. Later, Murphy et al. expanded the information relative to this less explored small G protein. Indeed, in addition to the JNK signaling and the filopodial formation, RHOQ was found to activate the transcription factors SRF and NFκB²³⁰.

Despite less studied, interesting works highlight the importance of RHOQ in nerve regeneration and elongation^{231,232}. Moreover, RHOQ is found to participate in the insulin-regulated translocation of the glucose transporter 4 (GLUT4) and in the regulation of exocytic vesicle fusion^{107,233}. Noteworthy, interesting data show also the involvement of RHOQ in the modulation of the cystic fibrosis transmembrane conductance regulator (CFTR) expression, as results of its direct interaction with the CFTR-associated ligand (CAL)²³⁴.

1.3.3. RHOJ

RHOJ (also called, TC10-like or TCL) is the last discovered member of the CDC42 subfamily²³⁵. The protein is highly conserved and shares the ~62% and ~76% of identity with CDC42 and RHOQ, respectively. Accordingly, the alternative name TC10-like (TCL) derives from the high similarity shared with RHOQ (TC10)²³⁵. RHOJ is a 214 long protein whose gene of 86 kb is made of five exons and is located on chromosome 14. As CDC42 and RHOQ, RHOJ is involved in cytoskeleton dynamics modulation. Indeed, the GTP-bound RHOJ directly binds the CRIB domain of the effectors PAK and WASP and induces membrane actin-protrusion formation²³⁵. Accordingly, RHOJ is able to activate N-WASP inducing the consequent Arp2/3 complex-mediated actin polymerization, essential for neurite outgrowth²³². RHOJ is involved also in the regulation of the early stages of both endocytic processes²³⁶ and adipocyte differentiation^{237,238}.

Despite the contribution of other RHOGTPases²³⁹, one prominent distinguishing of RHOJ is its role in angiogenesis^{87,240–242}. Angiogenesis is an intricate and complex process that leads to the formation of new blood vessels during embryonic and fetal development and in adult organism²⁴³. The vital importance of the angiogenesis process put RHOJ at the center of the cell biology. Specifically, RHOJ controls angiogenesis by modulating endothelial cells motility and proliferation as well as the actomyosin contractility and the focal adhesions assembly²⁴⁴. Accordingly, RHOJ interact with the GIT–PIX complex, a regulator of focal adhesion disassembly²⁴⁵. Interestingly, RHOJ knockdown resulted in highly impaired tube formation in the *in vitro* models of angiogenesis HUVECs^{86,87,242,246}. The relevance of RHOJ in vasculature biology has been also assessed in ischemic retinopathy mouse models, where RHOJ activation prevented the assembly of disoriented blood vessels projections, distinctive features of the disorder²⁴¹. Consistently with its role in endothelial cells, RHOJ gene is found to be a target of the transcription factor ERG, member of the ETS (erythroblast transformation-specific) transcription factor family²⁴².

Concluding, CDC42 subfamily proteins own key functions in cell biology, where they contribute to the normal maintenance of tissues. Not surprisingly, in pathologic conditions their functional ability to regulate cytoskeletal dynamics and cell movement points them

to the center of cancer cell invasion and metastasis. Importantly, CDC42 proteins/PAK signaling represent one of the main route for cancer progression.

1.4. Therapeutic Relevance of the CDC42/PAK interaction

CDC42 proteins/PAK interaction mediates a wide variety of cellular functions by stimulating numerous signaling cascades. However, its importance in the physiological regulation of cytoskeleton dynamics, proliferation, mobility, apoptosis, and transcription is also reflected in its central role in cancer development and progression. PAK is a family of serine/threonine kinases that are effector proteins for both CDC42 and RAC proteins. Accordingly, GTP-bound CDC42 and RAC proteins target PAK kinases by binding to the CRIB (CDC42/RAC Interactive Binding) motif (I-S-X-P-(X)₂₋₄-F-X-H-X-X-H-V-G)^{247,248}. Based on sequence similarity, PAK kinases are classified in group I, which contains PAK1, PAK2 and PAK3 and group II, which contains PAK4, PAK5 and PAK6. Structurally, both PAK group members comprehend a highly conserved C-terminal catalytic kinase domain and an N-terminal regulatory domain, which includes the CRIB domain. Despite the similarities, group I and II PAKs follow a different regulation. Indeed, group I PAKs exist in a *in trans* autoinhibited dimeric conformation in which the catalytic domain binds the other dimerizing monomer through an autoinhibitory domain (AID), which overlaps with adjacent CRIB domain²⁴⁹⁻²⁵³. The binding of CDC42 to the CRIB domain displaces the dimeric interaction allowing a conformational change and the subsequent phosphorylation at critical sites of the activation loop for achieving and maintaining PAK kinase activity^{249,254-260}. Although their regulation is controversial, group II PAKs also have an AID-like domain but they seem to exist as monomer, unlike group I PAKs. The major hypothesis is that group II PAKs exist as monomer in an inactive conformation in which the AID-like domain of group II PAKs binds the catalytic kinase domain, which is relieved by the binding of CDC42 to the CRIB motif. Unlike group I PAKs, group II PAKs are constitutively phosphorylated at the activation loop, indicating that CDC42 could allosterically modulate the conformation of the constitutively phosphorylated kinases²⁶¹.

Despite the difference in their scheme of activation, once triggered by CDC42, PAKs are able to transfer the ATP γ -phosphate to a downstream substrate, modulating important signaling cascades, including cytoskeleton dynamics organization, cell proliferation, gene transcription, apoptosis and mobility. The list PAK-phosphorylated substrates is considerable and includes key regulators such as the LIM domain kinase (LIMK), the myosin light-chain kinase (MLCK), the Op18/stathmin, the extracellular signal-regulated kinase (ERK), the Aurora A kinases, the Polo-like kinase 1 (PLK1), the pro-apoptotic protein BAD, RAF1, Merlin and MEKK1^{1,179,204,206,223,262–268}. Notably, those signaling cascades are deregulated in cancer, where PAKs are found to contribute to neoplastic transformation and to the invasion of secondary sites, promoting metastasis^{205,269–272}.

PAK1 is involved in the modulation of the initial tumor phases as well as in the malignant progression. Accordingly, PAK1 is found to be overexpressed and/or upregulated in diverse type of tumor, including Ewing sarcoma, pancreatic, breast, colon, lung, prostate, gastric, hepatic, ovarian, thyroid and bladder cancer^{273–283}. In breast cancer, PAK1 is upregulated and induces potent malignant transformation, by triggering the MAPK, and MET signaling^{284,285}. Additionally, PAK1 promotes the transcription of the IL-6 gene, which encodes for the highly cancer-associated interleukin-6^{286,287}, as well as an increment of the proliferative processes, by overstimulating the cyclin D expression²⁸⁸. Moreover, the deregulated PAK1 activity supports the high invasiveness of breast cancer cells also by stimulating the anchorage-independent growth of cell and the abnormal organization of mitotic spindles during mitosis^{289,290}. Consistently with its role in aggressive breast cancer promotion, PAK1 induces tamoxifen resistance, by altering the estrogen receptors regulation^{291–294}. Proliferation, migration and invasion of mammary epithelial cells is also promoted by PAK1 through the phosphorylation of the Calcium/Calmodulin-Dependent Protein Kinase II (CaMKII), a breast cancer-associated protein^{295,296}. Interestingly, ivermectin drug has been shown to induce autophagy in breast cancer cells by inducing PAK1 ubiquitin-mediated degradation, which results in the blockade of the AKT/mTOR signaling²⁹⁷. Indeed, AKT/mTOR signaling is involved in lots of functions, among which autophagy regulation²⁹⁸.

The blockade of the PAK1/AKT/mTOR signaling is a successful strategy also in lung cancer treatment. Deeply, the treatment with *Ipomoea batatas* polysaccharides (IBPs) results in reduced lung cancer cell proliferation, as a consequence of the PAK1 ubiquitin-mediated degradation, activator of the AKT/mTOR pathway²⁹⁹. Upregulation of the PAK1/AKT/mTOR signaling has been also found to be the leading cause of adverse disease course in inflammatory bowel diseases and colitis-associated cancer³⁰⁰. Still in the context of lung cancer, PAK1 activity correlates with enhanced epithelial-to-mesenchymal transition and unfavorable prognosis^{301,302}. In addition, lung cancer is sustained by the PAK1 phosphorylation of the adaptor protein c-Crk, implicated in cancer aggressiveness and invasiveness^{303,304}. Finally, evidences highlight that PAK1 knockdown in cancer lung cells results in reduced phosphorylation level in key components of the MAPK signaling, such as MEK and ERK, which are fundamental to sustain tumor growth³⁰². PAK1-dependent MAPK pathway activation has been also associated to colorectal cancer progression and reduced chemosensitivity to 5-fluorouracil (5-FU). Specifically, PAK1 knockdown weakened G1/S cell-cycle transition, JNK and CDK4/6 activation and cyclin D1 expression³⁰⁵. Consistently, PAK1 and PAK4 upregulation is associated with colorectal cancer metastasis and enhanced infiltration^{306,307}.

PAK1 is also overexpressed in endometrial cancer, where it promotes cell proliferation and anchorage-independent growth by inhibiting caspase-3 mediated apoptosis^{308,309}. In pancreatic cancer, PAK1 is linked to boosted epithelial–mesenchymal transition and gemcitabine resistance through the downstream phosphorylation of TAK1, a serine/threonine kinase that controls a variety of cell functions, including apoptosis^{310,311}. Moreover, PAK1 weakens the efficacy of onartuzumab treatment in pancreatic adenocarcinoma³¹². Finally, in neurofibrosarcoma PAK1 induces and sustains Schwann cell transformation³¹³.

PAK2 is overexpressed in pancreatic cancer where it promotes cancer cell migration and metastasis by enhancing the matrix metalloproteinase MMP2 and MMP9 activity³¹⁴. In agreement with the importance of extracellular matrix remodeling in cancer cell migration, PAK2 is found to be enhance cancer cells migration in collagen type I (COLL) in ovarian malignancy³¹⁵. PAK2 is also overexpressed in adult T-cell

leukemia/lymphoma, where it regulates the activity of CADM1, a cell adhesion molecule involved in the migration of leukemic cells³¹⁶. In head and neck cancer, PAK2 is overexpressed and correlates with enhanced cell proliferation and paclitaxel and dimethylxaloylglycine chemoresistance³¹⁷. To achieve such malignant transformation and progression, PAK2 activates c-Myc, a transcription factor that regulate diverse function, among which cellular proliferation and growth^{318,319}. Indeed, downstream PAK2-dependent c-Myc activation induces the PKM2 gene expression, which encodes for the pyruvate kinase M2 (PKM2), a key enzyme in the Warburg cancer metabolism that contributes to tumor survival^{317,320–322}. In NF2-deficient mesotheliomas, PAK2 deletion results in decreased tumor cell viability and migration. Deeply, PAK2 phosphorylates the NF2 gene product Merlin, a tumor suppressor whose activity depends on its capacity to form an intramolecular interaction between its N- and C- terminals. Indeed, Merlin exist in an inactive open conformation and active closed conformations. PAK2 weakens the tumor suppressor activity of Merlin through its Ser518 phosphorylation, which inhibits Merlin self-interaction and its tumor suppressor activity^{266,323,324}. In breast cancer, PAK2 is a strong tamoxifen-resistance inducer³²⁵. Consistently, PAK2 has been shown to mediate therapy chemoresistance by negatively regulating cellular apoptosis. Specifically, PAK2 bind and phosphorylates at multiple site the caspase-7, a key protease involved in apoptosis and inflammation, resulting in chemotherapeutic resistance^{326,327}.

PAK3 promotes epithelial-mesenchymal transition in hepatocellular carcinoma, resulting in cancer progression, migration and metastasis³²⁸. In pancreatic cancer, PAK3 sustains malignant transformation through the AKT pathway triggering that, ultimately, increase β -catenin expression³²⁹. In ovarian carcinoma, PAK3 is overexpressed and reduces paclitaxel sensitivity. Additionally, the targeting-PAK3 miR-193b-3p is found to be downregulated in ovarian cancer cells, increasing PAK3 transforming activity³³⁰. miR-193-3p in also downregulated in colorectal cancer, where PAK3 is oppositely upregulated³³¹. In glioblastoma, PAK3 cooperates with the phosphoinositide-3-kinase (PI3K) isoform PI3KCD to promote aggressiveness and invasion³³². Despite controversial, PAK3 seems to be involved in the development and maintenance of human papillomavirus (HPV)-associated cervical carcinogenesis^{333,334}. Finally, in thymic

carcinoid PAK3 is overexpressed and promotes cell migration by activating the JNK pathway³³⁵.

In ovarian cancer, PAK4 upregulation significantly correlates with ovarian cancer progression. Specifically, PAK4 promotes ovarian cancer proliferation and migration by stimulating the downstream c-Src and MEK1/ERK signaling pathways, respectively^{223,336–338}. Indeed, PAK4/c-Src signaling cascade was found to control the G1-phase cell cycle progression through the epidermal growth factor receptor (EGFR), which in turn regulates cyclin D1 and CDC25A expression^{337–342}. Conjunctly, PAK4/MEK1/ERK signaling enhanced cell invasiveness by stimulating MMP2 activity, resulting in intensified cancer migration^{223,343,344}. In pancreatic cancer, cancer stem cells are responsible for tumor-maintenance and metastasis formation. Notably, PAK4 maintains stemness in those pancreatic cancer cells, by activating the STAT3 (signal transducer and activator of transcription 3) pathway, which, in turn, reinforces the oncogenic phenotype^{345,346}. Moreover, PAK4 promotes i) anchorage-independent growth and cell migration in pancreatic ductal adenocarcinoma by modulating p85 α , the regulatory subunit of phosphoinositide 3-kinase (PI3K)^{193,347} and ii) proliferation through the AKT- and ERK-dependent activation of NF- κ B pathway³⁴⁸. Remarkably, PAK4 overexpression is reported in various human cancer cell lines, where it is associated to unfavorable prognosis^{349–359}.

PAK5 role in cell migration and invasion has been reported in glioma³⁶⁰, as well as in lung³⁶¹, liver³⁶², gastric³⁶³, pancreatic³⁶⁴, colon^{365–367}, bladder³⁶⁸, breast cancer³⁶⁹ and other types of tumor^{370,371}. In breast cancer PAK5 promotes cell proliferation by enhancing cyclin D1 expression, through the activation of the transcription factor NF- κ B³⁷². Moreover, PAK5 sustains breast cancer development through the phosphorylation of i) the apoptosis-inducing factor AIF in mitochondria, preventing its translocation to nucleus where it can trigger apoptotic processes³⁷³, ii) the RNA helicase DDX5, promoting the processing of the microRNA-10b, a recognized tumorigenesis-stimulating factor^{374,375}, and iii) the aspartyl aminopeptidase DNPEP, modulating the activity of the downstream tumor promoter USP4 (Ubiquitin Specific Peptidase 4)³⁷⁶. In glioma and breast cancer, PAK5/Erg1/MMP2 pathway is also connected to cell migration and invasion^{360,377}. Deeply, Erg1 is a transcription factor that controls the MMP2 promoter³⁷⁸. In ovarian cancer, PAK5

induces epithelial-to-mesenchymal transition and promotes cell migration and invasion by activating the PI3K/AKT pathway. Specifically, PI3K catalyzes the phosphorylation of PIP2 to generate the lipid second messenger PIP3, which, in turn, activates AKT³⁷⁹. Next, AKT modulates various cellular functions including cell survival, proliferation, growth, migration, and invasion³⁸⁰. PAK5 is also associated to enhanced osteosarcoma progression and lung metastasis. Deeply, the matrix metalloproteinase 2 (MMP2) was found to be the downstream substrate involved in the metastatic progression³⁸¹. PAK5 is also overexpresses in myelodysplastic syndrome patients, where it downstream modulates LMO2 and GATA1, important transcriptional regulators hematopoietic stem cell development^{382,383}. Finally, PAK5 phosphorylates the special AT-rich sequence-binding protein-1 (SATB1) inducing epithelial–mesenchymal transition of cervical cancer cells and lung metastasis³⁸⁴.

PAK6 promotes cervical cancer proliferation, migration and invasion during oncogenesis in cervical cancer, by positively regulating the Wnt/ β -catenin signaling pathway³⁸⁵. In hepatocellular carcinoma, PAK6 activity is upregulated and correlates with clinical parameters³⁸⁶. Increased PAK6 expression and activity are also found in prostate cancer, where IQGAP1 and the Ser/Thr protein phosphatases PP1B have been identified as downstream substrates^{387,388}. Additionally, in prostate cancer PAK6 knockdown boosted the antitumor effect of docetaxel³⁸⁹. Likewise, PAK6 confers resistance to 5-fluorouracil (5-FU) chemotherapy treatment in colon cancer³⁹⁰. In prostate cancer, PAK6 inhibition is associated to increased radiosensitivity. Interestingly, the molecular mechanism underlying the protective function of PAK6 involves i) the hampering of apoptotic pathways by phosphorylating the BAD (Bcl-2 agonist of cell death) factor, ii) the protection of cancer cells from the double stranded DNA damage induced by the radiotherapy, and iii) the promotion of the cell cycle progression^{391,392}. Similarly, in gastric cancer PAK6 induces oxaliplatin chemoresistance by enhancing the ATR signaling-mediate homologous recombination (HR) DNA repair^{393,394}. Furthermore, PAK6 has been proposed to be a suitable biomarker of adenocarcinoma³⁹⁵ and clear cell renal cell carcinoma (ccRCC)³⁹⁶. Finally, PAK6 is required for carcinoma cell–cell adhesions disassembly to drive cancer cells through the epithelial-to-mesenchymal transition, by

interacting with IQGAP and β -catenin at the E-cadherin cell junctions³⁹⁷. Interestingly, PAK6 is found to target cellular junctions in a CDC42-dependent way³⁹⁸.

Despite their central role in oncogenesis, PAKs are also involved in other non-cancer disorders including Alzheimer^{399,400}, Huntington⁴⁰⁰ and Parkinson's⁴⁰¹ diseases, diabetes⁴⁰², cardiac⁴⁰³ and pancreatic acinar cells dysfunctions^{404,405}. Concluding, CDC42/PAK interaction triggers downstream cascades linked to pathological conditions development and progression, making of it a promising protein-protein interface to pharmacologically target.

1.5. Targeting CDC42/PAK signaling: *the state of art*

Due to the associated therapeutic importance, several efforts have been done to quench deregulated CDC42/PAK signaling by trying to target both CDC42 and PAK proteins.

1.5.1. CDC42 family inhibitors

Because of their globular structure with limited small-molecule binding pockets and their high affinity for GTP/GDP, CDC42 proteins have been always considered *undruggable*⁴⁰⁶. Nevertheless, some rational approaches to inhibit CDC42 signaling have been proposed, among which hampering the CDC42/GEF interaction and nucleotide binding are the most investigated. Indeed, based on the structural information of the known RAC1 inhibitor NSC23766⁴⁰⁷, the small molecule inhibitor EHop-016 has been firstly identified as a RAC/GEF inhibitor able to affect also CDC42 at concentration higher than 10 μ M^{406,408}. The pharmacokinetic improvement of EHop-016 inhibitor led to the development of MBQ-167, a dual RAC/CDC42 activation inhibitor that showed IC50 values of 103 and 78 nM for RAC and CDC42, respectively⁴⁰⁸. Additionally, the development of the reported CDC42/GEF interaction inhibitors AZA1⁴⁰⁹ and AZA197⁴¹⁰ has been also based on the RAC1 inhibitor NSC23766 structure. Finally, ZCL278 targets the specific interaction between CDC42 and the CDC42-GEF intersectin⁴¹¹. Outstandingly, secramine A is found to inhibit CDC42 acting at the RHOGDI level control

of the regulation cycle, by stabilizing the CDC/RHO GDI complex and, thus, blocking the CDC42 membrane recruitment⁴¹².

An alternative investigated strategy to inhibit CDC42 proteins has been to prevent nucleotide binding. Indeed, a series of isoquinolines and phenantridine derivatives⁴¹³ and the small molecule MLS000532223⁴¹⁴ are general RHO GTPases inhibitor that prevents GTP-binding in a dose-dependent fashion. Nevertheless, because of the high cellular GTP concentration, their pharmacological power is limited. Also, compound CID2950007 and its analog CID44216842 are CDC42 non-competitive allosteric inhibitor whose proposed mode of action is to bind to an allosteric pocket adjacent to the nucleotide binding site to promote nucleotide dissociation, locking the protein in an inactive conformation⁴¹⁵.

Despite the evidence regarding the positive effects of small molecules inhibitors in CDC42-mediated cancer promotion, there are still some selectivity-related limits. For instance, CDC42 and RAC1 have overlapping roles in platelet function⁴¹⁶ and the blockade of both signaling from RAC/CDC42 inhibitors often results in thrombocytopenia *in vivo*⁴¹⁷ and cardiotoxicity^{418,419}. Thus, it is extremely needed to identify small inhibitors compounds able to avoid off-target effects, improving the therapeutic beneficial. Indeed, despite some inhibitors are found to be specific for CDC42, the related RHOQ and RHOJ have redundant activity and could counterbalance the small molecules inhibitory effect, by feeding the deregulated signaling pathways^{140,230,235,420}. Accordingly, RHOQ AND RHOJ intensively contribute to oncogenesis, by aberrantly regulating key pathways in melanoma⁴²¹, breast cancer⁴²², gastric cancer⁴²³, tumor angiogenesis⁴²⁴⁻⁴²⁸, chemoresistance^{424,429} and cancer invasion^{430,431}. Overall, the motivating results of these investigations overcome the definition of CDC42 as *undruggable* proteins, encouraging to look for new therapeutic strategies that target all members of the CDC42 family.

1.5.2. PAK inhibitors

Considering the critical roles of PAK family members in cancer development, diverse ATP-competitive and allosteric inhibitors have been identified. For instance, the small-molecule FRAX597 has been identified through a structure-activity relationship

approach starting from a chemical series identified from high-throughput screening. The X-ray structure of PAK1/FRAX597 co-crystal highlighted the ATP-competitive mechanism underlying the detected inhibition⁴³². PF-3758309, FL172, K-252a and OSU-03012, other ATP-competitive inhibitors, have been shown to inhibit tumor growth^{433–436}. Despite the enormous efforts to develop PAK-specific ATP-competitive inhibitors as therapeutic drugs, the high structural similarities within the ATP catalytic pockets has impeded the identification of high-affinity inhibitors. Accordingly, broad and robust analysis highlighted the ability of ATP-competitive inhibitors to inhibit a large number of other kinases in addition to their aimed targets^{437,438}. Undoubtedly, the biological consequences of multi-kinase activity compounds would lead to the deregulation of pathways not involved in the disease, further complicating the clinical condition^{437,439}. In line with the complications to identify selective ATP-competitive small molecules, the promising PF-3758309 inhibitor did not proceed beyond phase I studies^{440,441} and CEP-1347, despite the preliminary detected PAK1-selectivity, was found to be about 100-fold more selective for the kinase MLK3 than PAK^{406,442}.

An alternative route towards PAK inhibition was to try to develop non-competitive inhibitors, able to modulate kinase activity by binding to other protein site ad not in the ATP catalytic pocket. Accordingly, IPA-3 was developed as an allosteric inhibitor able to prevent PAK activation by covalently interacting with the regulatory domains rather than the ATP-binding site, stabilizing the autoinhibited PAK conformation^{443,444}. Unfortunately, despite the shown potency and PAK group I selectivity in experimental conditions, IPA-3 disulfide moiety is reduced under physiologic conditions, resulting in consequent ineffectiveness^{439,445–447}.

To the best of my knowledge, up to date only the ATP-competitive inhibitor KPT-9274 is ongoing in phase I clinical trials (NCT04914845 and NCT04281420). However, it is worthy to note that this small molecules is not PAK-specific but it is a dual inhibitor that targets both PAK4 and NAMPT (Nicotinamide phosphoribosyltransferase)^{448–451}. So far, it clearly emerges the necessity to develop new drug design strategies to target the CDC42/PAK signaling, acting on the blockade of the protein-protein interaction established between the active CDC42 and PAK proteins, the crucial moment in which the activation signal is downstream activated and transmitted.

1.6. Investigation of protein-protein interactions to uncover druggable interaction

The characterization of protein-protein interactions (PPIs), such as CDC42/PAK, is advantageous to address the development of new drug design strategies, predicting key residues involved in the recognition mechanism and, thus, facilitating the identification of druggable interactions. Protein-protein interactions are dynamic, but specific, noncovalent associations through which cells receive, integrate, and distribute regulatory information^{452,453}. Many key biological functions, including cell regulation and signaling, involve the formation of protein-protein complex, as described for CDC42/PAK. On the other hand, many human diseases result from aberrant regulation of protein-protein interactions. For this reason, drug discovery projects often aim to selectively target disease-specific protein-protein contacts involved in the deregulated signaling pathway. An approach to get insights in the established interactions and identify the pivotal residues in the binding, called *hotspot*, is to compare the affinity between *wild-type* and mutant systems. The affinity between the two proteins results from the particular shape and physico-chemical complementarity between the two protein interfaces in contact, in addition to other environmental factors. Mutagenesis is undoubtedly a leading experimental technique for the study of protein-protein interactions that can reveal key residues that, upon their mutations, affect protein-protein binding the most. However, the number of possible mutants to consider can be excessively high and the resulting experimental procedure could be markedly time consuming. In this regard, computational methods capable of predicting the effects of mutations and quantifying the binding affinity between proteins would help rank the most relevant mutations to validate in experimental studies.

Described structural bioinformatics tools to address this problem have been developed based on various characteristics of PPIs, including protein and genome sequences, function and protein structure^{453–455}. The sequence-based methods use the information contained in the amino acid sequence of the considered proteins. Indeed, common methodologies aim to identify sequence motifs known to be patterns of interacting proteins or homology proteins with conserved function and, possibly, interactors. Besides protein sequences, genome sequences are also largely used to detect

proteins that are functionally related. Additionally, functional similarity or shared functions are considered in the function-based methods to predict PPIs. Recently, deep learning methods have been developed to predict protein binding interfaces⁴⁵⁶. Since PPIs depend on the shape and physico-chemical complementarity between the two interacting protein surfaces, it is not surprising that many computational structure-based methods have been developed. Among them, protein-protein docking aim to provide structural insights of the interaction. Noteworthy protein-protein docking developed tools are LZerD⁴⁵⁷, GRAMM-X⁴⁵⁸, ZDOCK⁴⁵⁹, RosettaDock⁴⁶⁰, HADDOCK⁴⁶¹, SwarmDock⁴⁶², HEX⁴⁶³ and ClusPro⁴⁶⁴. Overall, docking methods build protein-protein complex models starting from the discrete protein structures through the generation of thousands of different docking poses trying to find the best match based on the shape complementarity. The PPI models are subsequently ranked respect to the *docking score*, which derives from the contribution of the single established contacts (e.g. electrostatic, solvation and hydrophobic contributions)^{465–467}.

Despite flexible docking consider a much greater number of degrees of motion⁴⁶⁸, the possibility to take fully into account the protein flexibility, improving protein-protein prediction, has been achieved thanks to the great improvements in computing performance and atomistic molecular dynamics (MD) simulations. In this context, free energy calculations, such as MM/GBSA and alchemical free energy approaches, are computational methods routinely and successfully used to design small-molecule drugs^{469–472}. Despite less explored, alchemical free energy calculations can be used to rationalize or predict the effect of protein mutations by exploiting “unphysical” transformations between end-states^{473–476}. Accordingly, Friesner and co-workers have recently reported a study exploring the performance of alchemical free energy calculations for investigating mutations at antibody/glycoprotein interfaces, with encouraging results for the design of tailored antibodies^{477,478}. Interestingly, the application of physics-based free energy methods has been described in the context of protein-peptide binding^{479,480}.

Concluding , since proteins are not rigid bodies and protein-protein interactions are based on dynamic, but specific, arrangements of contacts, a comprehensive computational investigation should take into account the fully protein flexibility. In this

regard, recent indications opened the street towards the use of alchemical free energy calculations to guide the exploration of druggable interactions. Accordingly, alchemical free energy calculations are investigated in the present work as a suitable computational approach able to predict key residues involved in protein-protein binding, facilitating the identification of druggable interactions in the contest of a drug design project.

Chapter 2. Theory and Methods

Computational methods have become central in all the drug discovery stages, from hit identification to lead optimization, as well as in the study of the complex mechanism underlying biological systems⁴⁸¹. With the purpose of uncover drug design strategies to target deregulated RHO GTPases signaling, together with the evaluation of *in silico* methods able to predict key residues involved in the recognition mechanism, diverse computational approaches have been employed in this thesis. Correspondingly, molecular docking, molecular dynamics simulations and free energy calculation methods will be described.

2.1. Molecular Docking

Molecular docking is a multistep computational technique introduced by Kuntz et al.⁴⁸², aimed at predicting and evaluating the interaction between a target (e.g. biomolecule) and a ligand. Specifically, molecular docking calculations are achieved by implementing two interconnected steps, which are the sampling of the ligand orientation in the defined site of the target and the ranking of the generated conformations via a scoring function^{483,484} (Figure 5).

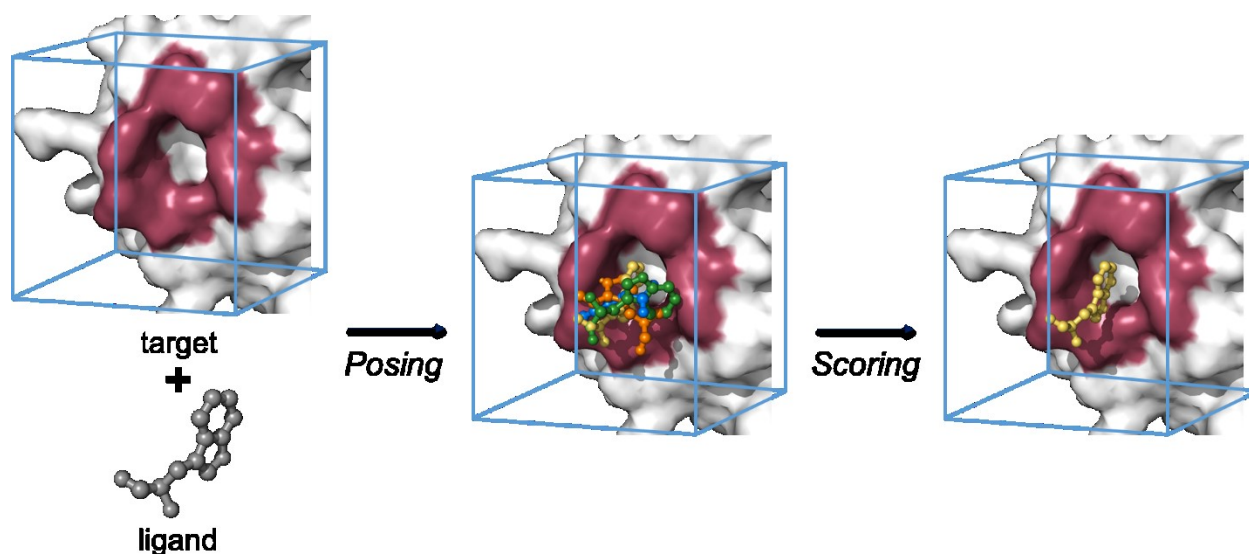


Figure 5. Molecular Docking. The general Molecular Docking procedure is represented. The main two steps of the molecular docking method are the targeted pocket-ligand exploration through the implementation of sampling algorithms and the estimation of the score value for each pose, computed through the implementation of the so-called scoring functions. The score is the rational used to evaluate the chemical-physical and geometric complementarity between target and ligand and to rank the generated poses. In the reported example, the target is represented as white surface, with the pocket explored highlighted in red, while the ligand is illustrated as gray sticks. The generated poses during the posing step are reported in multicolor. Finally, although the standard molecular docking output is a ranking of the generated poses, in the Figure only the highest score pose is reported in yellow.

Since the goal of molecular docking is to find the best target-ligand match, the sampling of the ligand orientation in the defined site of the target, also called *posing*, is an essential step⁴⁸⁵. Indeed, sampling algorithms have been developed to explore the conformational space and, thus, the possible orientations and chemical-physical and geometric complementarity of the target-ligand binding. Noteworthy, among them i) *matching algorithms* (MA) are geometry-based algorithms in which both the target and the ligand are represented as pharmacophores^{486,487}; ii) *incremental construction* (IC) are fragment-based algorithms in which the ligand is docked incrementally^{488,489}; iii) *multiple copy simultaneous search* (MCSS)⁴⁹⁰ and *LUDI*⁴⁹¹ are fragment-based algorithms which are particularly used for the *de novo* design of ligands or to modify and improve the structure of known ligands; finally, iv) *Monte Carlo* (MC)⁴⁹² and *genetic algorithms*^{493,494} are stochastic methods which explore the conformational space by randomly modifying the ligand conformation. The software *Glide*, employed in this thesis, is an example of docking program that apply MC methods⁴⁹⁵. The posing procedure is also strictly dependent on the docking approach employed⁴⁸³⁻⁴⁸⁵. For instance, when both ligand and target are considered rigid, the search space is very restricted and ligand flexibility could be taken into account by pre-generating a set of ligand conformations. However, the dynamic nature of the ligand-target interaction cannot be taken fully into account in this rigid approach. To face these limits, semi-flexible and flexible docking approaches have been developed⁴⁸³. Indeed, higher degrees of complexity are included in the semi-flexible docking, where the target is still considered rigid, but the ligand is free to move adopting

diverse conformations. In flexible docking both the ligand and the target are treated as flexible. Since the flexible treatment of the full target would be computationally demanding, most of the available docking programs allow the movement of the target side chains. Indeed, the number of possible binding modes between the ligand and the target would be excessive and their prediction computationally prohibitive, if all the translational and rotational degrees of freedom are considered. However, thanks to the considerable computational resources available nowadays, molecular dynamics (MD) based methods, the so-called *dynamic docking*, can significantly improve the atomic-level description of the ligand-target binding. Indeed, *dynamic docking* allows to fully take into account the structural flexibility of the ligand-target interaction, but also to compute quantitative thermodynamics and kinetics estimations associated with the binding^{496,497}.

The *posing* procedure is intersected with the evaluation of the ligand-target affinities for each generated pose, through the so-called *scoring functions*. Indeed, the resultant *score* is the rationale used to rank the generated conformations, allowing the identification of poses, or compounds in case of multiple ligands, of potential interest. Overall, scoring functions can be divided in force field-based, empirical and knowledge-based⁴⁸³. Force field-based scoring functions calculate the ligand-target affinity by evaluating the contributions of the non-bonded electrostatics and van der Waals interactions according to the molecular mechanics (MM). Specifically, the electrostatic terms are calculated according to the Coulombic formulation, while the van der Waals terms are described by a Lennard-Jones potential^{498,499}. Force field-based scoring functions have been extended taking into account hydrogen bonds, solvations and entropy contributions in docking softwares, such as DOCK⁵⁰⁰, GOLD⁵⁰¹ and AutoDock⁵⁰². Empirical scoring functions compute the final score by summing the contribution of the single ligand-target contacts, such as hydrogen bonds, ionic and hydrophobic interactions, that are firstly multiplied by weighting factors, called *coefficients*. In details, the *coefficients* used in empirical scoring functions are obtained by regression analysis performed on reported experimental data⁵⁰³. Finally, knowledge-based scoring functions evaluate ligand-target affinity from the statistical analysis of reported ligand-target complexes crystal structures. Specifically, knowledge-based scoring functions consider the contact frequencies and/or distances between ligands and biomolecules in reported

crystal structures and generate a related frequency distribution. Next, knowledge-based scoring functions calculate the score assigning higher values to interactions that occur with high frequency in the generated frequency distribution⁵⁰⁴. Additionally, physics-based scoring functions based on MMPB/SA (Molecular Mechanics Poisson-Boltzmann Surface Area) and MMGB/SA (Molecular Mechanics Generalized Born Surface Area) have been developed to consider also the solvation effect⁵⁰⁵. The software *Glide* employs a scoring function that combines empirical and force field-based terms⁴⁹⁵.

A relevant application of molecular docking is in Virtual Screening (VS) campaigns, where chemical libraries of small molecules is docked into the target in order to identify hit compounds that are subsequently synthesized, or purchased, and submitted to biological assay⁴⁸⁴. Conceptually, the experimental counterpart of VS is represented by the high-throughput screening (HTS), in which large chemical libraries are tested *in vitro* towards the biological target of interest⁵⁰⁶. However, while HTS necessitates expensive equipment and facilities, VS is cheaper, less time demanding and allows the evaluation of a broader chemical space. For this reason, VS is a routinely employed in the early-stage of mostly of the drug discovery projects^{481,483,484,507,508}.

2.2. Molecular Dynamics Simulations

Developed in the late 1970s, molecular dynamics (MD) simulations are computational methods regularly used in research to study the atomic-level evolution of structural and quantitative properties of molecular systems over time^{509–511}. Indeed, molecular dynamics simulations represent key tools to investigate complex dynamic processes that take place in biological systems, such as protein folding, conformational changes, molecular recognition, ions transport, but also ligand-target interaction, as in the dynamic docking^{512–515}.

2.2.1. Force field

MD simulations theory is based on the principles of the molecular mechanics (MM) approach, avoiding the complex formalism of quantum mechanics (QM). Indeed, in MD

simulations the molecular systems are modelled according to the laws of classical mechanics, allowing the simulation of the motion system with reasonable computational resources. Specifically, atoms are represented as rigid beads, by neglecting the contribution of electrons, endowed of precise properties, such as atom type (e.g., atom hybridization, radius, etc.) and partial charge, while bonds are treated as springs, also described by detailed physicochemical properties (e.g. lengths, angles, and dihedrals)⁵¹⁶. Importantly, within classical MD simulations, covalent bond breaking and forming is not allowed. Indeed, the inter- and intra- molecular interactions within a simulated system are described according to the classical mechanics calculation of the potential energy, which, in turn, is associated to the atoms rearrangements during the MD simulation. Specifically, potential energy results from the contribution of bonds, angles and dihedrals to shorten-lengthen (*stretching*), flex (*bending*) and rotate (*torsion*), respectively, but also from the *non-bonded* contacts contribution (Figure 6). The stated contributions are combined in a potential energy function, called *force field*^{515,517,518} (eq. 1):

$$V = V_{stretching} + V_{bending} + V_{torsion} + V_{non-bonded} \quad (\text{eq.1})$$

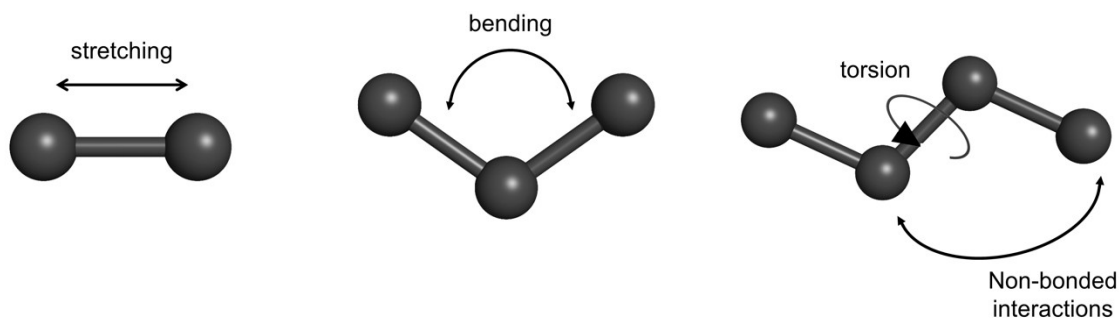


Figure 6. Force field contribution. In molecular mechanics (MM), molecular systems are modelled according to classical physics in which atoms and bonds are treated as beads and springs, respectively. The calculation of the system potential energy results from the contribution of bonds stretching, angles bending, dihedrals torsion and non-bonded contacts.

Being atoms and bonds respectively treated as beads and springs, the bond is not rigid, but flexible, and allows the two atoms to move away and closer depending on the extension of the spring, *stretching* respect to reference equilibrium values. Indeed, the first term of the equation describes the potential energy associated to the interactions between the pairs of atoms in the system considering the displacement of the extension of the spring respect to a reference equilibrium value. An approach to describe $V_{stretching}$ is to use the Morse potential⁵¹⁹ (eq.2), in which the potential stretching energy between two directly bonded atoms is stated as:

$$V_{stretching} = D_e [1 - e^{-a(l-l_0)}]^2 \quad (\text{eq.2})$$

where l is the bond length l_0 is the equilibrium bond length, D_e is the dissociation energy at the minimum of the curve (i.e. when $l = l_0$) and a is parameter that expresses the mass of the oscillating particles and the frequency of the bond vibration. Although the Morse potentials is highly accurate, it is also expensively time-consuming to calculate, because of the exponential term. Accordingly, when bonds are not expected to deviate significantly from their equilibrium values, the simpler harmonic function (eq.3) is used to describe the oscillation around the equilibrium bond length values. In detail, the Hooke's law formula is used to describe the spring deformation as:

$$V_{stretching} = \sum_i^{Nbonds} k_{b,i} (l_i - l_{0,i})^2 \quad (\text{eq.3})$$

where l is the bond length of the bond i , l_0 is the equilibrium bond length, and k_b is a bond-specific constant which determines the deformation of the spring. For each type of bond, k_b and l_0 values are assigned according to the nature of the bond and to the type of the forming atoms (e.g. C-C, C-H, C-O, etc.). Noteworthy, the total $V_{stretching}$ is computed as a Taylor series expansion for every pair of bonded atoms^{509,515,518,520}.

The second term of the equation describes the potential energy associated to the angle stretching, called *bending*, also respect to a reference equilibrium value. Notably, *bending* can describe in-plane symmetric (*scissoring*), in-plane asymmetric (*rocking*), out-of-plane symmetric (*twisting*) and out-of-plane asymmetric (*wagging*) angle stretching

events. Despite higher-order terms can be included to improve the accuracy of the angles description, generally $V_{bending}$ is mathematically defined for every triplet of bonded atoms as a harmonic function (eq.4) that describes the oscillation around an equilibrium angle value:

$$V_{bending} = \sum_i^{N_{angles}} k_{\theta,i} (\theta_i - \theta_{\theta,i})^2 \quad (\text{eq.4})$$

where θ is the bond angle, θ_0 is the equilibrium bond angle, and k_{θ} is a angle-specific constant which determines the angular deformation stiffness of the spring. As for bond stretching, for each type of angle, k_b and l_0 values are assigned according to the nature of the bond and to the type of the forming atoms (e.g. C-C-C, C-C-O, C-C=O, etc.) and the total $V_{bending}$ is computed as a Taylor series expansion for every triplet of bonded atoms^{509,515,518,520}.

The third term of the equation describes the change in potential energy resulting from the bonds rotation. In detail, given four sequentially bonded atoms, the torsion energy is defined as the rotation angle around the bond between the middle two atoms. Because of the intrinsic periodic nature of the torsion angle, torsional potential energy is described as a periodic sinusoidal function^{509,515,518,520} (eq.5):

$$V_{torsion} = \sum_i^{N_{torsions}} k_{\omega,i} [1 + \cos(n\omega_i + \gamma_i)] \quad (\text{eq.5})$$

where k_{ω} is the torsion-specific force constant that regards the amplitude of the periodic function, n is a parameter describing the function periodicity, ω is the angle torsion i and γ is the corresponding phase angle. As for bond stretching and angle bending, detailed and distinctive parameters for torsional rotation are assigned to each bonded quartet of atoms based (e.g. C-C-C-C, C-O-C-N, H-C-C-H, etc.).

Finally, the fourth term of the equation 1 describes the potential energy associated to the inter- and intra- *non-bonded* contacts within the simulated system. Specifically,

$V_{non-bonded}$ arises from the contribution of both electrostatic and non-electrostatic interactions between all pairs of atoms^{509,515,518,520}.

$$V_{non-bonded} = V_{electrostatic} + V_{non-electrostatic}$$

As stated before, in the MM approach atoms are described as point charge beads, which reproduce the electrostatic properties of the system. Specifically, electrostatic interactions depend on the partial atomic charge, as well as on the distance and the dielectric interposed (eq.6). Accordingly, the electrostatic energy $V_{electrostatic}$ is given by Coulomb's formulation^{509,515,518,520}:

$$V_{electrostatic} = \sum_{i,j}^{pairs} \frac{q_i q_j}{4\pi\epsilon_0 r_{ij}} \quad (\text{eq.6})$$

where q_i and q_j are the partial charges of the pair of considered atoms, ϵ_0 describes the vacuum permittivity and r_{ij} is the distance between particles i and j .

Non-electrostatic interactions are represented by the Van der Waals interactions, which are attractive or repulsive forces established between atoms. Deeply, at short distances these interactions are strongly repulsive due to the overlap of electron cloud, while at intermediate distances, *electron correlation* induces atoms attraction generating a temporarily induced dipole moment. The resulting attractive forces are called *dispersion forces* or *London forces*. Attractive London forces are described according to the *Drude model* that predict that the dispersion interactions vary with $1/r^6$. Conversely, repulsion forces are modeled according to an equation stating that the repulsive interactions vary with $1/r^{12}$. Accordingly, Van Der Waals interactions are overall modelled according to the so-called 6-12 potential (eq.7), or Lennard-Jones potential^{509,515,518,520}:

$$V_{non-electrostatic} = \sum_{i,j}^{pairs} 4\epsilon_{i,j} \left[\left(\frac{\sigma_{i,j}}{r_{i,j}} \right)^{12} - \left(\frac{\sigma_{i,j}}{r_{i,j}} \right)^6 \right] \quad (\text{eq.7})$$

where $\epsilon_{i,j}$ is a parameter defining the depth of the energy well, $\sigma_{i,j}$ is the collision diameter (i.e. the distance at which the interaction energy cancels out), while $r_{i,j}$ is the

interatomic distance. Thus, Lennard-Jones potential describes the energy variation as a function of the geometric variable $r_{i,j}$, with a negative (attractive) term proportional to $1/r^6$ and a positive (repulsive) term proportional to $+ 1/r^{12}$.

Deductible, the reliability of a force field to compute the total potential energy of a system extremely depends on the use of descriptors, the *parameters*, suitable to appropriately describe the simulated system. Parameters include physicochemical properties describing the system atoms (e.g., atom hybridization, radius, charge) as well as the established bonds, angles, and dihedrals that can be predetermined via either experiments or high-level-of-theory methods. Accordingly, the overall process, called parameterization, is extremely elaborate. To date, various force fields are regularly used in MD simulations, including AMBER⁵²¹, OPLS⁵²², GROMOS⁵²³ and CHARMM⁵²⁴.

2.2.2. Non-bonded interactions computation

A representative simulation of a biomolecular system should consider a solvent that extends infinitely. However, the limited computational resources make it impracticable, leading to the assume some approximations. One of them is represented by the representation of the solvent is a simulation box, including water, ions and/r other molecules, if desired. In the simulation box, the number of possible interactions grows linearly with the dimension of the system, and so does the calculation work for the non-bonded terms. Accordingly, in order to limit the computational cost of the non-bonded terms calculations, a threshold values, called *cut-off* is introduced⁵²⁵. Specifically, cut-off is defined as a spherical radius expressed in Å beyond which interactions are not considered. The choice of the cut-off value is not random, but depends on the size of the system, the number of atoms and a series of considerations ascribable to the simulated system. Indeed, the choice of the cut-off value can be seen as a compromise between the needed computational time and the desired information to be obtained, so that the value will not be too large to make the computational calculations prohibitive, but nor too small to not consider important interactions that define the behavior of the system. Simply cutting the non-bonded interactions off at a given distance could lead to discontinuities in the energy computation. To smoothly moderate these effects, the cut-off is associated

with a parameter relative to the atoms located at the cut-off boundary: the *switching atoms*. The switching atoms are atoms placed at the boundary shaped by the cut-off radius, which, during the simulation, can move within and beyond this boundary. The switching parameter, in particular, indicates the distance within which this movement is allowed. Thus, the switching function is used to truncate the non-bonded interactions potential energy smoothly at the cutoff distance^{525,526}.

However, the evaluation of the electrostatic interactions through the only cut-off truncation is often not adequate to treat the simulated system. Greater accuracy can be obtained with the Particle Mesh Ewald (PME) method that is efficiently used in molecular dynamics to compute the long-range electrostatic interactions^{525,527}. The method is based on the Ewald summation and requires *periodic boundary conditions* and charge neutrality of the molecular system in order to accurately performs. Periodic boundary conditions (PBC) denote a scheme used to infinitely replicate the primary simulation box in all three x, y and z directions. The purpose of using PBC is to minimize the effects the borders of such box that could cause the molecules placed near the surface to experience forces different from those to which the molecules arranged internally are subject, influencing the result of the simulation⁵¹⁸. Thus, molecules in the main box and their periodic images move in the same way. As consequence, when a molecule leaves the central box one of its images will enter it from the opposite side, allowing the description of the simulated system from the analysis of the primary simulation box. Based on these assumptions, Ewald sum method (eq.8) calculates the electrostatic energy of N point charges as:

$$V_{electrostatic} = \frac{1}{2} \sum_i^N \sum_j^N \sum_{n_{xyz}}^* \frac{q_i q_j}{4\pi\epsilon_0 r_{i,j+n_{x,y,z}}} \quad (\text{eq.8})$$

where $n_{x,y,z}$ represent the lattice points expressed as integers, q_i and q_j are the partial charges of the pair of considered atoms and r_{ij} is the distance between particles i and j . The * symbol indicates that terms with $i = j$ should be omitted when $((n_x, n_y, n_z) = (0,0,0))$. Notably, this sum converges very slowly. Later, with the idea to speed-up this single slowly converging sum, the PME method, that is based on the split of the calculation of in two faster-converging sums, was introduced^{525,528}. Accordingly, the

essential idea of PME method for the calculation of the electrostatic interactions is to replace the direct sum of the interaction energies between point particles with two sums: a direct sum for the short-range potential and a sum, through the Fast Fourier transforms, for the long-range part^{525,529}.

2.2.3. MD simulation procedures

In order to investigate the time-dependent behavior of the system at atomic level, MD simulations have to generate a time-dependent series of configurations of the simulated system. To address this goal, MD simulations implement a series of consecutively steps, whose starting point is a set of coordinates that define the system. Being the cartesian coordinates the most common approach, for N atoms 3N cartesian coordinates specify the atomic-level system position. Specifically, the initial atoms positions can be obtained from experimental data (NMR, X-ray, CryoEM) or by computational modeling (homology modeling). However, coordinates are not the only requirement for the generation of time-dependent series of the system configurations. Indeed, initial velocities need to be set. Accordingly, initial velocities are randomly assigned to each atom according to the Maxwell-Boltzmann distribution⁵³⁰ (f_{MB}) at the chosen temperature T (eq.9). Deeply, the Maxwell-Boltzmann distribution exploits the speed-temperature relationship to provide the probability that a given particle of mass m has a certain velocity v as a function of temperature T :

$$f_{MB} = \left(\frac{m}{2\pi k_b T} \right)^{\frac{3}{2}} 4\pi v^2 e^{-\frac{mv^2}{2k_b T}} \quad (\text{eq.9})$$

where f_{MB} represent the probability distribution function, k_b is the Boltzmann constant and T is the temperature. Thus, atoms position and velocities at time $t = t_0$ are determinant for the MD simulation evolution^{509,520}. Generally, MD simulation consists of three important steps: minimization, equilibration and the final production, when atoms are moved according to Newton's second law of motion.

2.2.3.1 Minimization

Minimization consist in the practice to relax the input initial system to a minimum energy conformation through the adjustment of degrees of freedom (i.e. stretching, bending and torsion). As described before, the potential energy associated with a molecular system is a multidimensional function of the coordinates that can be described by a *potential energy surface* (PES). Deeply, the PES is a mathematical function that shows the relationship between the system energy and its geometry (i.e., atom positions) providing useful information about the system's properties. Indeed, even if PES in theory would admit infinite configurations, in reality only a subset of molecular geometries are possible and, among them, the more stable ones, with lower energy, correspond to the conformations that the molecule assumes with greater probability. The derived energy profile creates an energy *landscape* made up of *valleys* and *passes*, which identifies points of interest defined by local and global minimum points, local and global maximum points and saddle points⁵²⁵. Minimum points correspond to low-energy conformations and, therefore, greater stability, with the global minimum point corresponding to the conformation associated to the lowest energy. Conversely, maximum points describe high-energy conformations with the global maximum point corresponding to a highest energy point. Finally, saddle points represent transition states that connect two minima through a path of energy as minimum as possible. Indeed, high saddle points make energetically prohibitive the access to some minima⁵²⁵.

To identify the low-energy conformations, the most intuitive approach is to scan the PES space. However, this is inapplicable for large systems with many degrees of freedom. Consequently, algorithms are employed to calculate the derivatives of the energy with respect to the coordinates. Two common algorithms used are *steepest descent* and *conjugate gradient*. As deducible from the name, the *steepest descent* algorithm drives the search towards low-energy conformations shifting along the maximum slope until the closest minimum point is identified^{525,531–533}. Steepest descent algorithm iteratively employs as starting point the molecular conformation obtained from the previous step and performs the next step following a direction that is orthogonal to the previous. For this reason, although the algorithm is very efficient in the early stages of the search, in the vicinity of minimum energy conformations the path assumes a *zig-zag*

pattern which makes it unsuccessful. On the other hand, the conjugate gradient algorithm searches for low-energy conformations through mutually conjugate directions, so that at each successive step there is a refinement of the direction towards the minimum. This aspect makes the conjugate gradient particularly suitable for performance near minima^{525,532,534,535}. Accordingly, a standard and efficient procedure is to use the steepest descent algorithm for the first minimization steps and, then, switch to the conjugate gradient algorithm for the remaining process.

2.2.3.2 Equilibration

Equilibration represent the preliminary step for the following MD production. Accordingly, equilibration stage is not beneficial for analysis purposes, but it is needed to conduct the previously minimized system at physiological temperature and pressure conditions. At this point the importance of temperature and pressure setting in MD simulation clearly emerges. Specifically, the thermodynamic parameters defining a thermodynamic state are defined by the *ensembles*. Accordingly, an ensemble is determined by a set of parameters (e.g. pressure, temperature, volume)^{525,536,537}. Deeply, i) in the NVT (or *canonical*) ensemble the number of particles N , the volume V and the temperature T remain constant, ii) in the NPT (or *isothermal-isobaric*) ensemble the number of particles N , the pressure P and the temperature T remain constant, and iii) in the NVE (or *microcanonical*) ensemble the number of particles N , the volume V and the energy E remain constant. Since in real-life experiments, both pressure and temperature are usually kept constant, the NPT ensemble represent the best choice to resemble the experimental conditions. Accordingly, all the simulations carried out in this thesis have been performed in the NTP ensemble. Nevertheless, NVT ensemble was employed at some stages of the equilibrium phase of the MD simulation to bring the system art the desired temperature value. The equilibration phase was concluded in NPT to stabilize also the pressure of the system. Notably, temperature and pressure are maintained constant thought thermostats and barostats, respectively. In detail, thermostats and barostats are algorithms which respectively allow temperature and pressure of the system to fluctuate around reference values^{525,536–538}.

2.2.3.3 MD production

The time-dependent behavior of the simulated system at atomic level is described by a time-dependent series of configurations (*frames*), which are collected in the so-called *trajectory*. To simulate the motion of the system, the positions of atoms are moved according to Newton's second law of motion^{509,515,520} (eq. 10).

$$F_i = m_i a_i \quad (\text{eq. 10})$$

where F_i is the force applied on atom i , m_i is the mass of atom i , and a_i is the acceleration of particle i . Importantly, the force F_i can be also stated as the negative gradient of the potential energy (eq. 11).

$$F_i = -\frac{dV}{dr_i} = m_i \frac{d^2 r_i}{dt^2} \quad (\text{eq. 11})$$

Thus, the force acting on each atom F_i is dependent on the resolution of the force field equation (eq. 1). Next, the acceleration is computed from the determined forces according to the Newton's equation of motion and atomic positions and velocities are updated^{509,515,520}.

In order to obtain a succession of frames that describe the evolution of the simulated system, the Newton's law of motion has to be simultaneously solved for all the system atoms. However, since the calculation cannot be computed analytically, numerical algorithms are employed. Indeed, the integration of Newton's equation of motion is fundamental for MD simulations and allows to describe the position occupied by each system atoms. Numerical integration algorithms are based on time discretization⁵³⁹. Accordingly, the iterative steps are repeated at every time step (Δt), until the aimed simulation time is achieved. A good practice is to choose a value of Δt ($\Delta t \sim 1-2$ fs) so that the fastest vibrational motions are still captured in the trajectory. Typically bond vibrations in bonds involving hydrogen atoms exhibit the fastest degrees of freedom. A widely used algorithm for integrating the equation of motion is the Velocity-Verlet algorithm^{540,541} (eq.12), which calculates positions at time $(t + \Delta t)$ calculated starting from the current positions, velocities and accelerations as:

$$r_i(t + \Delta t) = r_i(t) + v_i(t)\Delta t + \frac{1}{2} a_i(t) \quad (\text{eq. 12})$$

where $r_i(t)$ and $v_i(t)$ specify the coordinates and velocities at time t respectively, and $a_i(t)$ are computed according to equation 10. Then, velocities are calculated as (eq.13):

$$v_i(t + \Delta t) = v_i(t) + \frac{1}{2} [a_i(t) + a_i(t + \Delta t)]\Delta t \quad (\text{eq. 13})$$

Overall, i) an initial set of coordinates for all the system atoms is specified, ii) initial velocities are randomly assigned to each atom according to the Maxwell-Boltzmann distribution, iii) the force acting on each atom is computed according to the force field equation, iv) the acceleration for each atom is derived from the force, v) coordinates and velocities at time $t + \Delta t$ are calculated, vi) the new molecular configuration of the atoms is updated, vii) these iterative steps are repeated at every time step (Δt), until the desired simulation time is achieved.

Concluding, MD simulations represent a significantly convenient computational tool to employ in research projects to investigate complex molecular phenomena, like protein-ligand and protein-protein interactions. Noteworthy, in agreement with the ergodic hypothesis that states that if the simulation time is sufficiently long to sample the entire space of configurations an observable coincides with its ensemble average, a computed property from MD simulation reflects the experimentally measured value⁵⁴². Correspondingly, in this thesis MD simulations have been employed to both investigate the simulated systems, but also to compute thermodynamics properties from which derive information relative to protein-protein affinities.

2.3 Data collection and structural analysis from MD Simulations

Analysis of MD trajectory of protein-ligand and protein-protein complexes are fundamental to get insights in the nature of the established contact. Deeply, data collection regards the monitoring over time of specific bonds, bond angles, dihedral angles, changes in the structure, etc. This information can be addressed by taking into

account various descriptors, among which Root Mean Square Deviation (RMSD) and Root Mean Square Fluctuation (RMSF). RMSD is a convenient parameter to analyze to investigate the conformational behavior of the system over time in relation to the starting structure. Specifically, RMSD is a distance, expressed in Å, computed as the displacement of the coordinates of the same atom between two compared structures (eq.14):

$$RMSD = \sqrt{\frac{1}{N} \sum_{i=1}^N (r_i - r_0)^2} \quad (\text{eq. 14})$$

where N is the number of atoms, r_i is the atom position and r_0 is the position in the reference structure. The lower is the RMSD value, the better is the overlap between the considered structure. Notably, the RMSD analysis is computed for every frame leading to a time-series description of the system evolution of in the MD simulation. Accordingly, RMSD value is often used to assess the stability of the simulated system, but also to detect conformational changes in apo and/or bound protein complexes. Additionally, despite RMSD analysis is often performed on the protein backbone to investigate protein conformational changes, it also represent a convenient approach to evaluate the reliability of predicted binding poses from docking results. Also, RMSD represent a reliable parameter to use to compare the structure of related proteins.

On the other hand, RMSF represent a measure of the averaged protein flexibility. Accordingly, RMSF is computed as (eq.15):

$$RMSF = \sqrt{\frac{1}{N} \sum_{i=1}^N (r_i - \langle r \rangle)^2} \quad (\text{eq. 15})$$

where N is the number of atoms, r_i is the atom position and $\langle r \rangle$ is the position in the average position. Indeed, RMSD does not indicate positional differences over time, but measures the individual residue flexibility, indicating protein portions associated to higher fluctuations. The RMSF can be particularly useful when apo and bound system are compared revealing protein portions, which are, for instance, stabilized by the binding.

When a MD trajectory is analyzed, one of the main goal is to investigate the sampled space in order to detect configurations of the system of potential interest. For instance, in case of protein-protein complexes an interesting aspect to evaluate is how the proteins are structurally affected by the binding, comparing apo and bound forms. Indeed, this comparison can guide towards the acquirement of information regarding the rearrangements of the proteins upon binding, detecting key protein portions, or residues, important for the binding process. A type of analysis particularly advantageous is the *clustering analysis*. Clustering analysis consist in grouping object based on their similarity⁵⁴³. Accordingly, clustering is performed to identify similar structures sampled during MD simulation. Despite various clustering methods have been developed, they share some general principles. Indeed, all the clustering methods aim to cluster data maximizing and minimizing the intra-cluster and inter-cluster similarities, respectively. Also, the identified clusters are mutually exclusive, so that a structure can only be a member of a single cluster. Among the clustering algorithms, the *density peaks algorithm* has been implemented in this thesis for its higher reported accuracy⁵⁴⁴. The algorithm assumes that cluster centers are surrounded by neighbors with lower local density and that they are at a relatively large distance from any points with a higher local density. Accordingly, for each data point i , the local density ρ_i and its distance δ_i from points of higher density are computed (eq.16). Specifically, the local density ρ_i is computed as:

$$\rho_i = \sum_j \chi (d_{ij} - d_c) \quad (\text{eq. 16})$$

where d_{ij} is the distance between the data points and d_c is a cut-off distance. Thus, local density ρ_i describes the number of data points within the distance d_c (i.e. number of point that are closer to i than d_c). δ_i is instead computed as the minimum distance between the point i and any other point with higher density (eq.17):

$$\delta_i = \min_{j:p_j > p_i} (d_{ij}) \quad (\text{eq. 17})$$

Once, ρ_i and δ_i have been computed for each data point i , the plot of δ_i as a function of ρ_i will define the so-called *decision graph*. The graphical representation of the

computed values allow to determine the cluster centers as the point that have high δ_i value and a relative high ρ_i . Graphically, cluster centers are represented as *outliers* in the plot. Finally, once cluster centers have been identified, each remaining point is assigned to the closest cluster with higher density. Notably, the possible descriptors employed to cluster the structural conformations from a trajectory include the RMSD parameter. Accordingly, clustering analysis based on the structural information (i.e. RMSD) is often a good practice to detect and study the sampled geometric conformations.

2.4. MM/GBSA Calculations

In thermodynamics, free energy G refers to the amount of available energy of a system that can be used to execute work. Every protein-protein binding involves a change in free energy, which can be quantify to estimate the binding affinity between proteins, but also to evaluate the effect of single point mutations at the protein interface. Specifically, ΔG is defined as (eq.18):

$$\Delta G = \Delta H - T\Delta S \quad (\text{eq. 18})$$

where T , H and S are temperature, enthalpy and entropy, respectively. Enthalpy (H) is the total internal energy of a system, while entropy (S) is a measure of system disorder. Accordingly, ΔG is obtained by subtracting the amount of lost energy (entropy) from the total energy change of the system (enthalpy)⁵⁴⁵. For a ligand-protein and/or protein-protein binding process, ΔH reflects the energy change of the system when the first molecule binds to the second partner. Deeply, this energetic change results from several formations and breakings of noncovalent individual contacts, which involve also the solvent. Indeed, the formation of new interactions between the ligand and the protein, or between the two proteins, corresponds to the breakings of interactions between ligand/protein(s) and the solvent, as well as to a new solvent rearmament around the new complex surface. On the other hand, entropy describes the disorder of the overall system resulting from the contribution of ligand, protein(s) and surrounding solvent. The total entropy change associated with the binding process can be decomposed into 3 terms (eq.19):

$$\Delta S = \Delta S_{solv} + \Delta S_{conf} + \Delta S_{r/t} \quad (\text{eq. 19})$$

where ΔS_{solv} represents the change in solvent entropy resulting from the release of the solvent from the surface after complexation, ΔS_{conf} represents the change in the conformational entropy resulting from the changes in the conformational degree of freedom of both protein(s) and ligand upon complexation, and $\Delta S_{r/t}$ represents the loss of rotational-translational degrees of freedom of protein(s) and ligand upon complexation⁵⁴⁶. Overall, the net total entropy change resulting from these three contributions can favor or disfavor the binding. Indeed, while ΔS_{conf} can affect the net ΔS according to whether the conformational freedom increases or decreases, generally binding reactions have to overcome entropy penalties $\Delta S_{r/t}$ via solvent entropy ΔS_{solv} or through favorable protein-ligand, or protein-protein, interactions, which lead to a negative ΔH .

The ΔG of protein-protein binding can be negative or positive, depending on the spontaneity of the interaction. Indeed, a negative ΔG indicates a spontaneous exergonic process, while a positive ΔG a non-spontaneous endergonic process that requires external energy contribution to happen. Accordingly, change in free energy determines the direction of the thermodynamic process and drives all molecular processes, including protein-protein association, which specifically results from various interactions and energetic exchanges between the two proteins and the solvent. ΔH and ΔS can be considered as the driving forces for the binding processed, since their contribution determines the sign and magnitude of the ΔG . Explicitly, a phenomenon, called *entropy-enthalpy compensation*, describes this fine balance. For instance, the establishment of a strong ligand-protein, or protein-protein, binding resulting from favorable new noncovalent interactions, is counterbalance by a negative entropy change due to the loss of ligand and protein(s) degrees of freedom⁵⁴⁶. Notably, various molecular events can contribute to the entropy-enthalpy compensation (e.g. protein flexibility, solvent rearrangement). Importantly, from the sign and size of the ΔG we can deduce the binding affinity. Indeed,

binding free energy is directly related to the equilibrium concentration of the bound complex ($[P_1P_2]$) and of the single unbound proteins ($[P_1]$ and $[P_2]$), according to (eq.20):

$$\Delta G_{binding} = RT \ln K_d \quad (\text{eq. 20})$$

where T is the temperature, R is the gas constant and K_d is the dissociation constant defined by (eq. 21):

$$K_d = \frac{[P_1][P_2]}{[P_1P_2]} \quad (\text{eq. 21})$$

Of course, experimental measurements are essential, but the employment of computational methods able to predict protein-protein binding affinity often determines a less expensive and time-consuming overall process. Among them, *end point* methods represent one of the most used approach to estimate the change in free energy, despite the compromises traded between speed and accuracy⁵⁴⁷. Indeed, although more rigorous computational approaches, such as alchemical free energy calculations, are more accurate, end points methods present the advantages to be computationally less time-demanding. Indeed, end point methods estimate the change in free energy by simulating only the two end states of interest (e.g. proteins in free from and in complex), without considering intermediates. Among end points methods, MM/GBSA (Molecular Mechanics Generalized Born Surface Area) present one of the most commonly used, whose accuracy and reliability lie between molecular docking and more rigorous physics-based approaches, such as alchemical free energy calculations^{548–551}.

Formerly proposed in the late 1990s, MM/GBSA method combines an explicit molecular mechanics model for the solute with an implicit continuum model for the solvent^{548,550}. Accordingly, binding free energy is computed, according to the thermodynamic cycle in Figure 7, as (eq.22):

$$\begin{aligned} \Delta G_{binding,solvated} &= \Delta G_{binding,gas} + \Delta G_{complex,solvation} \\ &\quad - [\Delta G_{protein\ 1,solvation} + \Delta G_{protein\ 2,solvation}] \end{aligned} \quad (\text{eq. 22})$$

where $\Delta G_{\text{binding, gas}}$ is a gas-phase molecular mechanics (MM) energy, while $\Delta G_{\text{complex, solvation}}$, $\Delta G_{\text{protein 1, solvation}}$, $\Delta G_{\text{protein 2, solvation}}$ are solvation free energies calculated using the Generalized Born (GB) implicit solvent method.

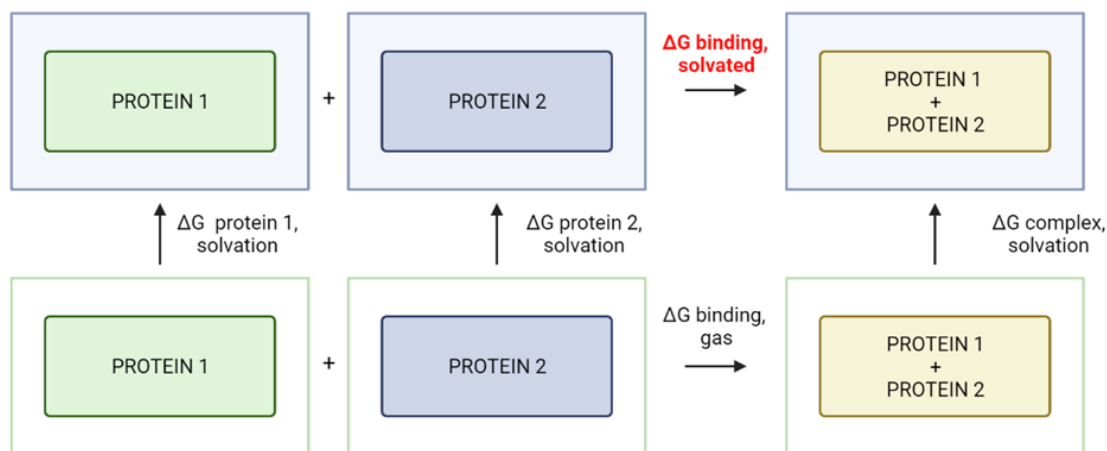


Figure 7. MM/GBSA thermodynamic cycle. Thermodynamic cycle implemented in MM/GBSA method to compute binding free energy. The color code defining the components of the thermodynamic cycle are green for the protein 1, blue for the protein 2 and beige for the protein-protein complex.

Another important aspect to clarify is that MM-GBSA is a post-processing method. Indeed, binding free energy results from an ensemble of representative structures (*frames*) derived from classical MD (Molecular Dynamics) or MC (Monte Carlo) simulations. The generated ensembles can derive from a single bound complex trajectory or from separate trajectories for each state. These approaches are respectively defined *single trajectory protocol* (STP) and *multiple trajectory protocol* (MTP). In this thesis, MM/GBSA calculations have been carried out with STP protocol using MMPBSA.py, a program written in Python and nab, released with the AmberTools package⁵⁵².

An interesting implementation of MM/GBSA method is represented by the *alanine scanning*. Indeed, alanine scanning allows the study of protein-protein interactions through the estimation of the change in the binding free energy deriving from the mutation of selected residues to alanine. Consequently, alanine scanning discloses how binding

free energy is affected, eventually emphasizing the importance of specific residues. Specifically, during an alanine scanning calculations the thermodynamic cycle shown in Figure 7 is executed for both *wild-type* and mutant proteins and a $\Delta\Delta G$ is given as output. Since the mutation to alanine is directly implemented in the method, the advantage of using alanine scanning is to avoid to perform an additional MD or MC simulation with the aim of generate an ensemble for the mutant system⁵⁵². Overall, despite the great benefits deriving from the use of end points methods, due to the formulated approximations, the results are often qualitative and more rigorous methods, such as alchemical free energy calculations are required to obtain detailed binding information.

2.6. Alchemical Free Energy Calculations

The development of force fields able to accurately describe the physicochemical properties of biomolecules along with the advancement in computing architecture and algorithms (e.g. GPUs), boosted the routinely use of molecular dynamics (MD) based methods in several research projects. Indeed, in addition to the time-dependent description of the investigated system, molecular dynamics (MD) simulations can be used to obtain quantitative thermodynamics estimations, from which derive the binding affinity between a drug like molecule and a biological target or between two interacting proteins⁵⁴². In the context of protein-protein interaction, the comparison between the binding affinities of *wild-type* and mutant systems is often a winning strategy to disclose key interactions in their molecular recognition. Among the computational methods developed to address this goal, alchemical free energy calculations represent a rigorous physics-based approach, efficiently employed during lead optimization in the context of structure-based drug design (SBDD) projects^{470,476}. Despite less explored, alchemical free energy calculations can also be applied for studying the characterization of protein-protein interfaces^{477,478}.

Alchemical methods drive the transformation of one molecule into another via an alchemical pathway of nonphysical intermediate states and estimate the associated change in free energy, the ΔG ^{470,547}. Specifically, the alchemical pathway between the two systems is determined by a virtual coordinate, called λ , which has a value of $\lambda=0$ for

the initial system and $\lambda=1$ for the final one. All the nonphysical alchemical intermediate are associate to values of $0 < \lambda < 1$. An ordinary description of the system at any point of the transformation is accomplished using a linear λ -dependent potential⁵⁵³ (eq.23):

$$V(\lambda) = (1 - \lambda) V_0 + \lambda V_1 \quad (\text{eq. 23})$$

However, in a free energy calculation where atoms appear or disappear in the two states the use of the linear potential often leads to poor convergence. Indeed, atom appearance and disappearance in the two end-point states is often associated to numerical instabilities when λ becomes close to 0 or 1, defined as *end-point catastrophe*^{470,554,555}. Such *end-point catastrophe* can be beneficially overcome by introducing a modified potential for the Lennard-Jones and the electrostatic interactions, called *softcore potential*, to treat appearing and/or disappearing atoms, i.e. those that are "unique" in each system^{556,557}.

Once chosen the appropriate potential description for the system and the transformation is accomplished, the final aim is to compute the difference in free energy between the two states of interest. Notably, the associated change in free energy can be computed using the free energy perturbation⁴⁷⁴ (FEP) and thermodynamic integration⁵⁵⁸ (TI) methods. Although, both methods are widely used and recognized to provide a comparable and reliable prediction of binding affinities, in this work the thermodynamic integration (TI) approach was employed, in which the ΔG is computed as a weighted sum of the ensemble averages of the derivative of potential energy function with respect to the coupling parameter λ (eq.24):

$$\Delta G = G(\lambda = 1) - G(\lambda = 0) = \int_0^1 \langle \partial V / \partial \lambda \rangle_\lambda d\lambda = \sum_i w_i \langle \partial V / \partial \lambda \rangle_i \quad (\text{eq. 24})$$

Importantly, the valuable application of alchemical methods does not regard merely computing of the ΔG associated to the system transformation, but rather to the estimation of the difference in binding free energies, the $\Delta \Delta G_{\text{binding}}$, between two ligands in the drug design context or between *wild-type* and mutant proteins. In the context of protein-protein interfaces, this purpose is addressed by implementing the thermodynamic cycle reported in Figure 8.

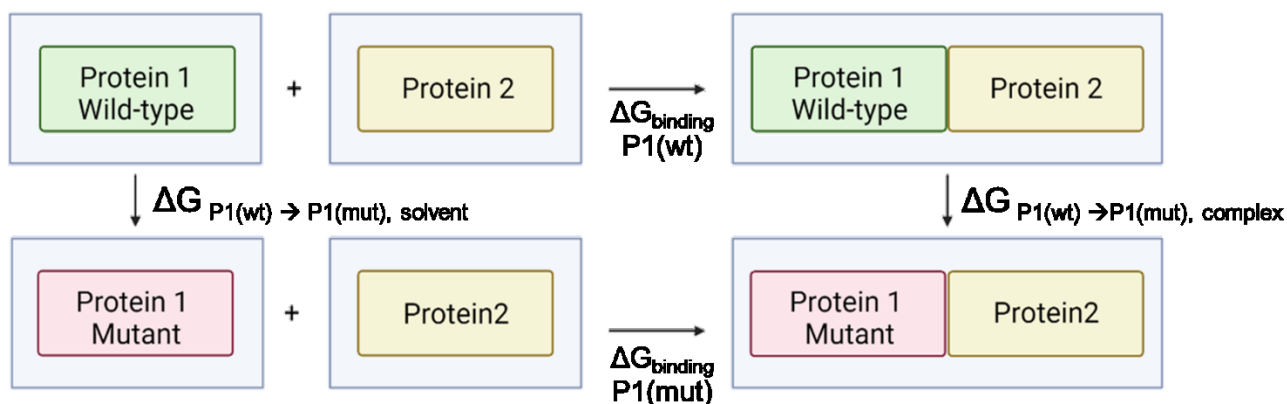


Figure 8. Thermodynamic cycle used in alchemical methods. Thermodynamic cycle implemented in alchemical methods to compute binding free energy. The color code defining the components of the thermodynamic cycle are green for the protein 1 *wild-type*, red for the mutant protein 1 and beige for the protein 2.

Notably, while horizontal transformations in the thermodynamic cycle are hard and computationally excessively time-consuming, the vertical ones, which correspond to the alchemical transformations, are significantly more achievable. Indeed, the $\Delta\Delta G_{\text{binding}}$ is computed as (eq.25):

$$\begin{aligned}\Delta\Delta G_{\text{binding}} &= \Delta G_{\text{binding}, P1(\text{mut})} - \Delta G_{\text{binding}, P1(\text{wt})} \\ &= \Delta G_{P1(\text{wt}\rightarrow\text{mut}),\text{complex}} - \Delta G_{P1(\text{wt}\rightarrow\text{mut}),\text{solvent}}\end{aligned}\quad (\text{eq. 25})$$

Deeply, alchemical free energy transformations are carried out by transmuted the protein 1 *wild-type* to mutant in solvent as well in the bound complex with the protein 2. In behalf of the use of the thermodynamic cycle in Figure 8, the difference between the binding free energies of the protein *wild-type* and mutant respect to protein 2, $\Delta\Delta G_{\text{binding}}$, equals the difference between the change in free energy of the two alchemical transformations. Concluding, despite more time-consuming and complex to apply respect to more simple approaches, alchemical free energy calculations often deliver quantitatively accurate and precise result in agreement with experiment. In accordance with their well established and successfully use in the design of small-molecule drugs, in this thesis it is explored their application in the context of protein–protein interactions.

Chapter 3. Structure-based design of CDC42 effector interaction inhibitors

3.1. Approaching the CDC42/PAK signaling blockade

By stimulating numerous transduction pathways, CDC42/PAK signaling mediates a wide variety of cellular functions, including cytoskeleton regulation, gene expression, vesicle trafficking, phagocytosis, cell cycle, cell morphogenesis, cell–cell adhesion and cell migration. However, despite their central role in cell homeostasis, CDC42 proteins' dysfunction is often associated with different pathological processes, including cancer development and progression. Despite CDC42 is the best characterized member among the CDC42 proteins, also RHOJ and RHOQ have been found to modulate cell-cycle progression, tumor cell migration/invasion, therapies cell resistance, and tumor growth and angiogenesis in multiple human cancers^{424–426,559}. Accordingly, RHOJ aberrantly controls important pathways in melanoma, breast cancer and gastric cancer^{421–423,560}.

Melanoma is a type of skin cancer that derives from the tumor transformation of melanocytes in which the BRAF gene is frequently mutated. Accordingly, BRAF gene is oncogene, that is a gene that, when mutated, contribute to malignant transformation. Specifically, BRAF gene encodes for the serine/ threonine protein kinase B-RAF, which plays a pivotal role in several important cell functions. Notably, up to 50% of BRAF mutant human melanomas express RHOJ high levels, highlighting such small GTPases as a novel target to investigate. Specifically, RHOJ activates PAK in melanoma cells and modulates both the phases of tumor initiation and tumor progression, by altering the actin cytoskeleton dynamics and by quenching apoptosis signals^{421,560}. Deeply, RHOJ/PAK signaling modulates melanoma cell migration by downstream phosphorylating cytoskeletal regulation proteins, such as LIMK, colifin and P41-ARC⁵⁶⁰.

Apoptosis is instead downgraded by modulating the expression of the pro-apoptotic proteins. In detail, PAK, once activated by RHOJ, phosphorylates and inhibits the pro-apoptotic protein BAD, accelerating both the formation and the growth of melanoma tumors metastasis⁴²¹. In breast carcinoma, RHOJ contributes to tumor cell

migration in synergistic activity with the oncogene EVI1, which encodes a zinc-finger transcription factor⁴²². In gastric cancer, high RHOJ expression significantly correlated with poor overall patients' survival. Indeed, RHOJ positively contributes to malignance development by increasing the mobility and the invasiveness of gastric cancer cells. Also, RHOJ has been proposed as a promising therapeutic target for anti-angiogenesis treatment in cancer. Indeed, in order to survive and proliferate, malignant cells require oxygen and nutrients acquired from the blood circulation system. However, cancer cells are also able to orchestrate the formation of a network of new blood vessels through a highly complex process, called *tumor angiogenesis*, which supplies the tumor growth. Notably, RHOJ has been found to be a keynote factor in the process. Moreover, RHOJ/PAK signaling has been found to induce melanoma chemoresistance by suppressing pathways that modulate cell sensitivity to DNA damage. Despite less studies, RHOQ is also known to promote tumor invasion in colorectal cancer and to modulate angiogenesis^{428,430}. Taken together, these observations highlight CDC42 family as novel therapeutic target for cancer treatment.

As the other RHOGTPases, CDC42 proteins act as molecular switches, cycling between the GTP-bound active state and the GDP-bound inactive state. The regulation cycle modulation is driven by the regulators GAPs, GEFs and GDIs. Only the GTP-bound active conformation has the proper structural arrangement to interact with effector proteins and, thus, transmit the signal downstream. In order to inhibit CDC42, some inhibitors hampering of the CDC42/GEF interaction or nucleotide binding the have been proposed. However, selectivity-related limits have been described, such as thrombocytopenia and cardiotoxicity that are induced by the blockade of both CDC42 and RAC signaling. Here, aiming to identify small inhibitor compounds able to improve the therapeutic beneficial avoiding off-target effects, a structure-based drug design approach is explored for CDC42 and RHOJ, two of the three CDC42 family members that have the most defined roles in cancer. Specifically, since the CDC42/PAK protein-protein interaction represents the crucial moment in which the activation signal is activated and transmitted, the blockade of this protein complexation is considered as a new strategy to target the CDC42/PAK signaling.

3.2. Investigation of a drug-binding pocket present in GTP-bound RHOJ and CDC42

Starting from preliminary results obtained in our labs, the structural investigation of a previously unappreciated putative drug-binding pocket located at the CDC42-RHOJ-RHOQ/PAK protein-protein binding interfaces has been performed. In detail, the project started with the exploration of the crystal structure of CDC42 in complex with the CRIB domain of PAK6 (PDB ID 2ODB, resolution of 2.4 Å), where a previously unappreciated effector binding pocket was detected. Specific residues of the structural motifs switch I (Val36, Phe37) and switch II (Ala59, Tyr64, Leu67, Leu70, Ser71) on the CDC42 surface define the pocket, which accommodates the binding of Trp40 on PAK6 (Figure 9A). Notably, the pocket is unfolded, and not formed, in the GDP-bound inactive state (Figure 9B).

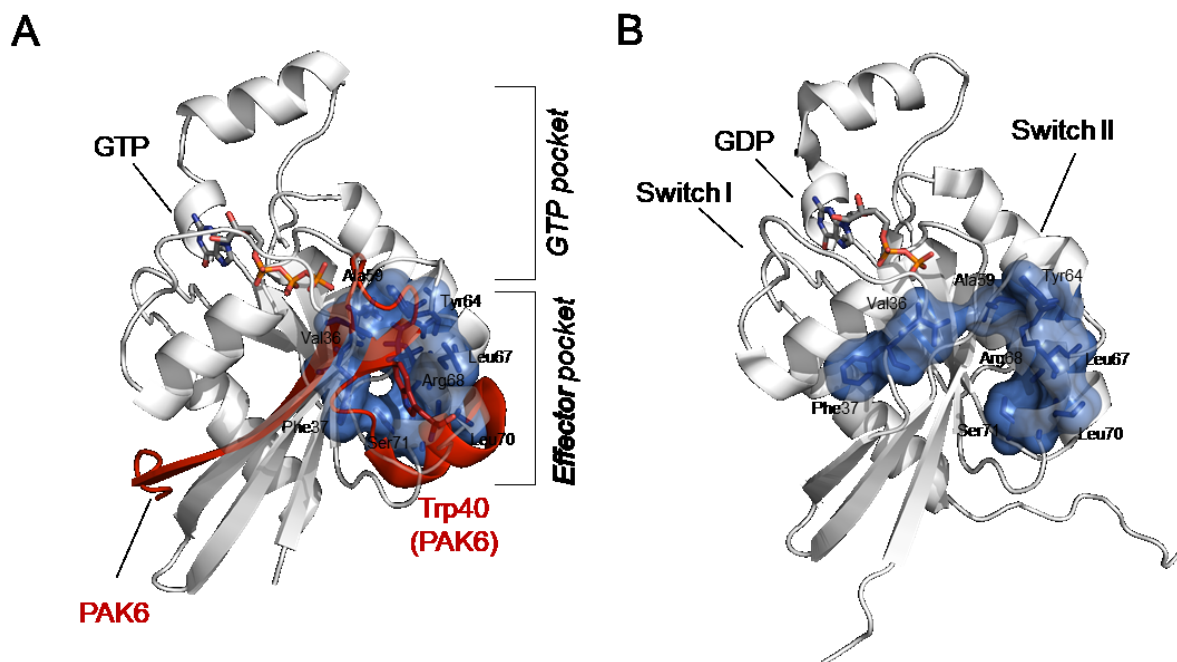


Figure 9. Structural identification of RHOJ/CDC42 allosteric effector binding pocket. A) Identification of a drug binding pocket in GTP bound CDC42. Structural modeling identified an effector pocket that is folded in the GTP-bound state (blue). CDC42 binds with PAK6 (transparent red) by Trp40 (red) mediated interaction (PDB ID 2ODB) in this putative drug binding pocket. B) Putative drug binding pocket is not folded in the GDP bound CDC42 structure. The

structure of CDC42 is represented in GDP-bound (grey) state (PDB ID 1DOA), where the effector pocket is unfolded (blue).

Because of the lack of X-ray structure of RHOJ protein, homology modelling was used to determine whether this same allosteric pocket could be used to target RHOJ effector interactions. Specifically, homology modelling was performed using the CDC42/PAK6 crystal structure (PDB ID 2ODB) as template to generate the RHOJ-PAK1 structural homology. As result, both sequence and structural analysis revealed homology in the RHOJ domains interacting with PAK (Figure 10). Deeply, a similar binding pocket was found structurally conserved in RHOJ, as well as the binding of Trp103 from PAK1.

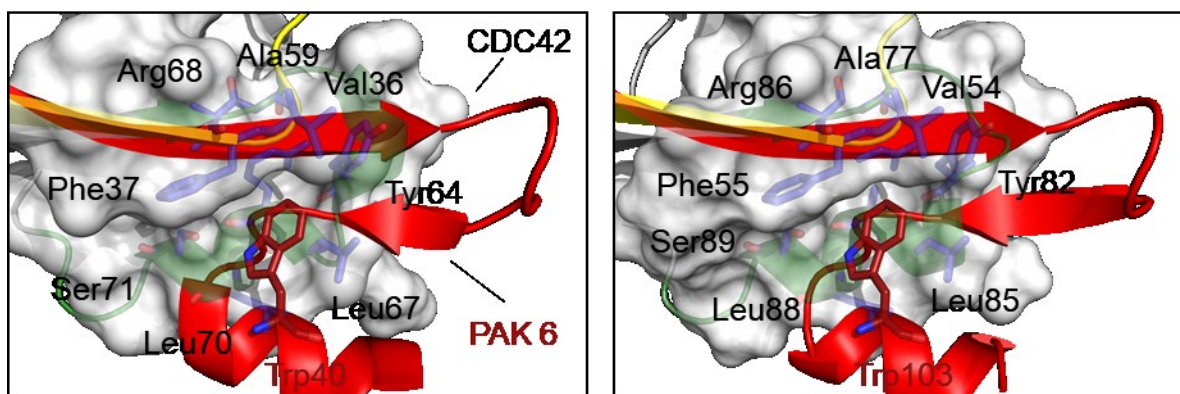


Figure 10. Structural analysis of the CDC42-RHOJ/PAK interactions. On the left, close-view of the CDC42/PAK6 interaction interface. For comparison, modeling of the interaction between Trp103 (red) of PAK1 (transparent red) and the effector binding pocket (light blue) of RHOJ (grey) is shown. Switch I and II regions are highlighted in yellow and green, respectively.

Notably, such pocket is structurally distinct from the GTP binding site, that is located ~ 17 Å away, but also from the GTPases' pocket targeted in other drug design campaigns. Indeed, recent works have identified covalent inhibitors, which bind to structural pockets in the related small GTPases K-RAS(G12C). Deeply, taking advantage of the nucleophilicity of the mutant cysteine thiols, cysteine-reactive small molecules have been designed^{561–566}. Structurally, the mutated cysteine residue, where the covalent inhibitors bind, is located in proximity of the nucleotide binding pocket and affects the GTP

hydrolysis. Therefore, the identified pocket on CDC42 defines a distinct binding site (Figure 9A and 11A).

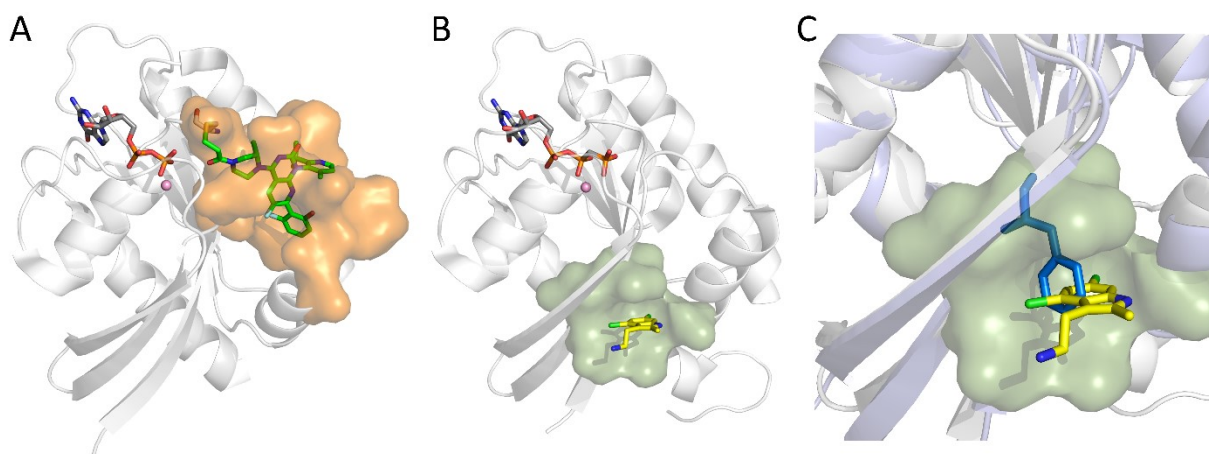


Figure 11. Structural analysis and comparison of the pocket of the CDC42 GTPases compared to K-RAS. A) The K-RAS(G12C) covalent inhibitors AMG-510 (green sticks, PDB: 6OIM) at the inhibitor's pocket (orange surface). B) The K-RAS-selective inhibitor DCAI bound to the pocket (green surface, PDB: 4DST). C) The DCAI binding model by simply structural overlap of K-RAS (PDB ID 4DST, white cartoon) and CDC42 (PDB ID 2ODB, light blue cartoon) proteins is reported. The occupation of Phe56 in CDC42 (blue sticks) of the correspondent space occupied by DCAI to K-RAS could be the explanation of the prevented DCAI binding to CDC42.

The putative drug-binding pocket located at the CDC42/PAK interface is also structurally different from the one targeted by other developed RAS inhibitor, such as DCAI⁵⁶⁷ (Figure 11B) and other succeeding designed small molecules^{568–571}. DCAI is an inhibitor developed to block the SOS-mediated nucleotide release and, consequently, RAS activation. Despite DCAI binds the GDP-bound K-RAS in an adjacent site to the switch regions, such pocket is not conserved in CDC42 and RHOJ. Accordingly, DCAI specifically inhibits the SOS-mediated nucleotide exchange on RAS and not the DBS-mediated nucleotide exchange on CDC42. Possibly, the bulky residue Phe56 that occupies the space equivalent to the DCAI-binding site in CDC42 prevents DCAI binding (Figure 11C). Consistently, the residues constituting the DCAI binding pocket define a different 3D cavity respect to ours.

Likewise, the pocket targeted by the small molecule inhibitor EHop-016 is structurally divergent⁴⁰⁸. Deeply, EHop-016 has been designed as a RAC/GEF inhibitor able to affect also CDC42 at high concentration. Importantly, the CDC42-RAC/EHop-016 complex has not been co-crystalized and the structural information available are based on the co-crystal structure of GDP-bound RAC1 complexed with the GEF-inhibitor NSC23766⁴⁰⁷ (Figure 12), where our pocket is not formed. Indeed, EHop-016 development was based on the structural information of the known RAC1 inhibitor NSC23766. Accordingly, to investigate the putative EHop-016 binding, the coordinates of RAC1/NSC23766 complex were used to perform predictive molecular docking. Specifically, after removing NSC23766 from the crystal structure, EHop-016 was centered in the original position of NSC23766. Consequently, since based on the same structural information, also the pocket targeted by the succeeding improved small molecule MBQ-167 diverges from ours⁵⁷². Finally, likewise based on the available structural information relative to the inhibitor NSC23766, the small molecules AZA1⁴⁰⁹ and AZA197⁴¹⁰ has been designed to inhibit the CDC42/GEF interaction. Lastly, the specific interaction between GDP-bound CDC42 and intersectin is targeted by the small compound ZCL278⁴¹¹. Concluding, all the available inhibitors target the GDP-bound form of CDC42, where our pocket doesn't exist.

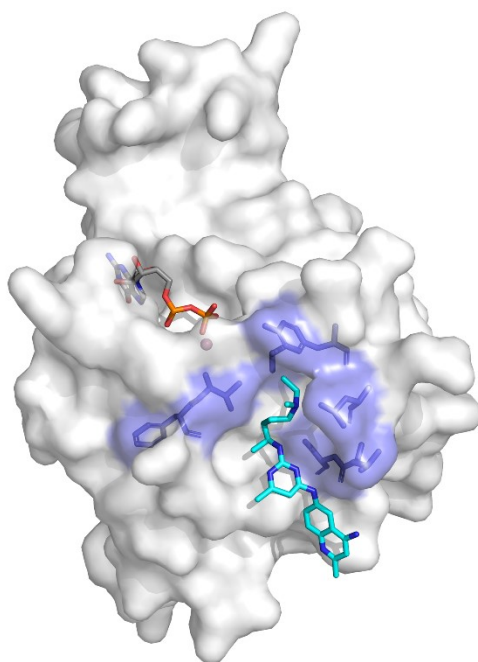


Figure 12. GDP-bound RAC1/ NSC23766 co-crystal structure. The available GDP-bound RAC1 in complex with the small compound NSC23766 from the National Cancer Institute chemical database is reported. The protein is represented as white surface, while GDP and Mg²⁺ ion are illustrated as sticks and balls, respectively. The corresponding residues of our identified drug-binding pocket in RAC1 are shown in both stick and transparent surface (blue). NSC23766 is reported as cyan sticks.

The structural analysis of the identified pocket has been not only restricted to the 2ODB X-Ray structure, but it has been extended to the other CDC42 available structures. As showed in Figure 13A and 13B, the identified effector pocket is only present in the GTP-active state (Figure 13A), while is not formed in the GDP-inactive states (Figure 13B).

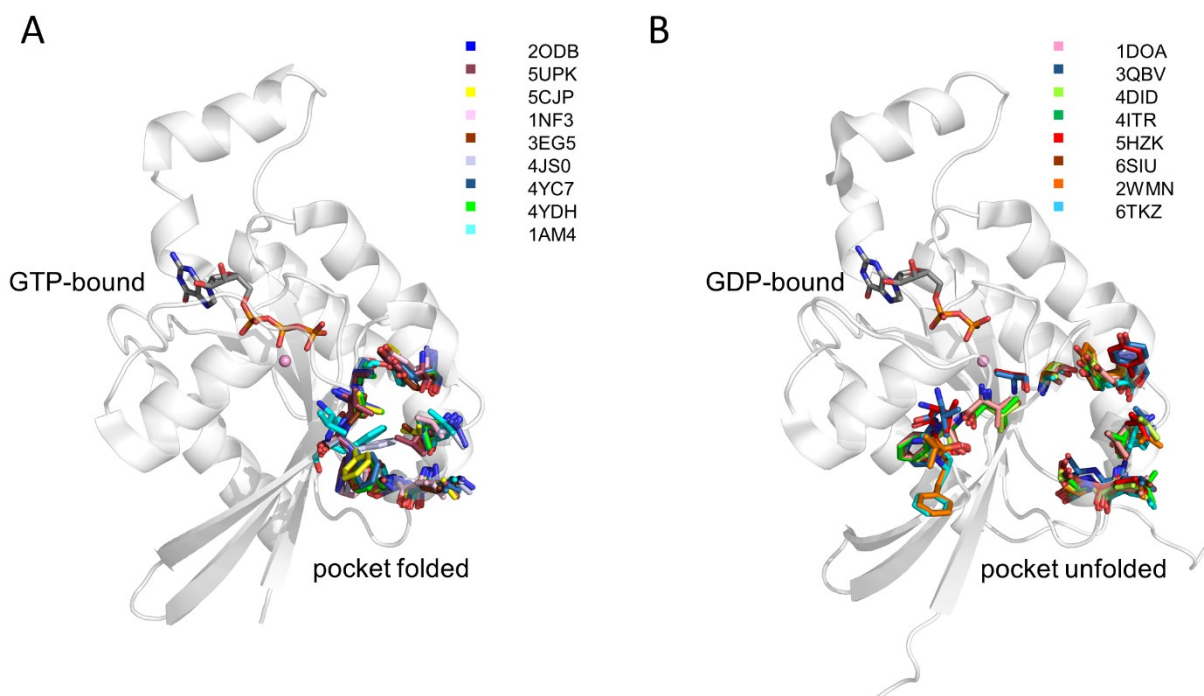


Figure 13. Structural analysis of the CDC42 crystal structure. Structures of GTP-bound CDC42 (A) and GDP-bound CDC42 (B) are reported. The protein is represented as cartoon, while the residues at the CDC42-effector interface are highlighted as sticks. Residues' folding define the effector pocket only in the GTP-bound state (A).

In addition to the static analysis of crystal structures, molecular dynamics (MD) simulations have been run to investigate the time-dependent configurations of the pocket. Specifically, 500-ns-long molecular dynamics (MD) simulations of the GTP-bound CDC42 disclosed the pocket stability, with a RMSD value of $2.06 \pm 0.33 \text{ \AA}$ (Figure 14A and 14B). Furthermore, unsupervised analysis of the MD trajectories, through the software *pocketron*, identified our pocket and defines its volume, compatible with small molecules binding (Figure 14C and 14D).

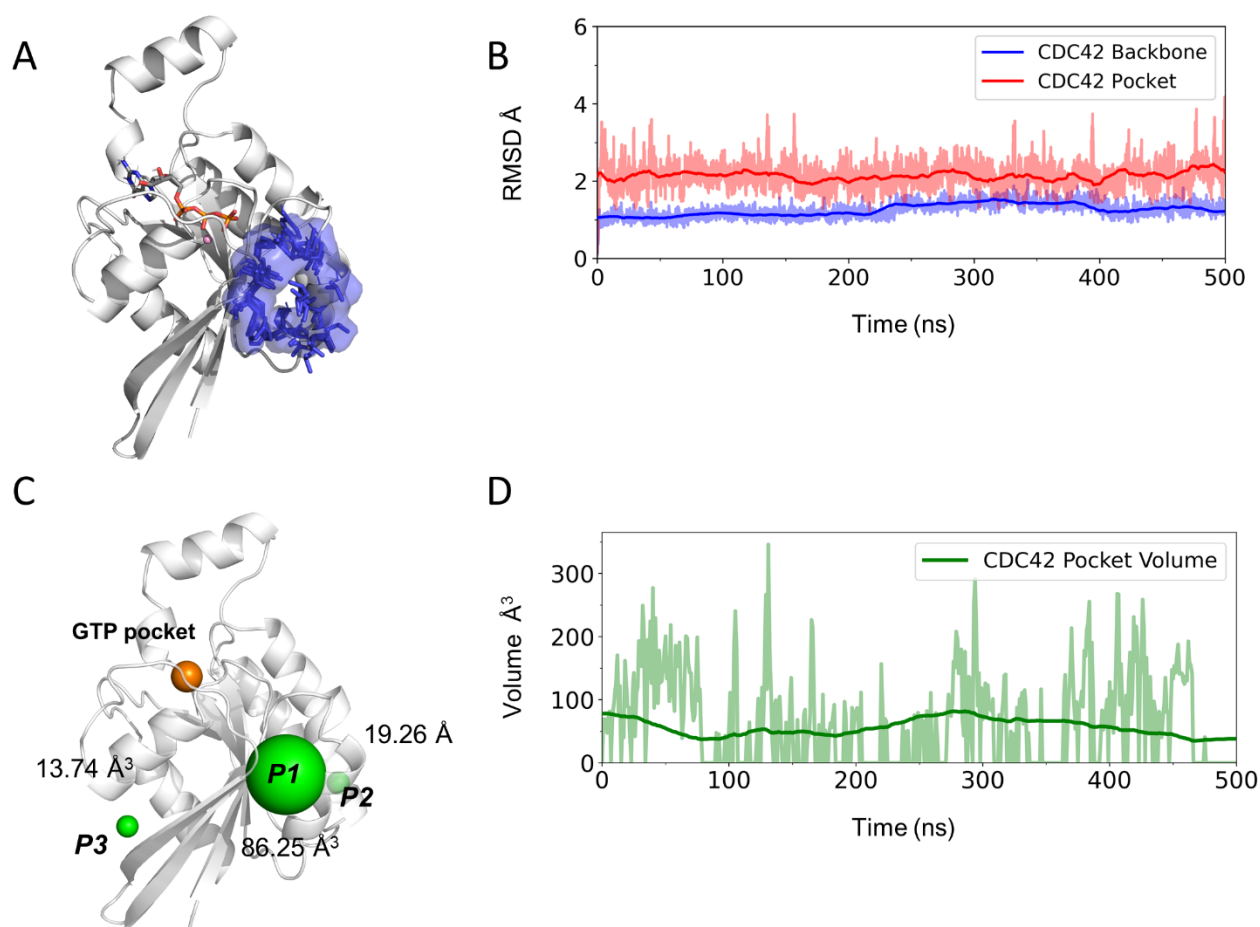


Figure 14. MD simulations of GTP-bound CDC42. A) The structural representation of GTP-bound CDC42 is reported. CDC42 is represented as cartoon, while the binding pocket is highlighted as blue transparent surface. Multiple MD snapshots of the pocket residues (blue) are shown as sticks. B) The Root-Mean Square Deviation (RMSD) and the volume (D) of the pocket for CDC42 are reported. The running average is in bold in each graph. C) The structural representation of GTP-bound CDC42 with the pocket represented in green spheres is reported. The volume of each pocket is reported.

Equally, the pocket in GTP-bound RHOJ was found to be stable along during 500-ns-long molecular dynamics (MD) simulations with a RMSD value of 2.07 ± 0.27 Å (Figure 15A and 15B). Unsupervised analysis of the MD trajectories revealed again the compatibility of the our pocket volume with a small molecule binding (Figure 15C and 15D).

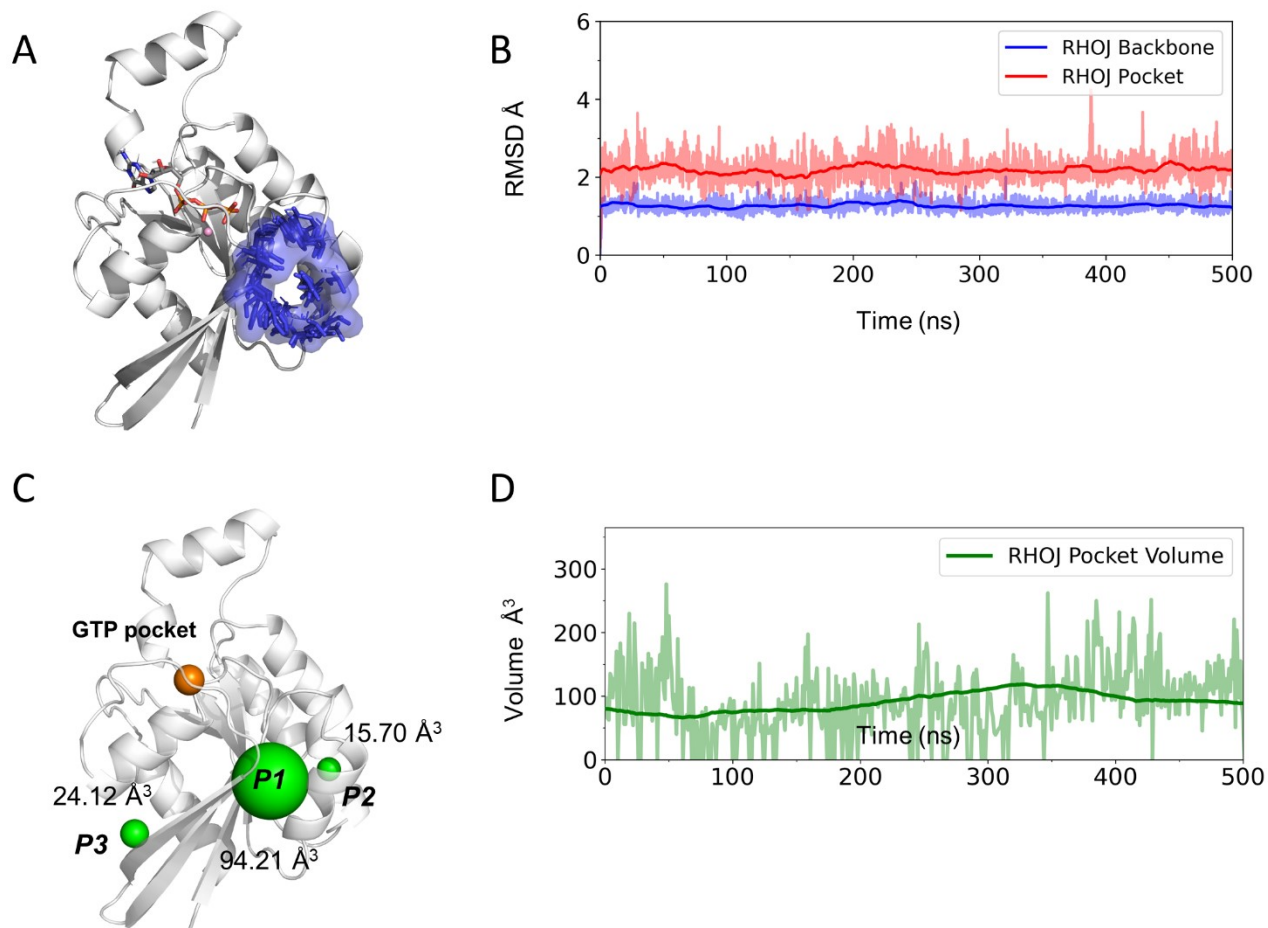


Figure 15. MD simulations of GTP-bound RHOJ. A) The structural representation of GTP-bound RHOJ is reported. RHOJ is represented as cartoon, while the binding pocket is highlighted as blue transparent surface. Multiple MD snapshots of the pocket residues (blue) are shown as sticks. B) The Root-Mean Square Deviation (RMSD) and the volume (D) of the pocket for RHOJ are reported. The running average is in bold in each graph. C) The structural representation of GTP-bound RHOJ with the pocket represented in green spheres is reported. The volume of each pocket is reported.

Because of the high sequence and structural similarity, the arrangement of the corresponding residues forming our pocket in RAC1 was also investigated. Interestingly, the identified pocket is found always in an *open* conformation in CDC42 and RHOJ, but not in RAC1, where Phe37 has been captured also in a *closed* conformation that occludes the binding pocket (PDB: 1MH1)⁵⁷³ (Figures 16). The residues defining the drug-binding pocket are conserved in all the proteins, despite the close bulky Trp56 is only present in RAC1, as in CDC42 and RHOJ Trp56 is replaced by Phe56 and Tyr74, respectively. Consequently, the Trp56 may be responsible of the closed orientation of the Phe37 in RAC1.

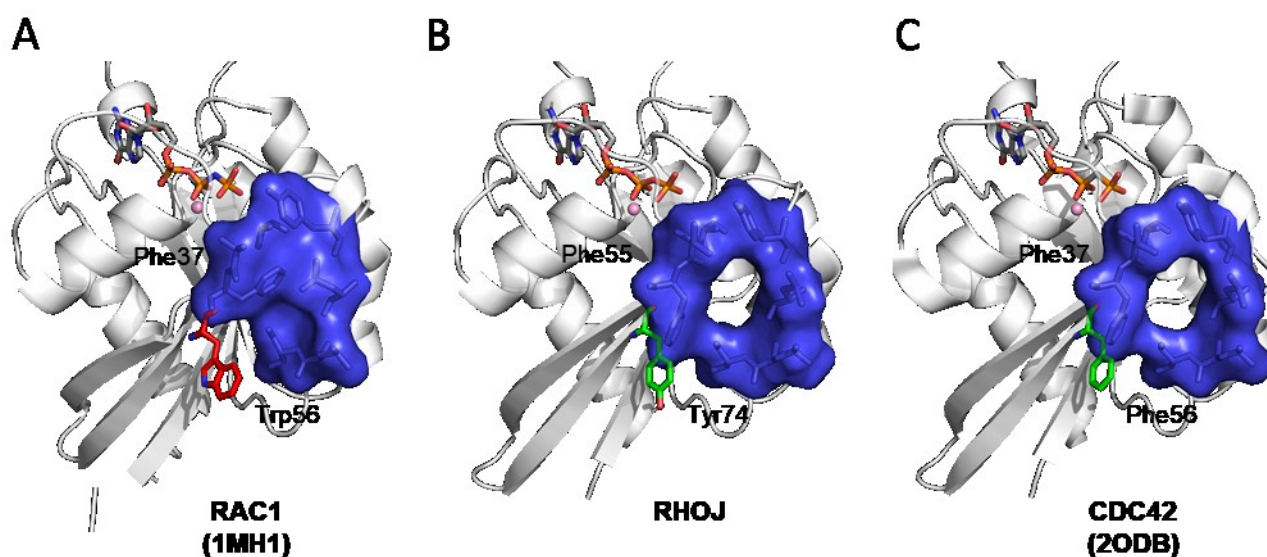


Figure 16. Structural comparison of RHOJ, CDC42 and RAC1 effector binding pocket. A) Structural representation of the *closed* conformations of Phe37 as captured in RAC1 X-ray structures (PDB: 1MH1) is reported. The open conformations of Phe37 and Phe55 found in RHOJ homology model (B) and CDC42 X-ray structures (C) are shown. The proteins are represented as white cartoon, while guanine nucleotides and Mg²⁺ ions are illustrated as sticks and balls, respectively. The identified drug-binding pocket is shown in both stick and transparent surface (blue).

The detected RAC1, RHOJ and CDC42 conformations were also evaluated during 500 ns of MD simulations through, where have been found to be stably maintained

(Figures 17). In detail the value of the side chain dihedral angle of Phe37 in RAC1 (Figure 17A) vs Phe55 in RHOJ (Figure 17B) and Phe37 in CDC42 (Figure 17C) was evaluated along the simulation time. The analysis highlighted the different Phe orientation and conformational flexibility.

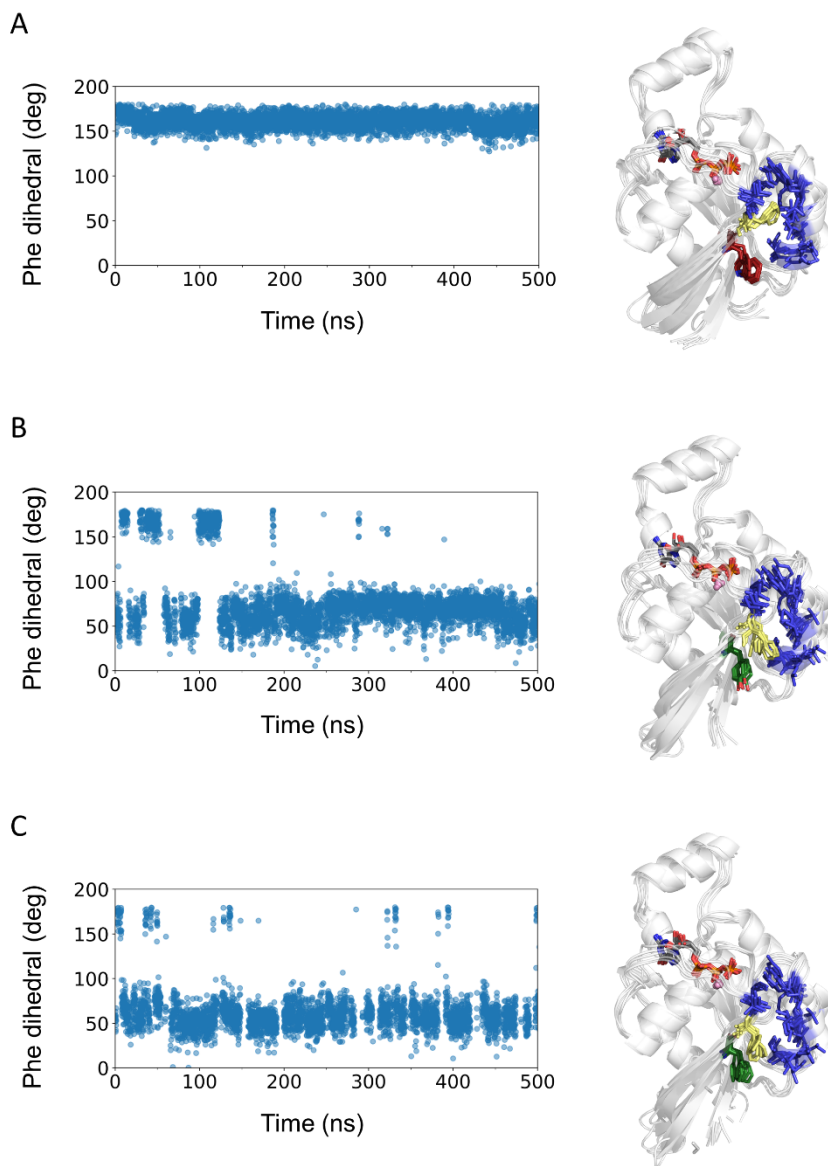


Figure 17. MD simulations of GTP-bound RAC1, CDC42 and RHOJ proteins. The structural RAC1 (A), RHOJ (B) and CDC42 (C) conformations were evaluated during 500 ns of MD simulations. On the right, proteins are represented as cartoon, while guanine nucleotides and Mg^{2+} ions are illustrated as sticks and balls, respectively. The residues defining the binding pocket are shown as blue sticks, while the Phe37 in CDC42, the Phe55 in RHOJ and Phe37 in RAC1 are highlighted in yellow. The Trp56 residue in RAC1 is shown as red sticks while the

corresponding Phe56 (CDCD42) and Tyr74 (RHOJ) are reported in green. In RAC1, the presence of Trp56 favors the stabilization of Phe37 in a closed conformation, hampering the accessibility of the drug-binding pocket.

Because of the interesting and promising information emerging from this extensive structural analysis, the druggability of the pocket was further investigated, starting from the implementation of a virtual screening protocol.

3.3. Identification of a CDC42-RHOJ effector interaction *hit compound* inhibitor

Following the interesting results obtained from the structural analysis of the new identified putative drug-binding pocket, a virtual screening (VS) campaign has been performed in order to identify RHOJ/CDC42 effector inhibitors. In detail, an internal IIT (Italian Institute of Technology) chemical collection of ~20,000 diverse and non-redundant compounds has been screened. First, with the aim to obtain accurate 3D molecular models as starting point, the database compounds were prepared for the VS using *LigPrep*. *LigPrep* is a software implemented in Maestro able to generate energy minimized 3D molecular structures. In detail, hydrogens have been added to generate ionization states corresponding to a pH of 7.4 ± 0.5 . Next, tautomers and stereochemical isomers have been generated. Also, for each structure containing a ring moiety, the low-energy conformation was computed and retained. Last, a short minimization step was carried out to relax the 3D structure of each molecule. All the prepared compounds have been later subject of a computational ADME (absorption, distribution, metabolism, and excretion) analysis through *QikProp*. *QikProp* is also implemented in Maestro and predict a wide variety of pharmaceutically relevant properties starting from the 3D molecular structure. Therefore, the resulting compounds have been filtered the resulting to discard molecules that are not endowed with drug-like properties by applying the software *LigFilter*. As filter, all the molecules that do not respect the Lipinsky's rule of five were discarded. Then, the receptor and the $26 \times 26 \times 26 \text{ \AA}^3$ grid were generated using the identified pocket as guide. Lastly, docking was performed using Glide, utilizing the Single

Precision approach and retaining one pose for each ligand. The overall virtual screening protocol used is reported in the workflow in Figure 18.

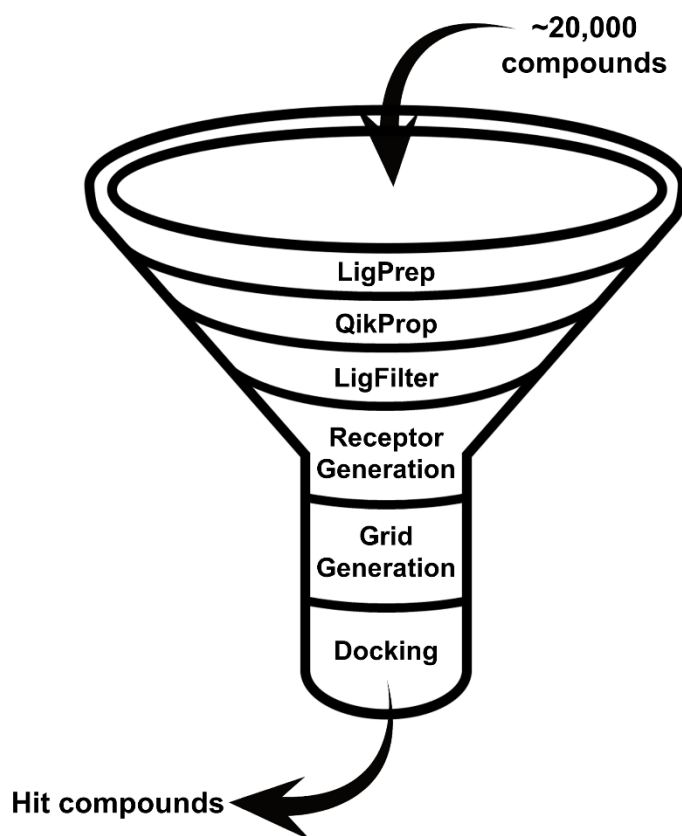


Figure 18. Virtual Screening workflow. A set of of ~20,000 compounds has been screened and prepared for the VS using LigPrep. Then, QikProp predicted ADME properties and, based on this analysis, Ligfilter discarded all the non drug-like molecules. Receptor and grid have been set and Glide has been used to carry out the final docking calculation.

During docking analysis, 68 promising compounds have been selected and experimentally tested. Specifically, the half maximal inhibitory concentrations (IC₅₀s) of the selected compounds have been evaluated in a cell line of melanoma cells (in SKMe128 melanoma cells). From the IC₅₀ values obtained, 14 compounds were selected for further analyses. Next, on the basis of kinetic solubility and compounds' ability to inhibit the interaction between RHOJ or CDC42 and its downstream effector PAK, ARN12405 was selected as a promising hit. In detail, our hit compound has a IC₅₀ value of 16.4 mM in the SKM28 cell line and a high kinetic solubility of 222 μM. Importantly, the selected hit

compound inhibits RHOJ/CDC42-PAK interactions in an assay, which specifically measures the interaction between RHOJ/ CDC42 and the PAK binding domain. Structurally, ARN12405 is composed by a central pyrimidine scaffold connected with 3-piperidine, a 4-chloro aniline and a 4-pyridine in positions 2, 4 and 6, respectively. The docking prediction of ARN12405 in the effector pocket of RHOJ and CDC42 is reported in Figure 19.

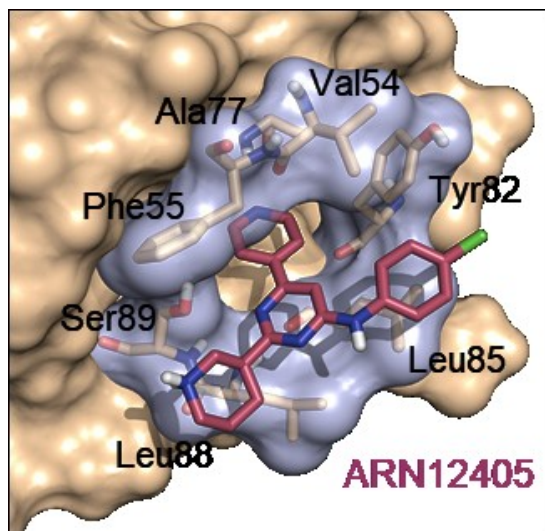


Figure 19. Docking pose prediction of ARN12405. The model structure of ARN12405 bound to CDC42/RHOJ is shown. The protein is represented as white surface, with the pocket residues highlighted as light blue surface and gray sticks. ARN12405 is reported in red sticks.

Next, to further assess the predicted binding poses from our docking results, MD simulations of both RHOJ and CDC42 in complex with ARN12405 were performed. As shown in Figures 20, the hit compound steadily binds the target pocket throughout the simulations. In detail, the RMSD analysis over time of the MD trajectory revealed an RMSD values of $2.00 \pm 0.40 \text{ \AA}$ and $3.24 \pm 0.85 \text{ \AA}$ for ARN12405 in RHOJ- and CDC42-ligand complexes, respectively.

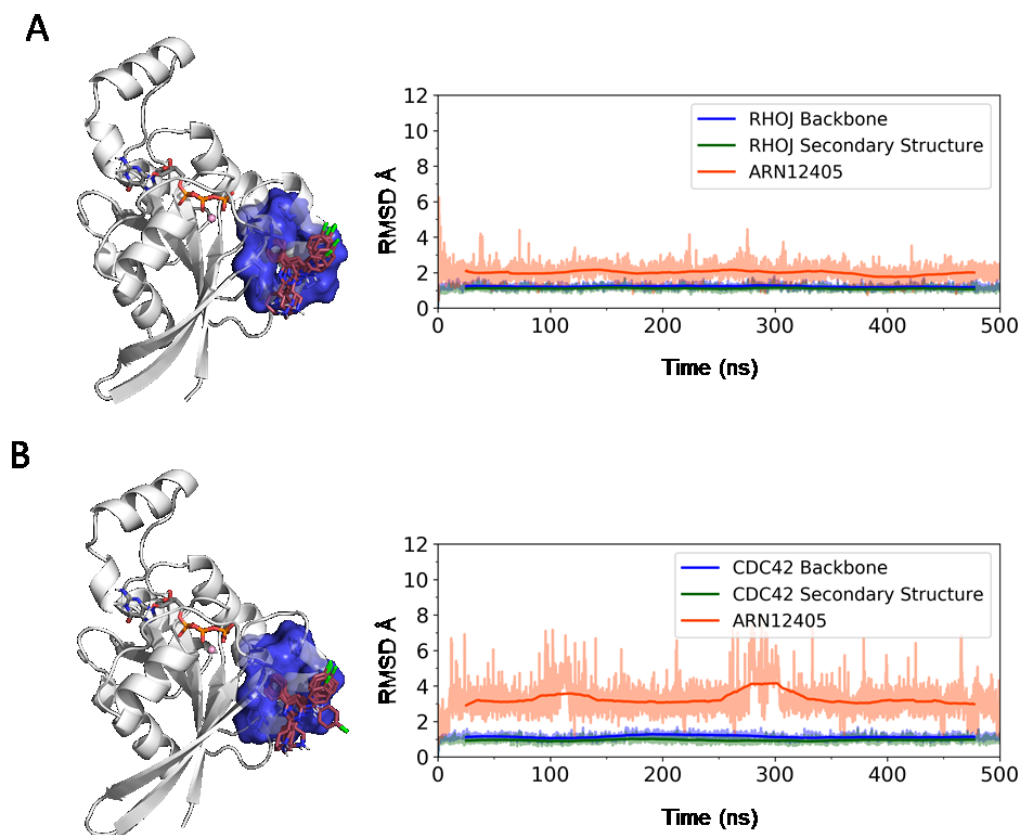


Figure 20. Docking pose prediction of ARN12405. The structural representation of RHOJ (A) and CDC42 (B) in complex with ARN12405 is reported on the left. Both RHOJ and CDC42 are represented as cartoon, while the binding pocket is highlighted as blue transparent surface. Multiple MD snapshots of the ARN12405 are shown as red sticks. On the right, the RMSD over time for both RHOJ (A) and CDC42 (B) binding complexes. The RMSD running averages is in bold.

3.4. Hit-to-lead optimization

In order to improve the potency and the drug-like properties of the hit compound ARN12405, the three functional groups of the pyrimidine core scaffold were explored. The new generated structural analogues have been tested in terms of IC₅₀ in five different cancer cell lines (SKM28, WM3248, SKMe13, A375 and SW480), while only the drug-like properties of the most potent compounds were evaluated. To explore the chemical space of ARN12405, firstly the pyridine heterocycle has been replaced with pyridines with different nitrogen positions and with other aromatic rings. Despite the evaluated

modification did not significantly affected the potency in the SKM28 cell line, the substitution of the pyridine with a phenyl ring (ARN21698) slightly increased the activity (IC₅₀ 6.3–10.9 μM). This outcome is in line with the hydrophobic nature of the identified pocket. Next, the 4-chloro aniline in position 4 was explored considering electron-donating or electron-withdrawing groups in *ortho*, *meta*, and *para* positions. Interestingly, the generated modifications led to a marked decrease in potency in the cell SKM28. For instance, removal or moving the chlorine from the *para* to the *meta* position (ARN21699 and ARN21700), maintaining 4-pyridine, decreased the activity 2-fold compared to the hit compound in SKM28 cells. In addition, new aniline substituents, while keeping the 3-piperidine heterocycle and the phenyl ring I position 2 and 6 were considered. Deeply, the replacement of chlorine in *para* position in ARN21698 by a methoxy (ARN22097) or a dimethyl amino group (ARN22093) resulted in a total or partial loss of activity. In contrast, introducing the same substituents (methoxy and dimethylamino groups) in the *meta* position (ARN22091 and ARN22164) moderately diminished the activity of the compounds.

Finally, position 2 of the central pyrimidine scaffold was explored. Deeply, methoxy and dimethylamino substituents on the aniline moiety were explored, while moving the piperidine nitrogen from position 3 to 4. Notably, this modification aimed to improve synthesis and chirality of the compounds, by removing the stereocenter in the molecules. Accordingly, ARN22090 and ARN22089 have been synthesized as compound having either a methoxy or a dimethyl amino substituent in the *meta* position, respectively, while keeping the piperidine nitrogen in position 4. ARN22090 and ARN22089 have moderate inhibitory activity in SKM28 cells (ARN22090 = IC₅₀ 38.1 μM, ARN22089 = IC₅₀ 24.8 μM). Furthermore, the replacement of the piperidine with a tetrahydropyran completely annihilated the activity in ARN22162 and ARN22163 in SKM28 cells, suggesting that the pyrane is not tolerated. Indeed, it was decided not to test them in the other melanoma cell lines and to do not evaluate their drug-like properties. To summarize, ARN22089 has a single-digit micromolar IC₅₀ activity against the more sensitive cell lines that were tested (WM3248, SKMe13, A375, and SW480), an optimal kinetic and thermodynamic solubility (>250 and 268 μM, respectively), and a good half-life in mouse plasma (71 min) and microsomes (27 min). In addition, ARN22089 does not have chiral centers in the

structure. In consideration of all the described features, ARN22089 was chosen as *lead compound*. In Figure 21, all the explored and synthesized compounds are reported. Also, in Table 1 and 2 all the related IC₅₀ and pharmacokinetics properties for the considered compounds are illustrated.

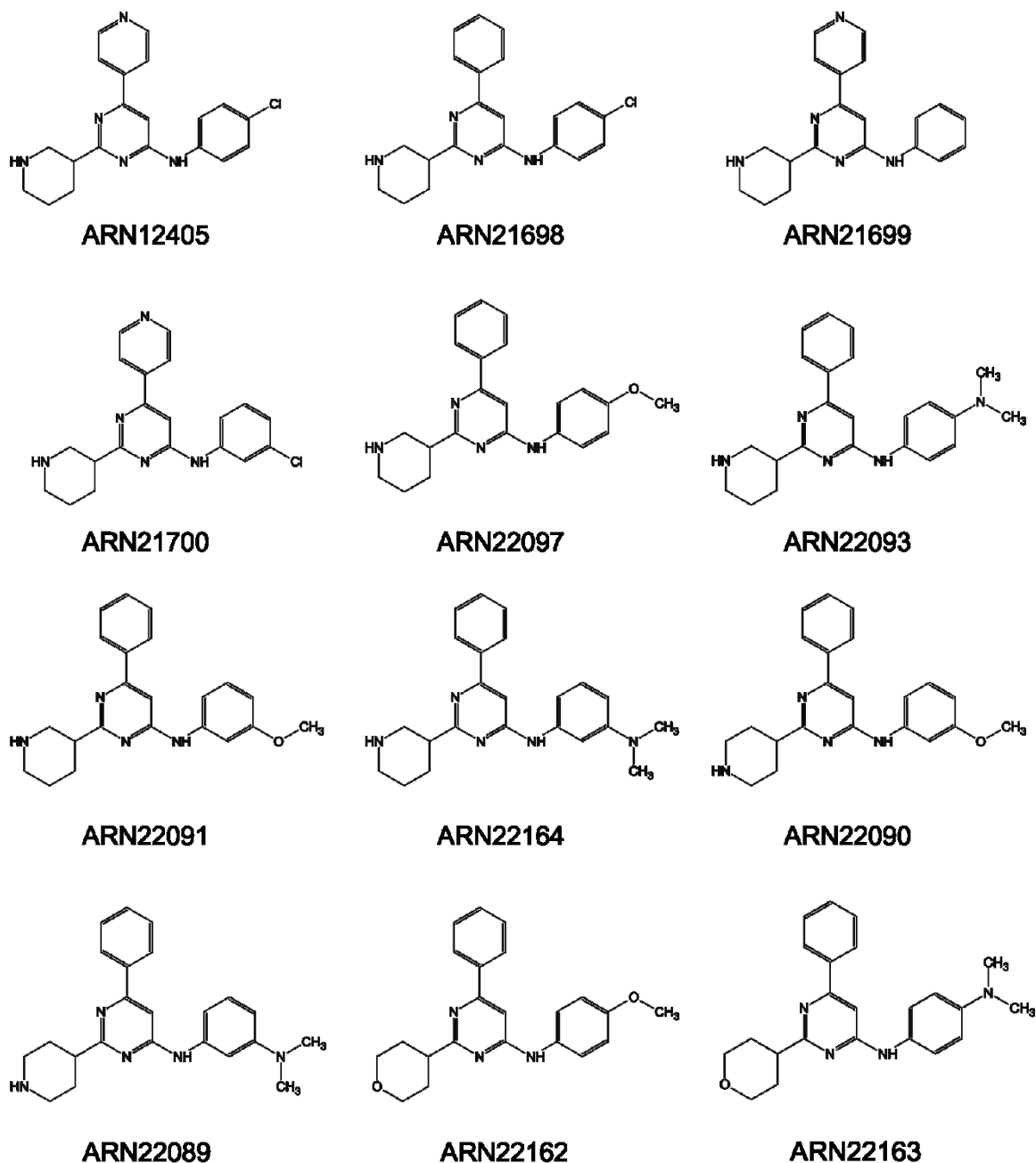


Figure 21. Synthesized compounds. The 2D structures of the *hit compound* along with the synthesized derivatives structural analogues is reported.

Compound	SKM28	WM3248	Skme13	A3755	SW480
ARN12405	16.37	14.38	13.47	15.27	14.8
ARN21698	10.21	8.423	6.3	10.94	11.91
ARN21699	ND	23.08	26.87	22.47	26.78
ARN21700	38.31	30.85	10.24	11.33	25.28
ARN22097	>50	27.53	13.27	22.94	25.04
ARN22093	45.02	12.76	11.84	13.14	17.66
ARN22091	24.2	11.28	11.77	12.52	17.75
ARN22164	31.4	10.97	8.138	14.61	11.4
ARN22090	38.12	9.468	4.588	9.787	10.49
ARN22089	24.8	4.523	4.257	4.92	8.608
ARN22162	>50	ND	ND	ND	ND
ARN22163	>50	ND	ND	ND	ND

Table 1. IC50 values. The IC50 values of the *hit compound* along with the synthesized derivatives structural analogues are reported for the five different cancer cell lines considered (SKM28, WM3248, SKMe13, A375 and SW480). IC50 values are expressed in μM . ND = not determined.

Compound	S kinetic	t 1/2 Plasma	t 1/2 Microsomes
ARN12405	222±6	>120	48
ARN21698	<1	>120	46
ARN21699	NA	NA	NA
ARN21700	NA	NA	NA
ARN22097	NA	NA	NA
ARN22093	246±2	>120	43
ARN22091	237±1	>120	21
ARN22164	>250	119±12	20
ARN22090	>250	>120	27
ARN22089	250±4	71	27
ARN22162	ND	ND	ND
ARN22163	ND	ND	ND

Table 2. Pharmacokinetics properties. Solubility, plasma and mouse microsomal half-life of the *hit compound* along with the synthesized derivatives structural analogues are reported.

Next, IC₅₀ values for ARN22089 was determined in a panel of 100 cancer cell lines with various different mutations. As results, the lead compound showed an IC₅₀

value smaller than 10 μM for fifty-five of the 100 cell lines tested, highlighting the broad spectrum anti-cancer activity of ARN22089.

3.5. ARN22089 binding mode analysis

In order to evaluate the lead compound binding mode, structural analysis has been performed. Specifically, docking prediction of ARN22089 in the effector pocket of RHOJ and CDC42 revealed a binding mode consistent with the one observed for ARN12405 (Figure 22).

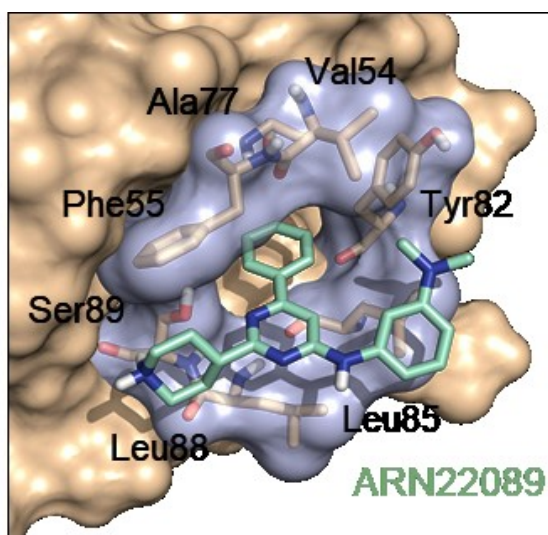


Figure 22. Docking pose prediction of ARN22089. The model structure of ARN22089 bound to CDC42/RHOJ is shown. The protein is represented as white surface, with the pocket residues highlighted as light blue surface and gray sticks. ARN22089 is reported in cyan sticks.

As for the hit compound, to further assess the predicted binding poses, MD simulations of both RHOJ and CDC42 in complex with ARN22089 have been performed. As shown in Figures 23, the lead compound steadily binds the target pocket throughout the simulations. In detail, the RMSD analysis over time of the MD trajectory revealed an RMSD values of $3.55 \pm 0.62 \text{ \AA}$ and $2.80 \pm 0.61 \text{ \AA}$ for ARN22089 in RHOJ- and CDC42-ligand complexes, respectively.

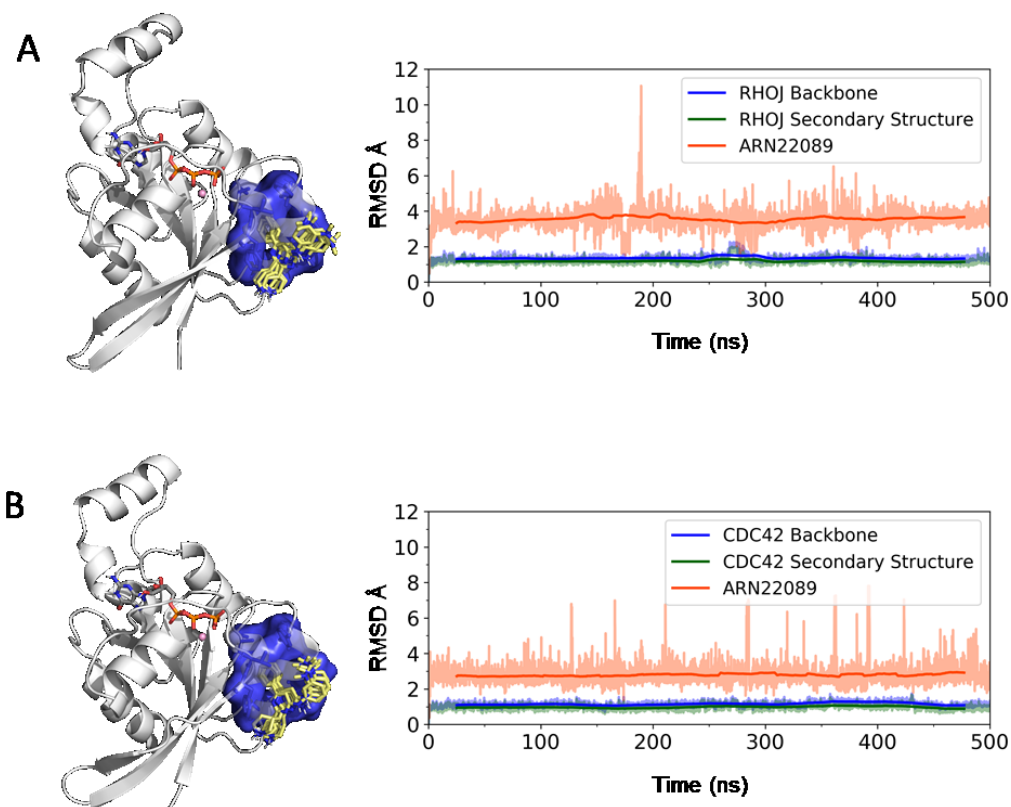


Figure 23. Docking pose prediction of ARN22089. The structural representation of RHOJ (A) and CDC42 (B) in complex with ARN22089 is reported on the left. Both RHOJ and CDC42 are represented as cartoon, while the binding pocket is highlighted as blue transparent surface. Multiple MD snapshots of the ARN22089 are shown as yellow sticks. On the right, the RMSD over time for both RHOJ (A) and CDC42 (B) binding complexes. The RMSD running averages is in bold.

To experimentally corroborate the predicted binding mode for ARN22089, the ability of the lead compound to bind to a purified CDC42 protein fragment was assessed. In agreement with the structural analysis outcomes and modeling results, which revealed the presence of our identified drug-binding pocket only in the GTP-bound active state, ARN22089 was found to bind CDC42 preferentially when the protein is in the GppNHP (a GTP analog) loaded state in microscale thermophoresis experiments. In addition, microscale thermophoresis disclosed also a better binding of ARN22089 to CDC42 respect to other known CDC42 inhibitors (ZCL278, ML141, R-ketoralac, and Casin). Also

ARN22089 selectivity was evaluated. To do this, a set of experiments have been carried out. Firstly, ARN22089 was tested using an established CDC42 effector assay, which measures the binding between GTPases and their downstream effectors, to verify that the lead compound could specifically inhibit CDC42-RHOJ binding to PAK, without affecting the interaction between RAC1 and PAK. Next, the ability of ARN22089 to inhibit the interaction between less closely related members of the RAS family and their downstream effectors was also investigated. ARN22089 inhibited the interaction between RHOJ or CDC42 and PAK1, without interfering with RAC1, RAS, or RAL effector interactions. Notably, ARN22089 selectivity towards CDC42 family could avoid cardiotoxicity effects often associated with RAC1 signaling blockade, as reported for other existing inhibitors. Again, in agreement with the predicted binding mode, ARN22089 inhibited the interaction between RHOJ or CDC42 and PAK1 at only when cell lysates were incubated with GTP, while interactions were detected between GDP-bound RHOJ or CDC42 and PAK1. CDC42 family effector interactions ARN22089 inhibition was also verify in cells using a bifluorescence complementation (BiFC) assay. In consideration of IC50 estimates, drug-like profile, experimental and computational binding mode analysis, ARN22089 was chosen as the most promising compound for further *in vitro* and *in vivo* studies.

3.6. ARN22089 *in vitro* and *in vivo* studies

To understand the effect of ARN22089 on cancer cells, the activation of kinase signaling pathways were examined in melanoma cells. Interestingly, ARN22089 treatment significantly influenced the abundance of 38 proteins and the phosphorylation of 10 proteins, among which the ribosomal protein S6 and the extracellular signal-regulated kinase ERK. Deeply, GTP-bound CDC42 binds to and activates the p70S6 kinase whose target is represented by the ribosomal protein S6. This particular phosphorylation event was found to be inhibited by ARN22089 in a time-dependent fashion. ARN22089 also inhibited ERK phosphorylation. ERK is a key component of the MAPK signaling that is upstream regulated by PAK through the phosphorylation of MEK. Taken together, the results indicate that ARN22089 modulates the functions of both the

CDC42 effector p70S6K and PAK *in vitro*. Furthermore, RNA sequencing was used to identify transcripts that were up- or downregulated upon ARN22089 treatment. As result, ARN22089 treatment was shown to induce the expression of genes involved in cell death.

Moreover, because of the described role of both CDC42 and RHOJ in angiogenesis related processes, the ability of ARN22089 to inhibit vessel formation around tumors was explored. To do this, vascularized microtumor platforms (VMT) were used. VMTs are platforms which reproduce a “tumor-on-a-chip” and incorporates human melanoma cells in a 3D extracellular matrix (ECM), where nutrient are delivered to the cells via perfused micro-vessels. Remarkably, ARN22089 significantly inhibited the growth of tumor blood vessels and caused their significant regression. Importantly, *in vivo* test in induced BRAF mutant melanoma tumors in mice as well as in patient-derived xenografts (PDXs) showed that ARN22089 can inhibit the tumor growth. Finally, tests aimed to examine whether ARN22089 engages targets known to be an impediment to developing safe drugs were carried out. As results, ARN22089 has no significant off-target effects as an agonist or an antagonist for a panel of 47 classical pharmacological target, such as the hERG channel. Taken together, these results demonstrated that ARN22089 i) has broad activity against a panel of cancer cell lines and a favorable pharmacokinetic profile, ii) inhibits S6 phosphorylation and MAPK activation and activates apoptotic signaling, iii) does not have off-target activity, iv) blocks tumor growth and angiogenesis in 3D vascularized microtumor models (VMT) *in vitro*, and v) inhibits tumor growth *in vivo* in both BRAF mutant mouse melanomas and patient-derived xenografts. All these reported results make ARN22089 a very promising drug candidate.

3.7. Discovery and optimization of follow-up inhibitors

Despite the high promising results obtained from the computational and experimental studies on ARN22089, modifications of the lead compound have been explored to synthesize and evaluate structural derivatives, according to synthetic feasibility and computational results. Starting from the ARN22089 structure, the aniline moiety was investigated, maintaining the 4-piperidine and the phenyl substituents of the pyrimidine core scaffold in position 2 and 6, respectively. Indeed, methoxy (*in orto*

position), 3,4-dimethoxyphenyl, 3-methoxyethoxyphenyl and dimethyl (in *ortho* position) substituents were evaluated in five different cancer cell lines (SKM28, WM3248, SKMe13, A375 and SW480). As results, the synthesized compounds exhibited different activities in the considered cell lines, pushing towards the exploration of new derivatives. Accordingly, the trifluoromethyl group in *meta* position in ARN25062 boosted the potency in all five cancer cell lines, with single-digit micromolar IC₅₀ (Figure 22 and Table 3). Considering the activity of both ARN22089 and ARN25062, the *meta*-trifluorophenyl and *meta*-dimethylamino substituents of the aniline moiety were considered as the best functionalities in combination with the 4-piperidine and the phenyl and in position 2 and 6, respectively.

Aimed to continue the structural exploration, also a triazine core was considered. Specifically, the triazine core counterparts of ARN22089 (namely ARN24928) and ARN25062 were generated and tested, showing a single-digit micromolar IC₅₀, with the exception of ARN25062 counterpart compound in SKM28 cells (IC₅₀ = 20.7 μM). Of the ~30 compounds synthesized and tested, the nineteen most potent compounds were further investigated for their kinetic solubility and plasma and microsomal stability in mice. With some exceptions, almost all compounds exhibited an excellent kinetic solubility (>150 μM), a good plasma stability (>70 min) and an acceptable microsomal stability (t_{1/2} > 40 min). Interestingly, the *meta*-trifluorophenyl on the aniline moiety in ARN25062 moderately diminished the solubility compared to ARN22089, while determined a solubility equal to 1 μM in the triazine core counterpart. While the compounds with low drug-like properties were excluded, further investigations were carried out for the other selected compounds. Accordingly, the solubility of such compounds was also confirmed by NMR measurement and microscale thermophoresis (MST) and NMR analysis were performed to evaluate the binding to CDC42. In consideration of the activity in all the considered cell lines (IC₅₀ values of 6.1 e 5.7 μM in SKM28 cells for ARN25062 and ARN24928, respectively), kinetic solubility, plasma and microsomal stability and *in vitro* binding data, ARN25062 and ARN24928 (Figure 24, Table 3 and Table 4) were selected as novel follow-up drug-like CDC42/RHOJ inhibitors to investigate. Indeed, ARN25062 and ARN24928 were subject of *in vivo* pharmacokinetics studies, which revealed that both compounds are well tolerated after a single injection and possess a favorable PK

profile, comparable to that of ARN22089. As for the lead compound, *in vivo* tests on patients-derived xenografts (PDXs) have been performed. Notably, both ARN25062 and ARN24928 exhibited a significant ability to inhibit tumor in PDXs *in vivo*, with an efficacy comparable to ARN2089 and no observed toxicity in the drug-treated animals.

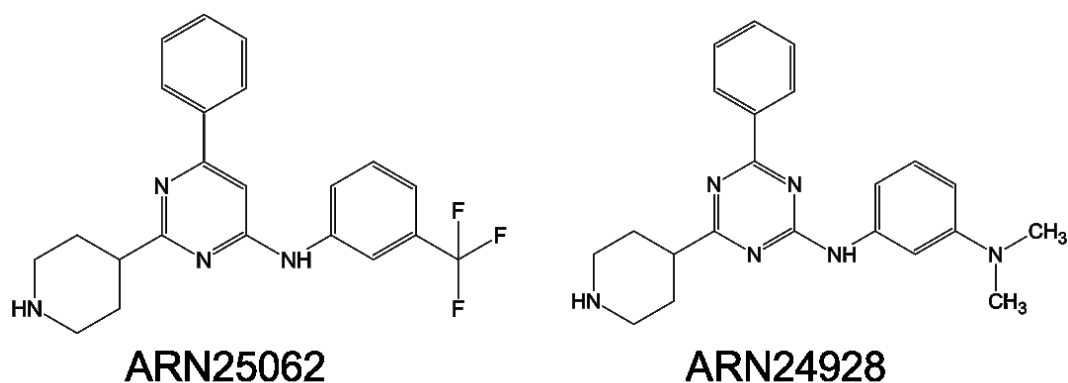


Figure 24. Follow-up compounds. The 2D structures of the ARN25062 and ARN24928 is reported.

Compound	SKM28	WM3248	Skme13	A3755	SW480
ARN25062	6.1	4.6	9.3	5.1	5.9
ARN24928	5.7	5.6	6.9	3.8	4.8

Table 3. IC50 values. The IC50 values of the ARN25062 and ARN24928 are reported for the five different cancer cell lines considered (SKM28, WM3248, SKMe13, A375 and SW480). IC50 values are expressed in μM .

Compound	S kinetic	t 1/2 Plasma	t 1/2 Microsomes
ARN25062	168	>120	45
ARN4928	209	>120	>60

Table 4. Pharmacokinetics properties. Solubility, plasma and mouse microsomal half-life of ARN25062 and ARN24928 are reported.

3.8. ARN25062 and ARN24928 binding mode analysis

In order to predict the binding mode of these new selected follow-up drug-like CDC42/RHOJ inhibitor compounds, the previously identified drug-binding pocket, localized at the CDC42-RHOJ/PAK protein-protein interfaces, was used as starting point for computational studies. Firstly, molecular docking calculations of the follow-up lead compounds ARN25062 and ARN24928 on the GTP-bound active form of CDC42 were performed. Modeling predicts that both ARN25062 and ARN24928 fit within the effector pocket of CDC42 (Figure 25A and 25B), consistently with the binding mode of both ARN12405 and ARN22089.

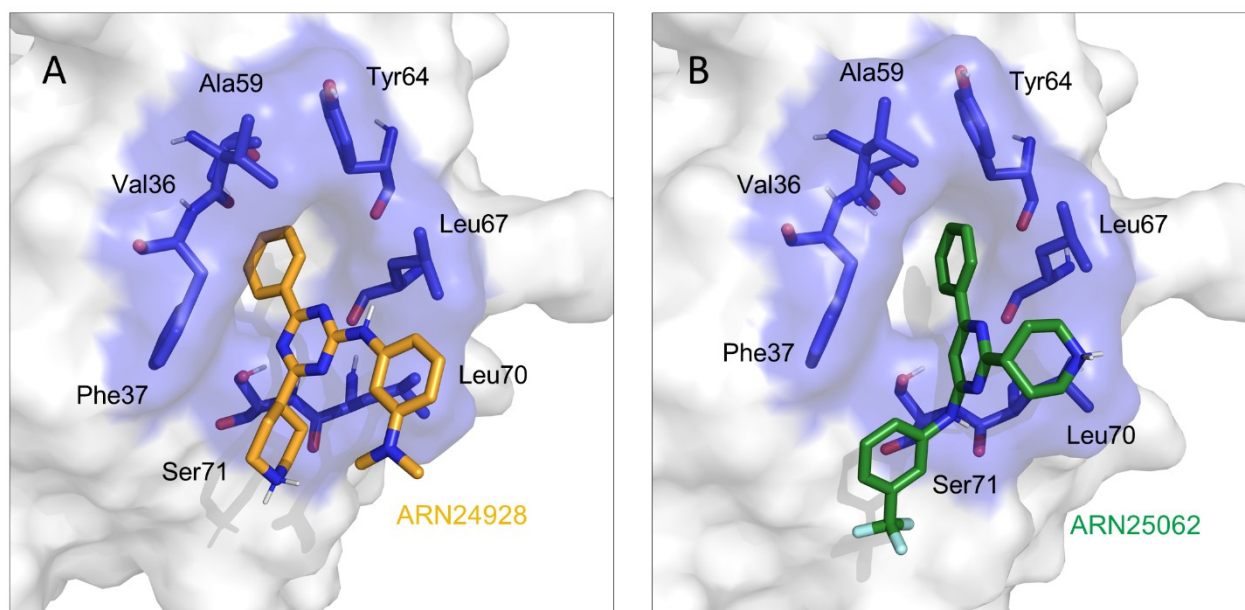


Figure 25. Structural identification of RHOJ/CDC42 allosteric effector binding pocket. The model structure of ARN25062 (A) and ARN24928 (B) compounds bound to the identified drug-binding pocket of CDC42 is reported. The structure of CDC42 is represented as white surface while the identified drug-binding pocket is shown in both stick and transparent blue surface. ARN25062 and ARN24928 are reported as green sticks and yellow, respectively.

The hydrophobic nature of the pocket easily accommodates the phenyl in position 6 of both pyrimidine and triazine core scaffold, which represents the anchor point for these novel follow-up compounds as well as for ARN22089 (Figure 26).

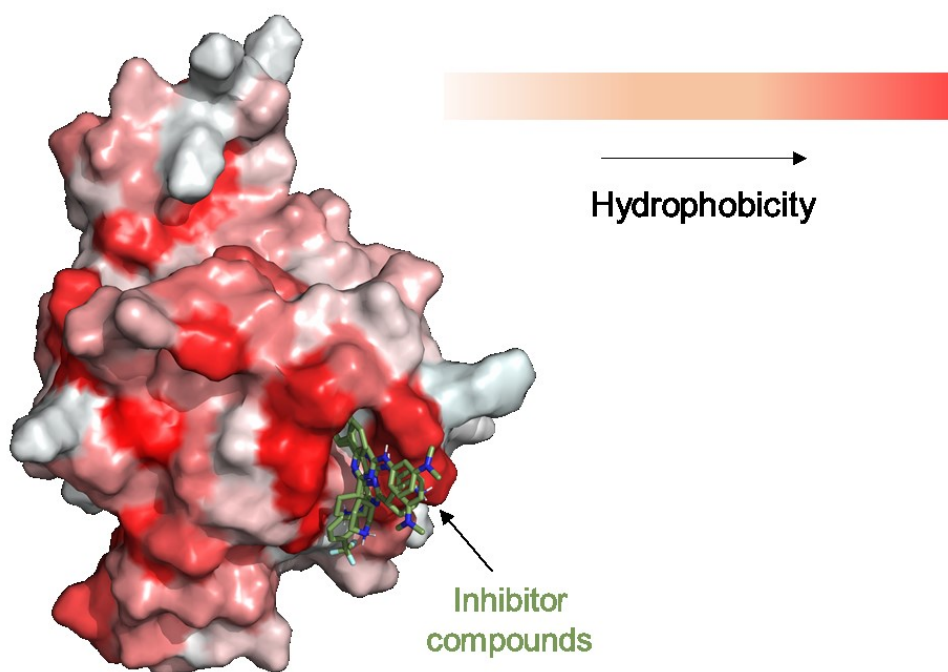


Figure 26. The phenyl in position 6 represents the predicted anchor point of the reported set of compounds. The model structure of ARN22089, ARN25062 and ARN24928 compounds bound to CDC42 is reported. The structure of CDC42 is represented as surface while the inhibitor compounds are shown as green sticks. The color scheme used to represent the protein surface is based on the Eisenberg hydrophobicity scale. As shown, the hydrophobic nature of the allosteric drug-binding pocket smoothly accommodates the phenyl in position 6, which represents the anchor point in all the reported docking poses.

Outstandingly, a different orientation of the piperidine portion in the binding mode with respect to the other active compounds has been predicted for compound ARN25062, where the accommodation of the phenyl ring is maintained, while the positioning of the pyridine core is inverted (Figure 25B). This is probably due to the close positively charged Lys5 of CDC42, which attracts the electronegative group $-CF_3$ (Figure 27).

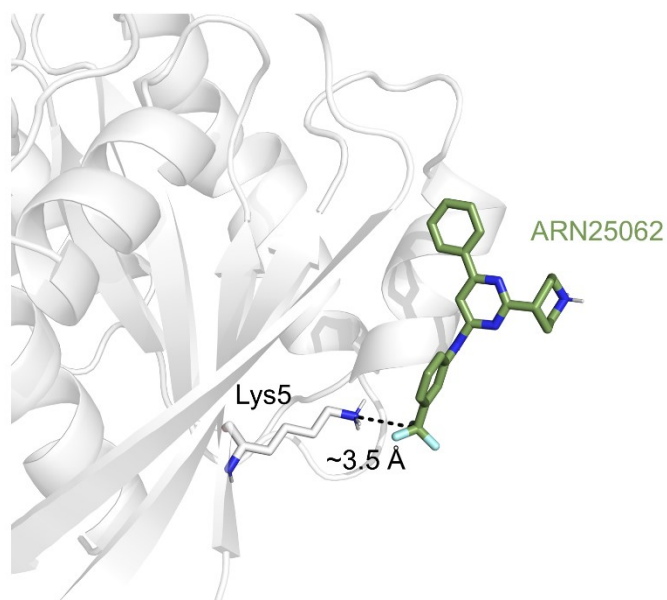


Figure 27. Lys5 could determine ARN25062 binding mode to the CDC42 effector pocket. The model structure of compound ARN25062 bound to the allosteric drug-binding pocket of CDC42 is reported. The structure of CDC42 is represented as white cartoon while ARN25062 and the close Lys5 residue are reported as green and white sticks, respectively. The observed inverted arrangement of pyridine core could be due to the attraction between the positive and the negative charges of the amino and trifluoromethyl group present in Lys5 and ARN25062, respectively, whose centers of mass lay ~ 3.5 Å apart from each other.

Of course, supporting structural analyses are needed in order to determine the accurate compound binding mode. In this regard, to further assess the predicted binding poses, molecular dynamics (MD) simulations of both ARN25062 and ARN24928 in complex with CDC42 were performed (Figure 28). As for the hit and lead compounds ARN12405 and ARN22089, the binding pose of both ARN25062 and ARN24928 in the CDC42-ligand complexes is preserved during 500 ns-long MD simulations (RMSD = 3.90

$\pm 1.30 \text{ \AA}$ and 3.80 ± 1.64 for ARN25062 and ARN24928 CDC42 complexes, respectively (Figure 28, right panels). Indeed, as shown in Figure 28 (left panels), ARN25062 and ARN24928 steadily bind the target pocket throughout the MD simulations.

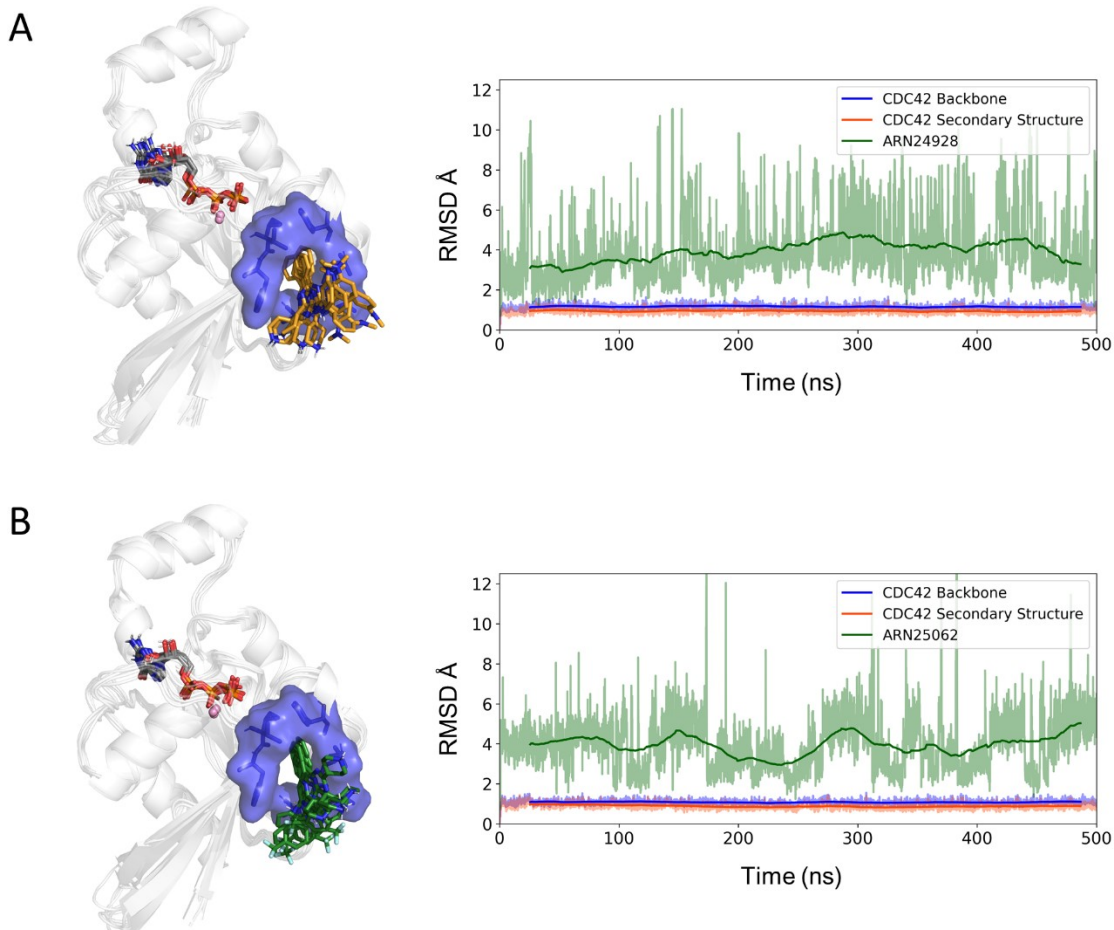


Figure 28. MD simulations of protein-ligand complexes. The structural representation of CDC42 in complex with ARN24928 (A) and ARN25062 (B) compounds is reported on the left. CDC42 is represented as cartoon, while the binding pocket is highlighted as both stick and transparent blue surface. Multiple MD snapshots of ARN24928 (yellow) and ARN25062 (green) binding poses are shown as sticks. On the right, the RMSD over time for the CDC42-ligand complexes is reported with the RMSD running averages highlighted in bold.

Overall these computational and experimental results, further demonstrate the potential of this novel chemical class of CDC42/RHOJ inhibitors, with lead compounds ready for advanced preclinical studies to develop new cancer treatments.

3.9. MD simulation details

Molecular dynamics (MD) simulations were performed considering both the RHOJ structural homology model and the CDC42 X-Ray structure (PDB ID 2ODB) in their ligand-free state, as well as the different protein-ligand complexes as obtained from our docking calculations. The RHOJ homology modeling process employed the CDC42 protein bound to the CRIB domain of PAK6 (PDB ID 2ODB) as a template structure. Employing Prime software⁵⁷⁴ within Maestro, the FASTA sequence of RHOJ was modeled based on the X-ray structure of 2ODB. The resulting structure was refined using the Protein Preparation Wizard workflow⁵⁷⁵ in Maestro. During this procedure, hydrogen atoms were added, and charges and protonation states were assigned according to physiological pH conditions. To alleviate steric clashes, a small number of minimization steps were performed until the RMSD of non-hydrogen atoms reached 0.30 Å. To assess the predicted binding mode, MD simulations were conducted on systems constructed using the RHOJ structural homology model bound to either ARN22089 or ARN12405. Other four systems included CDC42 (PDB ID 2ODB) in complex with ARN12405, ARN22089, ARN25062 and ARN24928. For RAC1 MD exploration, the available X-Ray structure of RAC1 complexed with the non-hydrolyzable GTP analogue GNP (or Gpp(NH)p) was employed (PDB ID 1MH1, resolution of 1.4 Å)⁵⁷³. To accurately represent RAC1 protein, the accidental mutation F78S present in the crystal was reverted to the *wild-type* and the GNP nucleotide was converted into GTP. Indeed, the GTP substrate as well as the catalytic Mg²⁺ ion are present at the active site of the proteins, in all the systems. These models were hydrated with a 14Å layer of TIP3P water molecules from the protein center. The coordinates of the water molecules at the catalytic center were taken from PDB ID 2ODB. Table 5 summarizes the size and the simulated time of the performed MD simulations described in this chapter. Sodium ions were added to neutralize the charge of the systems. The final models are enclosed in a box of ~89·89·89 Å³, containing ~18,500 water molecules, resulting in ~59,000 atoms for each system. The AMBER-ff14SB force field was used for the parametrization of the protein. The parameters for the ligands were determined via Hartree-Fock calculation, with 6-31G* basis set, convergence criterium SCF = Tight after structure optimization (DFT B3LYP functional; 6-31G* basis set). Merz-Singh-Kollman scheme was used for the atomic

charge assignment. The GTP and the Mg^{2+} were parametrized according to Meagher KL et al. and Allner et al., respectively. Joung-Cheatham parameters were used for monovalent ions. All MD simulations were performed with Amber 20 and all the systems were object of the following equilibration protocol.

To relax the water molecule and the ions, an energy minimization imposing a harmonic potential of 300 kcal/mol \AA^2 on the backbone, the GTP and the docked compound, when present, was performed. Then, two consecutive MD simulations in NVT and NPT ensembles (1 ns and 10 ns, respectively) were carried out, imposing the previous positional restraints. To relax the solute, two additional energy minimizations steps were performed imposing positional restraints of 20 kcal/mol \AA^2 and without any restraints, respectively. Such minimized systems were heated up to 303 K with four consecutive MD simulations in NVT (~ 0.1 ns, 100 K) and NPT ensembles (~ 0.1 ns, 100 K; ~ 0.1 ns, 200 K; ~ 0.2 ns, 303 K), imposing the previous positional restraints of 20 kcal/mol \AA^2 . The Andersen-like temperature-coupling scheme was used, while pressure control was achieved with Monte Carlo barostat at reference pressure of 1 atm. Long-range electrostatics were treated with particle mesh Ewald method. Next, an additional MD simulation (~ 1.5 ns) in the NPT ensemble at 303 K without any restraint to relax the system at such temperature was performed. Finally, multiple replicas of 500 ns were performed in the NPT ensemble for each system with an integration time step of 2 fs.

	N° atoms system	N° atoms solvated system	Simulated time
RHOJ	$\sim 2,830$	$\sim 59,000$	500 ns
CDC42	$\sim 2,830$	$\sim 60,300$	500 ns
RHOJ-ARN12405	$\sim 2,880$	$\sim 58,100$	500 ns
CDC42-ARN12405	$\sim 2,880$	$\sim 60,200$	500 ns
RHOJ-ARN22089	$\sim 2,890$	$\sim 58,000$	500 ns

CDC42-ARN22089	~ 2,890	~ 60,150	500 ns
RAC1	~ 2,900	~ 65,000	500 ns
CDC42-ARN24928	~ 2,890	~ 59,300	500 ns
CDC42-ARN25062	~ 2,880	~ 59,400	500 ns

Table 5. MD simulations summary. An overview summarizing both the size and simulated time of the conducted MD simulations is reported.

Chapter 4. Alchemical Free Energy Calculations for protein–protein interface studies

4.1. CDC42/PAK interaction as test case for free energy calculations

Protein–protein interactions (PPIs) are dynamic, but specific, noncovalent associations between protein partners that are fundamental for biological activities, including cell regulation and signaling. Indeed, the formation of protein-protein complexes is required for cells to receive, integrate, and distribute regulatory information. The central role of PPIs in cell homeostasis is exemplified by signaling pathways, in which a consecutive series of protein-protein interactions work together to carry out a specific cell function, for which the signaling was triggered. Interestingly, interactome networks are emerging with the aim to map and uncover the intricate set of molecular interactions within a cell, which are mainly represented by PPIs⁵⁷⁶. Despite the large progresses achieved in the determination of protein–protein complex structures, the comprehension of their recognition and association mechanisms is still challenging. This has particular relevance if we consider that many of the human diseases are linked to abnormal activation of signaling pathways and, therefore, to an anomalous regulation of protein-protein interaction events⁵⁷⁷. Accordingly, targeting PPIs is nowadays a strategic therapeutic approach aimed to prevent the formation of aberrant protein complexes^{578–584}.

To address this goal, the prediction of key residues involved in the recognition mechanism would facilitate the identification of druggable interactions. A way to investigate protein–protein interactions is to estimate the affinity between the protein partners, upon mutations of selected residues. Despite mutagenesis is undoubtedly a leading experimental technique, the procedure could be markedly time consuming, if the number of possible mutants is considered. In this regard, computational methods capable of predicting the effects of mutations and quantifying the binding affinity between proteins would help rank the most relevant mutations to validate in experimental studies. However, because of the diverse nature of protein-protein interactions, a detailed knowledge of the

system is required. Accordingly, atomic-level MD simulations based method allow to fully take into account protein flexibility, characterizing both the structure and dynamics of the protein–protein complex. In this regard, alchemical free energy calculations can be used to estimate the change in free energy associated to residues' mutations, from which derive the binding affinity. Despite such methods are routinely and successfully used to design small-molecule drug, its use in the context of protein–protein interactions is limited.

In accordance with the therapeutic relevance of CDC42/PAK interaction, such interface has been used as test case to explore the use of alchemical free energy calculations to inspect the effect of single point mutations on protein–protein interactions. The benchmark study has been used to quantitatively evaluate, assess, compare and explore the performance of the method, exploiting available binding affinity data towards PAK1 reported for 16 CDC42 mutants.

4.2. CDC42/PAK1 Homology Modeling and Systems set-up

The crystal structure of CDC42 in complex with the CRIB domain of PAK6 (PDB ID 2ODB, resolution of 2.4 Å) was used as a template for comparative modeling to build a model of the CDC42/PAK1 complex (Figure 29), as well as to set up a model of CDC42 alone by removing the effector.

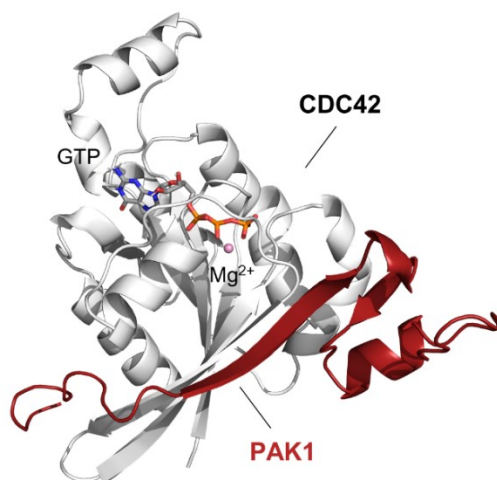


Figure 29. Structural representation of the CDC42/PAK1 model. The CDC42/PAK1 complex is reported. CDC42 is represented as white cartoon, while PAK1 is shown in red. The GTP nucleotide and the Mg²⁺ ion are in sticks and balls, respectively.

For CDC42, residues 2 to 178 were considered, excluding the flexible carboxylterminal region, which regulates homodimer formation and the proper subcellular localization but is not involved in the binding of effectors^{27,28}. For PAK1, modeling included residues 70 to 117, which have been proven to comprise the smallest PAK1 fragment required for the interaction with CDC42⁵⁸⁵. Utilizing MODELLER version 10.1⁵⁸⁶, comparative modeling was carried out by modeling the FASTA sequence of PAK1 on the X-ray structure of the CDC42 protein bound to the CRIB domain of PAK6 (PDB ID 2ODB), which served as the template structure. The model with the lowest DOPE score was selected for system setup. To assess the reliability of the model, a structural comparison with available X-ray structures of GTPases/PAK complexes was carried out⁵⁸⁷ (Figure 30).

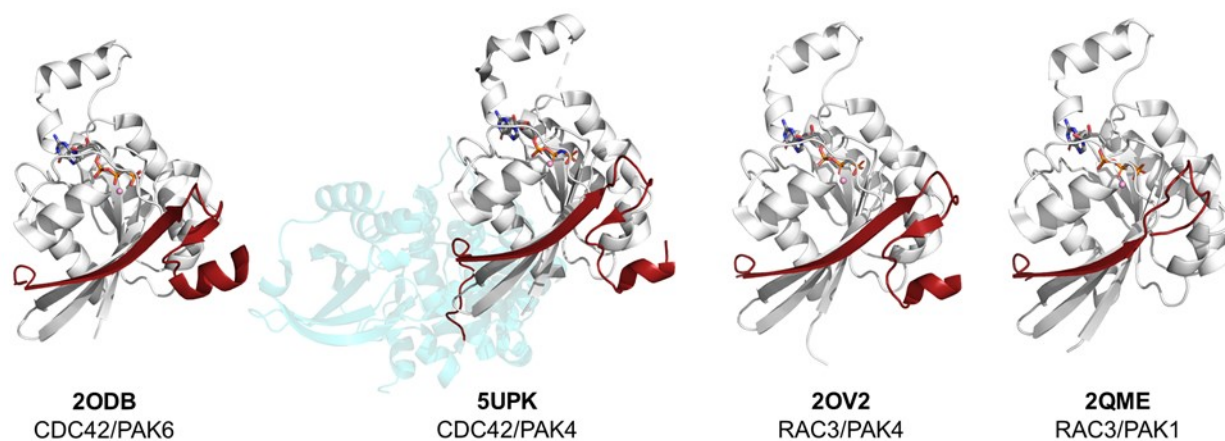


Figure 30. Structural representation of the available X-ray structures of GTPases/PAK complexes. The structural representation of the available X-ray structures of GTPases/PAK complexes are reported (from left to right: CDC42/PAK6, PDB code 2ODB, 2.4 Å resolution; CDC/42/PAK4, PDB code 5UPK, 2.4 Å resolution, RAC3/PAK4, PDB code 2OV2, 2.1 Å resolution, RAC3/PAK1, PDB code 2QME, 1.75 Å resolution). GTPase and PAK proteins are represented as white and red cartoon, respectively.

In detail, the root mean square deviation (RMSD) analysis of interfacial residues did not showed structural variations between the model and experimental structures (Figure 31).

	MODEL	2ODB	5UPK	2OV2	2QME
MODEL	0				
2ODB	0.16	0			
5UPK	0.41	0.38	0		
2OV2	0.40	0.34	0.36	0	
2QME	0.42	0.36	0.40	0.30	0

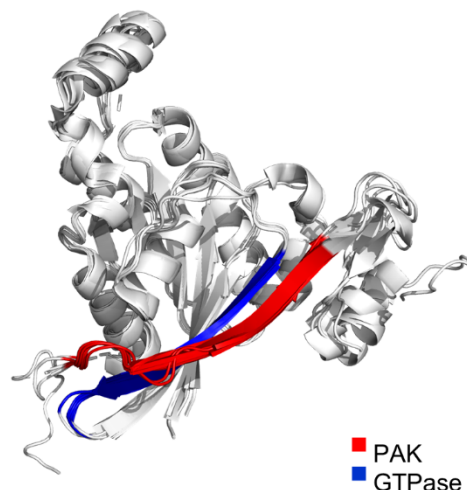


Figure 31. Structural analysis of available X-ray structures of GTPases/PAK complexes. On the left, the interface RMSD matrix among the described X-ray structures and the CDC42/PAK1 homology model is reported. The RMSD values given in the table are expressed in Å. On the right, the structural representation of the analyzed GTPases/PAK complexes is reported. Interface residues are highlighted as blue and red cartoon for the GTPase and PAK, respectively.

Furthermore, conserved contacts established between the interface β -sheets of CDC42 and PAK were maintained in the model (Figure 32), highlighting the consistency of the structural model with known structures of homologous complexes.

	MODEL	2ODB	5UPK	2OV2	2QME
M45-S76	3.0	3.1 (M45-S13)	2.9 (M45-S12)	2.9 (M45-S12)	2.9 (M45-S76)
M45-S76	3.8	3.1 (M45-S13)	2.8 (M45-S12)	3.0 (M45-S12)	2.9 (M45-S76)
T43-S79	2.8	2.8 (T43-Q16)	2.9 (T43-S15)	2.8 (N43-S15)	2.8 (N43-S79)
T43-S79	2.8	2.8 (T43-Q16)	2.7 (T43-S15)	2.8 (N43-S15)	2.9 (N43-S79)
A41-E82	2.9	2.9 (A41-Q19)	3.1 (A41-E18)	2.9 (S41-E18)	2.9 (S41-E82)
A41-E82	2.8	2.8 (A41-Q19)	2.9 (A41-E18)	2.8 (S41-E18)	2.9 (S41-E82)
N39-T84	3.0	2.9 (N39-V22)	3.1 (N39-R20)	2.8 (N39-R20)	2.9 (N39-T84)
N39-I85	3.2	3.2 (N39-V22)	3.4 (N39-V21)	3.3 (N39-V21)	3.2 (N39-I85)
N39-I85	2.9	3.0 (N39-V22)	3.1 (N39-V21)	3.0 (N39-V21)	3.0 (N39-I85)
F37-V87	2.9	3.0 (F37-T24)	2.8 (F37-T23)	2.9 (F37-T23)	2.9 (F37-V87)
G47-E74	5.9	3.6 (G47-E11)	3.0 (G47-E10)	2.8 (D37-E10)	2.8 (D37-E74)

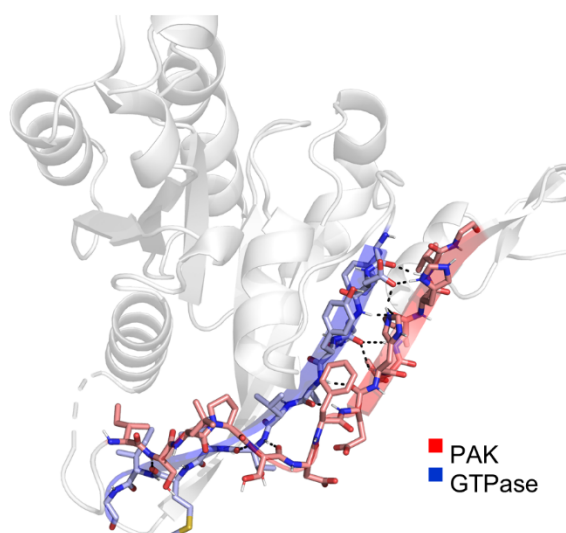


Figure 32. Structural analysis of available X-ray structures of GTPases/PAK complexes. On the left, the distance values of conserved contacts at the β/β -sheets GTPase/PAK interface are reported in the Table. The distance values given in the table are expressed in Å. On the right, the structural representation of the analyzed GTPases/PAK complexes is reported. Interface residues are highlighted as both blue and red cartoon and sticks for the GTPase and PAK, respectively.

The GTP substrate, catalytic Mg^{2+} ion, and experimentally determined water molecules at the active site were included in both the apo and PAK1-bound CDC42 forms. Systems were solvated in cubic simulation boxes extending at least 14 Å from the protein surface. Sodium ions were added randomly to neutralize the charge of the systems. Final models included ~60,000 atoms in a $85 \times 85 \times 85 \text{ \AA}^3$ box for apo CDC42 and ~78,500 atoms in a $\sim 93 \times 93 \times 93 \text{ \AA}^3$ box for the complex.

Aimed to explore the impact of single-point mutations on the stability of the complex, CDC42/PAK1 complexes with either the Y40C or the F37A mutation in CDC42 were additionally considered and generated. This choice was done as both mutations are detrimental for binding of CDC42 to PAK1⁵⁸⁸. In particular, the Y40C mutation is among the most harmful mutations, causing a >100-fold increase in K_d . Specifically, the Y40C mutation of CDC42 was observed experimentally to destabilize its binding to PAK1 by >2.3 kcal/mol (calculated by first converting in kcal/mol the experimental K_d value of >1000 nM). The F37A mutation in CDC42 generated a decrease of 1.3 kcal/mol in the affinity for PAK1 (calculated from the experimental K_d value of ~190 nM). Also, F37A exemplifies a mutation often explored in mutagenesis studies, in which the bulky residue Phe is changed to the smaller apolar Ala residue⁵⁸⁹. Models of CDC42 Y40C and F37A variants in a PAK1-bound form were built from the *wild-type* (*wt*) model.

4.3. MD simulations of CDC42/PAK1 complexes

To assess the CDC42/PAK1 complex stability 1 μ s MD simulations were run and analyzed. First, the *wt* CDC42/PAK1 complex equilibrated after ~15 ns and remained stable for the rest of the simulation (Figure 33A). The initial GTP binding pose and the

coordination of the catalytic Mg^{2+} ion were also well maintained throughout the simulations (Figure 33B and 33C). In addition, the CDC42/PAK1 protein interface appeared highly stable compared to the unbound CDC42, which exhibited larger fluctuations of the residues 35–72 belonging to the switch motifs and to the β -sheet in contact with PAK1 (Figure 33D) in all the *wt* and mutants simulations.

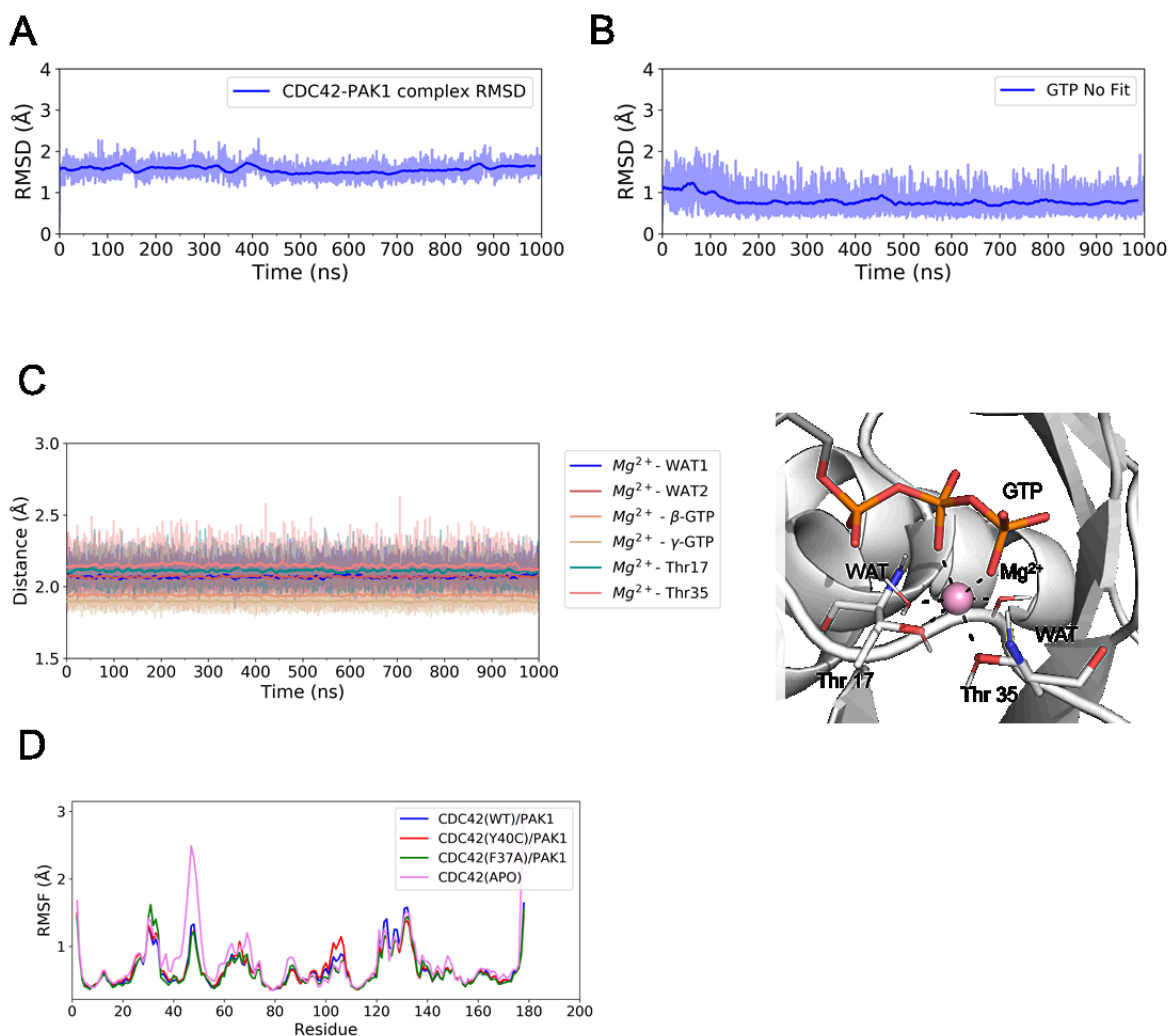


Figure 33. MD simulations of CDC42/PAK1 complexes. The time series RMSD descriptor for the system's backbone of CDC42(*wt*)/PAK1 is reported in A. The conservation of the GTP catalytic pocket was investigated through the time series RMSD for the GTP nucleotide (B) and by monitoring the length of the Mg^{2+} coordination bonds (C). Both RMSD and distance values descriptors are shown as shaded areas, while the associated running averages are represented as lines. The Root mean square fluctuation (RMSF) per residue of CDC42 alone and in

CDC42/PAK1 complexes is reported in D. Compared to the unbound CDC42, in all the case studies the formation of the complex reduces the fluctuations of residues located at the interface.

In order to evaluate the conformational structures sampled during MD simulation, the density peaks algorithm has been implemented⁵⁴⁴. Indeed, structures from all our simulations (*wt* and two mutated systems) were clustered based on the RMSD of the interface residues, revealing very similar conformations (Figure 34).

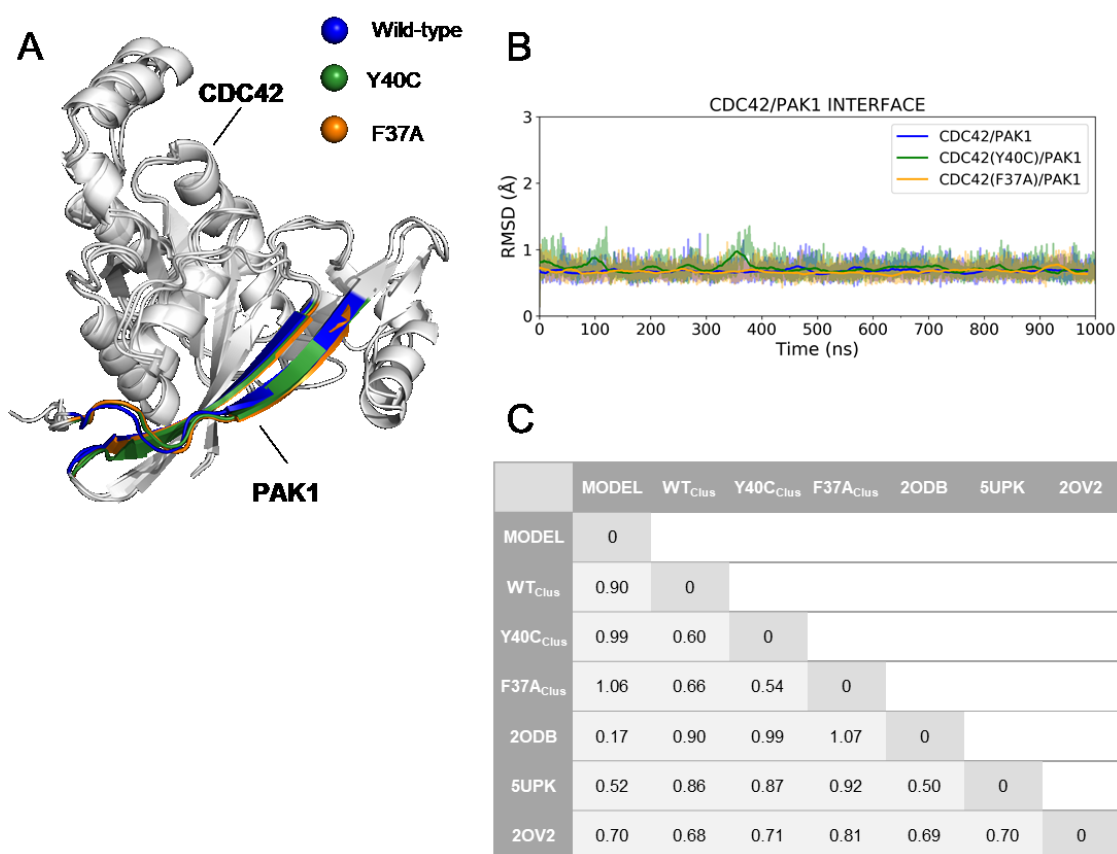
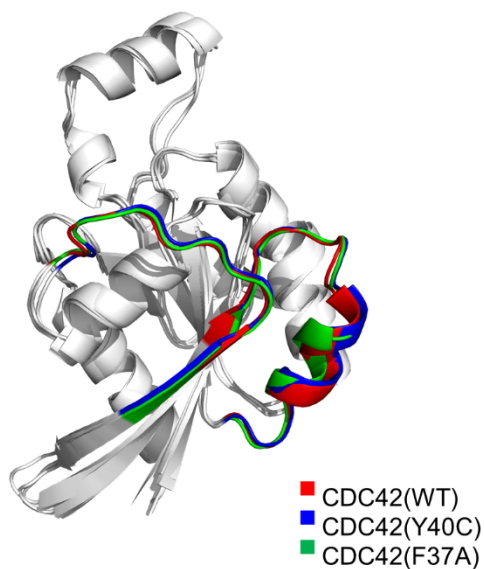


Figure 34. RMSD analysis of the interface of the CDC42/PAK1 systems. The structural alignment of representative conformations from MD simulations is reported in A. The protein structures are represented as white cartoon, while the GTP nucleotide and Mg²⁺ ion are illustrated as sticks and balls, respectively. Interface residues on both CDC42 and PAK1 are highlighted as blue, green and orange for the *wt*, Y40C and F37A systems, respectively. The time-series RMSD descriptors for CDC42 *wt* (blue), Y40C (green) and F37A (orange) variants are reported in B.

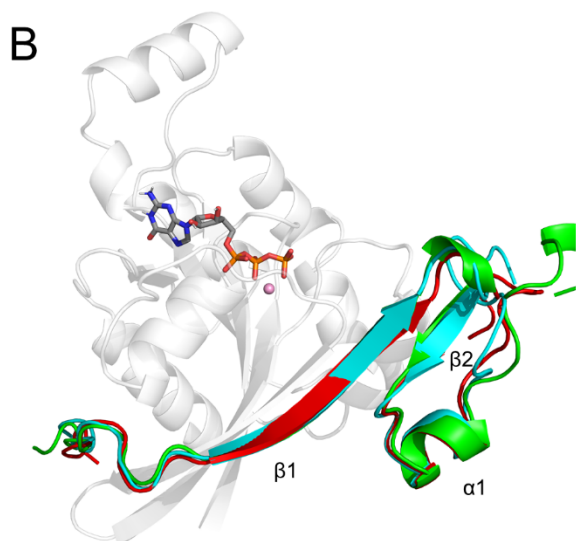
RMSD values (in Å) of interface residues between different structures, including MD representative structures, the initial model and experimental structures are reported in C.

Additionally, switch motifs (switch I and II) of CDC42 maintained the active conformation along the entire simulations, remaining aligned to the initial structure (Figure 35A) in all cases. Also, PAK1 showed no difference in the *wt* versus mutated complexes (Figure 35B) during the simulations. In particular, the β -sheets forming the intermolecular interactions between CDC42 and PAK1 were quite stable. These overall analyses of the MD trajectories were propaedeutic to the alchemical free energy calculations.

A



	CLUSTER _{WT}	CLUSTER _{Y40C}	CLUSTER _{F37A}
CLUSTER _{WT}	0		
CLUSTER _{Y40C}	0.48	0	
CLUSTER _{F37A}	0.84	0.84	0



Full length PAK1

	CLUSTER _{WT}	CLUSTER _{Y40C}	CLUSTER _{F37A}
CLUSTER _{WT}	0		
CLUSTER _{Y40C}	0.80	0	
CLUSTER _{F37A}	0.76	0.71	0

β 1 PAK1

	CLUSTER _{WT}	CLUSTER _{Y40C}	CLUSTER _{F37A}
CLUSTER _{WT}	0		
CLUSTER _{Y40C}	0.73	0	
CLUSTER _{F37A}	1.12	1.33	0

β 2 PAK1

	CLUSTER _{WT}	CLUSTER _{Y40C}	CLUSTER _{F37A}
CLUSTER _{WT}	0		
CLUSTER _{Y40C}	1.44	0	
CLUSTER _{F37A}	1.24	0.88	0

α 1 PAK1

	CLUSTER _{WT}	CLUSTER _{Y40C}	CLUSTER _{F37A}
CLUSTER _{WT}	0		
CLUSTER _{Y40C}	1.77	0	
CLUSTER _{F37A}	1.49	1.33	0

Figure 35. Switch motifs and PAK1 clustering analysis. A) On the left, superposition of representative structures of the clusters obtained by grouping the configurations along the MD trajectories of CDC42/PAK1 complexes based on the RMSD of the switch regions of CDC42. Switches residues are highlighted as red, blue and green cartoon for the *wt*, Y40C and F37A CDC42 forms, respectively. On the right, RMSD values of the switch regions expressed in Å. B) On the left, superposition of representative structures of the clusters obtained by grouping the configurations along the MD trajectories of CDC42/PAK1 complexes based on the RMSD of PAK1. PAK1 are highlighted as green, red and cyan cartoon for the *wt*, Y40C and F37A CDC42 forms, respectively. On the right, RMSD values of different structural elements of PAK1 (expressed in Å).

4.4. Alchemical free energy calculations based on sidechain transformation

Once assessed the overall stability of the model system in classical MD, the relative binding free energies ($\Delta\Delta G_{\text{binding}}$) of 16 CDC42 single-point mutants towards PAK1 has been calculated⁵⁸⁸ (Figure 36).

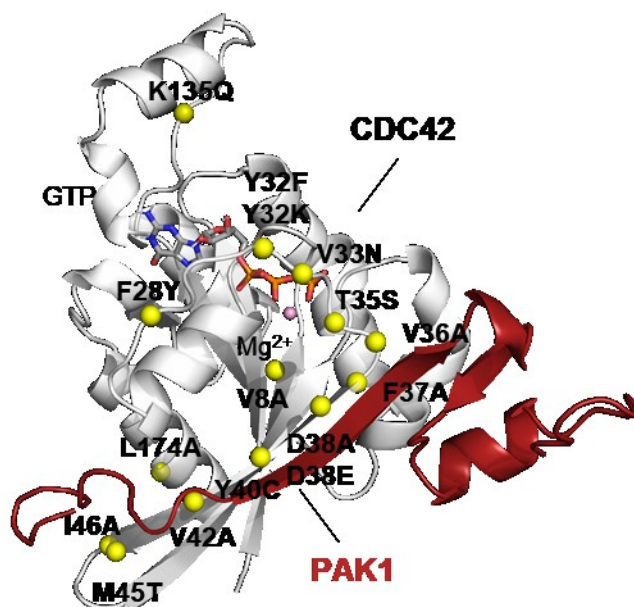


Figure 36. Structural representation of the investigated single-point mutations. The analyzed single-point mutations are represented as yellow balls on the CDC42/PAK1 complex structure. CDC42 is represented as white cartoon, while PAK1 is showed in red. The GTP nucleotide and the Mg²⁺ ion are in sticks and balls, respectively.

In detail, the $\Delta\Delta G_{\text{binding}}$ was computed by alchemically transforming CDC42 from *wt* into the mutant form in both the apo and PAK1-bound forms. Thus, from equilibrated configurations of the CDC42/PAK1 complex and CDC42, a total of 34 systems were built (including a control calculation on the *wt* system) and used to run alchemical transformations carried out in 12 λ -windows of 10 ns each for a total of 120 ns per

transformation. In total, a cumulative time of $\sim 4 \mu\text{s}$ was collected. All systems remained stable during the alchemical transformations, with low RMSD values for residues at the CDC42/PAK1 interface (Figures 37) as well as for the GTP binding pose, of which an example is reported in Figure 38.

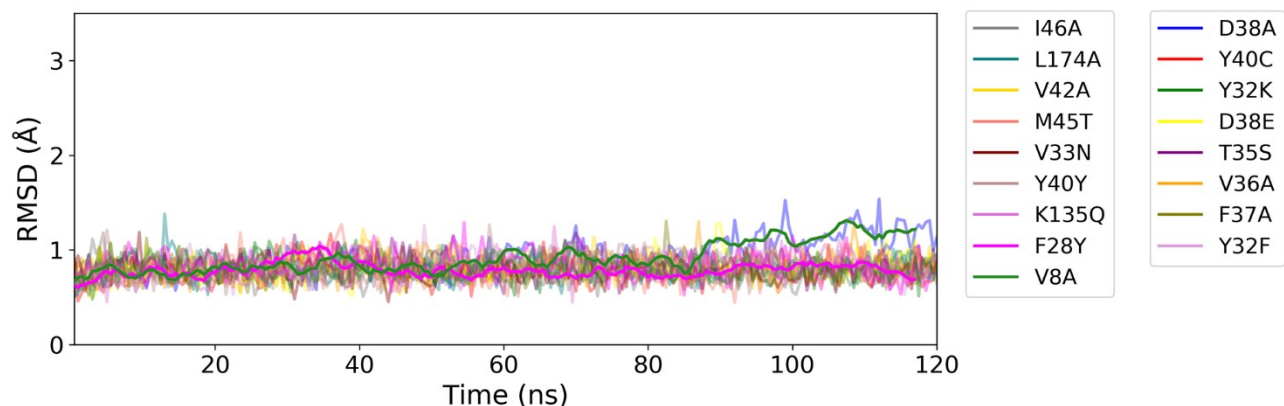


Figure 37. CDC42/PAK1 alchemical simulations analysis. The time series of the RMSD of the backbone of interface residues is reported for each investigated mutation.

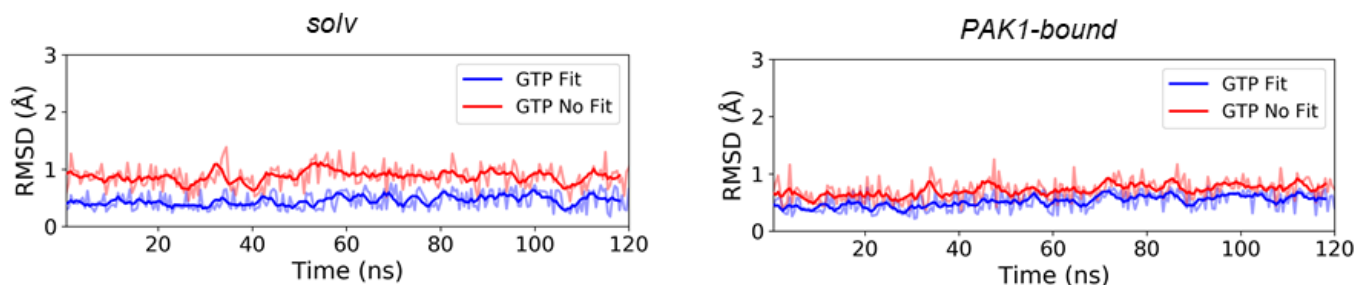


Figure 38. CDC42 and CDC42/PAK1 alchemical simulations analysis. For each investigated mutation, the time series of the RMSD of the GTP nucleotide for both apo and PAK1-bound CDC42 forms have been computed. The RMSD was computed after aligning the nucleotide (blue line) and after aligning the protein backbone (red line). Only the time series of the RMSD of the GTP nucleotide is reported for the F28Y mutation, as example.

A good agreement of the computed $\Delta\Delta G_{\text{binding}}$ values with experimental data is shown in the plot in Figure 39.

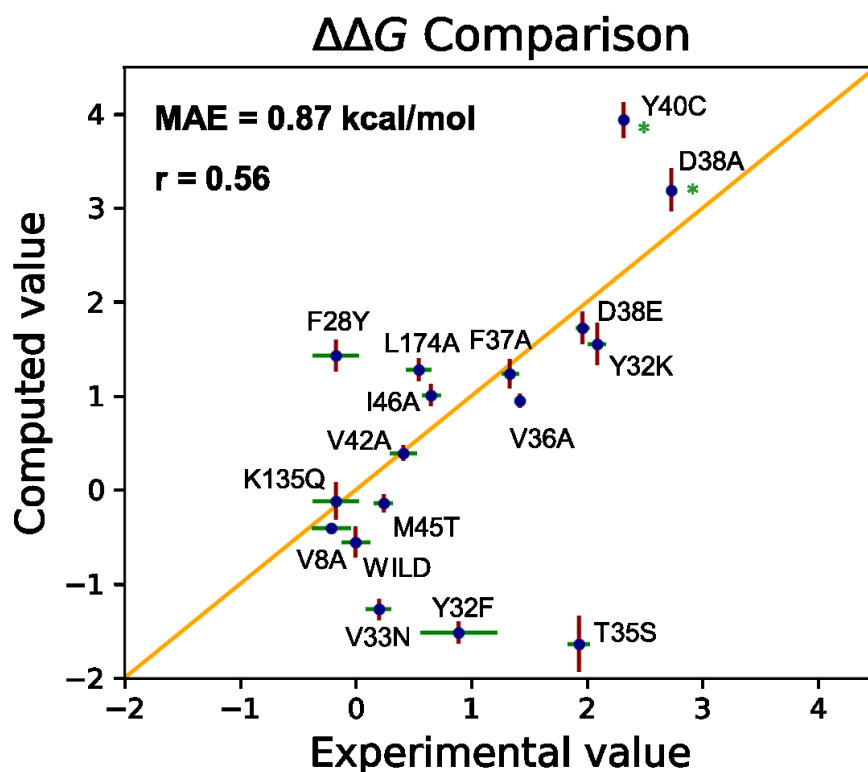


Figure 39. $\Delta\Delta G_{\text{binding}}$ values (in kcal/mol) computed using the alchemical transformations and plotted against the experimental values. The computed $\Delta\Delta G_{\text{binding}}$ (in kcal/mol) are plotted against the experimental values. The examined single-point mutations are reported together with their computed (red) and experimental (green) error bars. The asterisk (*) marks mutations for which the experimental error was not reported.

The mean absolute error (MAE) is 0.87 kcal/mol, which is in the range of successful applications of alchemical free energy calculations in drug design^{471,476,590}. Notably, for 10 mutations out of 16, the error is below 0.5 kcal/mol (Table 6). In addition, CDC42 mutations V8A, V42A, M45T, and K135Q have a marginal effect on the free energy of binding to PAK1, while Y32K, D38A, D38E, and Y40C mutations are suggested to disfavor the binding between the two partners. Specifically, D38A mutation is found to be particularly detrimental, in line with the experimental data (K_d value > 2000 nM). Overall, the results indicate that alchemical binding free energy calculations can locate those mutations that can affect binding affinity. For example, D38A leads to a >1000-fold lower affinity for PAK1 compared to the *wt* enzyme. Furthermore, the positive sign (indicative

of a harmful mutation) of $\Delta\Delta G_{\text{binding}}$ was predicted correctly for all mutations having a reported $\Delta\Delta G_{\text{binding}} > 0.5$ kcal/mol. Also, the $\Delta\Delta G_{\text{binding}}$ for CDC42 mutants Y40C and F37A estimated from the alchemical transformations is in good agreement with the experimental data. A value of 3.94 ± 0.04 kcal/mol for Y40C and 1.24 ± 0.30 kcal/mol for F37A was computed (vs >2.32 and 1.33 ± 0.07 kcal/mol from experiments, respectively).

4.5. Improving alchemical free energy calculations results

Despite the encouraging agreement of the computed free energy changes compared to the experimental data, the estimates for four mutations exhibit deviations larger than the mean error. Namely, this is the case for T35S, F28Y, Y32F, and V33N. This is particularly worrying given that the predicted change is sometimes in the opposite direction with respect to the experimental determination. To address this apparent issue, different atom mapping schemes to preserve the key interactions established by the residues involved in single-point mutation has been explored.

4.5.1. Tuning the mapping scheme for T35S and F28Y

4.5.1.1. T35S mutation

Side-chain alchemical transformations predict this mutation to be favorable by -1.6 ± 0.2 kcal/mol contrary to the experimental determination (1.9 ± 0.1 kcal/mol). The side chain of T35 is bound to the catalytic Mg^{2+} , whose coordination sphere is considered fundamental for preserving the active conformation^{11,13,17} (Figure 40A). During the alchemical transformation of the whole side chain of T35 into a serine residue, the hydroxyl group of the latter does not maintain the initial interaction of T35 with Mg^{2+} (Figure 40B and 41). This leads to a destabilization of the active site.

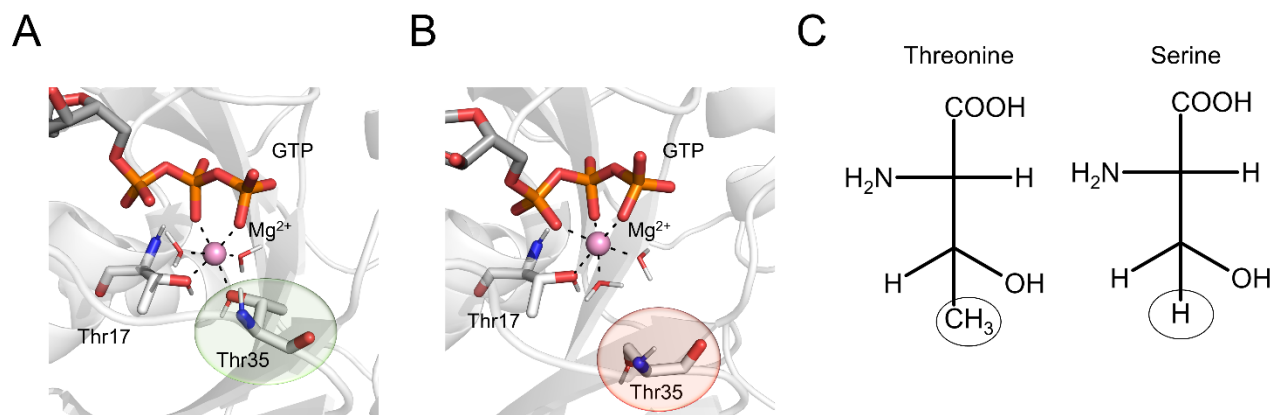


Figure 40. T35S CDC42 mutant analysis. The interaction between the catalytic Mg²⁺ and the hydroxyl group of Thr35 as observed in the equilibrium MD simulations of the *wt* system is reported in A. After the initial alchemically transform Thr25 into Ser, the coordination sphere of Mg²⁺ was disrupted (B). The protein is represented as white cartoon, the GTP nucleotide and the residues coordinating Mg²⁺ as sticks, and the Mg²⁺ ion as a ball. The revised atom mapping used to improve the $\Delta\Delta G_{\text{binding}}$ estimate is reported in C. The circled atoms are those considered unique for the transformation.

Notably, this occurs in both the bound and unbound CDC42 alchemical transformation calculations (Figure 41). Thus, a different mapping scheme was decided to be used to transform a threonine into a serine, in which only the terminal methyl group of the threonine and the corresponding hydrogen atom of serine were considered unique to each residue⁵⁵⁷ (i.e., the atoms of the $-\text{C}\beta\text{HOH}$ group were considered common atoms, Figure 40C).

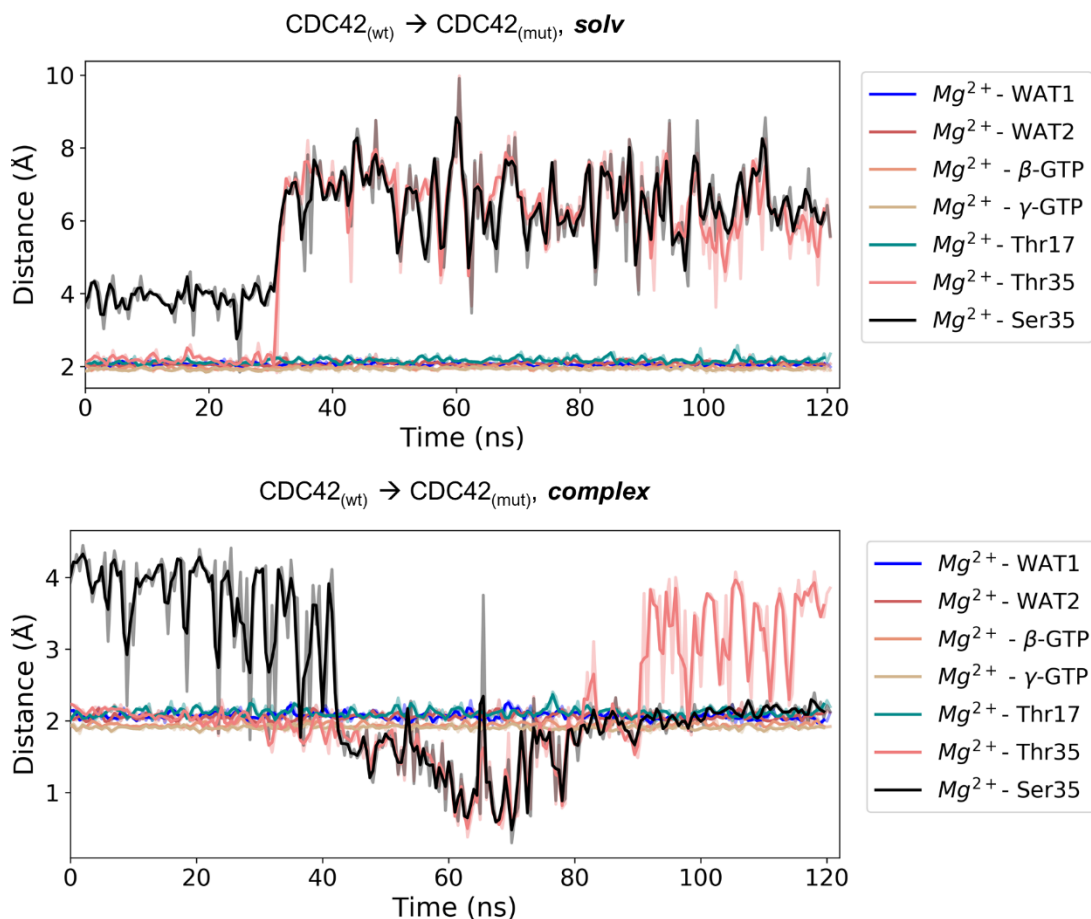


Figure 41. Alchemical simulations analysis for the T35S mutation. The time series of the Mg^{2+} coordination bonds lengths for both unbound (top) and PAK1-bound CDC42 (bottom) is reported for the whole side chains transformation atom mapping scheme.

With this mapping scheme, the integrity of the Mg^{2+} coordination sphere was maintained during the alchemical transformation (Figure 42), resulting in a much better $\Delta\Delta G_{\text{binding}}$ estimate of 1.7 ± 0.1 (vs 1.9 ± 0.1 kcal/mol from experiments).

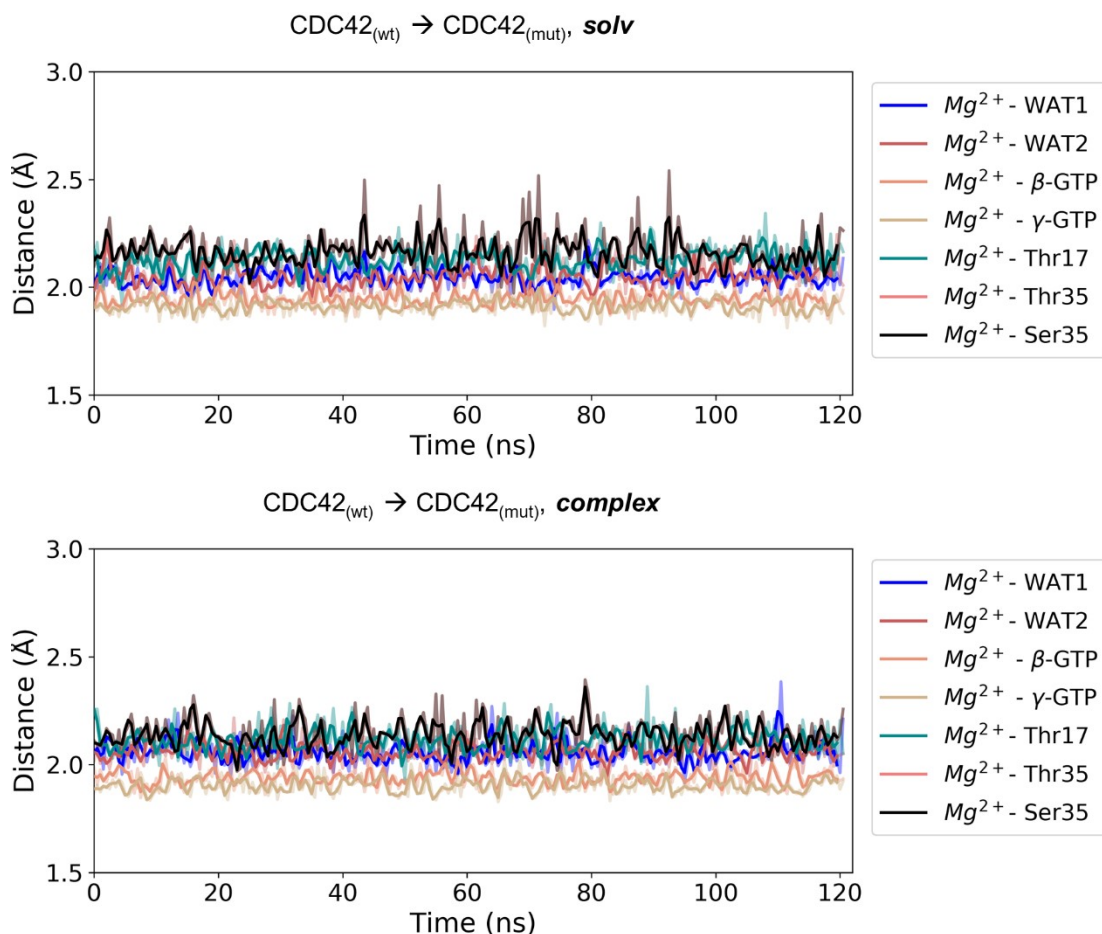


Figure 42. Alchemical simulations analysis for the T35S mutation. The time series of the Mg^{2+} coordination bonds lengths for both unbound (top) and PAK1-bound CDC42 (bottom) is reported for the minimal softcore atom mapping scheme.

4.5.1.2. F28Y mutation

A second case is the F28Y mutation. According to the sidechain alchemical transformations, the $\Delta\Delta G_{\text{binding}}$ for this mutation is disfavored by 1.4 ± 0.2 kcal/mol, differing from the experimental outcome, which shows this single-point mutation to be neutral (-0.2 ± 0.2 kcal/mol). The side chain of the highly conserved F28 is recognized to stabilize the binding of the guanine ring of substrate GTP at the catalytic pocket^{17,591} (Figure 44A).

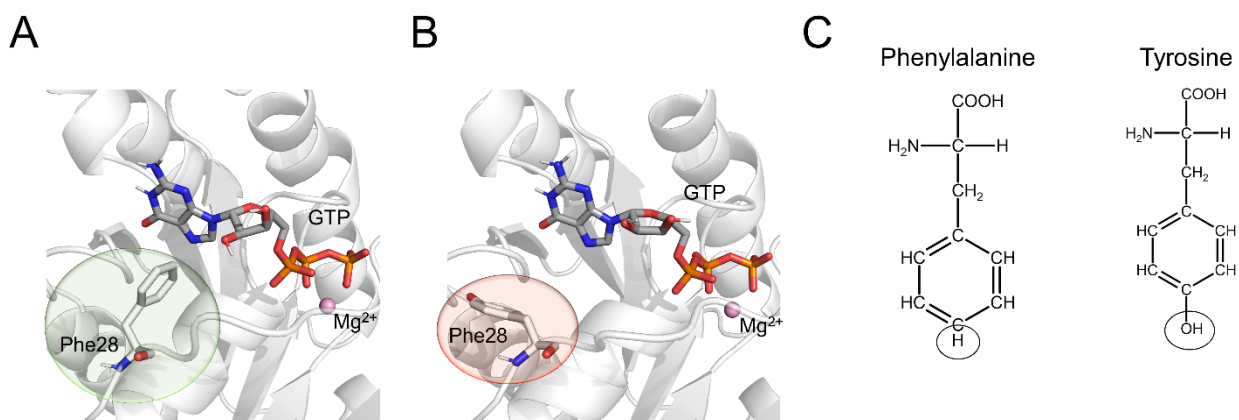


Figure 44. F28Y CDC42 mutant analysis. The interaction between GTP and the aromatic ring of Phe28 as observed in the equilibrium MD simulations of the *wt* system is reported in A. After the initial alchemical transformation of Phe28 into Tyr, the aromatic ring was no longer in contact with GTP (B). The protein is represented as white cartoon, the GTP nucleotide and the residues involved in the single-point mutation as sticks, and the Mg^{2+} ion as a ball. The revised atom mapping used to improve the $\Delta\Delta G_{\text{binding}}$ estimate is reported in C. The circled atoms are those considered unique for the transformation.

The analysis of the alchemical transformation trajectories revealed larger fluctuations of the sidechain rings compared to the equilibrium MD simulations of the *wt* enzyme (Figures 44B and 43).

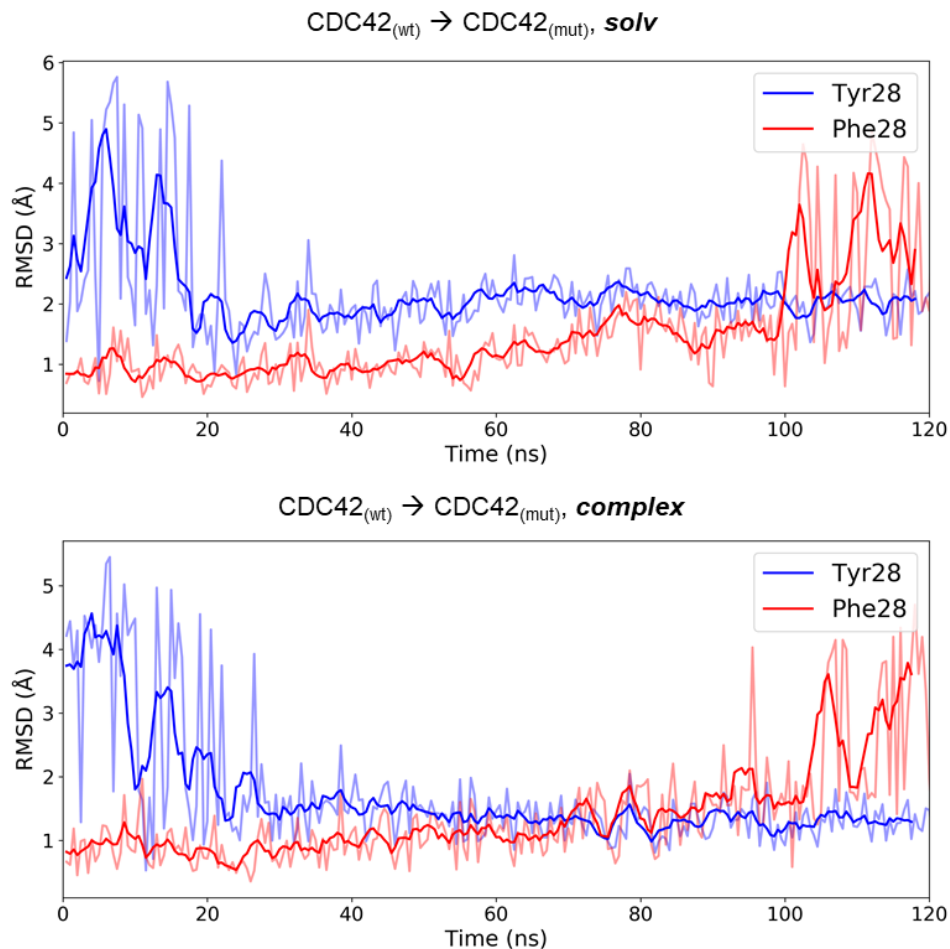


Figure 43. Alchemical simulations analysis for the F28Y mutation. The time series of the RMSD of residues F28 and Y28 for both unbound (top) and PAK1-bound CDC42 (bottom) is reported for the whole side chains transformation atom mapping scheme.

In this case, a new atom mapping scheme between the phenylalanine and the tyrosine was considered. In detail, the hydroxyl group of the latter and the corresponding hydrogen of the former were treated with softcore potentials⁵⁵⁷ (Figure 44C). With this scheme, the aromatic ring common to both amino acids preserves the conformation observed in crystal structures, also stably reproducing what is observed in the equilibrium simulation of the *wt* enzyme (Figure 45). This mapping scheme and sampling resulted in a $\Delta\Delta G_{\text{binding}}$ estimate of -0.2 ± 0.1 kcal/mol, which perfectly matches the experimental data.

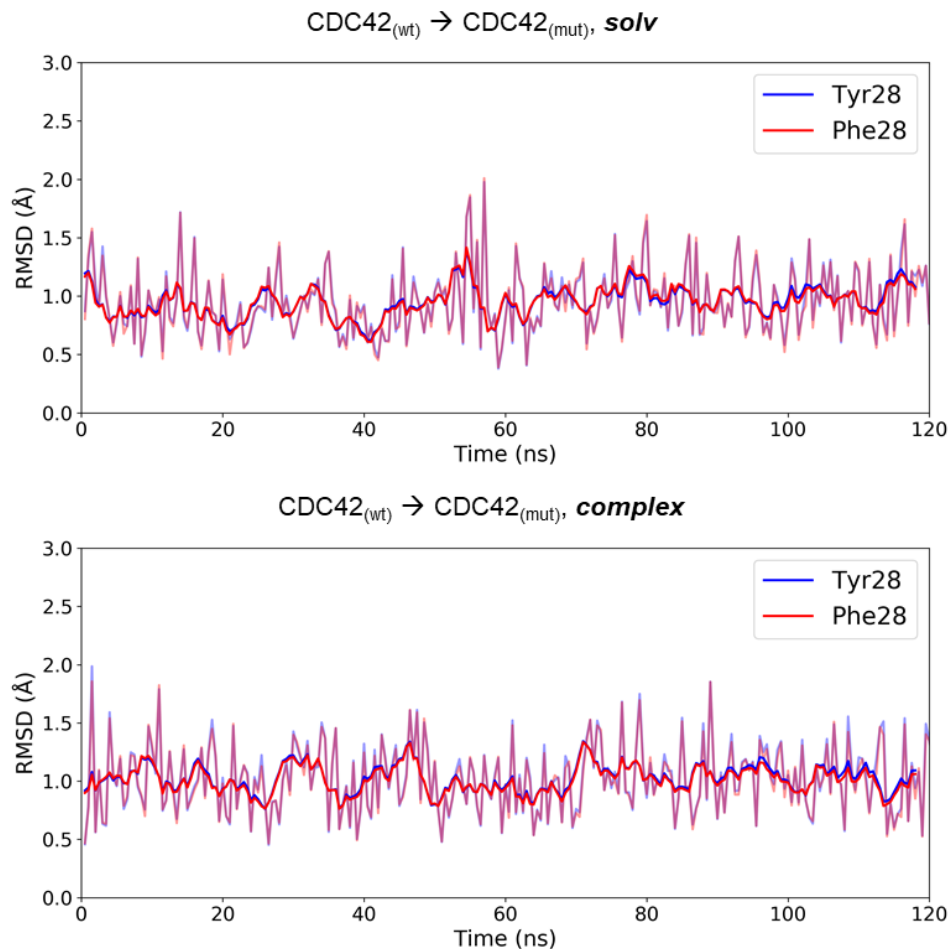


Figure 45. Alchemical simulations analysis for the F28Y mutation. The time series of the RMSD of residues F28 and Y28 for both unbound (top) and PAK1-bound CDC42 (bottom) is reported for the minimal softcore atoms mapping scheme.

4.5.2. Right Pick of the Initial Conformation for Y32F and V33N

4.5.2.1. Y32F mutation

The apparent poor prediction of these two mutations was resolved by looking into the conformational equilibrium of the side chain and how this was sampled during the calculations. For Y32F mutation, the sidechain alchemical transformations returned an estimate of -1.5 ± 0.1 kcal/mol, contrary to the experimental value (0.9 ± 0.3 kcal/mol). Firstly, a different mapping was considered, reducing the number of atoms unique to each

residue during the alchemical transformation ($-OH$ for the tyrosine and the corresponding $-H$ atom for the phenylalanine). This reduces the error (-0.9 ± 0.04 kcal/mol), although the computed estimate remained negative compared to the positive value from experiments. Thus, the re-analysis of the MD trajectories of the *wt* CDC42/PAK1 complex, showed that the configuration used to start the alchemical transformation did not belong to the most populated conformational state of the complex. Indeed, Y32 visits two conformations during the equilibrium MD simulations (Figure 46). One is predominant over the other (90%).

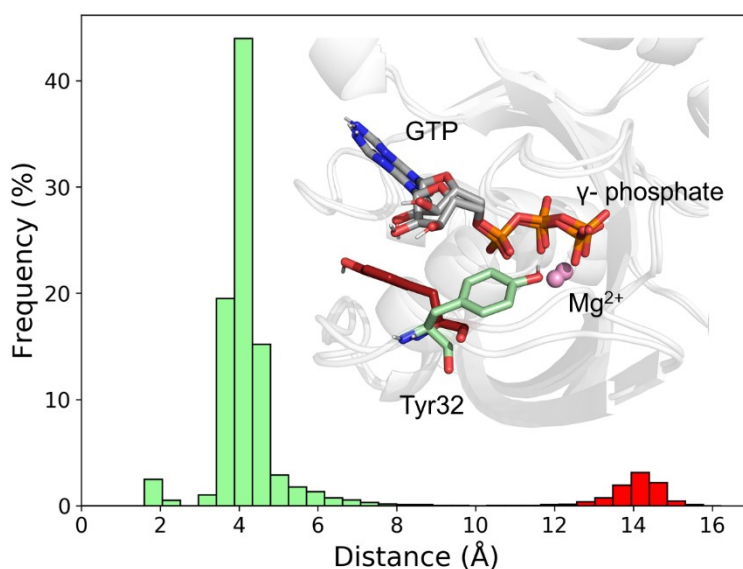


Figure 46. Conformational analysis for the Y32F mutation. The distribution of the distance between Tyr32 and the γ -phosphate of GTP is reported. The green and red color code indicate the most and the least populated Tyr32 conformation, respectively. In the upper right panel, representative conformations of the side chain of Tyr32 observed during the equilibrium MD simulations of the *wt* system are reported. CDC42 is represented as white cartoon, while Tyr32 and the GTP nucleotide in sticks and Mg^{2+} ion as ball.

Repeating the calculation using a structure taken from the most populated conformational state led to a $\Delta\Delta G_{\text{binding}}$ estimate in line with the experimental determination (0.9 ± 0.1 kcal/mol), showing how the starting point initial structure for the alchemical transformation can impact on the computation of the $\Delta\Delta G_{\text{binding}}$.

4.5.2.2. V33N mutation

The same issue was observed with the mutation V33N. Sidechain alchemical transformations estimated this mutation to improve binding by -1.3 ± 0.1 kcal/mol, while experimentally it was observed to be neutral (0.20 ± 0.1 kcal/mol). Conformational analysis of the MD trajectories revealed that the configuration used to start the alchemical transformation belonged to a low-populated conformation of V33 (Figure 47). Indeed, repeating the alchemical transformation starting from a configuration taken from the most populated state of V33 returned a $\Delta\Delta G_{\text{binding}}$ that agreed with the experimental data (-0.1 ± 0.1 kcal/mol).

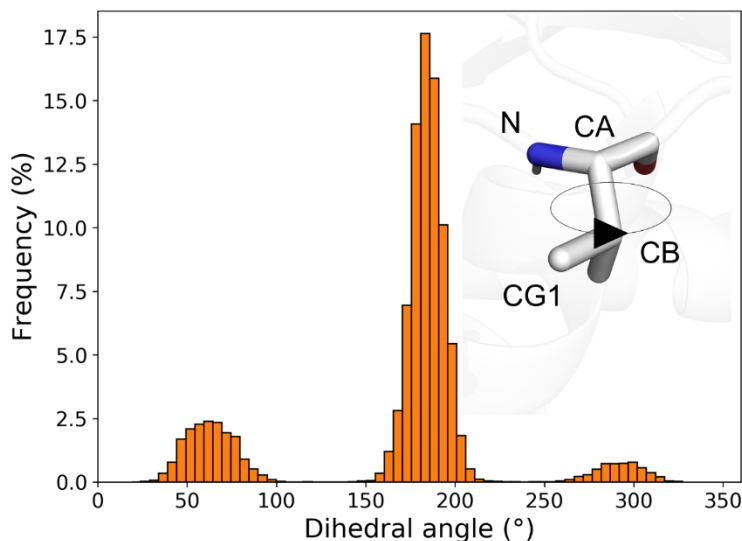


Figure 47. Conformational analysis for the V33N mutation. The distribution of the N-CA-CB-CG1 V33 dihedral angle is reported. In the upper right panel, a representative conformation of the side chain of Val33 as observed during the equilibrium MD simulations of the *wt* system is reported. CDC42 is represented as white cartoon, while Val33 is shown as sticks.

4.5.3. Structural analysis as keystone for alchemical free energy calculations

Overall, these four examples show how a preliminary structural knowledge of the investigated system is strongly required. Indeed, the initial poor agreement of the computed estimates with experimental values for the T35S and F28Y mutations, was resolved by an *ad hoc* atom mapping scheme, demonstrating how drastic changes in the original interatomic interactions of the mutated residue with the surroundings can significantly affect the outcome of alchemical free energy calculations. In the other hand, Y32F and V33N mutations showed how in real-case scenarios, where the conformational sampling is finite, the initial structure could affect the free energy estimates. Thus, a careful analysis of the conformational preference of the mutating residues as well as of the established interactions may thus lead to better free energy estimates. The overall results for the 16 CDC42 mutants are reported in the plot in Figure 48 and in Table 6.

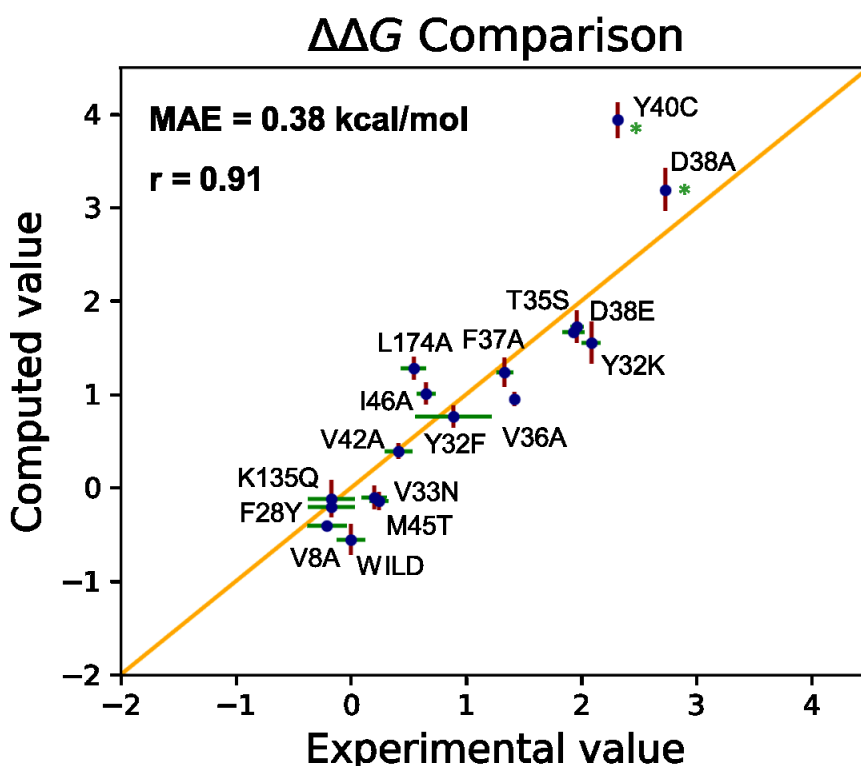


Figure 48. $\Delta\Delta G_{\text{binding}}$ values (in kcal/mol) computed using the alchemical transformations and plotted against the experimental values. The computed $\Delta\Delta G_{\text{binding}}$ (in kcal/mol) are plotted against the experimental values. The examined single-point mutations

are reported together with their computed (red) and experimental (green) error bars. The asterisk (*) marks mutations for which the experimental error was not reported.

Mutation	K_d	ΔΔG_{binding}^{exp}	ΔΔG_{binding}^{comp}	ΔΔG_{binding}^{MM/GBSA}
Wild-type	20 ± 4	0 ± 0.12	-0.56 ± 0.16	
V8A	14 ± 4	-0.21 ± 0.17	-0.41 ± 0.04	0.01 ± 0.02 **
F28Y	15 ± 5	-0.17 ± 0.20	-0.20 ± 0.05	
Y32F	90 ± 50	0.89 ± 0.33	0.88 ± 0.12	
Y32K	680 ± 90	2.09 ± 0.08	1.55 ± 0.22	
V33N	28 ± 5	0.20 ± 0.11	-0.11 ± 0.12	
T35S	520 ± 82	1.93 ± 0.09	1.67 ± 0.05	
V36A	220 ± 13	1.42 ± 0.03	0.95 ± 0.07	2.82 ± 0.65 **
F37A	190 ± 23	1.33 ± 0.07	1.24 ± 0.16	-0.27 ± 0.12 4.11 ± 1.03 **
D38A	>2000	2.73*	3.19 ± 0.23	14.28 ± 1.54 **
D38E	550 ± 53	1.96 ± 0.06	1.73 ± 0.17	
Y40C	>1000	2.32 *	3.94 ± 0.19	-0.95 ± 0.15
V42A	40 ± 8	0.41 ± 0.12	0.39 ± 0.08	2.26 ± 0.74 **
M45T	30 ± 4	0.24 ± 0.08	-0.14 ± 0.09	
I46A	60 ± 8	0.65 ± 0.08	1.01 ± 0.11	1.53 ± 0.58 **
K135Q	15 ± 5	-0.17 ± 0.20	-0.12 ± 0.20	

L174A	50 ± 9	0.54 ± 0.11	1.28 ± 0.12	0.69 ± 0.43 **
-------	--------	-------------	-------------	----------------

Table 6. Equilibrium constants and relative binding free energy values for the association of CDC42 mutants and PAK1. The examined single-point mutations are reported together with their K_d equilibrium constants, the experimental $\Delta\Delta G_{\text{binding}}$ values, the computed $\Delta\Delta G_{\text{binding}}$ values through alchemical free energy calculations and MM/GBSA methods. * symbol indicates the absence of estimated experimental error. ** symbol indicates that the value has been calculated by alanine scanning.

With a correlation coefficient of 0.91 and a MAE of 0.4 kcal/mol between experimental and computed data, this benchmark study demonstrates the predictive power of alchemical binding free energy calculations in the context of protein–protein interactions. This computational procedure can compute how single-point mutations affect such protein–protein complexation, indicating key druggable interactions. However, such remarkable accuracy could be achieved only through a careful preliminary structural analysis. Conversely, the initial $\Delta\Delta G_{\text{binding}}$ of four mutations (namely, T35S, F28Y, Y32F, and V33N) was far from the experimental value. These four problematic cases were solved by considering two key factors. The first factor is the chemical nature of the transformation, which defines the alchemical path to transform one residue into another. As exemplified by mutants T35S and F28Y, an improved match with the experimental value was obtained when key interactions established by such residues during the transformation were considered. Importantly, the computed outcome matched the experimental value only when these key interactions were preserved by tuning the atom mapping scheme. In fact, all side-chain atoms were initially considered as unique atoms (and thus treated via softcore potentials). In this case, the side chain of the transformed residue was not able to recover key interactions at the end of the transformation. It is thus advisable, as often remarked in the context of drug design, to minimize the number of unique atoms. In the case of T35S, a careful definition of the atom mapping scheme allowed to maintain the interaction of the hydroxyl group with the catalytic Mg^{2+} ion and thus the structural integrity of the site throughout the transformation.

The second factor for improved $\Delta\Delta G_{\text{binding}}$ concerns the importance of picking the most representative structure of a populated state to start the alchemical transformation from. Ideally, exhaustive sampling would solve this issue as well as the one above. In practice, real-case scenarios may limit the configurational sampling of the chemical structure undergoing alchemical transformation. This was exemplified by the Y32F and V33N mutants. In these cases, better results were obtained when the initial protein structure was representative of the most visited ensemble of configurations retrieved from equilibrium MD simulations. Thus, a conformational analysis of the system may be propaedeutic to identify the conformational preference of the residue undergoing transformation. This will indicate the best configuration to start the alchemical transformation from, facilitating the proper sampling of significant configurations. This observation is in line with recent studies that report larger errors in binding free energy predictions associated with insufficient sampling or incorrect conformation of the mobile loops^{592–594}. Alternatively, as already implemented in the context of drug design^{595,596}, it may be advisable to perform replicas of the alchemical transformation starting from different configurations retrieved from equilibrium MD. Interestingly, and in line with these results and recommendations, recent studies have reported potential issues in calculating the effect of point mutations in antibodies, in particular, for mutations in which a small residue was turned into a bulky one, suggesting the use of structural prediction methods to identify the most representative structures to start alchemical transformations⁴⁷⁷. Furthermore, mutations involving a change of charge in the system (Y32K, D38A, and K135Q), treated with the alchemical co-ion approach, were well reproduced, suggesting that the ion distribution in the simulation box was sufficiently sampled.

Summarizing, alchemical free energy calculations represent a powerful method in the context of studying protein–protein interactions, as also recently reported for in the context of peptides and neutralizing antibodies^{477,478}. Because of the encouraging results, this study corroborates alchemical free energy calculations as a computational tool capable of prioritizing mutants that may lead to larger effects, impacting positively on the efficiency (i.e., economy) of the experimental counterpart. Indeed, despite experimental mutagenesis investigations represent a leading practice to study protein–protein interactions, this method exploration of the alchemical free energy calculations expand

their application. Indeed, along with drug design projects, alchemical free energy calculations emerge as tool to be successfully employed to guide the investigation of druggable interactions to target to quench deregulated signaling pathways.

4.6. Free energy methods results comparison

In order to compare the results from the rigorous alchemical free energy calculations and time-cheaper end points methods, MM/GBSA calculations were performed to quantify the $\Delta\Delta G_{\text{binding}}$ of the CDC42/PAK1 complex in the *wt*, compared to the mutated systems F37A and Y40C (using $\sim 10,000$ snapshots from equilibrium MD runs). As results, the relative binding free energy ($\Delta\Delta G_{\text{binding}}$) estimates were of -0.27 ± 0.12 and -0.95 ± 0.15 kcal/mol for F37A and Y40C, respectively (Table 6). These estimates match poorly with the $\Delta\Delta G_{\text{binding}}$ from experiments for such two mutations, indicating the inherent difficulties in quantifying exactly the effect of point mutations at the protein interface using MM/GBSA. Furthermore, for the mutations to alanine, the comparison between the alchemical transformation results (MAE value of 0.3 kcal/mol) and the computationally cheaper alanine scanning approach⁵⁹⁷ (MAE value of 2.7 kcal/mol) demonstrates the better accuracy of alchemical transformations to predict the effect of single-point mutations to alanine in this system. In line with other reported studies, in the present work alchemical free energy calculations outperformed MM/GBSA, with an accuracy that can assist in the design of mutagenesis experiments.

4.7. Computational details

4.7.1. MD simulations

MD simulations were performed with the pmemd module of AMBER20⁵⁹⁸. The AMBER-ff14SB force field⁵⁹⁹ was used for the protein, while parameters from recent literature were adopted for GTP and Mg^{2+} ^{600,601}. Monovalent ions were described with Joung–Cheatham parameters⁶⁰², and the TIP3P model⁶⁰³ was used for water. Simulations were performed with a distance cutoff of 10 Å. Long-range electrostatics were

treated with the particle mesh Ewald method. Bonds involving hydrogen atoms were constrained, allowing a time step of 2 fs. After solvent equilibration, systems were energy minimized and gently heated to 303 K for 0.5 ns while restraining protein backbone atoms to stay close to the experimental structure. The Andersen-like temperature-coupling scheme⁶⁰⁴ and a Monte Carlo barostat were used to maintain temperature and pressure close to room temperature conditions. About 1 μ s of MD simulations in the NPT ensemble were accumulated for each system. Table 7 summarizes the size and the simulated time of the performed MD simulations described in this chapter.

	N° atoms system	N° atoms solvated system	Simulated time
CDC42	~ 2,830	~ 60,300	1 μ s
CDC42/PAK1	~ 3,600	~ 78,500	1 μ s
CDC42(F37A)/PAK1	~ 3,600	~ 78,500	1 μ s
CDC42(Y40C)/PAK1	~ 3,600	~ 78,500	1 μ s
CDC42 APO TRANSFORMATION	~ 2,840	~ 60,300	120 ns
CDC42 PAK1- BOUND TRANSFORMATION	~ 3,600	~ 78,600	120 ns

Table 7. MD simulations summary. An overview summarizing both the size and simulated time of the conducted MD simulations is reported.

4.7.2. Alchemical Free Energy calculations

Binding free energies ($\Delta\Delta G_{\text{binding}}$) between mutated forms of CDC42 and the binding domain of PAK1 were computed with respect to the *wt* using alchemical

transformations⁴⁷⁰. Accordingly, CDC42 was transformed from *wt* into the mutant in both the apo and PAK1-bound forms. The free energy change associated with each transformation was estimated using thermodynamic integration⁵⁵⁸ (eq. 24), and their difference provided an estimate of $\Delta\Delta G_{\text{binding}}$ according to the thermodynamic cycle in Figure 49.

$$\Delta G = G(\lambda = 1) - G(\lambda = 0) = \int_0^1 \langle \partial V / \partial \lambda \rangle_\lambda d\lambda = \sum_i w_i \langle \partial V / \partial \lambda \rangle_i \quad (\text{eq. 24})$$

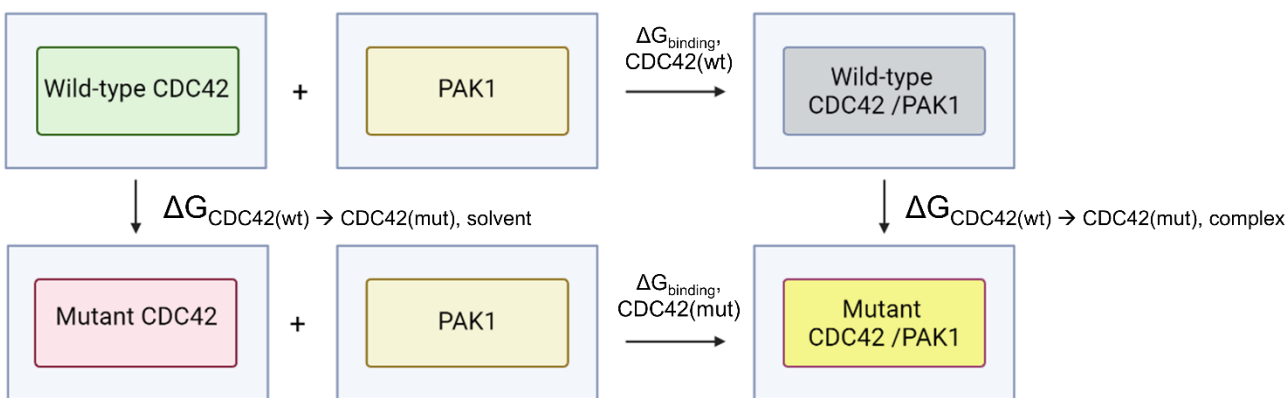


Figure 49. Thermodynamic cycle employed to compute binding affinity estimates.

The thermodynamic cycle used to compute relative binding free energies for the analyzed single-point mutations is reported. CDC42 was transformed from *wild-type* into mutant in both the apo and PAK1-bound forms. The color code defining the components of the thermodynamic cycle are green for the *wild-type* CDC42, red for mutant CDC42, beige for PAK1, grey for the *wild-type* CDC42/PAK1 complex and, finally, yellow for the mutant CDC42/PAK1 complex.

Binding free energies ($\Delta G_{\text{binding}}$) were computed from experimental data using the measured K_d value and the equation 20 ($\Delta G_{\text{binding}} = RT \ln K_d$). Experimental $\Delta\Delta G_{\text{binding}}$ values were then obtained by using the calculated $\Delta G_{\text{binding}}$ for the *wt* and mutated forms of CDC42 in the CDC42/PAK1 complex. Alchemical calculations were started from equilibrated configurations from equilibrium MD simulations of the CDC42/PAK1 complex and CDC42 alone. Each transformation was carried out in 12 windows (corresponding to λ values: 0.00922, 0.04794, 0.11505, 0.20634, 0.31608, 0.43738, 0.56262, 0.68392, 0.79366, 0.88495, 0.95206, and 0.99078 and weights 0.02359, 0.05347, 0.08004, 0.10158, 0.11675, 0.12457) performing 10 ns simulations at each λ value. Bonds were

not constrained requiring an integration time step of 1 fs. Backbone atoms of the residues involved in the mutations were transformed linearly, while side-chain atoms were treated with softcore potentials for both Lennard-Jones and electrostatic interactions⁵⁵⁷. For certain mutations, different atom mapping schemes were considered. Some mutations involve a change of charge in the system. To treat these cases, the alchemical co-ion approach was adopted^{605,606}: when a negative charge was annealed (D38A), concomitantly a Na^+ ion was converted into a water molecule; when a positive charge was annealed (K135Q), concomitantly a water molecule was converted into a Na^+ ion; and when a positive charge was created (Y32K), concomitantly a Na^+ ion was converted into a water molecule (Figure 50). Transformations were performed at constant volume (the equilibrated volume from MD simulations) and temperature. Data analysis was performed after discarding the first 10% of the simulation time (corresponding to the first ns of simulation) of each window. In order to estimate errors on ΔG (eq. 24) the time series of $\partial V/\partial \lambda$, values from each window were resampled to obtain uncorrelated samples⁶⁰⁷, from which averages and variances were computed. The error on $\Delta \Delta G_{\text{binding}}$ was obtained by combining the errors of the individual transformations. The convergence of the computed $\Delta \Delta G_{\text{binding}}$ was assessed by estimating it as a function of simulation time, considering intervals both in the forward and the reverse direction⁶⁰⁸.

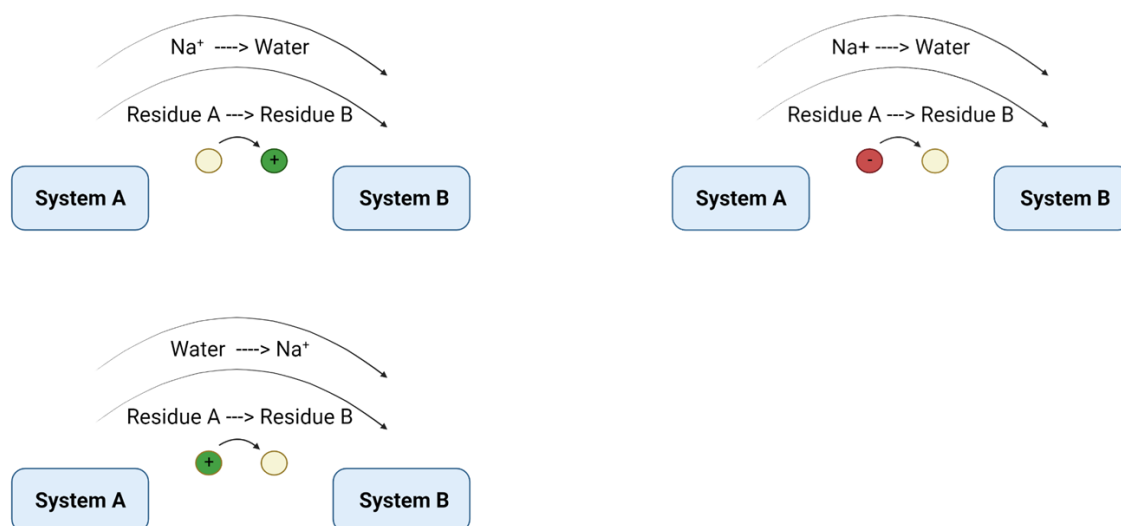


Figure 50. Co-ion approach employed. The scheme represents the alchemical co-ions approach used to treat mutations which involve residues of different charge. For the single-point

mutations implying a change in net charge of the protein, either a Na⁺ counterion was converted into a water molecule or vice versa. Specifically, for the Y32K mutation the positive charge acquired by the protein was counterbalanced by the concomitant transformation of a Na⁺ ion into a water molecule; for the D38A mutation the disappearing negative charge on the protein was proceeded with the concomitant transformation of a Na⁺ ion into a water molecule; and, lastly, for the K135Q mutation the disappearing positive charge on the protein was compensated by the concomitant transformation of a water molecule in a Na⁺ ion.

4.7.3. MM/GBSA calculations

Implicit solvent calculations (Generalized Born model in the Onufriev–Bashford–Case formulation)^{609,610} were combined with vacuum molecular mechanical energy evaluations to estimate $\Delta G_{\text{binding}}$. Calculations were performed for the CDC42/PAK1 complex and for each partner separately using configurations from the equilibrium MD simulations of the *wt* CDC42/PAK1 complex and CDC42 Y40C and F37A variants. The *wt* CDC42/PAK1 trajectory was also used to evaluate the effect of mutating certain residues into alanine (alanine scanning). All steps required by the calculation were automatized with MM/PBSA.py distributed with AmberTools⁵⁵². A 0 M ion concentration was used in the GB calculation, and the linear combination of a pairwise overlap method⁶¹¹ was used to calculate the molecular surface area.

Chapter 5. Alchemical Free Energy Calculations to predict key residues at the RHOA/ROCK1 interface

CDC42/PAK is undoubtedly an interesting protein-protein interaction to characterize and target. However, the RHOA/ROCK1 cascade represents another stimulating and attractive RHOGTPases signaling as its deregulation is associated to diverse pathological conditions. In the current chapter, after an introduction regarding the overall signaling functions, the role of the RHOA/ROCK1 signaling in pathological conditions will be discussed. Next, following the promising results obtained on the CDC42/PAK interface, classical MD simulation and alchemical free energy calculation will be employed to investigate key residues involved in the recognition mechanism.

5.1. The RHOA/ROCK1 signaling is central for diverse cellular functions

RHOA is 193 residues long protein that, together with RHOB and RHOC, constitutes the RHOGTPases subfamily RHO. As the other RHOGTPases, RHOA is structurally composed by six helices, six β -strands and eleven polypeptide loops of which the G1–G5 loops define the highly conserved nucleotide binding site^{1–4,6,10,11}. Likewise, RHOA signaling activity is regulated by the GTP binding and its hydrolysis to GDP, facilitated by the interacting regulator proteins GEFs, GAPs and GDIs^{1,6,13}. Acting as a molecular switch, GTP-bound active RHOA directly interacts with downstream effectors and controls essential cellular processes, including actin dynamics, cell-cycle progression and cell migration. Specifically, one of the main function of RHOA concerns the regulation of both polymerization and organization of the actin and microtubule cytoskeleton^{1,6,7,9}, which, in turn, is strictly connected to the coordination of key cellular processes, such as cell morphogenesis, proliferation and migration. In this regard, a well-characterized pathway involves the activation of the RHOA downstream effector ROCK1, also called serine/threonine RHO-kinase 1.

ROCK, or RHO-associated protein kinase, is a family of serine/threonine kinases that play important roles in regulating various cellular processes. Within ROCK family, it is possible to distinguish two isoforms, ROCK1 and ROCK2, which share structural similarities and perform overlapping functions in many cases⁸¹. ROCK1 is 1354 residues long kinase composed by an N-terminal kinase domain followed by a coiled-coil structure and by a C-terminal regulatory domain, constituted by a pleckstrin homology region and a cysteine-rich zinc fingerlike motif⁶¹². Consistently with the ROCK1 constitutive activation upon its deletion, the C-terminal domain acts as an autoinhibitory region by binding and hampering the kinase N-terminal domain^{613,614}. When the GTP-bound active RHOA binds to the RHO binding domain (RBD), located in the coiled-coil region, the negative regulation is disrupted and the ROCK1 kinase is activated⁸¹. Notably, the RHOA/ROCK1 pathway is central for many cellular processes, including actin organization, cell migration and proliferation, cell adhesion, apoptosis, as well as for key processes related to neurobiology and vascular biology. For instance, RHOA/ROCK1 activity regulates the formation and the organization of stress fibers, cytoskeleton components formed by bundle of actin and myosin that play an important role in cellular contractility. In detail, ROCK1 phosphorylates the myosin light chain (MLC) inducing its interaction with actin filaments, resulting in an overall enhanced cell contractility. In addition, ROCK1 is found to increase cell contractility by phosphorylating the myosin light chain phosphatase (MLCP), which negatively regulates actomyosin-based contractility by dephosphorylating the MLC. The resulting processes increase the myosin activity and, thus, the cell contractility^{51,52,80,81,615,616}. In addition, ROCK1 phosphorylates the LIM kinase (LIMK) that, in turn, targets, phosphorylates and inhibits the actin-binding protein ADF/cofilin. Since the ADF/cofilin primary function is to sever and disassemble actin filaments, its inhibition results in an increased actin polymerization⁶¹⁷⁻⁶²⁴. Moreover, the phosphorylation of members of the ERM (ezrin/radixin/moesin) protein family operated by ROCK1 modulate the cytoskeleton-plasma membrane interactions, allowing actin filaments to anchor to integral proteins⁶²⁵.

RHOA/ROCK1-induced cell contractility is fundamental also for cell migration. Indeed, while other RHOGTPases mediate the initial steps of the process (e.g. determination of the direction), RHOA/ROCK1 signaling directs the stabilization of the

migrating cell by generating adhesions to the extracellular matrix (ECM) as well as the cell contraction needed to move forward following the determined direction^{6,9,59,61,62}. Specifically, RHOA/ROCK1 signaling is involved in the development of stable and large cell-ECM adhesions, called *focal adhesions*^{6,52,74–77,613,626,627}, which provide a strategic anchorage between the stress fibers of the migrating cell and the ECM, but also in the generation of actomyosin traction forces at the rear of moving cells, mainly reached by stimulating the myosin light chain (MLC) activity^{62,84,85,628}. High levels of active RHOA/ROCK1 signaling is also associated to bleb-based migration where RHOA, acting through ROCK1, stimulates the myosin light chain phosphorylation (MLC) and, thus, actomyosin contractility^{59,629,630}. Notably, RHOA/ROCK1 signaling is also required for the actomyosin contraction of the cleavage furrow during the cytokinesis phase of the cell cycle and promotes the overall cell proliferation^{80,81,101–105,631}. Likewise, RHO/ROCK1 signaling pathways are required to allocate centrosomes during the mitotic phase M of cell cycle^{1,96}. Moreover, RHOA/ROCK1 signaling stimulates G1/S cell cell cycle progression by increasing cyclin D1 and Cip1 proteins⁶³².

RHOA/ROCK1 signaling is also involved in the reorganization of the cytoskeleton during apoptosis and membrane-trafficking processes. Indeed, when cells become committed to apoptosis, one of the first morphological change to occur is usually *membrane blebbing*, which implies the loss of focal adhesions and the detachment of cells from the surrounding substratum⁶³³. Interestingly, during apoptosis ROCK1 is also cleaved by the caspase-3 to remove the autoinhibitory C-terminal domain, with consequent constitutive kinase activation, which, in turn, activates MLC, fundamental for the apoptotic procedures^{633–637}. Similarly, cytoskeletal rearrangements are coupled to phagocytic processes. In detail, RHOA/ROCK1 signaling has been found to be involved in type II phagocytosis^{109,638}. In addition to cytoskeleton effects, RHOA/ROCK1 regulates the cell-substratum and cell-cell adhesion, indispensable to carry out various key cellular functions. Specifically, RHOA/ROCK1 signaling affects cell–cell adhesion in cells, by regulating the integrity of both *tight* and *adherens* junctions and cell-substratum adhesion by enhancing focal adhesions formation. This functional role is markedly crucial for the homeostasis of epithelial and endothelial cells. Consistently, RHOA/ROCK1 signaling is central in the vascular biology context because of their influence on the endothelial barrier

function, vascular smooth muscle contractility, vascular remodeling and angiogenesis^{639,640}. Indeed, the described mechanisms concerning the regulation of cell contractility operated by RHOA/ROCK1 signaling have been observed in the vascular smooth muscle cells, where the regulation of cell contractility modulates blood flow by contracting and distending, with regards to the received information and stimulation⁶⁴¹. RHOA/ROCK1 signaling is an important mediator in several angiogenic processes involving the vascular endothelial growth factor (VEGF), including cell migration, survival and permeability. In addition, RHOA-induced ROCK1 activation play a critical role in controlling the leukocyte transendothelial migration from the vasculature into tissues⁶⁴²⁻⁶⁴⁵. RHOA/ROCK1 is also involved in the regulation of the expression and the activity of endothelial NO synthase (eNOS), critical factor for preserving the endothelial and vascular function and avoiding dysfunctions related to oxidative stress⁶⁴⁶⁻⁶⁴⁸.

The regulation of cytoskeleton dynamics operated by RHOA/ROCK1 is also critical in different neuronal processes, such as *axon guidance* (or *axon pathfinding*), a key process in which neurons send out axons to reach the correct targets⁶⁴⁹⁻⁶⁵¹. Indeed, to correctly develop axons, the growth cones interact with various environmental factors that can cause either neurite retraction or axonal growth. The overall process implies the reorganization of the actin cytoskeleton determined by RHOA/ROCK signaling to modulate the shape and the movement of growth cones⁸⁰. Specifically, numerous evidences highlight how the neurite outgrowth and retraction depend on the activity levels of RHOA/ROCK signaling with high and low activity levels associated to axonal retraction and outgrowth, respectively^{650,652,653}. Accordingly, ROCK1 inhibition has been found to trigger axon initiation and to increase the size and the motility of growth cone filopodia during neuronal maturation⁶⁵⁰. The mechanism underlying the relationship between axonal development and RHOA/ROCK1 signaling concerns the phosphorylation levels of the myosin light chain (MLC) operated by ROCK1, that have been found to be decreased in neurite outgrowth^{80,654}. Accordingly, active mutant of either MLC or ROCK1 are not able to extend neurites⁶⁵⁵. RHOA/ROCK1 involvement in neural related processes is also significantly important after injury of the central nervous system (CNS), where the effects of this activation are associated to regenerative failure, mainly due to enhanced actomyosin contractility and to the formation of stress fibers^{651,656,657}. Further findings

providing evidences of RHOA/ROCK1 key role following CNS injury is represented by the stimulation of axon regeneration and recovery after spinal-cord injury upon ROCK signaling inhibition⁶⁵⁸. Concluding, despite RHOA/ROCK1 signaling plays key roles in the normal maintenance of cellular homeostasis, it also represent a noteworthy and attractive molecular target because of its reported aberrant activity in several human diseases, as thoroughly discussed in the next paragraph.

5.2. Therapeutic Relevance of the RHOA/ROCK1 interaction

RHOA/ROCK1 signaling possess a well-recognized role in the regulation of pivotal physiologic processes. However, several studies highlighted its contribution to cancer development as well as to a broad range of human disorders, making the RHOA/ROCK1 interaction an attractive and promising protein-protein interface to target⁶⁵⁹. Indeed, despite constitutively active mutants of ROCK1 have been identified⁶⁶⁰, more often its aberrant activity results from an abnormal upstream regulation operated by RHOA, which is consistently overexpressed and/or hyperactivated in several different types of cancer^{661–671}. In cancer, the aberrant phosphorylation of RHOA/ROCK1 downstream substrates determinates alterations in the actomyosin contractility as well as in the cytoskeleton organization that result in changes in cell adhesion, migration, and invasion, that collectively contribute to tumor development, progression and invasion, angiogenesis, metastasis and chemoresistance^{659,672–675}. Accordingly, malignant RHOA-mediated transformation is found to be correlated to the ability to bind and activate ROCK1 which is required for both the establishment and maintenance of tumor growth and progression, as well as for angiogenetic processes, where actomyosin contractility and the integrity of intercellular junctions modulate endothelial permeability^{667,668,670,671,676}.

In addition, RHOA/ROCK1 signaling modulates cancer cell cycle progression by controlling the furrow cleavage activity through the phosphorylation of downstream proteins, among which the MLC¹⁰², and by modifying the levels of cell cycle regulatory proteins, such as cyclin D1, cyclin A and p27⁶³². Being the modulation of cytoskeleton its main activity, it is not surprising that the abnormally activated RHOA/ROCK1 signaling cascade drives the transformation from normal cells to cancer cells by principally

modulating actin filaments dynamics. Indeed, RHOA/ROCK1 activity promotes cancer cells transcellular migration by acting on cell adhesion via focal adhesions and stress fibers formation⁶⁷⁷. In addition, RHOA/ROCK1 signaling strengthens the metastatic potential of cancer cells by increasing ECM stiffness, beneficial for tumor growth and progression^{678,679}. Interestingly, RHOA/ROCK1 has been found also to regulate cancer cells migration mechanisms through the ECM without proteolysis, by phosphorylating the MLC and, thus, generating a sufficient actomyosin force to deform collagen fibers and advance through the ECM^{680,681}.

Abnormal ROCK1 activity has been detected in bladder cancer, breast cancer and adenoid cystic carcinoma, where the RHOA/ROCK1 pathway contributes to increase the ability of cancer cells to migrate and invade new tissues^{682–684}. Accordingly, inhibition of ROCK1 signaling prevents human breast cancer metastasis to bone⁶⁸⁵. High-level expression and activity of ROCK1 is also associated to poor prognosis in breast cancer, where the RHOA/ROCK1/MLC cascade is found to be a critical determinant for the development of tumor invasive phenotype⁶⁸⁶. RHOA/ROCK1 signaling has been also reported as a beneficial therapeutic target for the treatment of neuroblastoma, where RHOA/ROCK1 signaling cascade blockade resulted in inhibition of cell growth, migration, and invasion⁶⁸⁷. Furthermore, RHOA/ROCK1 signaling represents one of the main factors contributing to medulloblastoma development, where it is associated to increased epithelial-mesenchymal transition (EMT), cancer growth and metastatic spread⁶⁸⁸, and to osteosarcoma malignancy, where high ROCK1 activity levels are associated with poor outcomes⁶⁸⁹. The RHOA/ROCK1 blockade as therapeutic strategy has been also proposed to treat prostate cancer, where this pathway is associated to tumor growth and metastasis. Indeed, the RHOA/ROCK1 cascade promotes prostate cancer VEGF-induced angiogenesis, fundamental for tumor advance progression and invasiveness⁶⁹⁰.

In lung cancer, RHOA/ROCK1 signaling is linked to processes related to cancer cell apoptosis, proliferation, migration, invasion and angiogenesis^{691,692}. Indeed, RHOA/ROCK1 cascade promotes apoptosis suppression and cancer cells immortality by inhibiting the caspase 3, a crucial apoptotic mediator⁶⁹³. Accordingly, ROCK1 inhibition prevents tumor growth and metastasis and induces apoptosis in small cell lung cancer cells (SCLC) and triggers apoptosis in non-small cell lung cancer (NSCLC)^{694,695}.

Additionally, RHOA/ROCK1/MLC signal transduction pathway has been shown to play an important role in promoting NSCLC proliferation when stimulated by the proto-oncogene DEK⁶⁹⁶. Interestingly, the chromodomain helicase DNA-binding protein 4 (CHD4) has been shown to contribute to cancer initiation and progression of NSCLC via the RHOA/ROCK1 pathway⁶⁹⁷. Activated ROCK1 sustains lung cancer carcinogenesis enhancing cancer cell migration and invasion through the phosphatase and tensin homolog (PTEN)/phosphoinositide 3-kinase (PI3K)/FAK pathway and the formation of lamellipodia⁶⁹⁸. Additionally, RHOA/ROCK1 signaling has been found to participate to invasion-related processes in lung cancer involving the matrix metalloproteinases MMP-2 and MMP-9⁶⁹⁹. Last, but not least, RHOA/ROCK1 signaling is critical for the formation of a vascular structure vital for lung tumor growth⁷⁰⁰.

In pancreatic ductal adenocarcinoma (PDAC), ROCK1 signaling governs the massive remodeling of the pancreatic stroma promoting tumor progression and resistance to chemotherapeutic therapy⁷⁰¹. In gastric cancer, RHOA/ROCK1 signaling enhances the aggressive phenotype by controlling both tumor cell mesenchymal and amoeboid movements, with consequent increased cancer cell motility and invasion, and promotes apoptotic processes^{702,703}. Furthermore, the multifunctional cytokine interleukin-6 (IL-6) promotes gastric cancer spread by triggering the signaling cascade c-Src/RHOA/ROCK1, determining aggressive lymph node metastasis and unfavorable survival⁷⁰⁴. In hepatocellular carcinoma (HCC) studies evidences the RHOA/ROCK1 involvement in the cellular and molecular mechanisms involved in the fundamental steps of HCC metastasis⁷⁰⁵.

In addition to cancer-related processes, abnormal RHOA/ROCK1 signaling is correlated to different neurological disorders⁶⁵². In Alzheimer's disease (AD), the RHOA/ROCK1 signaling pathway activation is strongly associated with the distinctive progressive cognitive and dysfunctional decline and contributes to the extensive deposition of extracellular β -amyloid ($A\beta$) plaques and intracellular neurofibrillary tangles (NFTs)⁷⁰⁶. Significant evidences corroborate the keynote role of RHOA/ROCK1 signaling pathway for the generation and deposition of $A\beta$ peptides, natural metabolites produced by the hydrolysis of amyloid precursor protein (APP) whose production/clearance imbalance is associated to the disorder⁷⁰⁷. For instance, statins and non-steroidal anti-

inflammatory drugs have been shown to reduce APP processing and A β 42 levels respectively by reducing RHOA/ROCK activity^{708,709}. In addition, ROCK1 levels have been found increased in the early and advanced stages of the Alzheimer's disease, while its genetic depletion has reduced A β production^{710,711}. Interestingly, APP is found to be a phosphorylated substrate of the RHOA/ROCK1 signaling at the S655 site, whose phosphorylation promotes amyloidogenic processing and pathology by increasing interaction APP with BACE1, the β -site APP-cleaving enzyme 1⁷¹¹. In conjunction with the β -amyloid (A β) plaques, the accumulation of intracellular neurofibrillary tangles (NFTs) represents the other main Alzheimer's disease pathological hallmark^{706,712}. The major component of the intracellular neurofibrillary tangles (NFTs) is the Tau protein, a microtubule-associated protein that under physiological conditions participates to the regulation of microtubules dynamics, spatial organization and the axonal transport of organelles^{713,714}. However, abnormally increased levels of hyper-phosphorylated tau protein are found in AD patients, where it aggregates to form the paired helical filaments (PHFs), the main components of the NFTs⁷¹³. Notably, numerous studies have demonstrated the involvement of ROCK signaling in the tau hyper-phosphorylation^{706,715–720}, making the RHOA/ROCK signaling pathway a promising target for the development of new treatment strategies. Interestingly, a role of RHOA/ROCK has also been proposed in other neurodegenerative diseases, including Parkinson disease, Huntington disease, and amyotrophic lateral sclerosis^{721–725}.

RHOA/ROCK signaling pathway has been also described as a potential target to treat traumatic brain injury (TBI) because of the promising outcomes deriving from blocking RHOA/ROCK activity that prevented TBI-induced cell death and neuronal damage and improves motor and cognitive performance post-injury^{726,727}. Likewise, RHOA/ROCK blockade has been shown to enhance locomotor recovery after spinal cord injury (SCI)⁷²⁸. After a central nervous system (CNS) injury, RHOA/ROCK1 activity modulates cytoskeleton dynamics and determinates the balance between neurite retraction and axonal growth^{80,650,651,725}. Specifically, ROCK activity contributes to regenerative failure by both enhancing the actomyosin contractility, leading to a major retraction forces at the axon terminal, and the stress fiber formation⁷²⁹. From a molecular point of view, RHOA/ROCK1 signaling enhances the axonal actomyosin contractility

intensifying the MLC phosphorylation level^{80,654}. Also, ROCK activity quenching has beneficial therapeutic outcome for the treatment of glaucoma, which involves a progressive optic nerve damage⁷³⁰.

RHOA/ROCK1 cascade is determinant also for the development of cardiovascular diseases, including atherosclerosis, cardiac hypertrophy, hypertension and vasospasm of coronary and cerebral arteries^{731–733}. Indeed, cardiovascular integrity and homeostasis are strongly regulated by RHO/ROCK-mediated processes that concern endothelial cells (ECs) and vascular smooth muscle cells (VSMCs). Specifically, RHOA/ROCK pathway positively and negatively regulates VSMCs contraction and NO production in ECs, respectively^{734,735}. In depth, MLC phosphorylation is a key event in the regulation of VSMC contraction that can be realized by ROCK1 through the direct MLC phosphorylation or by phosphorylating the myosin binding subunit (MYPT1) of myosin light chain phosphatase (MLCP), decreasing MLCP phosphatase activity and increasing the overall vascular contraction^{616,630,641}. Likewise, endothelial nitric oxide synthase (eNOS) activity is also mediated by RHOA/ROCK signaling as indicated by several evidences^{735–738}. Indeed, RHOA/ROCK pathway inhibition by ROCK inhibitors, inhibition of RHOA geranylgeranylation and dominant-negative mutant of RHOA has been shown to increase eNOS activity. Increased ROCK activity has been found to be associated to diverse cardiovascular diseases, such as arteriosclerosis and atherosclerosis^{737,739–744}. Atherosclerosis is an intricate pathological process characterized by progressive inflammation, lipid accumulation and arterial wall fibrosis that involves endothelial cells (ECs) dysfunction, abnormal vascular smooth muscle cells (VSMCs) contraction and inflammatory cells accumulation in the adventitia of blood vessels. Notably, these processes are also mediated by RHOA/ROCK^{745–749}. Consistently, statins, therapeutic agents for lowering serum cholesterol levels, have been shown to exert an atheroprotective effect, improving endothelial function and decreasing vascular inflammation, by inhibiting the RHO/ROCK pathway⁷⁴². In addition, the C-reactive protein (CRP), an important marker for cardiovascular events, is found to activate the RHOA/ROCK/NF- κ B pathway, resulting in increased expression of the plasminogen activator inhibitor-1 (PAI-1), which may result in atherothrombogenesis⁷⁵⁰. Additionally, RHOA/ROCK pathway is implicated in the mechanism of thrombus formation⁷⁵¹.

Cardiac hypertrophy is closely linked to RHOA/ROCK activity^{752–757} as demonstrated by the suppression of angiotensin II–induced hypertrophy after ROCK inhibitors treatment^{758,759} and the leptin-induction of cardiac hypertrophy through the stimulation of the RHOA/ROCK pathway⁷⁶⁰. From a molecular point of view, RHOA/ROCK1 signaling has been found to regulate the assembly and organization of sarcomeric units during myofibril formation and organization⁷⁶¹, cardiomyocyte apoptosis^{756,757} and myocardial remodeling and fibrosis^{755,762}. RHOA/ROCK signaling is also implicated in the pathogenesis of hypertension as demonstrated by the heart protection from pressure overload reached through the targeted deletion of ROCK1^{763,764}. In pulmonary hypertension, RHOA/ROCK signaling plays an important role in the pathogenesis development, as revealed from the improvement of pulmonary hypertension conditions in several experimental models in rats and mice after ROCK inhibition^{765–769}. Consistently, ROCK activity is demonstrated to be increased in patients with pulmonary arterial hypertension⁷⁷⁰. Interestingly, statins, negative RHOA regulators that inhibit protein activation by preventing its post-translational isoprenylation and its translocation to the plasma membrane, are found to ameliorate pulmonary hypertension and may be effective in patients^{765,771,772}. In addition, treatment with the type PDE-5 inhibitor sildenafil has been found to inhibit the RHOA/ROCK signaling by enhancing RHOA phosphorylation, cytosolic sequestration by GDI and by preventing its translocation to the plasma membrane, with consequent beneficial effects on pulmonary hypertension^{765,773,774}.

Last, but not least, aberrant RHOA/ROCK1 signaling regulation is involved in the development of autoimmune disorders, including systemic lupus erythematosus (SLE), rheumatoid arthritis and scleroderma^{775,776}. ROCK activation in lungs is associated to allergic airway responses regulation and asthma^{777–779}. In blood cells, ROCK activity seems to play an important role in regulating inflammatory and erythropoietic stress, as well as the growth and survival of leukemic cells⁷⁸⁰. Finally, ROCK inhibition in diabetic nephropathy prevents the progression of the disease^{781,782}. Concluding aberrant RHOA/ROCK1 signaling is associated to several human diseases, making of such interaction an interesting and promising target to quench the deregulated cascade. Up to

date, several efforts have been done to silence either RHOA or ROCK activity. A summary of the available information is reported in the following paragraph.

5.3. Blocking RHOA/ROCK1 signaling: the state of art

5.3.1. ROCK inhibitors

Protein kinases, including ROCK, play crucial roles in cellular biology and pathology, making them attractive targets for treating various diseases^{783,784}. However, developing specific kinase inhibitors is often challenging due to shared sequence and structural features in their catalytic cores. This lack of selectivity can lead to off-target toxicity^{783,784}. Indeed, despite the substrate and functional specificities of each kinase protein, mostly of the inhibitor drugs act similarly by blocking the transfer of the terminal phosphate from ATP to their substrates⁷⁸⁵. The intensive research efforts⁷⁸⁵ aimed to block ROCK signaling led to the development of four ROCK inhibitors that to date are available for clinic use, namely fasudil, ripasudil, netarsudil and belumosudil. Among them, fasudil and ripasudil have received clinical approval in Japan and in China (only fasudil) in 1995 and 2014 for the treatment of cerebral vasospasm and glaucoma, respectively^{785,786}.

Fasudil, also known as HA1077, was developed by modifying the structure of a calmodulin antagonist, called W-7, during the exploration of sulfonamide derivatives that led to the development of a series of inhibitors, called H-series inhibitors⁷⁸⁷. Chemically, fasudil is an isoquinoline-based molecule characterized by a sulfonyl group (Figure 51A). After clinical evaluation, fasudil has been officially determined to be safe and effective for the treatment of cerebral vasospasm and delayed cerebral ischemic symptoms. This assessment resulted in its initial approval for clinical use in Japan in the year 1995⁷⁸⁸⁻⁷⁹⁴.

proliferation, migration, invasion by modulating matrix metalloproteinases (MMPs) activity⁶⁹⁹ and angiogenetic processes⁷⁰⁰.

However, issues related to target-specificity are possible, as demonstrated by the numerous co-crystal X-Ray structures comprising fasudil in complex with other kinase proteins. Indeed, besides ROCK, fasudil partners include the myotonic dystrophy kinase-related Cdc42-binding kinase β (MRCK β)⁷⁹⁹, PAK4⁸⁰⁰ and the protein kinase A (PKA)^{801,802}. Accordingly, fasudil inhibits ROCK and PKA with equal potency⁷⁹⁵. The unrestricted activity of fasudil to ROCK denotes possible problematic issues because of the diverse signal transduction pathways regulated by other kinases. Indeed, the simultaneously inhibition of multiple kinases could disrupt the balance of signaling pathways, leading to unintended and adverse consequences on other cellular processes. Currently, there are three active clinical trials for fasudil, two in USA (NCT04734379, NCT05218668) and one in France (NCT03792490), for the treatment of amyotrophic lateral sclerosis, progressive supranuclear palsy and corticobasal syndrome.

Ripasudil, also known as K-115 or *Glanatec*, is a ROCK inhibitor clinically approved in Japan in 2014 for the treatment of ocular hypertension and glaucoma^{803,804}. As fasudil, ripasudil has an isoquinoline scaffold characterized by a sulfonyl group (Figure 51B) and exerts an ATP-competitive mechanism. Ripasudil ameliorates glaucoma acting as an *outflow* drug by lowering the intraocular pressure through the stimulation of aqueous humour drainage reached by modifying cytoskeletal dynamics of the ocular tissues^{803,805,806}. At present, there are six active clinical trials for ripasudil in USA (NCT03249337, NCT05275972, NCT05289661, NCT05528172, NCT05795699, NCT05826353) for the treatment of Fuchs' endothelial dystrophy and of corneal edema after cataract surgery, and one in Mexico (NCT05636579) for the treatment of corneal edema.

Netarsudil (AR-13324) is an amino-isoquinoline amide (Figure 51C) drug approved in USA in December 2017 as *Rhopressa* and in EU in 2019 as *Rhokiinsa* able to reduce elevated intraocular pressure (IOP) in patients with open-angle glaucoma or ocular hypertension⁸⁰⁷⁻⁸⁰⁹. Netarsudil does not exclusively inhibit ROCK, rather it operates as a dual inhibitor affecting both ROCK and the norepinephrine transporter (NET). As result,

increased aqueous outflow and decreased aqueous production is achieved through ROCK and NET inhibition, respectively^{730,810}. Currently, there are two active clinical trials for netarsudil in USA (NCT04752020, NCT05660447) for the treatment of Fuchs' endothelial dystrophy and proliferative vitreoretinopathy (PVR). Belumosudil (Figure 51D), or KD025, is an oral ROCK-2-specific inhibitor drug approved in the USA in July 2021 as *Rezurock* for the treatment of chronic graft-versus-host disease (GvHD)^{811–813}. By means of ROCK2 inhibition, belumosudil ameliorates GvHD by quenching proinflammatory responses via the downregulation of STAT3 phosphorylation and the decrease expression of type 17 T helper (Th17) cell-specific transcription factors^{814,815}. At present, there are three active clinical trials for belumosudil in USA (NCT03640481, NCT05305989, NCT05806749) for the treatment of GvHD and to improve immunological tolerance in patients with rejection kidney transplants.

Y-27632 is a ROCK inhibitor characterized by a 4-amidopyridine scaffold (Figure 51E) developed by Yoshitomi Pharmaceutical (Japan) in the late 1990s as a molecule able to inhibit the smooth-muscle contraction associated to hypertension pathophysiology⁹². Y-27632 inhibits ROCK by competing with ATP, which is necessary for ROCK's kinase activity, by positioning its pyridine ring in the correspondent space occupied by ATP adenine⁷⁹⁵. This inhibition reduces the phosphorylation of downstream targets and thereby affects cellular processes regulated, or deregulated in disease, by ROCK. However, despite with different binding orientation and potency, Y-27632 interacts also with and the protein kinase A (PKA), as evidenced by the co-crystal X-Ray structure of PKA with Y-27632^{795,801}. This underscores potential concerns regarding target specificity. Nowadays, Y-27632 is widely used for laboratory research as a valuable tool to study the role of ROCK in various cellular functions and disease development. Notably, Y-27632 has been explored for its potential therapeutic effects in aberrant ROCK signaling pathological conditions, such as cardiovascular diseases, pulmonary hypertension, neurological disorders, glaucoma and cancer^{767,768,786,816–826}. Currently, there are not active clinical trials for Y27632.

In summary, as of the most recent information available and as the best of my knowledge, there are four distinct ROCK inhibitors that have obtained approval and are accessible for clinical use. These inhibitors include fasudil, ripasudil, netarsudil, and

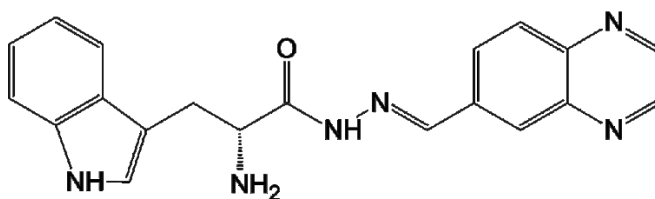
belumosudil. Fasudil and ripasudil have received clinical approval in Japan and in China (only fasudil) in 1995 and 2014 for the treatment of cerebral vasospasm and glaucoma, respectively^{785,786}. Ripasudil, known by the trade name *Glanatec*, was clinically approved in Japan in 2014 for the treatment of ocular hypertension and glaucoma^{803,804}. Netarsudil has been approved in USA in December 2017 as or *Rhopressa* and in EU in 2019 as *Rhokiinsa* to treat open-angle glaucoma or ocular hypertension^{807–809}. Lastly, belumosudil was approved as an oral ROCK-2-specific inhibitor in the USA in July 2021 under the name of *Rezurock* to treat chronic graft-versus-host disease (GvHD)^{811–813}. In addition, these medications are under consideration for the treatment of multiple pathological conditions, including Fuchs' endothelial dystrophy, corneal edema, proliferative vitreoretinopathy (PVR) and chronic graft-versus-host disease (GVHD).

It is important to stress that, although ROCK has been reported to play a significant role in cancer development, ongoing clinical trials are focused on addressing other pathological conditions than cancer. Furthermore, there are currently no ROCK inhibitors approved for treating cancer, and a recent clinical trial in this context yielded a negative outcome⁸²⁷. Specifically, despite the anti-metastatic and anti-proliferative activity demonstrated by the dual oral ROCK-AKT inhibitor AT13148 in preclinical models for the treatment of solid tumors, its narrow therapeutic index and the pharmacokinetic profile led to no further development of the compound. Effective targeting of ROCK activity with specific inhibitors could address important medical challenges. It is evident that more research efforts are necessary in the field to address the unmet need for effective cancer therapeutics and to ensure accessible and satisfactory treatments. In this regard, a promising therapeutic approach involves targeting the RHOA/ROCK1 signaling pathway, specifically focusing on interrupting this decisive protein-protein interaction, which represents the pivotal point at which the activation signal is initiated and transmitted downstream. The current work aims to investigate this approach.

5.3.2. RHOA inhibitors

Because of its association with disease^{828–830}, targeting RHOA is crucial for suppressing the dysregulated cascade in cancer that involves the downstream effector

ROCK1^{683,831,832}. One proposed strategy for effectively suppressing RHOA activity has been by focusing on its interactive interface with the Guanine Nucleotide Exchange Factors (GEFs), which is crucial for the guanine nucleotide exchange and activation processes. This approach was proven successful in designing the RHOGTPase RAC1-specific NSC23766 inhibitor⁴⁰⁷ that selectively bind to the surface groove of RAC1 that is involved in GEF interaction. In line with this approach, the same researchers' group have developed a RHO inhibitor, known as rhosin⁸³³, aimed at impeding RHO activation by disrupting the interaction between RHOGTPase subfamily RHO (RHOA, RHOB and RHOC) and GEFs. From a chemical perspective, rhosin is a compound comprising two aromatic fragments connected by a space linker having a K_d value of 354 nM for RHOA, as depicted in Figure 52.



Rhosin

Figure 52. RHOA inhibitor rhosin. The 2D structures of rhosin is reported.

The X-Ray structure of the inactive RHOA bound to the Rho guanine nucleotide exchange factor 12⁸³⁴ (ARHGEF12, or LARG) has been employed to detect a GEF-interacting surface region on RHOA located in proximity of the residue Trp58. Subsequently, a virtual screening protocol was applied to this specific region and the top scoring compounds experimentally tested *in vitro*. As result, rhosin demonstrated the ability to inhibit the binding of GEFs, but not of ROCK, to RHOA, RHOB, and RHOC. Additionally, it prevented RHO activation and RHO-mediated phosphorylation of MLC, as well as the formation of actin stress fibers and the assembly of focal adhesions in cells^{833,835}. Furthermore, subsequent research has shown that rhosin possesses the capacity to inhibit metastasis in both melanoma and breast cancer^{833,836}. Nonetheless,

although it represents a valuable research tool, rhosin did not progress beyond the stage of clinical studies.

Additional effective resources for RHOA investigations in cell biology include bacterial toxins and enzymes. For instance, the protein toxin cytotoxic necrotizing factor 1 (CNF1) from *Escherichia coli* is frequently utilized to stimulate RHOGTPases activation, including RHOA^{837,838}. On the other hand, the C3 exoenzyme from *Clostridium botulinum* serves to modify RHOA through ADP-ribosylation. This process keeps the protein in the inactive state, leading to alterations in its typical activity regulation^{839,840}. Other studies focused on statins, cholesterol-lowering drugs that have been found to inhibit RHOA prenylation, which is essential for its activation and function^{841,842}. Accordingly, RHOA inactivation by statins have been shown to induce osteosarcoma cell apoptosis^{843,844}, reduce metastasis in renal cell carcinoma⁸⁴⁵, but also to attenuate neuropathic pain by inhibiting the RHOA/LIMK/cofilin pathway⁸⁴⁶.

Nonetheless, it is critical to emphasize that, as of my last knowledge update, despite considerable efforts aimed at designing RHOA inhibitors, there are not candidate drugs currently undergoing clinical trials. Indeed, developing precise and effective inhibitors for the RHOA subfamily represents a significant challenge in the field of drug development. RHOGTPases, such as RHOA, hold critical functions in diverse cellular processes, and achieving precise targeting is challenging due to their shared structural and functional similarities. Accordingly, barriers related to efficacy, precision and feasibility of drug development represent significant challenges in this regard. It is evident that demanding to devise novel drug design approaches for targeting the RHOA/ROCK1 signaling pathway. The approach proposed in the present work involves intervening at the protein-protein interaction that occurs between active RHOA and ROCK proteins, which represents the pivotal step where the activation signal is subsequently initiated and transmitted downstream. Counting on the encouraging outcomes from investigating the CDC42/PAK interface, classical MD simulation and alchemical free energy calculation will be employed to assess critical residues involved in the protein-protein recognition mechanism. The overall process aims to identify interactions suitable for drug targeting. Due to the significance of conducting an initial and propaedeutic examination of the system's conformation, alchemical free energy calculations will be preceded by classical

molecular dynamics (MD) simulations aimed at exploring potential arrangements of the system.

5.4. Systems set-up

To initiate the exploration of the interaction between RHOA and ROCK1, the sole available X-Ray structure for the complex formed by the human RHOA and RHO-binding domain (RBD) of human ROCK1⁸⁴⁷ was employed (PDB ID 1S1C, resolution of 2.6 Å). In particular, the structure contains a truncated version of human RHOA, encompassing residues 1 to 181, bound to the non-hydrolyzable GTP analogue GNP (or Gpp(NH)p). For ROCK1, residues extending from position 947 to 1015 represent the RBD domain. Indeed, as previously described, ROCK1 is a kinase consisting of 1354 amino acid residues, whose structure comprises an N-terminal kinase domain, succeeded by a coiled-coil structure and a C-terminal regulatory domain. The C-terminal domain functions as an inhibitory region, restraining the kinase activity by binding to and obstructing the N-terminal kinase domain^{613,614}. Upon binding of GTP-bound active RHOA to the RHO binding domain (RBD) located in the coiled-coil region, this negative regulation is disrupted, resulting in activation of the ROCK1 kinase⁸¹.

The overall structure is depicted through an asymmetric unit featuring a 95 Å-long dimer of ROCK1-RBD in a α -helical parallel coiled-coil configuration, along with two RHOA molecules in which the GNP and Mg²⁺ binding is consistent with the well-preserved binding mode found in GTPases (Figure 53A). Notably, a 2-fold non-crystallographic symmetry axis runs through the central region of the coiled-coil dimer at the point where it interacts with RHOA (Figure 53B). The dimeric coiled-coil configuration of ROCK1-RBD is congruous with the X-ray structures of the kinase domains of both ROCK1 and ROCK2, in which two N-terminal regions interact to form a head-to-head homodimer^{795,796}. Additionally, this configuration is supported by X-ray structures of both ROCKs' coiled-coil segments, where RBD dimerizes to form a parallel head-to-head coiled-coil^{848,849}.

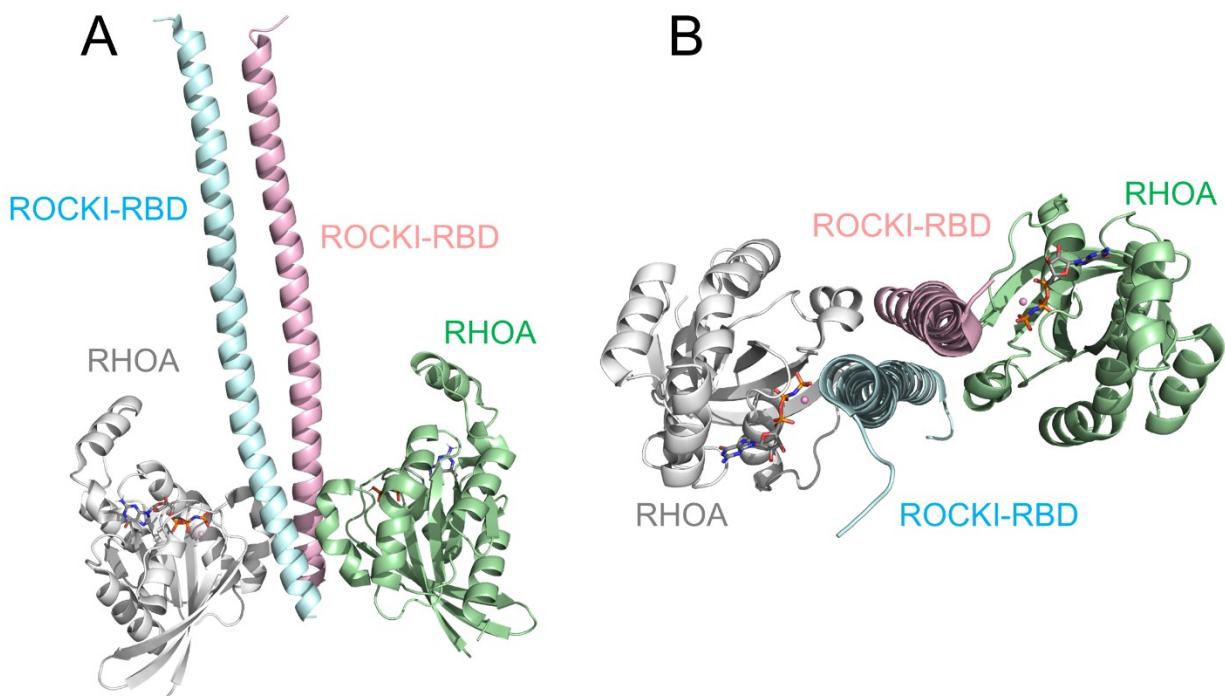


Figure 53. RHOA/ROCK1 X-Ray structure. The RHOA/ROCK1 complex is reported. RHOA molecules are represented as white and green cartoon, while ROCK1 α -helices are showed in light blue and pink. The GNP nucleotide and the Mg²⁺ ion are in sticks and balls, respectively. A 2-fold non-crystallographic symmetry axis runs through the center of the coiled-coil dimer at the interacting interface with RHOA (B).

The RHOA/ROCK1 crystal structure served as foundation for configuring the system for classical molecular dynamics (MD) simulations. Since the interaction between RHOA and ROCK1 was symmetric in the crystal, only a single RHOA molecule was taken into account (Figure 54A). Notably, RHOA makes contacts with both α -helices of the coiled-coil ROCK1 dimer. To optimize computational efficiency, careful consideration was given to reducing the number of atoms in the system, with a specific focus on the RBD-ROCK1 segment length. The structure identifies a critical RHOA binding motif spanning from position 998 to 1010 that was used as initial reference for constructing RBD-ROCK1 (Figure 54A) in the final system. Subsequently, the unmodeled C-terminal residues, one in an α -helix and two in the other, from the experimental fragment used were consistently modeled to match the α -helix conformation (Figure 54B). Furthermore, in order to

enhance the representation of the interaction, additional N-terminal residues were included up to a distance of ~ 12 Å from position 998 (Figure 54B). In summary, the final RHOA/ROCK1 system (Figure 54C) was constructed by comprising a single RHOA molecule and a 32-residues long RBD-ROCK1 dimer (986-1015). In addition, the GTP catalytic pocket was taken into account by converting the GNP nucleotide into GTP and thoroughly evaluating all the pivotal interactions.

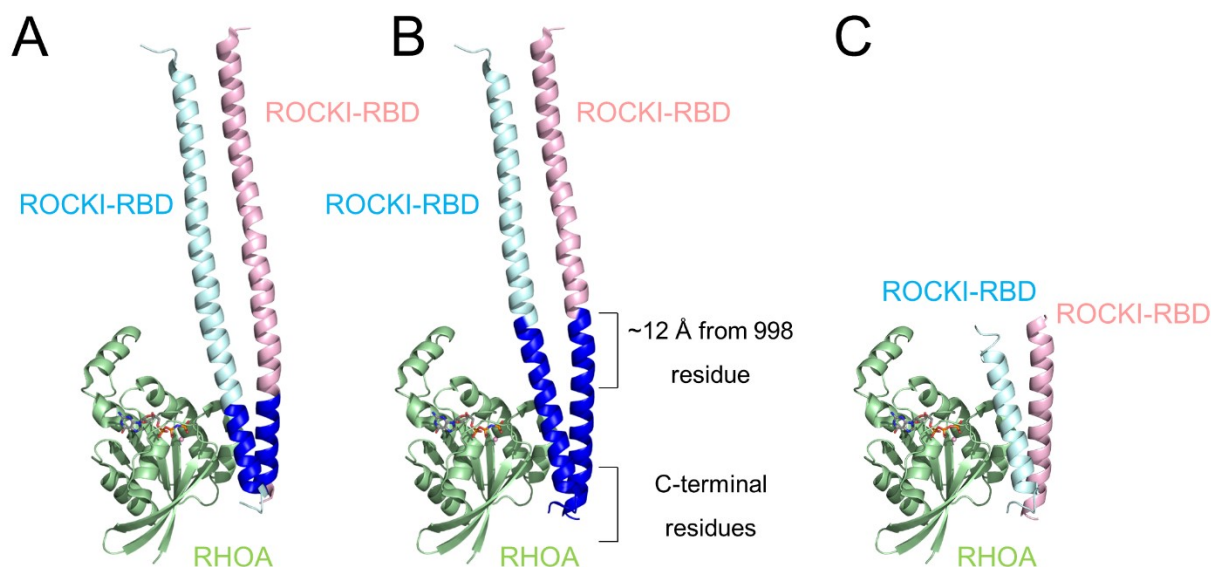


Figure 54. RHOA/ROCK1 system set up. The RHOA/ROCK1 system set up is summarized. RHOA is represented as green cartoon, while ROCK1 α -helices are showed in light blue and pink. The GNP nucleotide and the Mg^{2+} ion are in sticks and balls, respectively. The minimal RHOA binding motif is evidences in blue (A). Additional residues were considered in both C- and N-terminal direction (B). The final RHOA/ROCK1 system (C) is reported.

The RHOA/ROCK1 crystal structure was initially utilized as starting point to configure the apo form of RHOA by removing the effector. Unfortunately, removing ROCK1 had a substantial impact on the GTPase stability. Specifically, the switch regions of RHOA showed significant deviation from the active conformation across four 1 μ s replicas, rendering the structure unsuitable for further analysis. To address this issue, the X-ray structure of the RHOA apo form at its lowest resolution (PDB ID 1KMQ, resolution of 1.55 Å) was utilized⁸⁵⁰. As for the previous bound-form set up, the GNP nucleotide was converted into GTP, and all the established interactions were assessed. Furthermore, two

single-point mutations present in the structure (F25N and Q63L) were reverted to restore the *wild-type* form. Also, to ensure structural consistency in simulating both the apo and bound forms, the identical RHOA sequence spanning from residue in position 4 to 181 was utilized, as the apo form structure encompasses these residues (from 4 to 181). Systems were solvated with TIP3P water molecules in cubic simulation boxes extending at least 14 Å from the protein surface(s). Sodium ions were added randomly to neutralize the charge of the systems. Final models included ~54,000 atoms in a 86 × 86 × 86 Å³ box for apo RHOA and ~203,000 atoms in a ~132 × 132 × 132 Å³ box for the complex.

5.5. Classical MD simulations

5.5.1. Apo form RHOA MD simulation

To calculate $\Delta\Delta G_{\text{binding}}$ values through the alchemical transformation of RHOA from its *wild-type* state to the mutant form in both the unbound and ROCK1-bound states, equilibrated configurations from classical MD simulations of both states were necessary. Accordingly, 1 μs classical MD simulations were carried out for both systems. To assess RHOA stability in its apo form, both the stability of the backbone and secondary structure were considered and evaluated (Figure 55A). Similarly, the stability of the catalytic pocket was also assessed. Specifically, the initial GTP binding pose and the coordination of the catalytic Mg²⁺ ion remained stable throughout the entire simulation (Figure 55B and 55C). Additionally, the stable preservation of a key interaction characterizing the active state between the GTP nucleotide and Gly62 was observed (Figure 55D). The switch motifs (switch I and II) of RHOA retained their active conformation throughout the entire simulations, remaining in alignment with the initial structure (Figure 55E). To provide further confirmation, frames from the entire molecular dynamics (MD) simulation were clustered based on the root mean square deviation (RMSD) of the residues within both the switches and the entire RHOA backbone (Figure 55G). Distances defining the active conformation throughout the simulation were assessed to verify the preservation of the active state of RHOA (Figure 55F). After conducting a comprehensive structural analysis and clustering the frames obtained from the entire molecular dynamics (MD) simulation

on the basis of the RHOA backbone residues, a specific structure was chosen to initiate the alchemical transformation of RHOA from its *wild-type* to mutant form in the unbound state.

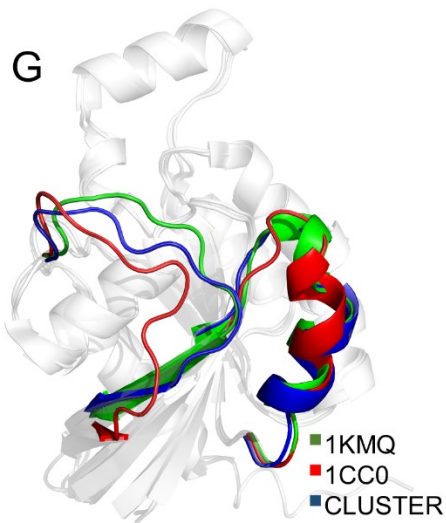
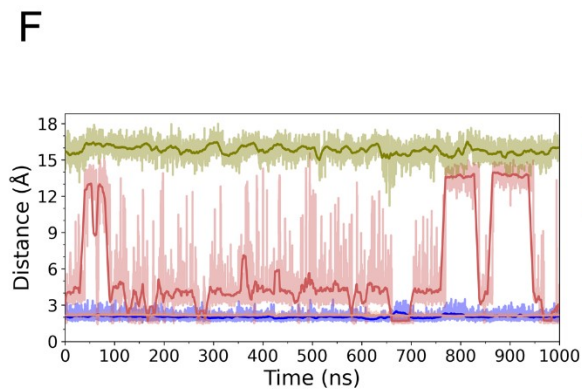
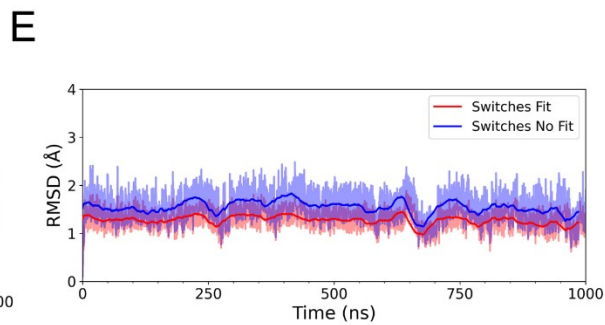
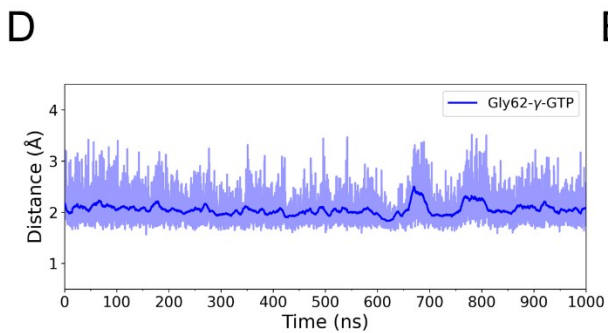
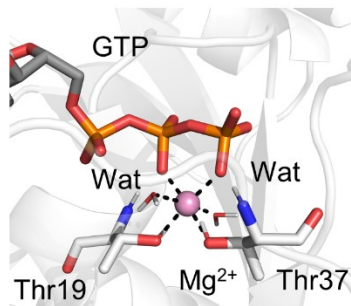
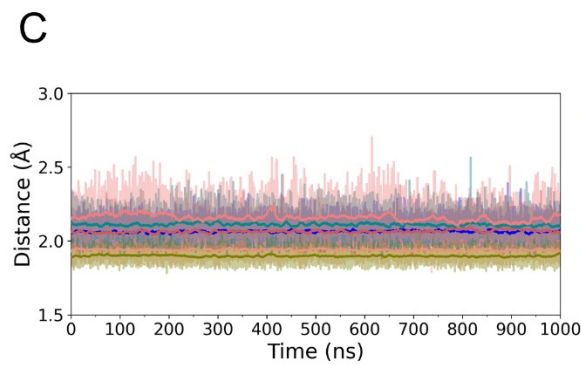
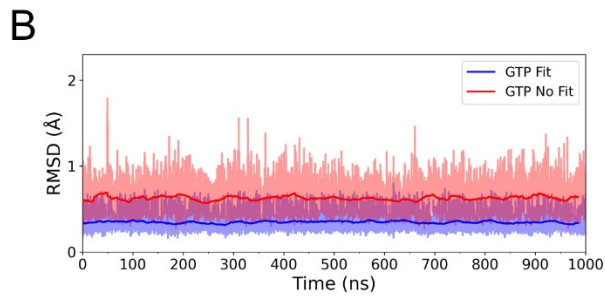
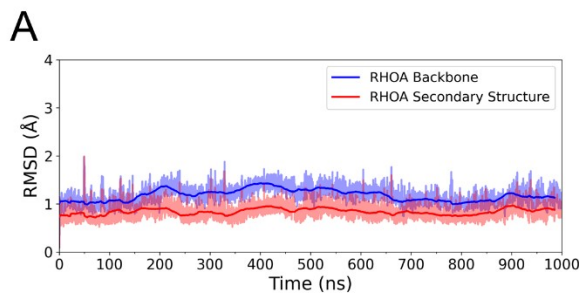
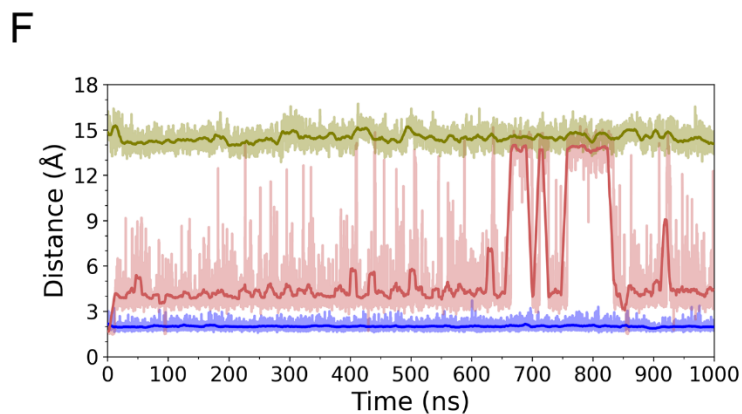
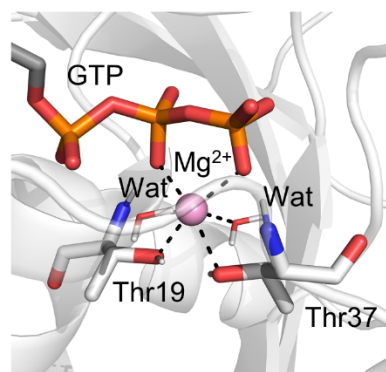
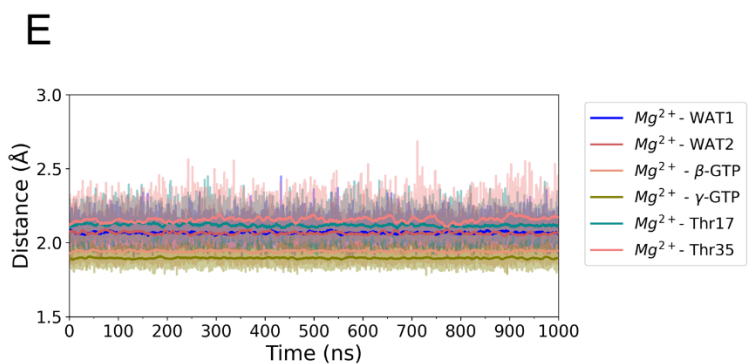
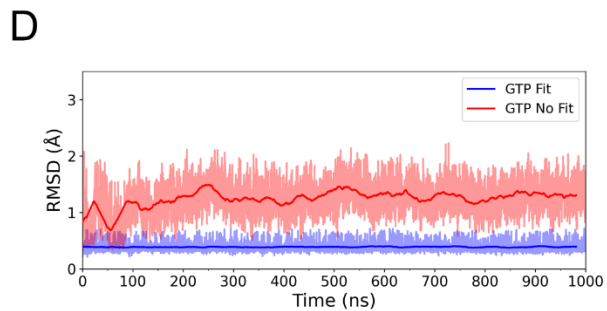
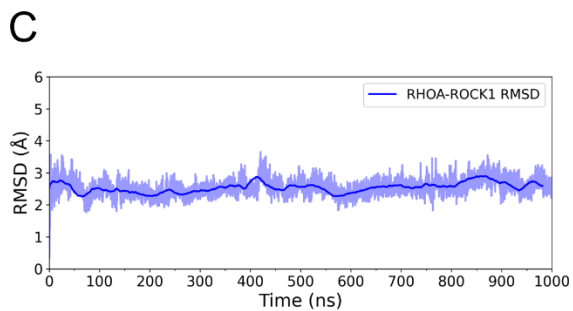
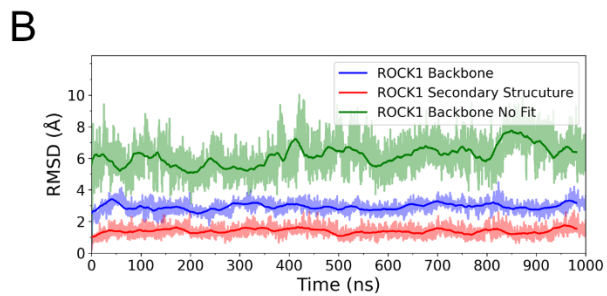
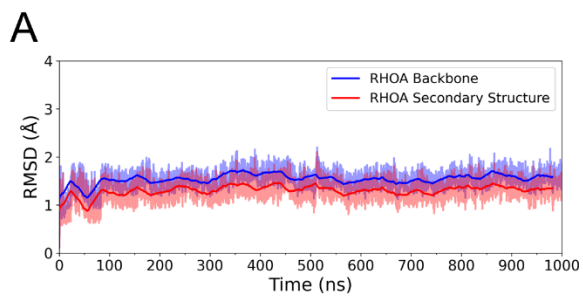


Figure 55. MD simulations of apo form RHOA. The time series RMSD descriptor for both the RHOA's backbone and secondary structure is reported in A. The conservation of the GTP catalytic pocket was investigated through the time series RMSD for the GTP nucleotide (B) and by monitoring the length of the Mg^{2+} coordination bonds (C). Both RMSD and distance values descriptors are shown as shaded areas, while the associated running averages are represented as lines. The monitoring of the GTP-Gly62 interaction as well as distances defining the active conformation is reported in D and F. The RMSD of switch motifs in RHOA is reported in E. The superposition of active (PDB ID 1KMQ) and inactive (PDB ID 1CC0) RHOA structures with the representative structure obtained by clustering the RHOA MD trajectory based on the RMSD of the switch regions is reported in G. Notably, the switch motifs in the representative structure (blue) resemble the active state (green), in contrast to the inactive state (red), having RMSD values of 1.5 Å and 2.5 Å respect to the active and inactive state, respectively.

5.5.2. ROCK1-bound form RHOA MD simulation

RHOA/ROCK1 complex was found stable along the whole simulation time, as assessed by the RMSD descriptors for the backbone and secondary structure for RHOA, ROCK1 and RHOA/ROCK1 complex (Figure 56A, 56B and 56C). As for the apo form RHO MD analysis, the stability of the catalytic pocket was also investigated. The GTP binding pose and the coordination of the catalytic Mg^{2+} ion were preserved throughout the entire simulation (Figure 56D and 56E). Likewise, the key interactions characterizing the active state were maintained (Figure 56F). The interactive region of RHOA with ROCK1 is defined by the RHOA switch motifs, which maintained their active conformation consistently throughout the entire simulation (Figure 56G). Clustering of frames from the molecular dynamics (MD) simulation using RMSD of the switches confirmed the permanent arrangement of switch motifs in their active state (Figure 56H).



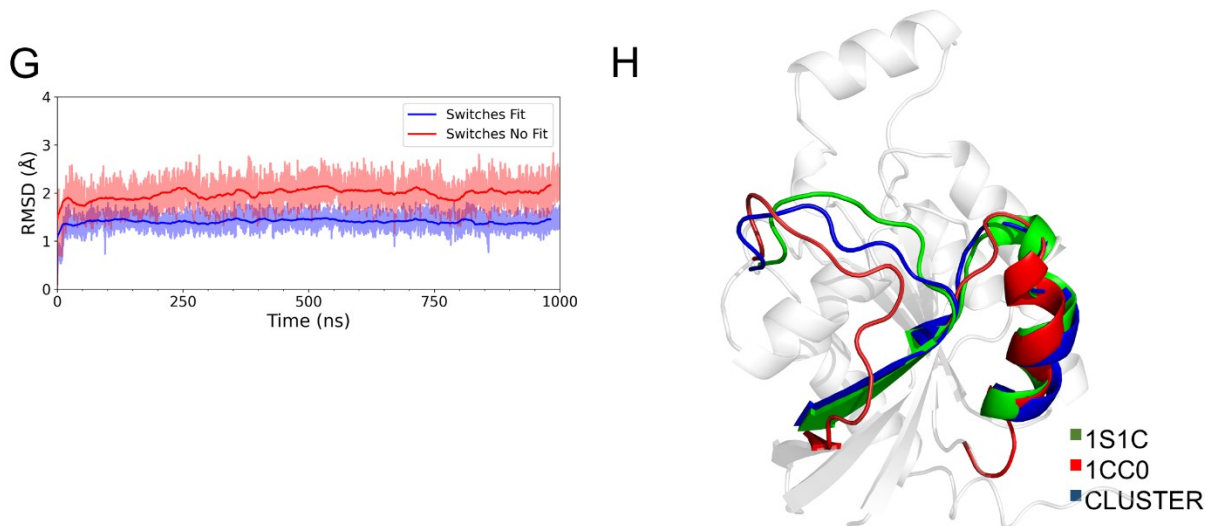


Figure 56. MD simulations of ROCK1-bound form RHOA. The time series RMSD descriptors for the RHOA, ROCK1 and RHOA/ROCK1 complex backbone and secondary structure residues are reported in A, B and C. The conservation of the GTP catalytic pocket was investigated through the time series RMSD for the GTP nucleotide (D) and by monitoring the length of the Mg^{2+} coordination bonds (E). Both RMSD and distance values descriptors are shown as shaded areas, while the associated running averages are represented as lines. The monitoring of distances defining the active conformation is reported in F. The RMSD of switch motifs in RHOA is reported in G. The superposition of active (PDB ID 1S1C) and inactive (PDB ID 1CC0) RHOA structures with the representative structure obtained by clustering the RHOA/ROCK1 MD trajectory based on the RMSD of the switch regions is reported in H. Notably, the switch motifs in the representative structure (blue) resemble the active state (green), in contrast to the inactive state (red), having RMSD values of 1.8 Å and 3.0 Å respect to the active and inactive state, respectively.

To explore the conformations observed during the molecular dynamics (MD) simulation, an analysis focused on the residues defining the protein-protein interface was conducted. Specifically, the stability of the root mean square deviation (RMSD) values for these interacting residues was assessed throughout the entire simulation duration (Figure 57A). Moreover, by applying the density peaks algorithm on the RMSD of the interface residues, the analysis demonstrated that conformations sampled during 1 μ s MD simulation were collectively represented by a structure exposing high similarity to the

experimentally reported structure of the RHOA/ROCK1 complex, with an RMSD value of 1.6 Å (Figure 57B).

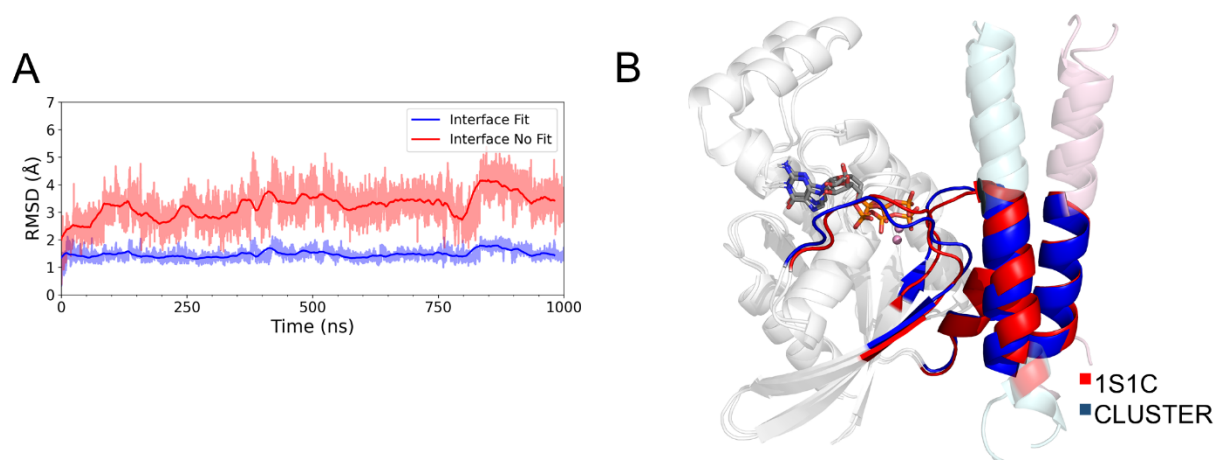


Figure 57. MD simulations of ROCK1-bound form RHOA. The time series RMSD descriptors for RHOA/ROCK1 interface backbone's residues is reported in A. The superposition of the experimental structure for the RHOA/ROCK1 complex (PDB ID 1S1C) with the representative structure obtained by clustering the RHOA/ROCK1 MD trajectory based on the RMSD of the interfacial residues is reported in B. Notably, the interface in the representative structure (blue) resemble the reported experimental data (red).

Upon the extensive structural analysis and clustering the frames obtained from the entire molecular dynamics (MD) simulation using the RHOA/ROCK1 backbone residues as reference, a precise structure was selected as the starting point for initiating the alchemical transformation of RHOA, transitioning the protein from its *wild-type* to the mutant form while in the ROCK1-bound state. Moreover, due to the optimization mentioned earlier for setting up the RHOA/ROCK1 system, the 32-residue RBD-ROCK1 dimer (residues 986-1015) was simulated to validate its structural stability. The dimer's stability was verified over a 1 μ s classical MD simulation by assessing RMSD descriptor for the backbone residues (Figure 58A). Additional demonstration of the dimer's stability was obtained through clustering analysis of frames from the MD simulation using RMSD of the backbone residues (Figure 58B).

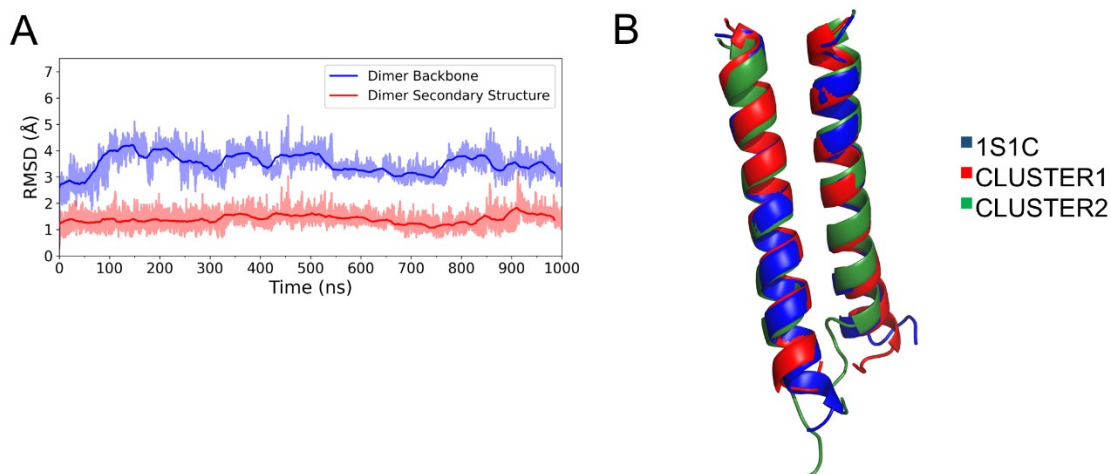


Figure 58. MD simulations of RBD-ROCK1 dimer. The time series RMSD descriptors for RBD-ROCK1 dimer backbone's residues is reported in A. The superposition of the corresponding experimental fragment from the RHOA/ROCK1 complex (PDB ID 1S1C) with the representative RBD-ROCK1 dimer structures obtained by clustering the MD trajectory based on the RMSD of the backbone residues is reported in B. Notably, the representative structures (red and green) resemble the reported experimental data (blue).

In conclusion, these comprehensive analyses of the MD trajectories, building upon the findings from the previous study of the CDC42/PAK1 interface, served as a preparatory step for the alchemical free energy calculations. As previously described, it is of substantial importance to select the most representative structure as the starting point for the alchemical transformation. While exhaustive sampling would be ideal in addressing this concern, real-case scenarios can constrain the extent of configurational sampling, as exemplified by the Y32F and V33N mutants in the CDC42/PAK1 test case. Consequently, a thorough conformational analysis of the system is essential to identify the most populated conformation of the structure undergoing transformation. Indeed, the information obtained from the structural analysis are advisable to guide the selection of the optimal configuration for initiating the alchemical transformation, enhancing accuracy.

5.5.3. Computational details

MD simulations were performed with the pmemd module of AMBER20⁵⁹⁸. The AMBER-ff14SB force field⁵⁹⁹ was used for the protein, while parameters from recent literature were adopted for GTP and Mg²⁺^{600,601}. Monovalent ions were described with Joung–Cheatham parameters⁶⁰², and the TIP3P model⁶⁰³ was used for water. Simulations were performed with a distance cutoff of 10 Å. Long-range electrostatics were treated with the particle mesh Ewald method. Bonds involving hydrogen atoms were constrained, allowing a time step of 2 fs. After solvent equilibration, systems were energy minimized and gently heated to 303 K for 0.5 ns while restraining protein backbone atoms to stay close to the experimental structure. The Andersen-like temperature-coupling scheme⁶⁰⁴ and a Monte Carlo barostat were used to maintain temperature and pressure close to room temperature conditions. About 1 μ s of MD simulations in the NPT ensemble were accumulated for each system. Table 8 summarizes the size and the simulated time of the performed MD simulations described in this chapter.

	N° atoms system	N° atoms solvated system	Simulated time
RHOA	~ 2,900	~ 54,400	1 μ s
RHOA/ROCK1	~ 3,900	~ 200,000	1 μ s
ROCK1 DIMER	~1,000	~ 50,600	1 μ s
RHOA APO TRANSFORMATION	~ 2,900	~ 54,400	120 ns
RHOA PAK1-BOUND TRANSFORMATION	~ 3,900	~ 200,000	120 ns

Table 8. MD simulations summary. An overview summarizing both the size and simulated time of the conducted MD simulations is reported.

5.6. Alchemical Free Energy Calculations for the RHOA/ROCK1 system

5.6.1. RHOA mutants selection

The RHOA and ROCK1 proteins interact at their interface through a combination of diverse interactions. One objective of this thesis is to explore how RHOA and ROCK1 interact, aiming to determine the crucial residues responsible for the protein-protein recognition mechanism that can be targeted with drugs. The promising results from the previous study on CDC42 and PAK1 validate the use of alchemical free energy calculations as a computational tool able to support research projects by prioritizing mutants that could have significant effects, ultimately improving the efficiency and economy of experimental efforts. Building upon these findings, alchemical free energy calculations are now applied to investigate the RHOA/ROCK1 protein-protein interaction, starting by examining specific control RHOA mutants to evaluate the reliability of future calculations. As reference, a remarkable experimental study aimed to identify mutations in RHOA that selectively disrupt binding with diverse effectors was considered⁶⁶⁸. Specifically, the analysis involved three experimental tests: yeast two-hybrid screening assay, *in vitro* binding assay and an assay aimed to assess the effects of RHOA mutants on cytoskeletal reorganization.

Yeast two-hybrid screening assay is a molecular biology technique used to study protein-protein binding by testing their physical interactions. The basis of this test lies in the activation of downstream reporter gene(s) through the binding of a transcription factor to an upstream activating sequence (UAS). In the yeast two-hybrid screening assay, the transcription factor is divided into two distinct fragments: the DNA-binding domain (DBD) and the activating domain (AD). The protein of interest is linked with the DNA binding domain (DBD) to create a construct referred to as *bait*, whereas the protein that might interact with it is linked with the activation domain (AD) to form a construct known as *prey*. The reconstitution of the transcription factor into its functional form, capable of activating the expression of reporter gene(s), occurs only when the DNA-binding domain (DBD) and activation domain (AD) are in close proximity. Consequently, the expression of the

reporter gene(s) serves as evidence that there was a physical interaction between the bait and prey proteins^{851,852}.

Specifically, RHOA (the bait) was fused to the GAL4 DNA-binding domain while a ROCK1 fragment (the prey) was fused with the GAL4 activation domain and the interaction was assayed by monitoring the GAL4-dependent HIS3 reporter gene expression in the yeast strain HF7C⁸⁵³. In detail, the HIS3 reporter gene encodes for an enzyme, called *imidazoleglycerol-phosphate dehydratase*, which holds a fundamental role in the histidine biosynthetic pathway. Indeed, yeasts lacking of a functional HIS3 gene are unable to synthesize histidine and to survive in a medium lacking histidine. The assay relied on the concept that the interaction between a RHOA mutant (acting as the bait) and ROCK1 (acting as the prey) would result in the reconstruction of the transcription factor, subsequently activating the HIS3 reporter gene. This activation would enable yeast cells to survive on histidine-deficient media, providing evidence of an occurred protein-protein interaction. In addition, the assessment of protein-protein interaction was conducted through a colony color assay, wherein the expression of β -galactosidase, an enzyme encoded by the LacZ reporter gene, was evaluated. This enzyme hydrolyzes X-Galactose (or X-GAL), resulting in a blue colored product when present in a medium, a technique commonly known as white-blue screening⁸⁵⁴. As results, the RHOA single-point mutants F39A, E40L and E40W were found unable to interact with ROCK1, while Y42C, F39V, E40N and E40T were able to successfully interact with ROCK1.

Next, to validate the results obtained from the yeast two-hybrid screening assay, *in vitro* binding assays were conducted. Specifically, RHOA mutants were tagged with the 9E10 antibody epitope⁸⁵⁵ (EQKLISEEDL), while ROCK1 was fused with GST (Glutathione-S-transferase) and bound to a glutathione affinity matrix. Subsequently, the levels of bound proteins were assessed through 9E10 immunoblotting after thorough washing. The results of the experiments indicated that, in general, the RHOA single-point mutants that interacted with ROCK1 in the yeast two-hybrid screening assay were also capable of binding to the effector *in vitro*. However, contrary to the findings from the yeast two-hybrid screening assay, the RHOA mutant E40W exhibited binding to ROCK1 *in vitro* as well.

Afterwards, due to the implications of RHOA/ROCK1 signaling in reorganizing the cytoskeleton, such as the formation of stress fibers and focal adhesions, the influence of RHOA mutants on cytoskeletal reorganization was examined in NIH-3T3 cells. The results showed that the expression of certain RHOA mutants—specifically E40N, E40T, and Y42C—efficiently triggered stress fiber formation. Conversely, RHOA mutants F39A, E40L, and E40W did not induce stress fiber formation effectively. These findings corroborated previous experimental results, despite some RHOA mutants exhibited unexpected behavior. Notably, F39V did not promote stress fiber formation, although binding to ROCK1 in both yeast two-hybrid and *in vitro* binding assays was detected. Similarly, E40W did not induce stress fiber formation, even though the E40W mutant bound ROCK1 in *in vitro* binding assay. In summary, for the purpose of evaluating the system and ensuring the reliability of future calculations, single-point mutations that did not consistently display the same behavior in all the experimental tests were excluded from the selection (Table 9). Instead, RHOA mutants Y42C, F39A, E40L, E40N, and E40T were selected and employed. Importantly, due to the absence of precise quantitative binding values, the resulting $\Delta\Delta G_{\text{binding}}$ values from alchemical free energy calculations were compared to the qualitative results obtained from experimental tests.

Mutation	Yeast two-hybrid screening	<i>in vitro</i> binding assay	Effects on cytoskeletal reorganization
Y42C	✓	✓	✓
F39A	✗	✗	✗
F39V	✓	✓	✗
E40L	✗	✗	✗
E40W	✗	✓	✗
E40N	✓	✓	✓
E40T	✓	✓	✓

Table 9. RHOA mutants experimental data. The experimental outcomes from for the yeast two-hybrid screening assay, *in vitro* binding assay and assay assessing the effects on mutations on cytoskeleton organization for the reported single-point mutations are shown. Notably, F39V and E40W did not consistently display the same behavior in all the experimental tests.

5.6.2. Computational details and preliminary results

Binding free energies ($\Delta\Delta G_{\text{binding}}$) between mutated forms of RHOA and ROCK1 were computed with respect to the *wild-type* using alchemical transformations⁴⁷⁰. Accordingly, RHOA was transformed from *wild-type* into the mutant in both the apo and ROCK1-bound forms. The free energy change associated with each transformation was estimated using thermodynamic integration⁵⁵⁸ (eq. 24), and their difference provided an estimate of $\Delta\Delta G_{\text{binding}}$ according to the thermodynamic cycle in Figure 59.

$$\Delta G = G(\lambda = 1) - G(\lambda = 0) = \int_0^1 \langle \partial V / \partial \lambda \rangle_\lambda d\lambda = \sum_i w_i \langle \partial V / \partial \lambda \rangle_i \quad (\text{eq. 24})$$

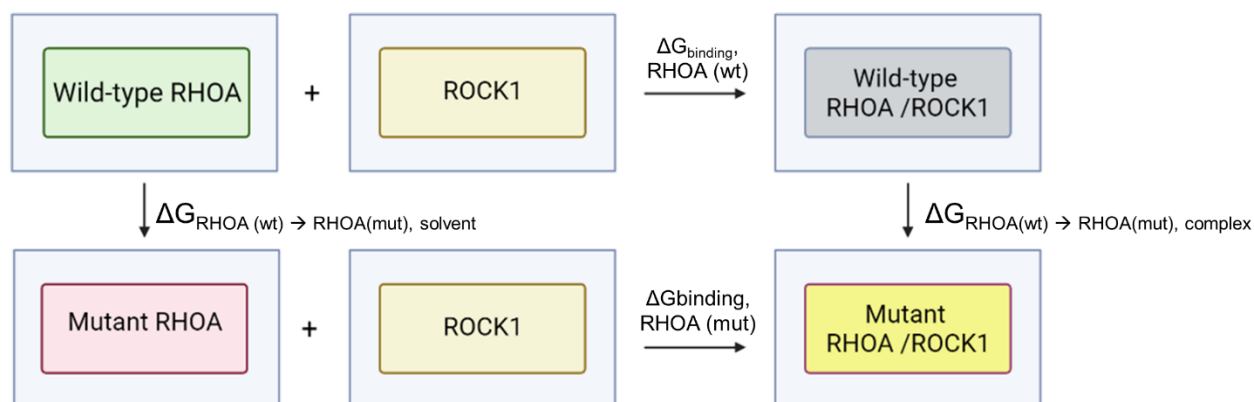


Figure 59. Thermodynamic cycle employed to compute binding affinity estimates.

The thermodynamic cycle used to compute relative binding free energies for the analyzed single-point mutations is reported. RHOA was transformed from *wild-type* into mutant in both the apo and ROCK1-bound forms. The color code defining the components of the thermodynamic cycle are green for the *wild-type* RHOA, red for mutant RHOA, beige for ROCK1, grey for the *wild-type* RHOA/ROCK1 complex and, finally, yellow for the mutant RHOA/ROCK1 complex.

Alchemical calculations were started from equilibrated configurations from equilibrium MD simulations of the RHOA/ROCK1 complex and RHOA alone, as previously described. Each transformation was carried out in 12 windows (corresponding to λ values: 0.00922, 0.04794, 0.11505, 0.20634, 0.31608, 0.43738, 0.56262, 0.68392, 0.79366, 0.88495, 0.95206, and 0.99078 and weights 0.02359, 0.05347, 0.08004, 0.10158, 0.11675, 0.12457) performing 10 ns simulations at each λ value. Bonds were not constrained requiring an integration time step of 1 fs. Backbone atoms of the residues involved in the mutations were transformed linearly, while side-chain atoms were treated with softcore potentials for both Lennard-Jones and electrostatic interactions⁵⁵⁷. Certain mutations result in a modification of the total charge within the system. In order to address such issues, as in the CDC42/PAK1 study, the alchemical co-ion method was implemented^{605,606}. Specifically, among the selected RHOA mutations, only Y42C and F39A had a neutral effect on the charge. Conversely, in the case of E40L, E40N, and E40T mutations, a negative charge was annealed. To address this issue, a Na⁺ ion was simultaneously transformed into a water molecule (Figure 60). Transformations were

performed at constant volume (the equilibrated volume from MD simulations) and temperature.

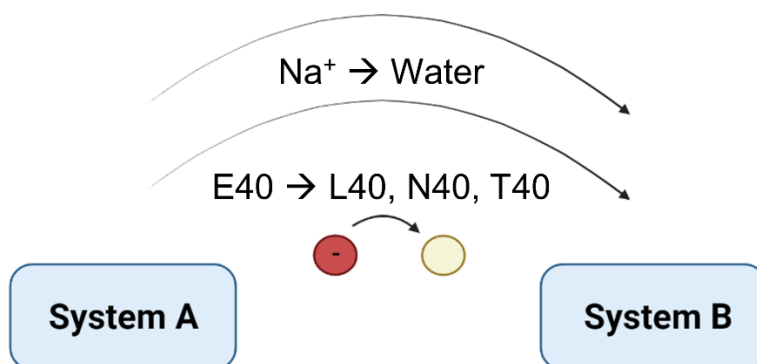


Figure 60. Co-ion approach employed. The scheme represents the alchemical co-ions approach used to treat mutations implying a change in the net charge of the system. Specifically, for the E40L, E40N, and E40T mutations the disappearing of the negative charge on the protein was counterbalanced by the concomitant transformation of a Na⁺ ion into a water molecule.

All systems remained stable during the alchemical transformations, with low RMSD values for RHOA and the residues at the RHOA/ROCK1 interface as well as for the GTP binding pose. Data analysis was performed after discarding the first 10% of the simulation time (corresponding to the first ns of simulation) of each window. In order to estimate errors on ΔG (eq. 24) the time series of $\partial V/\partial \lambda$, values from each window were resampled to obtain uncorrelated samples, from which averages and variances were computed. The error on $\Delta \Delta G_{\text{binding}}$ was obtained by combining the errors of the individual transformations. The convergence of the computed $\Delta \Delta G_{\text{binding}}$ was assessed by estimating it as a function of simulation time, considering intervals both in the forward and the reverse direction⁶⁰⁸.

Mutation	Yeast two-hybrid screening	<i>in vitro</i> binding assay	Effects on cytoskeletal reorganization	$\Delta\Delta G_b^{\text{comp}}$
Y42C	✓	✓	✓	$0.37 \pm 8.31e^{-4}$
F39A	✗	✗	✗	$3.41 \pm 1.05e^{-4}$
E40L	✗	✗	✗	$4.95 \pm 3.52e^{-4}$
E40N	✓	✓	✓	$0.82 \pm 3.08e^{-4}$
E40T	✓	✓	✓	$0.98 \pm 3.54e^{-4}$

Table 10. RHOA mutants experimental data and relative binding free energy values for the association of RHOA mutants and ROCK1. The computed $\Delta\Delta G_{\text{binding}}$ values (kcal/mol) for the examined single-point mutations are reported together with their experimental outcomes from for the yeast two-hybrid screening assay, *in vitro* binding assay and assay assessing the effects on mutations on cytoskeleton organization.

The results presented in Table 10 demonstrate a great concordance between the calculated $\Delta\Delta G_{\text{binding}}$ values and experimental data. Indeed, consistent with the experimental findings, mutations Y42C, E40N, and E40T in RHOA exhibit negligible impacts on the binding free energy to ROCK1. Conversely, mutations F39A and E40L are found to hamper the binding interaction between the two proteins. Collectively, these findings emphasize the capability of alchemical binding free energy calculations in identifying mutations that influence binding affinity. Specifically, residue Glu40 is engaged in an electrostatic interaction with a lysine residue (Lys1005) from ROCK1, a bond that remained stable throughout the entire preliminary classical MD simulation as depicted in Figure 61A. While examining the lack of significant influence of the E40N mutation on RHOA binding to ROCK1, it was observed that the Asp40 residue was capable of establishing an interaction with Lys1005 through its carboxamide sidechain, as illustrated in Figure 61B. This observation was corroborated by monitoring the distance between the

carboxamide oxygen of the asparagine and the positively charged group of Lys1005. Indeed, as the transformation progressed, in the last stages the distance between these two functional groups became comparable to the original distance between Glu40 and Lys1005.

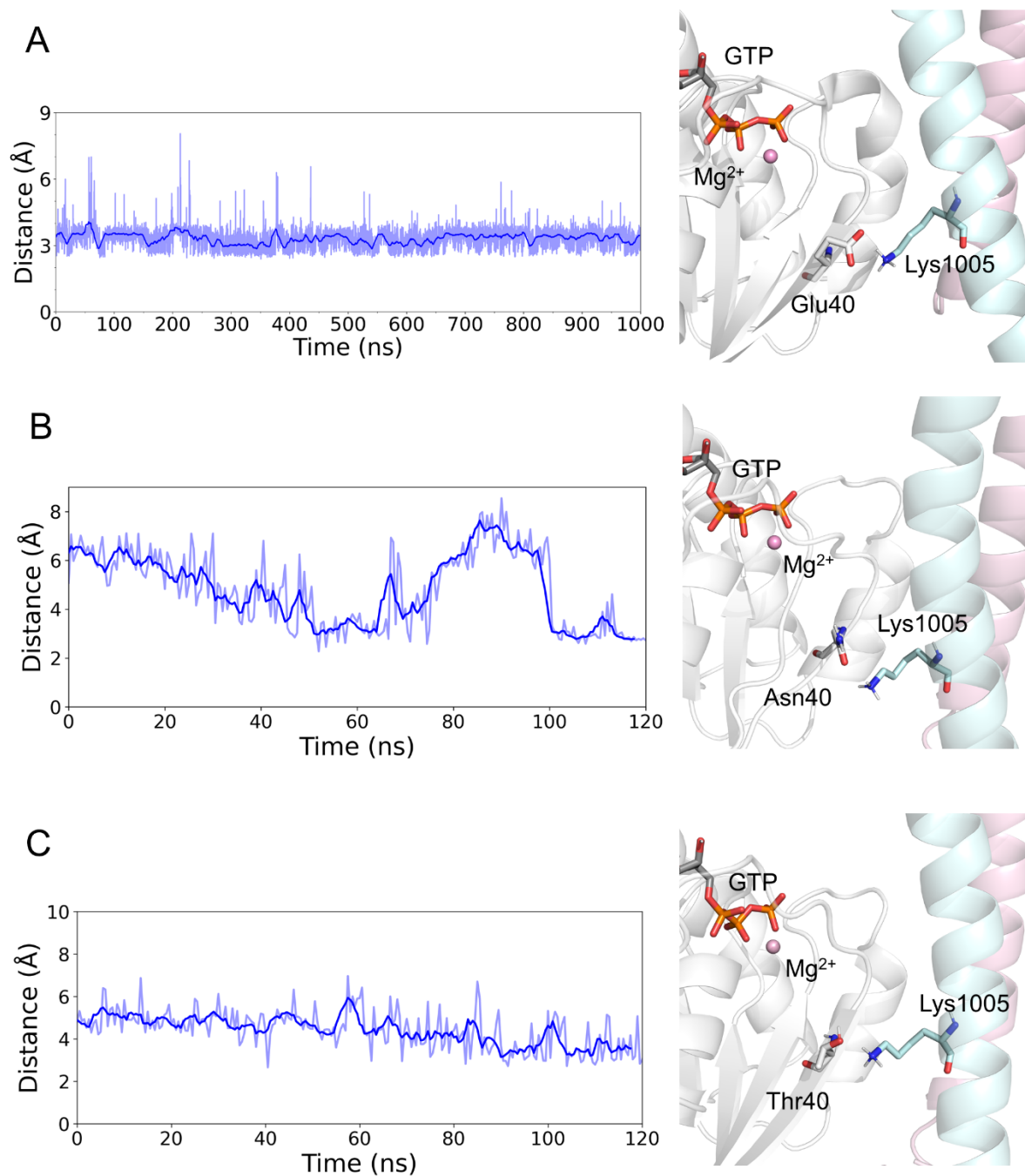


Figure 61. RHOA alchemical free energy calculations. A) The time series distances between the centers of mass of the amine group of Lys1005 (ROCK1), the carboxyl group of

Glu40 (RHOA) (A), the Asn40 carboxamide group oxygen (RHOA) (B) and the Thr40 hydroxyl group oxygen (RHOA) (C) are reported on the left. On the right, representative structures from trajectories.

Similar reasoning can be applied to the absence of noteworthy impact of the E40T mutation on RHOA binding to ROCK1. Indeed, the analysis revealed that the Thr40 residue can interact with Lys1005 through its hydroxy group sidechain, as illustrated in Figure 61C. This observation was corroborated by measuring the distance between the oxygen of the hydroxy group of the threonine and the positively charged moiety of Lys1005. As the transformation progressed, there a reduction in the distance between these particular functional groups was observed (Figure 61C). Probably, the effect of the E40L mutation may be attributed to the absence of functional groups capable of forming an electrostatic interaction with Lys1005. In relation to the impacts of F39A mutation, it is important to note that the Phe39 amino acid contributes to the creation of a hydrophobic patch between RHOA and ROCK1. The decreased binding to the effector is likely resulting from to the replacement of the phenylalanine's larger hydrophobic sidechain with the smaller alanine. In conclusion, this preliminary benchmark study underscores the efficacy of alchemical binding free energy calculations for predicting key RHOA/ROCK1 interactions and lay the foundations for further investigations on this interface, aiding to a deeper understanding of the molecular recognition process. Indeed, by adopting this strategy, the future objectives rely on the use alchemical free energy calculations to provide guidance for exploring novel mutations and new druggable interactions that can be targeted to quench the deregulated RHOA/ROCK1 signaling pathways.

Chapter 6. Conclusions and Future Perspectives

RHOGTPases, members of the RAS family, are monomeric signaling proteins with a relatively small molecular weight of approximately 21 kDa. These proteins play a crucial role in regulating cellular processes by modulating their activity through GTP to GDP binding and hydrolysis^{1-4,6,7}. The GTP-bound and GDP-bound states of RHOGTPases correspond to two distinct structural conformations, primarily differing in their switch regions. The active GTP-bound conformation is the only one with the appropriate structural arrangement to engage with effector proteins, allowing them to transmit signals downstream. Consequently, RHOGTPases can be thought of as molecular switches that alternate between two functional states: the active GTP-bound state and the inactive GDP-bound state^{1,2,10,11,13}. RHOGTPases control a broad spectrum of signal transduction pathways, thereby influencing various aspects of cellular life^{1,2,6,7,9,77}. Within the larger RHOGTPases family, the CDC42 subfamily consists of CDC42, RHOQ and RHOJ. Among these subfamily members, CDC42 and RHOJ are the most extensively studied in the context of pathology. Notably, the CDC42 proteins and PAK signaling pathway are crucial in driving cancer progression^{205,269,271,272,406,421,423-425,559,560,784}.

Due to the CDC42/PAK interaction's role in initiating downstream cascades associated with the development and progression of pathological conditions, this interaction represent an important protein-protein interface for targeted pharmacological interventions. Nevertheless, to the best of my knowledge, there are no approved drugs targeting RHOGTPases. Therefore, it is evident that novel drug design approaches are required to address CDC42/PAK signaling, specifically by disrupting the protein-protein interaction between active CDC42 and PAK proteins, a critical step in propagating the downstream activation signal. Accordingly, in this thesis efforts have been directed towards CDC42/PAK signaling exploring drug design, as well as investigating the interface. Specifically, a structure-based drug design strategy has been investigated for CDC42 and RHOJ. More specifically, a thorough analysis of a previously unappreciated putative drug-binding pocket situated at the CDC42-RHOJ-RHOQ/PAK protein-protein binding interfaces has been conducted. The analysis has been expanded to molecular

dynamics investigations, revealing that the identified effector pocket is exclusively present in the GTP-active state, whereas it is not formed in the GDP-inactive states.

Building upon the interesting outcomes from the comprehensive structural analysis performed, the study focused on identifying inhibitors for CDC42/RHOJ by exploring the new identified putative drug-binding pocket. Specifically, ARN12405 was identified as a promising compound through virtual screening and experimental tests. Molecular dynamics simulations confirmed its effective binding to the target pocket. Further research improved its properties, leading to ARN22089, which significantly exhibited broad anti-cancer activity, inhibited specific pathways and effectively hampered tumor and tumor blood vessel growth in various models, without detected off-target effects. Overall, ARN22089 emerged as a highly promising drug candidate. Subsequently, modifications were explored to synthesize and evaluate structural derivatives for CDC42/RHOJ inhibitors. ARN25062 and ARN24928 were selected as follow-up drug-like inhibitors considering their activity in cell lines, kinetic solubility, stability and binding affinity data. Molecular docking and molecular dynamics simulations confirmed their effective binding to the identified drug-binding pocket at CDC42-RHOJ/PAK protein-protein interfaces. These findings further demonstrated the potential of this novel chemical class of CDC42/RHOJ inhibitors for advanced preclinical studies in developing new cancer treatments.

In conjunction with drug design efforts, great importance has been dedicated on considering the study of protein-protein interfaces. This is essential for identifying interactions suitable for drug targeting and gaining mechanistic insights. Indeed, comprehending protein-protein interactions (PPIs) holds significant value in advancing strategies for drug design, enabling a deeper comprehension of the residues participating in the recognition mechanism. Mutagenesis is a leading experimental strategy for investigating protein-protein interactions. However, the large number of possible mutants and the laborious experimental protocols highlight the exceptional importance of computational tools capable of predicting the effects of mutations on binding affinity. Indeed, computational techniques capable of prioritizing the most relevant mutations for further experimental validation are highly valuable. In this scenario, alchemical free energy calculations⁴⁷⁰ have been used in this thesis work to assess critical residues

involved in the protein-protein recognition mechanism. Although these methods are commonly and effectively used in designing small-molecule drugs^{469–472}, their application in the context of protein–protein interactions is limited. In this thesis, one of the aims was to investigate if alchemical free energy calculations could pinpoint crucial residues, potentially suitable for drug targeting.

With available experimental data as reference⁵⁸⁸, the CDC42/PAK interface was utilized as a test case to investigate the application of alchemical free energy calculations in examining the impact of single-point mutations on protein-protein interactions. The benchmark study served as a means to quantitatively assess, evaluate, compare, and explore the method's performance utilizing existing binding affinity data related to PAK1 across 16 CDC42 mutants. The favorable correspondence between the calculated $\Delta\Delta G_{\text{binding}}$ values and experimental data strongly suggests potential integration of these methods in both research and drug design projects. Furthermore, the benchmark study emphasized the crucial role of having prior structural knowledge of the system under investigation. It highlighted that for certain mutations, like T35S and F28Y, initial disagreements between computed and experimental values could be resolved through a specific atom mapping approach. This demonstrated how substantial changes in the original interatomic interactions of the mutated residue can significantly impact alchemical free energy calculations. On the other hand, mutations Y32F and V33N revealed that in real scenarios with limited conformational sampling, the initial structure's influence on free energy estimates is remarkable. Therefore, a meticulous analysis of the conformational preferences of the mutating residues and their interactions is essential for achieving more accurate free energy estimates. The computational approach successfully evaluated the influence of single-point mutations on protein–protein complex formation, identifying essential druggable interactions. Consequently, alchemical free energy calculations have emerged as a valuable tool for the exploration of druggable interactions at protein-protein interfaces.

The same methodology was employed to investigate the interface between RHOA and ROCK1⁸⁴⁷. Undoubtedly, the CDC42/PAK is an interesting interface to study and target. Nonetheless, the RHOA/ROCK1 cascade presents another stimulating and attractive signaling pathway involving RHOGTPases, given its involvement in various

pathological conditions when deregulated^{659,661–668,670–675}. RHOA belongs to the RHOGTPases subfamily RHO, along with RHOB and RHOC^{1–4,6,10,11}. Its signaling activity is regulated by GTP binding and hydrolysis to GDP, acting as a molecular switch. GTP-bound active RHOA controls vital cellular processes and interacts with downstream effectors, including ROCK1. The RHOA/ROCK1 pathway is central for actin organization, cell migration, proliferation, cell adhesion, apoptosis, neurobiology, and vascular biology^{1,6,7,9,51,52,80,81,612}. Accordingly, abnormal RHOA/ROCK1 signaling is associated with cancer development and progression, but also linked to neurological disorders, traumatic brain injury (TBI), spinal cord injury (SCI), cardiovascular diseases, and autoimmune disorders^{657,706,721–724,726–728}. For these reasons, the RHOA/ROCK1 interface represents an appealing molecular target for potential therapeutic intervention.

Efforts have been made to suppress the RHOA/ROCK1 signaling⁷⁸⁵. However, developing specific ROCK1 inhibitors have been proven challenging due to common features in the catalytic core that it shares with other kinases, resulting in potential adverse off-target effects^{783,784}. Currently, four ROCK inhibitors (fasudil, ripasudil, netarsudil, and belumosudil) are available for clinical use, primarily for conditions like cerebral vasospasm, glaucoma, ocular hypertension and chronic graft-versus-host disease (GvHD)^{787,803,804,807–809,811–813}. In addition, these medications are under consideration for the treatment of multiple pathological conditions, including Fuchs' endothelial dystrophy, corneal edema, proliferative vitreoretinopathy (PVR) and chronic graft-versus-host disease (GVHD). Notably, while ROCK1 has been linked to cancer, clinical trials have focused on other conditions, and there are no approved ROCK inhibitors for cancer treatment. Additionally, attempts have been made to suppress RHOA activity by targeting its interaction with Guanine Nucleotide Exchange Factors (GEFs). A RHO inhibitor, called rhosin, was developed for this purpose but did not advance beyond clinical studies⁸³³. As of my last knowledge update, there are no RHOA inhibitors currently undergoing clinical trials for cancer treatment. Undoubtedly, additional research efforts are needed to develop effective therapeutics and address these unmet medical needs.

To explore the druggable interaction between RHOA and ROCK1 at their interface, a preliminary alchemical free energy calculations benchmark study has been conducted, establishing the foundation for successive novel investigations. Specifically, after

preliminary classical MD simulations, alchemical free energy calculations were utilized to assess the system's reliability, employing RHOA mutants as a control to validate future calculations. In detail, an experimental study identifying mutations disrupting RHOA binding with effectors, including ROCK1, was used as a reference⁶⁶⁸. Despite the lack of precise quantitative binding data, the $\Delta\Delta G_{\text{binding}}$ values obtained from alchemical calculations were compared with qualitative experimental results, revealing strong agreement.

This small-scale benchmark study served as a valuable preliminary investigation of the capability of alchemical binding free energy calculations in accurately predicting pivotal interactions between RHOA and ROCK1. Not only does it validate the reliability of this computational approach, but it also lays the initial foundation for further extensive and specific investigations into this interesting molecular interface. Indeed, these methodological studies on the use of alchemical free energy calculations open up to the deep exploration of RHOA/ROCK1 interface aimed to unveil mutations that could have a meaningful impact on the interactions and on the resultant signaling pathways. Indeed, this computational strategy provides a promising avenue for identifying and investigating potential druggable interactions, with the objective of effectively targeting and modulating the deregulated RHOA/ROCK1 signaling pathways. Looking ahead to future plans, the use of alchemical free energy calculations is expected to allow a deeper understanding of the molecular RHOA/ROCK1 interface, facilitating the identification of key hotspot residues and potential drug targets. Overall, this approach could be instrumental in advancing in the field and enhancing our ability to design tailored pharmaceutical interventions, optimizing results in clinical research.

Bibliography

1. Jaffe, A. B. & Hall, A. RHO GTPASES: Biochemistry and Biology. <http://dx.doi.org/10.1146/annurev.cellbio.21.020604.150721> **21**, 247–269 (2005).
2. Etienne-Manneville, S. & Hall, A. Rho GTPases in cell biology. *Nature* **2002** *420*:6916 **420**, 629–635 (2002).
3. Haga, R. B. & Ridley, A. J. Rho GTPases: Regulation and roles in cancer cell biology. *Small GTPases* **7**, 207–221 (2016).
4. Takai, Y., Sasaki, T. & Matozaki, T. Small GTP-binding proteins. *Physiol Rev* **81**, 153–208 (2001).
5. Stankiewicz, T. R. & Linseman, D. A. Rho family GTPases: key players in neuronal development, neuronal survival, and neurodegeneration. *Front Cell Neurosci* **8**, (2014).
6. Pedone, K. H. & Der, C. J. Small GTPases. *Encyclopedia of Biological Chemistry: Second Edition* 242–248 (2013) doi:10.1016/B978-0-12-378630-2.00365-0.
7. Bishop, A. L. & Hall, A. Rho GTPases and their effector proteins. *Biochemical Journal* **348**, 241 (2000).
8. Madaule, P. & Axel, R. A novel ras-related gene family. *Cell* **41**, 31–40 (1985).
9. Hall, A. Rho GTPases and the actin cytoskeleton. *Science* **279**, 509–514 (1998).
10. Paduch, M., LastNameJeleń, F. & Otlewski, J. Structure of small G proteins and their regulators. *Acta Biochim Pol* **48**, 829–850 (2001).
11. Vetter, I. R. The Structure of the G Domain of the Ras Superfamily. *Ras Superfamily Small G Proteins: Biology and Mechanisms 1: General Features, Signaling* 25–50 (2014) doi:10.1007/978-3-7091-1806-1_2.
12. Rojas, A. M., Fuentes, G., Rausell, A. & Valencia, A. The Ras protein superfamily: evolutionary tree and role of conserved amino acids. *J Cell Biol* **196**, 189–201 (2012).
13. Vetter, I. R. & Wittinghofer, A. The guanine nucleotide-binding switch in three dimensions. *Science* (1979) **294**, 1299–1304 (2001).
14. Milburn, M. V. *et al.* Molecular switch for signal transduction: structural differences between active and inactive forms of protooncogenic ras proteins. *Science* **247**, 939–945 (1990).
15. Gerwert, K., Mann, D. & Köttig, C. Common mechanisms of catalysis in small and heterotrimeric GTPases and their respective GAPs. *Biol Chem* **398**, 523–533 (2017).
16. Birnbaumer, L. & Zurita, A. R. On the roles of Mg in the activation of G proteins. *J Recept Signal Transduct Res* **30**, 372–375 (2010).
17. Pai, E. F. *et al.* Structure of the guanine-nucleotide-binding domain of the Ha-ras oncogene product p21 in the triphosphate conformation. *Nature* **1989** *341*:6239 **341**, 209–214 (1989).
18. Li, G. & Zhang, X. C. GTP hydrolysis mechanism of Ras-like GTPases. *J Mol Biol* **340**, 921–932 (2004).
19. Dreusicke, D. & Schulz, G. E. The glycine-rich loop of adenylate kinase forms a giant anion hole. *FEBS Lett* **208**, 301–304 (1986).
20. Feig, L. A. & Cooper, G. M. Inhibition of NIH 3T3 cell proliferation by a mutant ras protein with preferential affinity for GDP. *Mol Cell Biol* **8**, 3235–3243 (1988).
21. Bourne, H. R., Sanders, D. A. & McCormick, F. The GTPase superfamily: conserved structure and molecular mechanism. *Nature* **349**, 117–127 (1991).
22. Carvalho, A. T. P., Szeler, K., Vavitsas, K., Åqvist, J. & Kamerlin, S. C. L. Modeling the mechanisms of biological GTP hydrolysis. *Arch Biochem Biophys* **582**, 80–90 (2015).
23. Schlichting, I. *et al.* Time-resolved X-ray crystallographic study of the conformational change in Ha-Ras p21 protein on GTP hydrolysis. *Nature* **345**, 309–315 (1990).

24. Spoerner, M., Herrmann, C., Vetter, I. R., Kalbitzer, H. R. & Wittinghofer, A. Dynamic properties of the Ras switch I region and its importance for binding to effectors. *Proc Natl Acad Sci U S A* **98**, 4944–4949 (2001).
25. Schmidt, G. *et al.* Biochemical and biological consequences of changing the specificity of p21ras from guanosine to xanthosine nucleotides. *Oncogene* **12**, 87–96 (1996).
26. Zhong, J. M., Chen-Hwang, M. C. & Hwang, Y. W. Switching nucleotide specificity of Ha-Ras p21 by a single amino acid substitution at aspartate 119. *J Biol Chem* **270**, 10002–10007 (1995).
27. Roberts, P. J. *et al.* Rho Family GTPase modification and dependence on CAAX motif-signaled posttranslational modification. *J Biol Chem* **283**, 25150–25163 (2008).
28. Zhang, B. & Zheng, Y. Negative Regulation of Rho Family GTPases Cdc42 and Rac2 by Homodimer Formation *. *Journal of Biological Chemistry* **273**, 25728–25733 (1998).
29. Rossman, K. L., Der, C. J. & Sondek, J. GEF means go: turning on RHO GTPases with guanine nucleotide-exchange factors. *Nat Rev Mol Cell Biol* **6**, 167–180 (2005).
30. DerMardirossian, C. & Bokoch, G. M. GDIs: central regulatory molecules in Rho GTPase activation. *Trends Cell Biol* **15**, 356–363 (2005).
31. Lu, S. *et al.* Ras Conformational Ensembles, Allostery, and Signaling. *Chem Rev* **116**, 6607–6665 (2016).
32. Dias, S. M. G. & Cerione, R. A. X-ray crystal structures reveal two activated states for RhoC. *Biochemistry* **46**, 6547–6558 (2007).
33. Kumawat, A., Chakrabarty, S. & Kulkarni, K. Nucleotide Dependent Switching in Rho GTPase: Conformational Heterogeneity and Competing Molecular Interactions. *Scientific Reports 2017 7:1* **7**, 1–11 (2017).
34. Siegrist, S. E. & Doe, C. Q. Microtubule-induced cortical cell polarity. *Genes Dev* **21**, 483–496 (2007).
35. Assémat, E., Bazellères, E., Pallesi-Pocachard, E., Le Bivic, A. & Massey-Harroche, D. Polarity complex proteins. *Biochim Biophys Acta* **1778**, 614–630 (2008).
36. Stern, C. D. Evolution of the mechanisms that establish the embryonic axes. *Curr Opin Genet Dev* **16**, 413–418 (2006).
37. Arimura, N. & Kaibuchi, K. Neuronal polarity: from extracellular signals to intracellular mechanisms. *Nat Rev Neurosci* **8**, 194–205 (2007).
38. Watanabe, T., Noritake, J. & Kaibuchi, K. Regulation of microtubules in cell migration. *Trends Cell Biol* **15**, 76–83 (2005).
39. Delacour, D. & Jacob, R. Apical protein transport. *Cell Mol Life Sci* **63**, 2491–2505 (2006).
40. Krummel, M. F. & Macara, I. Maintenance and modulation of T cell polarity. *Nature Immunology 2006 7:11* **7**, 1143–1149 (2006).
41. Kemphues, K. J., Priess, J. R., Morton, D. G. & Cheng, N. Identification of genes required for cytoplasmic localization in early *C. elegans* embryos. *Cell* **52**, 311–320 (1988).
42. Tabuse, Y. *et al.* Atypical protein kinase C cooperates with PAR-3 to establish embryonic polarity in *Caenorhabditis elegans*. *Development* **125**, 3607–3614 (1998).
43. Watts, J. L. *et al.* par-6, a gene involved in the establishment of asymmetry in early *C. elegans* embryos, mediates the asymmetric localization of PAR-3. *Development* **122**, 3133–3140 (1996).
44. Etienne-Manneville, S. & Hall, A. Cell polarity: Par6, aPKC and cytoskeletal crosstalk. *Curr Opin Cell Biol* **15**, 67–72 (2003).
45. Johansson, A. S., Driessens, M. & Aspenstrom, P. The mammalian homologue of the *Caenorhabditis elegans* polarity protein PAR-6 is a binding partner for the Rho GTPases Cdc42 and Rac1. *J Cell Sci* **113 (Pt 18)**, 3267–3275 (2000).
46. Joberty, G., Petersen, C., Gao, L. & Macara, I. G. The cell-polarity protein Par6 links Par3 and atypical protein kinase C to Cdc42. *Nat Cell Biol* **2**, 531–539 (2000).

47. Garrard, S. M. *et al.* Structure of Cdc42 in a complex with the GTPase-binding domain of the cell polarity protein, Par6. *EMBO J* **22**, 1125 (2003).
48. Qiu, R. G., Abo, A. & Martin, G. S. A human homolog of the *C. elegans* polarity determinant Par-6 links Rac and Cdc42 to PKCzeta signaling and cell transformation. *Curr Biol* **10**, 697–707 (2000).
49. Yamanaka, T. *et al.* PAR-6 regulates aPKC activity in a novel way and mediates cell-cell contact-induced formation of the epithelial junctional complex. *Genes Cells* **6**, 721–731 (2001).
50. Lin, D. *et al.* A mammalian PAR-3-PAR-6 complex implicated in Cdc42/Rac1 and aPKC signalling and cell polarity. *Nat Cell Biol* **2**, 540–547 (2000).
51. Amano, M., Nakayama, M. & Kaibuchi, K. Rho-kinase/ROCK: A key regulator of the cytoskeleton and cell polarity. *Cytoskeleton (Hoboken)* **67**, 545–554 (2010).
52. Amano, M. *et al.* Formation of actin stress fibers and focal adhesions enhanced by Rho-kinase. *Science* **275**, 1308–1311 (1997).
53. Braga, V. M. M., Machesky, L. M., Hall, A. & Hotchin, N. A. The small GTPases Rho and Rac are required for the establishment of cadherin-dependent cell-cell contacts. *J Cell Biol* **137**, 1421–1431 (1997).
54. Villalonga, P., Ridley, A. J. & Verma, V. Cytoskeleton: Rho GTPases and actin cytoskeleton dynamics. *Encyclopedia of Biological Chemistry: Third Edition* **5**, 268–273 (2021).
55. Mayor, R. & Theveneau, E. The neural crest. *Development* **140**, 2247–2251 (2013).
56. Luster, A. D., Alon, R. & von Andrian, U. H. Immune cell migration in inflammation: present and future therapeutic targets. *Nature Immunology* **2005** *6*:12 **6**, 1182–1190 (2005).
57. Gilbert SF. Developmental Biology. Developmental Biology. *Development Biology: 6th edition* <http://www.ncbi.nlm.nih.gov/books/NBK10056/> (2000).
58. Torres, P., Castro, M., Reyes, M. & Torres, V. A. Histatins, wound healing, and cell migration. *Oral Dis* **24**, 1150–1160 (2018).
59. Ridley, A. J. Rho GTPase signalling in cell migration. *Curr Opin Cell Biol* **36**, 103–112 (2015).
60. Larjava, Hannu. Oral wound healing : cell biology and clinical management. 428 (2012).
61. Lauffenburger, D. A. & Horwitz, A. F. Cell migration: a physically integrated molecular process. *Cell* **84**, 359–369 (1996).
62. Hanna, S. & El-Sibai, M. Signaling networks of Rho GTPases in cell motility. *Cell Signal* **25**, 1955–1961 (2013).
63. Mattila, P. K. & Lappalainen, P. Filopodia: molecular architecture and cellular functions. *Nat Rev Mol Cell Biol* **9**, 446–454 (2008).
64. Davenport, R. W., Dou, P., Rehder, V. & Kater, S. B. A sensory role for neuronal growth cone filopodia. *Nature* **361**, 721–724 (1993).
65. Arjonen, A., Kaukonen, R. & Ivaska, J. Filopodia and adhesion in cancer cell motility. *Cell Adh Migr* **5**, 421 (2011).
66. Bornschlöggl, T. How filopodia pull: what we know about the mechanics and dynamics of filopodia. *Cytoskeleton (Hoboken)* **70**, 590–603 (2013).
67. Lammers, M., Meyer, S., Kühlmann, D. & Wittinghofer, A. Specificity of Interactions between mDia Isoforms and Rho Proteins. *J Biol Chem* **283**, 35236 (2008).
68. Kühn, S. & Geyer, M. Formins as effector proteins of Rho GTPases. *Small GTPases* **5**, (2014).
69. Mellor, H. The role of formins in filopodia formation. *Biochim Biophys Acta* **1803**, 191–200 (2010).
70. Goh, W. I. & Ahmed, S. mDia1-3 in mammalian filopodia. *Commun Integr Biol* **5**, 340 (2012).
71. Condeelis, J. How is actin polymerization nucleated in vivo? *Trends Cell Biol* **11**, 288–293 (2001).
72. Mejillano, M. R. *et al.* Lamellipodial versus filopodial mode of the actin nanomachinery: Pivotal role of the filament barbed end. *Cell* **118**, 363–373 (2004).

73. Price, L. S., Leng, J., Schwartz, M. A. & Bokoch, G. M. Activation of Rac and Cdc42 by integrins mediates cell spreading. *Mol Biol Cell* **9**, 1863–1871 (1998).
74. Wu, C. Focal adhesion: a focal point in current cell biology and molecular medicine. *Cell Adh Migr* **1**, 13–18 (2007).
75. Burridge, K. & Wennerberg, K. Rho and Rac Take Center Stage. *Cell* **116**, 167–179 (2004).
76. Bershadsky, A. D. *et al.* Assembly and mechanosensory function of focal adhesions: experiments and models. *Eur J Cell Biol* **85**, 165–173 (2006).
77. Hall, A. Rho GTPases and the control of cell behaviour. *Biochem Soc Trans* **33**, 891–895 (2005).
78. Leung, T., Chen, X.-Q., Tan, I., Manser, E. & Lim, L. Myotonic dystrophy kinase-related Cdc42-binding kinase acts as a Cdc42 effector in promoting cytoskeletal reorganization. *Mol Cell Biol* **18**, 130–140 (1998).
79. Wilkinson, S., Paterson, H. F. & Marshall, C. J. Cdc42-MRCK and Rho-ROCK signalling cooperate in myosin phosphorylation and cell invasion. *Nat Cell Biol* **7**, 255–261 (2005).
80. Riento, K. & Ridley, A. J. Rocks: multifunctional kinases in cell behaviour. *Nat Rev Mol Cell Biol* **4**, 446–456 (2003).
81. Julian, L. & Olson, M. F. Rho-associated coiled-coil containing kinases (ROCK): Structure, regulation, and functions. *Small GTPases* **5**, (2014).
82. Zhao, Z. & Manser, E. Myotonic dystrophy kinase-related Cdc42-binding kinases (MRCK), the ROCK-like effectors of Cdc42 and Rac1. *Small GTPases* **6**, 81 (2015).
83. Palecek, S. P., Huttenlocher, A., Horwitz, A. F. & Lauffenburger, D. A. Physical and biochemical regulation of integrin release during rear detachment of migrating cells. *J Cell Sci* **111** (Pt 7), 929–940 (1998).
84. Kurokawa, K. & Matsuda, M. Localized RhoA activation as a requirement for the induction of membrane ruffling. *Mol Biol Cell* **16**, 4294–4303 (2005).
85. Bolado-Carrancio, A. *et al.* Periodic propagating waves coordinate RhoGTPase network dynamics at the leading and trailing edges during cell migration. *Elife* **9**, 1–34 (2020).
86. Wilson, E. *et al.* RhoJ interacts with the GIT-PIX complex and regulates focal adhesion disassembly. *J Cell Sci* **127**, 3039–3051 (2014).
87. Kaur, S. *et al.* RhoJ/TCL regulates endothelial motility and tube formation and modulates actomyosin contractility and focal adhesion numbers. *Arterioscler Thromb Vasc Biol* **31**, 657–664 (2011).
88. Gad, A. K. B., Nehru, V., Ruusala, A. & Aspenström, P. RhoD regulates cytoskeletal dynamics via the actin nucleation-promoting factor WASp homologue associated with actin Golgi membranes and microtubules. *Mol Biol Cell* **23**, 4807–4819 (2012).
89. Troeger, A. & Williams, D. A. Hematopoietic-specific Rho GTPases Rac2 and RhoH and human blood disorders. *Exp Cell Res* **319**, 2375 (2013).
90. Fukata, Y., Kaibuchi, K., Amano, M. & Kaibuchi, K. Rho-Rho-kinase pathway in smooth muscle contraction and cytoskeletal reorganization of non-muscle cells. *Trends Pharmacol Sci* **22**, 32–39 (2001).
91. Sakurada, S., Okamoto, H., Takuwa, N., Sugimoto, N. & Takuwa, Y. Rho activation in excitatory agonist-stimulated vascular smooth muscle. *Am J Physiol Cell Physiol* **281**, (2001).
92. Uehata, M. *et al.* Calcium sensitization of smooth muscle mediated by a Rho-associated protein kinase in hypertension. *Nature* **389**, 990–994 (1997).
93. Olson, M. F., Ashworth, A. & Hall, A. An essential role for Rho, Rac, and Cdc42 GTPases in cell cycle progression through G1. *Science* **269**, 1270–1272 (1995).
94. Olson, M. F., Paterson, H. F. & Marshall, C. J. Signals from Ras and Rho GTPases interact to regulate expression of p21Waf1/Cip1. *Nature* **394**, 295–299 (1998).

95. Luo, L., Joyce Liao, Y., Jan, L. Y. & Jan, Y. N. Distinct morphogenetic functions of similar small GTPases: *Drosophila* Drac1 is involved in axonal outgrowth and myoblast fusion. *Genes Dev* **8**, 1787–1802 (1994).
96. Rosenblatt, J., Cramer, L. P., Baum, B. & McGee, K. M. Myosin II-dependent cortical movement is required for centrosome separation and positioning during mitotic spindle assembly. *Cell* **117**, 361–372 (2004).
97. Yasuda, S. *et al.* Cdc42 and mDia3 regulate microtubule attachment to kinetochores. *Nature* **428**, 767–771 (2004).
98. Zheng, J. *et al.* p21-activated kinase 6 controls mitosis and hepatocellular carcinoma progression by regulating Eg5. *Biochim Biophys Acta Mol Cell Res* **1868**, (2021).
99. Yu, W. X. *et al.* Kinesin-5 Eg5 is essential for spindle assembly, chromosome stability and organogenesis in development. *Cell Death Discovery* **2022 8:1 8**, 1–14 (2022).
100. She, Z. Y. *et al.* Kinesin-5 Eg5 is essential for spindle assembly and chromosome alignment of mouse spermatocytes. *Cell Div* **15**, 1–18 (2020).
101. Drechsel, D. N., Hyman, A. A., Hall, A. & Glotzer, M. A requirement for Rho and Cdc42 during cytokinesis in *Xenopus* embryos. *Curr Biol* **7**, 12–23 (1997).
102. Kosako, H. *et al.* Rho-kinase/ROCK is involved in cytokinesis through the phosphorylation of myosin light chain and not ezrin/radixin/moesin proteins at the cleavage furrow. *Oncogene* **19**, 6059–6064 (2000).
103. Yasui, Y. *et al.* Roles of Rho-associated kinase in cytokinesis; mutations in Rho-associated kinase phosphorylation sites impair cytokinetic segregation of glial filaments. *J Cell Biol* **143**, 1249–1258 (1998).
104. Piekny, A. J. & Mains, P. E. Rho-binding kinase (LET-502) and myosin phosphatase (MEL-11) regulate cytokinesis in the early *Caenorhabditis elegans* embryo. *J Cell Sci* **115**, 2271–2282 (2002).
105. Glotzer, M. Animal cell cytokinesis. *Annu Rev Cell Dev Biol* **17**, 351–386 (2001).
106. Stowers, L., Yelon, D., Berg, L. J. & Chant, J. Regulation of the polarization of T cells toward antigen-presenting cells by Ras-related GTPase CDC42. *Proc Natl Acad Sci U S A* **92**, 5027–5031 (1995).
107. Chiang, S. H. *et al.* Insulin-stimulated GLUT4 translocation requires the CAP-dependent activation of TC10. *Nature* **410**, 944–948 (2001).
108. Brown, A. M., O’Sullivan, A. J. & Gomperts, B. D. Induction of exocytosis from permeabilized mast cells by the guanosine triphosphatases Rac and Cdc42. *Mol Biol Cell* **9**, 1053–1063 (1998).
109. Caron, E. & Hall, A. Identification of two distinct mechanisms of phagocytosis controlled by different Rho GTPases. *Science* **282**, 1717–1721 (1998).
110. Komuro, R., Sasaki, T., Takaishi, K., Orita, S. & Takai, Y. Involvement of Rho and Rac small G proteins and Rho GDI in Ca²⁺-dependent exocytosis from PC12 cells. *Genes Cells* **1**, 943–951 (1996).
111. Lamaze, C., Chuang, T. H., Terlecky, L. J., Bokoch, G. M. & Schmid, S. L. Regulation of receptor-mediated endocytosis by Rho and Rac. *Nature* **382**, 177–179 (1996).
112. Perona, R. *et al.* Activation of the nuclear factor-kappaB by Rho, CDC42, and Rac-1 proteins. *Genes Dev* **11**, 463–475 (1997).
113. Sulciner, D. J. *et al.* rac1 regulates a cytokine-stimulated, redox-dependent pathway necessary for NF-kappaB activation. *Mol Cell Biol* **16**, 7115–7121 (1996).
114. Miralles, F., Posern, G., Zaromytidou, A. I. & Treisman, R. Actin dynamics control SRF activity by regulation of its coactivator MAL. *Cell* **113**, 329–342 (2003).
115. Hill, C. S., Wynne, J. & Treisman, R. The Rho family GTPases RhoA, Rac1, and CDC42Hs regulate transcriptional activation by SRF. *Cell* **81**, 1159–1170 (1995).
116. Coso, O. A. *et al.* The small GTP-binding proteins Rac1 and Cdc42 regulate the activity of the JNK/SAPK signaling pathway. *Cell* **81**, 1137–1146 (1995).

117. Minden, A., Lin, A., Claret, F. X., Abo, A. & Karin, M. Selective activation of the JNK signaling cascade and c-Jun transcriptional activity by the small GTPases Rac and Cdc42Hs. *Cell* **81**, 1147–1157 (1995).
118. Weernink, P. A. O. *et al.* Activation of type I phosphatidylinositol 4-phosphate 5-kinase isoforms by the Rho GTPases, RhoA, Rac1, and Cdc42. *J Biol Chem* **279**, 7840–7849 (2004).
119. Zheng, Y., Bagrodia, S. & Cerione, R. A. Activation of phosphoinositide 3-kinase activity by Cdc42Hs binding to p85. *Journal of Biological Chemistry* **269**, 18727–18730 (1994).
120. Houssa, B., De Widt, J., Kranenburg, O., Moolenaar, W. H. & Van Blitterswijk, W. J. Diacylglycerol kinase theta binds to and is negatively regulated by active RhoA. *J Biol Chem* **274**, 6820–6822 (1999).
121. Hess, J. A., Ross, A. H., Qiu, R. G., Symons, M. & Exton, J. H. Role of Rho family proteins in phospholipase D activation by growth factors. *J Biol Chem* **272**, 1615–1620 (1997).
122. Hirose, M. *et al.* Molecular dissection of the Rho-associated protein kinase (p160ROCK)-regulated neurite remodeling in neuroblastoma N1E-115 cells. *J Cell Biol* **141**, 1625–1636 (1998).
123. Jalink, K. *et al.* Inhibition of lysophosphatidate- and thrombin-induced neurite retraction and neuronal cell rounding by ADP ribosylation of the small GTP-binding protein Rho. *J Cell Biol* **126**, 801–810 (1994).
124. R, K., S, S., S, A. & L, L. Rho family GTPases and neuronal growth cone remodelling: relationship between increased complexity induced by Cdc42Hs, Rac1, and acetylcholine and collapse induced by RhoA and lysophosphatidic acid. *Mol Cell Biol* **17**, 1201–1211 (1997).
125. Nicole, S. *et al.* The human CDC42 gene: genomic organization, evidence for the existence of a putative pseudogene and exclusion as a SJS1 candidate gene. *Hum Genet* **105**, 98–103 (1999).
126. Richman, T. J., Sawyer, M. M. & Johnson, D. I. *Saccharomyces cerevisiae* Cdc42p Localizes to Cellular Membranes and Clusters at Sites of Polarized Growth. *Eukaryot Cell* **1**, 458 (2002).
127. Johnson, D. I. & Pringle, J. R. Molecular characterization of CDC42, a *Saccharomyces cerevisiae* gene involved in the development of cell polarity. *J Cell Biol* **111**, 143–152 (1990).
128. Drubin, D. G. Development of cell polarity in budding yeast. *Cell* **65**, 1093–1096 (1991).
129. Gotta, M., Abraham, M. C. & Ahringer, J. CDC-42 controls early cell polarity and spindle orientation in *C. elegans*. *Curr Biol* **11**, 482–488 (2001).
130. Kay, A. J. & Hunter, C. P. CDC-42 regulates PAR protein localization and function to control cellular and embryonic polarity in *C. elegans*. *Curr Biol* **11**, 474–481 (2001).
131. Murphy, A. M. & Montell, D. J. Cell type-specific roles for Cdc42, Rac, and RhoL in *Drosophila* oogenesis. *J Cell Biol* **133**, 617–630 (1996).
132. Shinjo, K. *et al.* Molecular cloning of the gene for the human placental GTP-binding protein Gp (G25K): identification of this GTP-binding protein as the human homolog of the yeast cell-division-cycle protein CDC42. *Proc Natl Acad Sci U S A* **87**, 9853–9857 (1990).
133. St Johnston, D. & Ahringer, J. Cell polarity in eggs and epithelia: parallels and diversity. *Cell* **141**, 757–774 (2010).
134. Butcher, E. C. & Picker, L. J. Lymphocyte homing and homeostasis. *Science* **272**, 60–66 (1996).
135. Pruyne, D., Legesse-Miller, A., Gao, L., Dong, Y. & Bretscher, A. Mechanisms of polarized growth and organelle segregation in yeast. *Annu Rev Cell Dev Biol* **20**, 559–591 (2004).
136. Joberty, G., Petersen, C., Gao, L. & Macara, I. G. The cell-polarity protein Par6 links Par3 and atypical protein kinase C to Cdc42. *Nat Cell Biol* **2**, 531–539 (2000).
137. Kemphues, K. PARsing embryonic polarity. *Cell* **101**, 345–348 (2000).
138. Sulston, J. E., Schierenberg, E., White, J. G. & Thomson, J. N. The embryonic cell lineage of the nematode *Caenorhabditis elegans*. *Dev Biol* **100**, 64–119 (1983).
139. Hung, T. J. & Kemphues, K. J. PAR-6 is a conserved PDZ domain-containing protein that colocalizes with PAR-3 in *Caenorhabditis elegans* embryos. *Development* **126**, 127–135 (1999).

140. Melendez, J., Grogg, M. & Zheng, Y. Signaling Role of Cdc42 in Regulating Mammalian Physiology. *J Biol Chem* **286**, 2375 (2011).
141. Peterson, F. C., Penkert, R. R., Volkman, B. F. & Prehoda, K. E. Cdc42 regulates the Par-6 PDZ domain through an allosteric CRIB-PDZ transition. *Mol Cell* **13**, 665–676 (2004).
142. Hong, Y. aPKC: The Kinase that Phosphorylates Cell Polarity [version 1; referees: 2 approved]. *F1000Res* **7**, (2018).
143. Plant, P. J. *et al.* A polarity complex of mPar-6 and atypical PKC binds, phosphorylates and regulates mammalian Lgl. *Nat Cell Biol* **5**, 301–308 (2003).
144. Yamanaka, T. *et al.* Mammalian Lgl forms a protein complex with PAR-6 and aPKC independently of PAR-3 to regulate epithelial cell polarity. *Curr Biol* **13**, 734–743 (2003).
145. Suzuki, A. *et al.* Atypical protein kinase C is involved in the evolutionarily conserved par protein complex and plays a critical role in establishing epithelia-specific junctional structures. *J Cell Biol* **152**, 1183–1196 (2001).
146. Etienne-Manneville, S. Cdc42--the centre of polarity. *J Cell Sci* **117**, 1291–1300 (2004).
147. Kurn, H. & Daly, D. T. Histology, Epithelial Cell. *StatPearls* (2023).
148. Rodriguez-Boulan, E. & Macara, I. G. Organization and execution of the epithelial polarity programme. *Nat Rev Mol Cell Biol* **15**, 225–242 (2014).
149. Bryant, D. M. & Mostov, K. E. From cells to organs: building polarized tissue. *Nat Rev Mol Cell Biol* **9**, 887–901 (2008).
150. Jaffe, A. B., Kaji, N., Durgan, J. & Hall, A. Cdc42 controls spindle orientation to position the apical surface during epithelial morphogenesis. *J Cell Biol* **183**, 625–633 (2008).
151. Buckley, C. E. & St Johnston, D. Apical-basal polarity and the control of epithelial form and function. *Nat Rev Mol Cell Biol* **23**, 559–577 (2022).
152. Kesavan, G. *et al.* Cdc42-mediated tubulogenesis controls cell specification. *Cell* **139**, 791–801 (2009).
153. Wu, X., Quondamatteo, F. & Brakebusch, C. Cdc42 expression in keratinocytes is required for the maintenance of the basement membrane in skin. *Matrix Biol* **25**, 466–474 (2006).
154. Cappello, S. *et al.* The Rho-GTPase cdc42 regulates neural progenitor fate at the apical surface. *Nat Neurosci* **9**, 1099–1107 (2006).
155. Chen, L. *et al.* Cdc42 deficiency causes Sonic hedgehog-independent holoprosencephaly. *Proc Natl Acad Sci U S A* **103**, 16520–16525 (2006).
156. Vicente-Manzanares, M. & Horwitz, A. R. Cell migration: an overview. *Methods Mol Biol* **769**, 1–24 (2011).
157. Ridley, A. J. *et al.* Cell migration: integrating signals from front to back. *Science* **302**, 1704–1709 (2003).
158. de Lucas, B., Pérez, L. M. & Gálvez, B. G. Importance and regulation of adult stem cell migration. *J Cell Mol Med* **22**, 746–754 (2018).
159. Horwitz, R. & Webb, D. Cell migration. *Curr Biol* **13**, (2003).
160. Tackenberg, H., Möller, S., Filippi, M. D. & Laskay, T. The Small GTPase Cdc42 Is a Major Regulator of Neutrophil Effector Functions. *Front Immunol* **11**, (2020).
161. Yang, L., Wang, L. & Zheng, Y. Gene targeting of Cdc42 and Cdc42GAP affirms the critical involvement of Cdc42 in filopodia induction, directed migration, and proliferation in primary mouse embryonic fibroblasts. *Mol Biol Cell* **17**, 4675–4685 (2006).
162. Nobes, C. D. & Hall, A. Rho, rac, and cdc42 GTPases regulate the assembly of multimolecular focal complexes associated with actin stress fibers, lamellipodia, and filopodia. *Cell* **81**, 53–62 (1995).
163. Symons, M. *et al.* Wiskott-Aldrich syndrome protein, a novel effector for the GTPase CDC42Hs, is implicated in actin polymerization. *Cell* **84**, 723–734 (1996).

164. Fu, J. *et al.* The role of cell division control protein 42 in tumor and non-tumor diseases: A systematic review. *J Cancer* **13**, 800 (2022).
165. Machesky, L. M. & Insall, R. H. Signaling to Actin Dynamics. *Journal of Cell Biology* **146**, 267–272 (1999).
166. Machesky, L. M. & Insall, R. H. Scar1 and the related Wiskott-Aldrich syndrome protein, WASP, regulate the actin cytoskeleton through the Arp2/3 complex. *Curr Biol* **8**, 1347–1356 (1998).
167. Ma, L., Rohatgi, R. & Kirschner, M. W. The Arp2/3 complex mediates actin polymerization induced by the small GTP-binding protein Cdc42. *Proc Natl Acad Sci U S A* **95**, 15362–15367 (1998).
168. Rohatgi, R. *et al.* The interaction between N-WASP and the Arp2/3 complex links Cdc42-dependent signals to actin assembly. *Cell* **97**, 221–231 (1999).
169. Erickson, J. W. & Cerione, R. A. Multiple roles for Cdc42 in cell regulation. *Curr Opin Cell Biol* **13**, 153–157 (2001).
170. Kim, A. S., Kakalis, L. T., Abdul-Manan, N., Liu, G. A. & Rosen, M. K. Autoinhibition and activation mechanisms of the Wiskott-Aldrich syndrome protein. *Nature* **404**, 151–158 (2000).
171. Cory, G. O. C., Cramer, R., Blanchoin, L. & Ridley, A. J. Phosphorylation of the WASP-VCA domain increases its affinity for the Arp2/3 complex and enhances actin polymerization by WASP. *Mol Cell Biol* **11**, 1229–1239 (2003).
172. Beli, P., Mascheroni, D., Xu, D. & Innocenti, M. WAVE and Arp2/3 jointly inhibit filopodium formation by entering into a complex with mDia2. *Nat Cell Biol* **10**, 849–857 (2008).
173. Kast, D. J. *et al.* Mechanism of IRSp53 inhibition and combinatorial activation by Cdc42 and downstream effectors. *Nat Struct Mol Biol* **21**, 413–422 (2014).
174. Krugmann, S. *et al.* Cdc42 induces filopodia by promoting the formation of an IRSp53:Mena complex. *Curr Biol* **11**, 1645–1655 (2001).
175. Goh, W. I. *et al.* mDia1 and WAVE2 Proteins Interact Directly with IRSp53 in Filopodia and Are Involved in Filopodium Formation. *J Biol Chem* **287**, 4702 (2012).
176. Chauhan, B. K. *et al.* Cdc42- and IRSp53-dependent contractile filopodia tether presumptive lens and retina to coordinate epithelial invagination. *Development* **136**, 3657–3667 (2009).
177. Sells, M. A. *et al.* Human p21-activated kinase (Pak1) regulates actin organization in mammalian cells. *Curr Biol* **7**, 202–210 (1997).
178. Abo, A. *et al.* PAK4, a novel effector for Cdc42Hs, is implicated in the reorganization of the actin cytoskeleton and in the formation of filopodia. *EMBO J* **17**, 6527–6540 (1998).
179. Edwards, D. C., Sanders, L. C., Bokoch, G. M. & Gill, G. N. Activation of LIM-kinase by Pak1 couples Rac/Cdc42 GTPase signalling to actin cytoskeletal dynamics. *Nat Cell Biol* **1**, 253–259 (1999).
180. Salminen, A., Suuronen, T. & Kaarniranta, K. ROCK, PAK, and Toll of synapses in Alzheimer's disease. *Biochem Biophys Res Commun* **371**, 587–590 (2008).
181. Dan, C., Nath, N., Liberto, M. & Minden, A. PAK5, a New Brain-Specific Kinase, Promotes Neurite Outgrowth in N1E-115 Cells. *Mol Cell Biol* **22**, 567 (2002).
182. Lämmermann, T. *et al.* Cdc42-dependent leading edge coordination is essential for interstitial dendritic cell migration. *Blood* **113**, 5703–5710 (2009).
183. Szczur, K., Zheng, Y. & Filippi, M. D. The small Rho GTPase Cdc42 regulates neutrophil polarity via CD11b integrin signaling. *Blood* **114**, 4527–4537 (2009).
184. Maître, J. L. & Heisenberg, C. P. Three Functions of Cadherins in Cell Adhesion. *Current Biology* **23**, R626 (2013).
185. Fukataf, M. *et al.* Regulation of cross-linking of actin filament by IQGAP1, a target for Cdc42. *J Biol Chem* **272**, 29579–29583 (1997).
186. Briggs, M. W. & Sacks, D. B. IQGAP proteins are integral components of cytoskeletal regulation. *EMBO Rep* **4**, 571 (2003).

187. Kuroda, S. *et al.* Role of IQGAP1, a target of the small GTPases Cdc42 and Rac1, in regulation of E-cadherin-mediated cell-cell adhesion. *Science* **281**, 832–835 (1998).
188. Fukata, M. *et al.* Cdc42 and Rac1 regulate the interaction of IQGAP1 with beta-catenin. *J Biol Chem* **274**, 26044–26050 (1999).
189. Aberle, H. *et al.* Assembly of the cadherin-catenin complex in vitro with recombinant proteins. *J Cell Sci* **107 (Pt 12)**, 3655–3663 (1994).
190. Kaibuchi, K., Kuroda, S., Fukata, M. & Nakagawa, M. Regulation of cadherin-mediated cell-cell adhesion by the Rho family GTPases. *Curr Opin Cell Biol* **11**, 591–596 (1999).
191. Kuroda, S. *et al.* Regulation of cell-cell adhesion of MDCK cells by Cdc42 and Rac1 small GTPases. *Biochem Biophys Res Commun* **240**, 430–435 (1997).
192. Manser, E. *et al.* Expression of constitutively active alpha-PAK reveals effects of the kinase on actin and focal complexes. *Mol Cell Biol* **17**, 1129–1143 (1997).
193. Qu, J. *et al.* Activated PAK4 regulates cell adhesion and anchorage-independent growth. *Mol Cell Biol* **21**, 3523–3533 (2001).
194. van Hengel, J. *et al.* Continuous cell injury promotes hepatic tumorigenesis in cdc42-deficient mouse liver. *Gastroenterology* **134**, 781–792 (2008).
195. Yang, L. *et al.* Rho GTPase Cdc42 coordinates hematopoietic stem cell quiescence and niche interaction in the bone marrow. *Proc Natl Acad Sci U S A* **104**, 5091 (2007).
196. Wang, L., Yang, L., Filippi, M. D., Williams, D. A. & Zheng, Y. Genetic deletion of Cdc42GAP reveals a role of Cdc42 in erythropoiesis and hematopoietic stem/progenitor cell survival, adhesion, and engraftment. *Blood* **107**, 98–105 (2006).
197. Johnson, D. I. Cdc42: An essential Rho-type GTPase controlling eukaryotic cell polarity. *Microbiol Mol Biol Rev* **63**, 54–105 (1999).
198. Palazzo, A. F. *et al.* Cdc42, dynein, and dynactin regulate MTOC reorientation independent of Rho-regulated microtubule stabilization. *Curr Biol* **11**, 1536–1541 (2001).
199. Prosser, S. L. & Pelletier, L. Mitotic spindle assembly in animal cells: a fine balancing act. *Nat Rev Mol Cell Biol* **18**, 187–201 (2017).
200. Scholey, J. M., Brust-Mascher, I. & Mogilner, A. Cell division. *Nature* **422**, 746–752 (2003).
201. Cleveland, D. W., Mao, Y. & Sullivan, K. F. Centromeres and kinetochores: From epigenetics to mitotic checkpoint signaling. *Cell* **112**, 407–421 (2003).
202. Tanaka, T. U. Chromosome bi-orientation on the mitotic spindle. *Philos Trans R Soc Lond B Biol Sci* **360**, 581–589 (2005).
203. Ocegueda-Yanez, F. *et al.* Ect2 and MgcRacGAP regulate the activation and function of Cdc42 in mitosis. *J Cell Biol* **168**, 221 (2005).
204. Maroto, B., Ye, M. B., Von Lohneysen, K., Schnelzer, A. & Knaus, U. G. P21-activated kinase is required for mitotic progression and regulates Plk1. *Oncogene* **27**, 4900–4908 (2008).
205. Molli, P. R., Li, D. Q., Murray, B. W., Rayala, S. K. & Kumar, R. PAK signaling in oncogenesis. *Oncogene* **28**, 2545–2555 (2009).
206. Zhao, Z. S., Lim, J. P., Ng, Y. W., Lim, L. & Manser, E. The GIT-associated kinase PAK targets to the centrosome and regulates Aurora-A. *Mol Cell* **20**, 237–249 (2005).
207. Korobeynikov, V. *et al.* Combined inhibition of Aurora A and p21-activated kinase 1 as a new treatment strategy in breast cancer. *Breast Cancer Res Treat* **177**, 369–382 (2019).
208. Bauerfeld, C. P., Hershenson, M. B. & Page, K. Cdc42, but not RhoA, regulates cyclin D1 expression in bovine tracheal myocytes. *Am J Physiol Lung Cell Mol Physiol* **280**, (2001).
209. Chou, M. M., Masuda-Robens, J. M. & Gupta, M. L. Cdc42 promotes G1 progression through p70 S6 kinase-mediated induction of cyclin E expression. *J Biol Chem* **278**, 35241–35247 (2003).
210. Ito, Y. *et al.* Cdc42 regulates bone modeling and remodeling in mice by modulating RANKL/M-CSF signaling and osteoclast polarization. *J Clin Invest* **120**, 1981–1993 (2010).

211. Lee, Y. D. *et al.* The dynactin subunit DCTN1 controls osteoclastogenesis via the Cdc42/PAK2 pathway. *Exp Mol Med* **52**, 514–528 (2020).
212. Dharmawardhane, S., Sanders, L. C., Martin, S. S., Daniels, R. H. & Bokoch, G. M. Localization of p21-activated kinase 1 (PAK1) to pinocytotic vesicles and cortical actin structures in stimulated cells. *J Cell Biol* **138**, 1265–1278 (1997).
213. Bryant, D. M. *et al.* A molecular network for de novo generation of the apical surface and lumen. *Nat Cell Biol* **12**, 1035–1045 (2010).
214. Farhan, H. & Hsu, V. W. Cdc42 and cellular polarity: Emerging roles at the Golgi. *Trends Cell Biol* **26**, 241 (2016).
215. Müsch, A., Cohen, D., Kreitzer, G. & Rodriguez-Boulan, E. cdc42 regulates the exit of apical and basolateral proteins from the trans-Golgi network. *EMBO J* **20**, 2171 (2001).
216. Garrett, W. S. *et al.* Developmental control of endocytosis in dendritic cells by Cdc42. *Cell* **102**, 325–334 (2000).
217. Norman, J. C., Price, L. S., Ridley, A. J. & Koffer, A. The small GTP-binding proteins, Rac and Rho, regulate cytoskeletal organization and exocytosis in mast cells by parallel pathways. *Mol Biol Cell* **7**, 1429 (1996).
218. Wu, W. J., Erickson, J. W., Lin, R. & Cerione, R. A. The gamma-subunit of the coatamer complex binds Cdc42 to mediate transformation. *Nature* **405**, 800–804 (2000).
219. Olson, E. N. & Nordheim, A. Linking actin dynamics and gene transcription to drive cellular motile functions. *Nat Rev Mol Cell Biol* **11**, 353–365 (2010).
220. Oeckinghaus, A. & Ghosh, S. The NF-kappaB family of transcription factors and its regulation. *Cold Spring Harb Perspect Biol* **1**, (2009).
221. Fanger, G. R., Johnson, N. L. & Johnson, G. L. MEK kinases are regulated by EGF and selectively interact with Rac/Cdc42. *EMBO J* **16**, 4961 (1997).
222. Nagata, K. I. *et al.* The MAP kinase kinase kinase MLK2 co-localizes with activated JNK along microtubules and associates with kinesin superfamily motor KIF3. *EMBO J* **17**, 149 (1998).
223. Park, E. R., Eblen, S. T. & Catling, A. D. MEK1 activation by PAK: A novel mechanism. *Cell Signal* **19**, 1488 (2007).
224. Maillet, M. *et al.* Cdc42 is an antihypertrophic molecular switch in the mouse heart. *J Clin Invest* **119**, 3079–3088 (2009).
225. Carè, A. *et al.* MicroRNA-133 controls cardiac hypertrophy. *Nat Med* **13**, 613–618 (2007).
226. Yuan, H. *et al.* Hepatocyte-specific deletion of Cdc42 results in delayed liver regeneration after partial hepatectomy in mice. *Hepatology* **49**, 240–249 (2009).
227. Drivas, G. T., Shih, A., Coutavas, E., Rush, M. G. & D'Eustachio, P. Characterization of four novel ras-like genes expressed in a human teratocarcinoma cell line. *Mol Cell Biol* **10**, 1793–1798 (1990).
228. Neudauer, C. L., Joberty, G., Tatsis, N. & Macara, I. G. Distinct cellular effects and interactions of the Rho-family GTPase TC10. *Curr Biol* **8**, 1151–1161 (1998).
229. Joberty, G., Perlungher, R. R. & Macara, I. G. The Borgs, a new family of Cdc42 and TC10 GTPase-interacting proteins. *Mol Cell Biol* **19**, 6585–6597 (1999).
230. Murphy, G. A. *et al.* Cellular functions of TC10, a Rho family GTPase: regulation of morphology, signal transduction and cell growth. *Oncogene* **18**, 3831–3845 (1999).
231. Tanabe, K. *et al.* The small GTP-binding protein TC10 promotes nerve elongation in neuronal cells, and its expression is induced during nerve regeneration in rats. *J Neurosci* **20**, 4138–4144 (2000).
232. Abe, T., Kato, M., Miki, H., Takenawa, T. & Endo, T. Small GTPase Tc10 and its homologue RhoT induce N-WASP-mediated long process formation and neurite outgrowth. *J Cell Sci* **116**, 155–168 (2003).
233. Kawase, K. *et al.* GTP Hydrolysis by the Rho Family GTPase TC10 Promotes Exocytic Vesicle Fusion. *Dev Cell* **11**, 411–421 (2006).

234. Cheng, J., Wang, H. & Guggino, W. B. Regulation of cystic fibrosis transmembrane regulator trafficking and protein expression by a Rho family small GTPase TC10. *J Biol Chem* **280**, 3731–3739 (2005).
235. Vignal, E. *et al.* Characterization of TCL, a new GTPase of the rho family related to TC10 and Cdc42. *J Biol Chem* **275**, 36457–36464 (2000).
236. De Toledo, M. *et al.* The GTP/GDP cycling of rho GTPase TCL is an essential regulator of the early endocytic pathway. *Mol Biol Cell* **14**, 4846–4856 (2003).
237. Nishizuka, M., Arimoto, E., Tsuchiya, T., Nishihara, T. & Imagawa, M. Crucial role of TCL/TC10beta L, a subfamily of Rho GTPase, in adipocyte differentiation. *J Biol Chem* **278**, 15279–15284 (2003).
238. Kawaji, A., Nishizuka, M., Osada, S. & Imagawa, M. TC10-like/TC10betaLong regulates adipogenesis by controlling mitotic clonal expansion. *Biol Pharm Bull* **33**, 404–409 (2010).
239. Bryan, B. A. & D'Amore, P. A. What tangled webs they weave: Rho-GTPase control of angiogenesis. *Cell Mol Life Sci* **64**, 2053–2065 (2007).
240. Leszczynska, K., Kaur, S., Wilson, E., Bicknell, R. & Heath, V. L. The role of RhoJ in endothelial cell biology and angiogenesis. *Biochem Soc Trans* **39**, 1606–1611 (2011).
241. Fukushima, Y. *et al.* Sema3E-PlexinD1 signaling selectively suppresses disoriented angiogenesis in ischemic retinopathy in mice. *J Clin Invest* **121**, 1974–1985 (2011).
242. Yuan, L. *et al.* RhoJ is an endothelial cell-restricted Rho GTPase that mediates vascular morphogenesis and is regulated by the transcription factor ERG. *Blood* **118**, 1145–1153 (2011).
243. Chung, A. S. & Ferrara, N. Developmental and pathological angiogenesis. *Annu Rev Cell Dev Biol* **27**, 563–584 (2011).
244. Kaur, S. *et al.* RhoJ/TCL regulates endothelial motility and tube formation and modulates actomyosin contractility and focal adhesion numbers. *Arterioscler Thromb Vasc Biol* **31**, 657–664 (2011).
245. Premont, R. T. *et al.* The GIT/PIX complex: An oligomeric assembly of GIT family ARF GTPase-activating proteins and PIX family Rac1/Cdc42 guanine nucleotide exchange factors. *Cell Signal* **16**, 1001–1011 (2004).
246. Bishop, E. T. *et al.* An in vitro model of angiogenesis: basic features. *Angiogenesis* **3**, 335–344 (1999).
247. Manser, E., Leung, T., Salihuddin, H., Zhao, Z. S. & Lim, L. A brain serine/threonine protein kinase activated by Cdc42 and Rac1. *Nature* **367**, 40–46 (1994).
248. Burbelo, P. D., Drechsel, D. & Hall, A. A conserved binding motif defines numerous candidate target proteins for both Cdc42 and Rac GTPases. *J Biol Chem* **270**, 29071–29074 (1995).
249. Lei, M. *et al.* Structure of PAK1 in an autoinhibited conformation reveals a multistage activation switch. *Cell* **102**, 387–397 (2000).
250. Parrini, M. C., Lei, M., Harrison, S. C. & Mayer, B. J. Pak1 Kinase Homodimers Are Autoinhibited in trans and Dissociated upon Activation by Cdc42 and Rac1. *Mol Cell* **9**, 73–83 (2002).
251. Combeau, G. *et al.* The p21-activated kinase PAK3 forms heterodimers with PAK1 in brain implementing trans-regulation of PAK3 activity. *J Biol Chem* **287**, 30084–30096 (2012).
252. Grebeňová, D. *et al.* PAK1, PAK1Δ15, and PAK2: similarities, differences and mutual interactions. *Sci Rep* **9**, (2019).
253. Pirruccello, M. *et al.* A dimeric kinase assembly underlying autophosphorylation in the p21 activated kinases. *J Mol Biol* **361**, 312–326 (2006).
254. Zenke, F. T., King, C. C., Bohl, B. P. & Bokoch, G. M. Identification of a central phosphorylation site in p21-activated kinase regulating autoinhibition and kinase activity. *J Biol Chem* **274**, 32565–32573 (1999).
255. Gatti, A., Huang, Z., Tuazon, P. T. & Traugh, J. A. Multisite autophosphorylation of p21-activated protein kinase gamma-PAK as a function of activation. *J Biol Chem* **274**, 8022–8028 (1999).

256. Renkema, G. H., Pulkkinen, K. & Saksela, K. Cdc42/Rac1-Mediated Activation Primes PAK2 for Superactivation by Tyrosine Phosphorylation. *Mol Cell Biol* **22**, 6719 (2002).
257. Benner, G. E., Dennis, P. B. & Masaracchia, R. A. Activation of an S6/H4 kinase (PAK 65) from human placenta by intramolecular and intermolecular autophosphorylation. *J Biol Chem* **270**, 21121–21128 (1995).
258. Wu, H. & Wang, Z. X. The mechanism of p21-activated kinase 2 autoactivation. *J Biol Chem* **278**, 41768–41778 (2003).
259. Walter, B. N. *et al.* Cleavage and activation of p21-activated protein kinase gamma-PAK by CPP32 (caspase 3). Effects of autophosphorylation on activity. *J Biol Chem* **273**, 28733–28739 (1998).
260. Chong, C., Tan, L., Lim, L. & Manser, E. The mechanism of PAK activation. Autophosphorylation events in both regulatory and kinase domains control activity. *J Biol Chem* **276**, 17347–17353 (2001).
261. Baskaran, Y., Ng, Y. W., Selamat, W., Ling, F. T. P. & Manser, E. Group I and II mammalian PAKs have different modes of activation by Cdc42. *EMBO Rep* **13**, 653 (2012).
262. Goeckeler, Z. M. *et al.* Phosphorylation of myosin light chain kinase by p21-activated kinase PAK2. *J Biol Chem* **275**, 18366–18374 (2000).
263. Wang, Z. *et al.* p21-activated kinase 1 (PAK1) can promote ERK activation in a kinase-independent manner. *J Biol Chem* **288**, 20093–20099 (2013).
264. Schürmann, A. *et al.* p21-activated kinase 1 phosphorylates the death agonist bad and protects cells from apoptosis. *Mol Cell Biol* **20**, 453–461 (2000).
265. Ye, D. Z., Jin, S., Zhuo, Y. & Field, J. p21-Activated kinase 1 (Pak1) phosphorylates BAD directly at serine 111 in vitro and indirectly through Raf-1 at serine 112. *PLoS One* **6**, (2011).
266. Kissil, J. L., Johnson, K. C., Eckman, M. S. & Jacks, T. Merlin phosphorylation by p21-activated kinase 2 and effects of phosphorylation on merlin localization. *J Biol Chem* **277**, 10394–10399 (2002).
267. Chaudhary, A. *et al.* Phosphatidylinositol 3-kinase regulates Raf1 through Pak phosphorylation of serine 338. *Curr Biol* **10**, 551–554 (2000).
268. Slack-Davis, J. K. *et al.* PAK1 phosphorylation of MEK1 regulates fibronectin-stimulated MAPK activation. *J Cell Biol* **162**, 281–291 (2003).
269. Kumar, R., Gururaj, A. E. & Barnes, C. J. p21-activated kinases in cancer. *Nature Reviews Cancer* **2006** 6:6 **6**, 459–471 (2006).
270. Huynh, N. & He, H. p21-activated kinase family: promising new drug targets. *Res Rep Biochem* **5**, 119–128 (2015).
271. Dummler, B., Ohshiro, K., Kumar, R. & Field, J. Pak protein kinases and their role in cancer. *Cancer Metastasis Rev* **28**, 51 (2009).
272. Radu, M., Semenova, G., Kosoff, R. & Chernoff, J. PAK signalling during the development and progression of cancer. *Nat Rev Cancer* **14**, 13–25 (2014).
273. Lu, H. *et al.* PAK signalling drives acquired drug resistance to MAPK inhibitors in BRAF-mutant melanomas. *Nature* **550**, 133–136 (2017).
274. SE, P. & JT, Y. PAK1 and PAK4 as therapeutic targets for Ewing sarcoma: a commentary. *J Cancer Biol* **2**, (2021).
275. Li, M. *et al.* Exosomal miR-485-3p derived from pancreatic ductal epithelial cells inhibits pancreatic cancer metastasis through targeting PAK1. *Chin Med J (Engl)* **135**, 2326 (2022).
276. Somanath, P. R., Chernoff, J., Cummings, B. S., Prasad, S. M. & Homan, H. D. Targeting P21-Activated Kinase-1 for Metastatic Prostate Cancer. *Cancers (Basel)* **15**, (2023).
277. Goc, A. *et al.* P21 activated kinase-1 (Pak1) promotes prostate tumor growth and microinvasion via inhibition of transforming growth factor β expression and enhanced matrix metalloproteinase 9 secretion. *J Biol Chem* **288**, 3025–3035 (2013).

278. Wang, G. *et al.* PAK1 regulates RUFY3-mediated gastric cancer cell migration and invasion. *Cell Death Dis* **6**, (2015).
279. Liu, F. *et al.* A Novel Pak1/ATF2/miR-132 Signaling Axis Is Involved in the Hematogenous Metastasis of Gastric Cancer Cells. *Mol Ther Nucleic Acids* **8**, 370 (2017).
280. Liu, F. *et al.* Downregulation of p21-activated kinase-1 inhibits the growth of gastric cancer cells involving cyclin B1. *Int J Cancer* **125**, 2511–2519 (2009).
281. Schraml, P. *et al.* Combined array comparative genomic hybridization and tissue microarray analysis suggest PAK1 at 11q13.5-q14 as a critical oncogene target in ovarian carcinoma. *Am J Pathol* **163**, 985–992 (2003).
282. McCarty, S. K. *et al.* Group I p21-activated kinases regulate thyroid cancer cell migration and are overexpressed and activated in thyroid cancer invasion. *Endocr Relat Cancer* **17**, 989–999 (2010).
283. Huang, K. *et al.* [Expression of PAK1 in bladder cancer and its influence on invasion of bladder cancer cells]. *Zhonghua Yi Xue Za Zhi* **96**, 3227–3231 (2016).
284. Wang, R. A., Zhang, H., Balasenthil, S., Medina, D. & Kumar, R. PAK1 hyperactivation is sufficient for mammary gland tumor formation. *Oncogene* **25**, 2931–2936 (2006).
285. Shrestha, Y. *et al.* PAK1 is a breast cancer oncogene that coordinately activates MAPK and MET signaling. *Oncogene* **31**, 3397 (2012).
286. Kim, J. H., Choi, H. S., Kim, S. L. & Lee, D. S. The PAK1-Stat3 Signaling Pathway Activates IL-6 Gene Transcription and Human Breast Cancer Stem Cell Formation. *Cancers (Basel)* **11**, (2019).
287. Kumari, N., Dwarakanath, B. S., Das, A. & Bhatt, A. N. Role of interleukin-6 in cancer progression and therapeutic resistance. *Tumour Biol* **37**, 11553–11572 (2016).
288. Balasenthil, S. *et al.* p21-activated kinase-1 signaling mediates cyclin D1 expression in mammary epithelial and cancer cells. *J Biol Chem* **279**, 1422–1428 (2004).
289. Vadlamudi, R. K. *et al.* Regulatable expression of p21-activated kinase-1 promotes anchorage-independent growth and abnormal organization of mitotic spindles in human epithelial breast cancer cells. *J Biol Chem* **275**, 36238–36244 (2000).
290. Adam, L., Vadlamudi, R., Mandal, M., Chernoff, J. & Kumar, R. Regulation of microfilament reorganization and invasiveness of breast cancer cells by kinase dead p21-activated kinase-1. *J Biol Chem* **275**, 12041–12050 (2000).
291. Bostner, J. *et al.* Amplification of CCND1 and PAK1 as predictors of recurrence and tamoxifen resistance in postmenopausal breast cancer. *Oncogene* **26**, 6997–7005 (2007).
292. Holm, C. *et al.* Association between Pak1 expression and subcellular localization and tamoxifen resistance in breast cancer patients. *J Natl Cancer Inst* **98**, 671–680 (2006).
293. Rayala, S. K. *et al.* P21-activated kinase 1 regulation of estrogen receptor-alpha activation involves serine 305 activation linked with serine 118 phosphorylation. *Cancer Res* **66**, 1694–1701 (2006).
294. Wang, R. A., Mazumdar, A., Vadlamudi, R. K. & Kumar, R. P21-activated kinase-1 phosphorylates and transactivates estrogen receptor-alpha and promotes hyperplasia in mammary epithelium. *EMBO J* **21**, 5437–5447 (2002).
295. Saldivar-Cerón, H. I. *et al.* p21-Activated Kinase 1 Promotes Breast Tumorigenesis via Phosphorylation and Activation of the Calcium/Calmodulin-Dependent Protein Kinase II. *Front Cell Dev Biol* **9**, (2022).
296. Chi, M. *et al.* Phosphorylation of calcium/calmodulin-stimulated protein kinase II at T286 enhances invasion and migration of human breast cancer cells. *Sci Rep* **6**, (2016).
297. Wang, K. *et al.* Ivermectin induces PAK1-mediated cytoskeletal autophagy in breast cancer. *Autophagy* **12**, 2498–2499 (2016).
298. Paquette, M., El-Houjeiri, L. & Pause, A. mTOR Pathways in Cancer and Autophagy. *Cancers (Basel)* **10**, (2018).
299. Bu, H. *et al.* Therapeutic potential of IBP as an autophagy inducer for treating lung cancer via blocking PAK1/Akt/mTOR signaling. *Mol Ther Oncolytics* **20**, 82 (2021).

300. Khare, V. *et al.* Overexpression of PAK1 Promotes Cell Survival in Inflammatory Bowel Diseases and Colitis-associated Cancer. *Inflamm Bowel Dis* **21**, 287 (2015).
301. Yang, Z. *et al.* Overexpression of PAK1 Correlates with Aberrant Expression of EMT Markers and Poor Prognosis in Non-Small Cell Lung Cancer. *J Cancer* **8**, 1484–1491 (2017).
302. Wang, S. *et al.* Knockdown of PAK1 Inhibits the Proliferation and Invasion of Non-Small Cell Lung Cancer Cells Through the ERK Pathway. *Appl Immunohistochem Mol Morphol* **28**, 602–610 (2020).
303. Rettig, M. *et al.* PAK1 kinase promotes cell motility and invasiveness through CRK-II serine phosphorylation in non-small cell lung cancer cells. *PLoS One* **7**, (2012).
304. Tsuda, M. & Tanaka, S. Roles for Crk in Cancer Metastasis and Invasion. *Genes Cancer* **3**, 334 (2012).
305. Qing, H. *et al.* PAK1-dependent MAPK pathway activation is required for colorectal cancer cell proliferation. *Tumour Biol* **33**, 985–994 (2012).
306. Carter, J. H. *et al.* Pak-1 expression increases with progression of colorectal carcinomas to metastasis. *Clin Cancer Res* **10**, 3448–3456 (2004).
307. Song, B., Wang, W., Zheng, Y., Yang, J. & Xu, Z. P21-activated kinase 1 and 4 were associated with colorectal cancer metastasis and infiltration. *J Surg Res* **196**, 130–135 (2015).
308. Lu, W. *et al.* Overexpression of p21-activated kinase 1 promotes endometrial cancer progression. *Oncol Rep* **29**, 1547–1555 (2013).
309. Porter, A. G. & Jänicke, R. U. Emerging roles of caspase-3 in apoptosis. *Cell Death Differ* **6**, 99–104 (1999).
310. Jagadeeshan, S. *et al.* P21-activated kinase 1 (Pak1) signaling influences therapeutic outcome in pancreatic cancer. *Ann Oncol* **27**, 1546–1556 (2016).
311. Mihaly, S. R., Ninomiya-Tsuji, J. & Morioka, S. TAK1 control of cell death. *Cell Death Differ* **21**, 1667 (2014).
312. Zhou, W. *et al.* PAK1 mediates pancreatic cancer cell migration and resistance to MET inhibition. *J Pathol* **234**, 502–513 (2014).
313. Tang, Y. *et al.* A role for Pak protein kinases in Schwann cell transformation. *Proc Natl Acad Sci U S A* **95**, 5139–5144 (1998).
314. Yao, G. W., Bai, J. R. & Zhang, D. P. P21 activated kinase 2 promotes pancreatic cancer growth and metastasis. *Oncol Lett* **17**, 3709–3718 (2019).
315. Flate, E. & Stalvey, J. R. D. Motility of select ovarian cancer cell lines: effect of extra-cellular matrix proteins and the involvement of PAK2. *Int J Oncol* **45**, 1401–1411 (2014).
316. Chung, E. Y. *et al.* PAK Kinase Inhibition Has Therapeutic Activity in Novel Preclinical Models of Adult T-Cell Leukemia/Lymphoma. *Clin Cancer Res* **25**, 3589–3601 (2019).
317. Gupta, A. *et al.* PAK2–c-Myc–PKM2 axis plays an essential role in head and neck oncogenesis via regulating Warburg effect. *Cell Death & Disease* **2018 9:8 9**, 1–15 (2018).
318. Dang, C. V. *et al.* Function of the c-Myc oncogenic transcription factor. *Exp Cell Res* **253**, 63–77 (1999).
319. Henriksson, M. & Luscher, B. Proteins of the Myc network: essential regulators of cell growth and differentiation. *Adv Cancer Res* **68**, 110–182 (1996).
320. Heiden, M. G. V., Cantley, L. C. & Thompson, C. B. Understanding the Warburg Effect: The Metabolic Requirements of Cell Proliferation. *Science* **324**, 1029 (2009).
321. Zhang, Z. *et al.* PKM2, function and expression and regulation. *Cell & Bioscience* **2019 9:1 9**, 1–25 (2019).
322. Huang, Z., Traugh, J. A. & Bishop, J. M. Negative control of the Myc protein by the stress-responsive kinase Pak2. *Mol Cell Biol* **24**, 1582–1594 (2004).

323. Sementino, E. *et al.* Inactivation of p21-Activated Kinase 2 (Pak2) Inhibits the Development of Nf2-Deficient Tumors by Restricting Downstream Hedgehog and Wnt Signaling. *Molecular Cancer Research* **20**, 699–711 (2022).
324. Xiao, G. H., Beeser, A., Chernoff, J. & Testa, J. R. p21-activated kinase links Rac/Cdc42 signaling to merlin. *J Biol Chem* **277**, 883–886 (2002).
325. Zhang, Y. *et al.* IGF1R signaling drives antiestrogen resistance through PAK2/PIX activation in luminal breast cancer. *Oncogene* **2018 37:14 37**, 1869–1884 (2018).
326. Li, X. *et al.* Phosphorylation of caspase-7 by p21-activated protein kinase (PAK) 2 inhibits chemotherapeutic drug-induced apoptosis of breast cancer cell lines. *J Biol Chem* **286**, 22291–22299 (2011).
327. Lamkanfi, M. & Kanneganti, T. D. Caspase-7: a protease involved in apoptosis and inflammation. *Int J Biochem Cell Biol* **42**, 21–24 (2010).
328. Gao, Z. *et al.* PAK3 promotes the metastasis of hepatocellular carcinoma by regulating EMT process. *J Cancer* **13**, 153–161 (2022).
329. Wu, H. Y., Yang, M. C., Ding, L. Y., Chen, C. S. & Chu, P. C. p21-Activated kinase 3 promotes cancer stem cell phenotypes through activating the Akt-GSK3 β - β -catenin signaling pathway in pancreatic cancer cells. *Cancer Lett* **456**, 13–22 (2019).
330. Zhang, J., Qin, J. & Su, Y. miR-193b-3p possesses anti-tumor activity in ovarian carcinoma cells by targeting p21-activated kinase 3. *Biomed Pharmacother* **96**, 1275–1282 (2017).
331. Ma, T., Li, H., Yang, W., Liu, Q. & Yan, H. Over-expression of miR-193a-3p regulates the apoptosis of colorectal cancer cells by targeting PAK3. *Am J Transl Res* **14**, 1361 (2022).
332. Shao, W., Azam, Z., Guo, J. & To, S. S. T. Oncogenic potential of PIK3CD in glioblastoma is exerted through cytoskeletal proteins PAK3 and PLEK2. *Lab Invest* **102**, 1314–1322 (2022).
333. Baldwin, A. *et al.* Kinase requirements in human cells: V. Synthetic lethal interactions between p53 and the protein kinases SGK2 and PAK3. *Proc Natl Acad Sci U S A* **107**, 12463–12468 (2010).
334. Zhou, N., Ding, B., Agler, M., Cockett, M. & McPhee, F. Lethality of PAK3 and SGK2 shRNAs to human papillomavirus positive cervical cancer cells is independent of PAK3 and SGK2 knockdown. *PLoS One* **10**, (2015).
335. Liu, R. X. *et al.* p21-activated kinase 3 is overexpressed in thymic neuroendocrine tumors (carcinoids) with ectopic ACTH syndrome and participates in cell migration. *Endocrine* **38**, 38–47 (2010).
336. Siu, M. K. Y. *et al.* p21-activated kinase 4 regulates ovarian cancer cell proliferation, migration, and invasion and contributes to poor prognosis in patients. *Proc Natl Acad Sci U S A* **107**, 18622–18627 (2010).
337. Summy, J. M. & Gallick, G. E. Src family kinases in tumor progression and metastasis. *Cancer Metastasis Rev* **22**, 337–358 (2003).
338. Guarino, M. Src signaling in cancer invasion. *J Cell Physiol* **223**, 14–26 (2010).
339. Shen, T. & Huang, S. The role of Cdc25A in the regulation of cell proliferation and apoptosis. *Anticancer Agents Med Chem* **12**, 631–639 (2012).
340. Wang, Z., Wang, M., Lazo, J. S. & Carr, B. I. Identification of epidermal growth factor receptor as a target of Cdc25A protein phosphatase. *J Biol Chem* **277**, 19470–19475 (2002).
341. Poch, B. *et al.* Epidermal growth factor induces cyclin D1 in human pancreatic carcinoma: evidence for a cyclin D1-dependent cell cycle progression. *Pancreas* **23**, 280–287 (2001).
342. Barbieri, F. *et al.* Increased cyclin D1 expression is associated with features of malignancy and disease recurrence in ovarian tumors - PubMed. *Clinical Cancer Research* **5**, 1837–1873 (1999).
343. Kuo, L., Chang, H. C., Leu, T. H., Maa, M. C. & Hung, W. C. Src oncogene activates MMP-2 expression via the ERK/Sp1 pathway. *J Cell Physiol* **207**, 729–734 (2006).
344. Pramanik, K. K. & Mishra, R. ERK-mediated upregulation of matrix metalloproteinase-2 promotes the invasiveness in human oral squamous cell carcinoma (OSCC). *Exp Cell Res* **411**, (2022).

345. Tyagi, N. *et al.* p-21 activated kinase 4 (PAK4) maintains stem cell-like phenotypes in pancreatic cancer cells through activation of STAT3 signaling. *Cancer Lett* **370**, 260 (2016).
346. Scholz, A. *et al.* Activated signal transducer and activator of transcription 3 (STAT3) supports the malignant phenotype of human pancreatic cancer. *Gastroenterology* **125**, 891–905 (2003).
347. King, H. *et al.* PAK4 interacts with p85 alpha: implications for pancreatic cancer cell migration. *Sci Rep* **7**, (2017).
348. Tyagi, N. *et al.* p-21 activated kinase 4 promotes proliferation and survival of pancreatic cancer cells through AKT- and ERK-dependent activation of NF- κ B pathway. *Oncotarget* **5**, 8778–8789 (2014).
349. Costa, T. D. F. & Strömblad, S. Why is PAK4 overexpressed in cancer? *Int J Biochem Cell Biol* **138**, (2021).
350. Bi, Y. *et al.* Study on the expression of PAK4 and P54 protein in breast cancer. *World J Surg Oncol* **14**, (2016).
351. He, L. F. *et al.* Activated-PAK4 predicts worse prognosis in breast cancer and promotes tumorigenesis through activation of PI3K/AKT signaling. *Oncotarget* **8**, 17573–17585 (2017).
352. Liu, Y. *et al.* The protein kinase Pak4 disrupts mammary acinar architecture and promotes mammary tumorigenesis. *Oncogene* **29**, 5883 (2010).
353. Park, J. J. *et al.* The p21-activated kinase 4-Slug transcription factor axis promotes epithelial-mesenchymal transition and worsens prognosis in prostate cancer. *Oncogene* **37**, 5147–5159 (2018).
354. Ahn, H. K. *et al.* P21-activated kinase 4 overexpression in metastatic gastric cancer patients. *Transl Oncol* **4**, 345–349 (2011).
355. Kobayashi, K. *et al.* Prognostic significance of PAK4 expression in gastric cancer. *J Clin Pathol* **69**, 580–585 (2016).
356. Siu, M. K. Y. *et al.* p21-Activated Kinases 1, 2 and 4 in Endometrial Cancers: Effects on Clinical Outcomes and Cell Proliferation. *PLoS One* **10**, (2015).
357. Xu, H. T. *et al.* PAK4 Phosphorylates p53 at Serine 215 to Promote Liver Cancer Metastasis. *Cancer Res* **76**, 5732–5742 (2016).
358. Huang, H. *et al.* p21-activated kinase 4 promotes the progression of esophageal squamous cell carcinoma by targeting LASP1. *Mol Carcinog* **60**, 38–50 (2020).
359. Kesanakurti, D., Chetty, C., Rajasekhar Maddirela, D., Gujrati, M. & Rao, J. S. Functional cooperativity by direct interaction between PAK4 and MMP-2 in the regulation of anoikis resistance, migration and invasion in glioma. *Cell Death Dis* **3**, (2012).
360. Han, Z. X. *et al.* Downregulation of PAK5 inhibits glioma cell migration and invasion potentially through the PAK5-Egr1-MMP2 signaling pathway. *Brain Tumor Pathol* **31**, 234–241 (2013).
361. Bao, Z. *et al.* PAK5 promotes the cell stemness ability by phosphorylating SOX2 in lung squamous cell carcinomas. *Exp Cell Res* **395**, (2020).
362. Fang, Z. P. *et al.* P21-activated kinase 5 plays essential roles in the proliferation and tumorigenicity of human hepatocellular carcinoma. *Acta Pharmacol Sin* **35**, 82–88 (2014).
363. Gu, J. *et al.* A role for p21-activated kinase 7 in the development of gastric cancer. *FEBS J* **280**, 46–55 (2013).
364. Giroux, V., Dagorn, J. C. & Iovanna, J. L. A review of kinases implicated in pancreatic cancer. *Pancreatology* **9**, 738–754 (2009).
365. Zhu, G. *et al.* PAK5-mediated E47 phosphorylation promotes epithelial-mesenchymal transition and metastasis of colon cancer. *Oncogene* **35**, 1943–1954 (2016).
366. Gong, W. *et al.* P21-activated kinase 5 is overexpressed during colorectal cancer progression and regulates colorectal carcinoma cell adhesion and migration. *Int J Cancer* **125**, 548–555 (2009).
367. Huang, S. *et al.* PAK5 facilitates the proliferation, invasion and migration in colorectal cancer cells. *Cancer Med* **9**, 4777–4790 (2020).

368. Ismail, A. F. *et al.* PAK5 mediates cell: Cell adhesion integrity via interaction with E-cadherin in bladder cancer cells. *Biochemical Journal* **474**, 1333–1346 (2017).
369. Wang, X. X. *et al.* PAK5-Egr1-MMP2 signaling controls the migration and invasion in breast cancer cell. *Tumour Biol* **34**, 2721–2729 (2013).
370. Li, Y. kun *et al.* Human p21-activated kinase 5 (PAK5) expression and potential mechanisms in relevant cancers: Basic and clinical perspectives for molecular cancer therapeutics. *Life Sci* **241**, (2020).
371. LaPak, K. M. *et al.* Melanoma-associated mutants within the serine-rich domain of PAK5 direct kinase activity to mitogenic pathways. *Oncotarget* **9**, 25386–25401 (2018).
372. Zhang, Y. C. *et al.* PAK5-mediated phosphorylation and nuclear translocation of NF- κ B-p65 promotes breast cancer cell proliferation in vitro and in vivo. *J Exp Clin Cancer Res* **36**, (2017).
373. Xing, Y. *et al.* PAK5-mediated AIF phosphorylation inhibits its nuclear translocation and promotes breast cancer tumorigenesis. *Int J Biol Sci* **17**, 1315 (2021).
374. Li, Y. *et al.* PAK5 promotes RNA helicase DDX5 sumoylation and miRNA-10b processing in a kinase-dependent manner in breast cancer. *Cell Rep* **37**, (2021).
375. Biagioni, F. *et al.* The locus of microRNA-10b: A critical target for breast cancer insurgence and dissemination. *Cell Cycle* **12**, 2371 (2013).
376. Geng, N. *et al.* A PAK5–DNPEP–USP4 axis dictates breast cancer growth and metastasis. *Int J Cancer* **146**, 1139–1151 (2020).
377. Wang, X. X. *et al.* PAK5-Egr1-MMP2 signaling controls the migration and invasion in breast cancer cell. *Tumour Biol* **34**, 2721–2729 (2013).
378. Zcharia, E. *et al.* Inhibition of matrix metalloproteinase-2 by halofuginone is mediated by the Egr1 transcription factor. *Anticancer Drugs* **23**, 1022–1031 (2012).
379. Li, D., Pan, Y., Huang, Y., Zhang, P. & Fang, X. PAK5 Induces EMT and Promotes Cell Migration and Invasion by Activating the PI3K/AKT Pathway in Ovarian Cancer. *Anal Cell Pathol (Amst)* **2018**, (2018).
380. Spangle, J. M., Roberts, T. M. & Zhao, J. J. The emerging role of PI3K/AKT-mediated epigenetic regulation in cancer. *Biochim Biophys Acta* **1868**, 123 (2017).
381. Han, K. *et al.* PAK5 overexpression is associated with lung metastasis in osteosarcoma. *Oncol Lett* **15**, 2202 (2018).
382. Pan, X. *et al.* PAK5 is a potential target in myelodysplastic syndrome through interacting with LMO2 and GATA1. *Cell Mol Biol (Noisy-le-grand)* **68**, 77–85 (2022).
383. Li, Y. *et al.* GATA1 induces epithelial-mesenchymal transition in breast cancer cells through PAK5 oncogenic signaling. *Oncotarget* **6**, 4345 (2015).
384. Huo, F. C., Pan, Y. J., Li, T. T., Mou, J. & Pei, D. S. PAK5 promotes the migration and invasion of cervical cancer cells by phosphorylating SATB1. *Cell Death Differ* **26**, 994 (2019).
385. Yang, Q. *et al.* PAK6 promotes cervical cancer progression through activation of the Wnt/ β -catenin signaling pathway. *Oncol Lett* **20**, 2387–2395 (2020).
386. Chen, H. *et al.* Expression and prognostic significance of p21-activated kinase 6 in hepatocellular carcinoma. *J Surg Res* **189**, 81–88 (2014).
387. Zapatero, A. *et al.* Predictive value of PAK6 and PSMB4 expression in patients with localized prostate cancer treated with dose-escalation radiation therapy and androgen deprivation therapy. *Urol Oncol* **32**, 1327–1332 (2014).
388. Kaur, R., Yuan, X., Lu, M. L. & Balk, S. P. Increased PAK6 expression in prostate cancer and identification of PAK6 associated proteins. *Prostate* **68**, 1510–1516 (2008).
389. Wen, X. *et al.* Knockdown of p21-activated kinase 6 inhibits prostate cancer growth and enhances chemosensitivity to docetaxel. *Urology* **73**, 1407–1411 (2009).

390. Chen, J. *et al.* PAK6 increase chemoresistance and is a prognostic marker for stage II and III colon cancer patients undergoing 5-FU based chemotherapy. *Oncotarget* **6**, 355–367 (2015).
391. Zhang, M., Siedow, M., Saia, G. & Chakravarti, A. Inhibition of p21-activated Kinase 6 (PAK6) Increases Radiosensitivity of Prostate Cancer Cells. *Prostate* **70**, 807 (2010).
392. Bui, N. L. C. *et al.* Bad phosphorylation as a target of inhibition in oncology. *Cancer Lett* **415**, 177–186 (2018).
393. Huang, W. *et al.* PAK6 promotes homologous-recombination to enhance chemoresistance to oxaliplatin through ATR/CHK1 signaling in gastric cancer. *Cell Death & Disease* **2022 13:7 13**, 1–14 (2022).
394. Jiang, Y. *et al.* Prognostic and Predictive Value of p21-activated Kinase 6 Associated Support Vector Machine Classifier in Gastric Cancer Treated by 5-fluorouracil/Oxaliplatin Chemotherapy. *EBioMedicine* **22**, 78–88 (2017).
395. Lee, E. J. *et al.* Distinct DNA methylation profiles between adenocarcinoma and squamous cell carcinoma of human uterine cervix. *Oncol Res* **18**, 401–408 (2010).
396. Liu, W. *et al.* Prognostic significance of p21-activated kinase 6 expression in patients with clear cell renal cell carcinoma. *Ann Surg Oncol* **21 Suppl 4**, 575–583 (2014).
397. Fram, S., King, H., Sacks, D. B. & Wells, C. M. A PAK6–IQGAP1 complex promotes disassembly of cell–cell adhesions. *Cellular and Molecular Life Sciences* **71**, 2759 (2014).
398. Morse, E. M. *et al.* PAK6 targets to cell–cell adhesions through its N-terminus in a Cdc42-dependent manner to drive epithelial colony escape. *J Cell Sci* **129**, 380 (2016).
399. Salminen, A., Suuronen, T. & Kaarniranta, K. ROCK, PAK, and Toll of synapses in Alzheimer's disease. *Biochem Biophys Res Commun* **371**, 587–590 (2008).
400. Ma, Q.-L., Yang, F., Frautschy, S. A. & Cole, G. M. PAK in Alzheimer disease, Huntington disease and X-linked mental retardation. *Cell Logist* **2**, 117–125 (2012).
401. Civiero, L. *et al.* Leucine-rich repeat kinase 2 interacts with p21-activated kinase 6 to control neurite complexity in mammalian brain. *J Neurochem* **135**, 1242 (2015).
402. Dammann, K., Khare, V., Coleman, Kc., Berdel, H. & Gasche, C. p-21 Activated Kinase as a Molecular Target for Chemoprevention in Diabetes. *Geriatrics* **3**, (2018).
403. Liu, W. *et al.* Pak1 as a novel therapeutic target for antihypertrophic treatment in the heart. *Circulation* **124**, 2702–2715 (2011).
404. Nuche-Berenguer, B., Ramos-Álvarez, I. & Jensen, R. T. The p21-activated kinase, PAK2, is important in the activation of numerous pancreatic acinar cell signaling cascades and in the onset of early pancreatitis events. *Biochim Biophys Acta* **1862**, 1122 (2016).
405. Ramos-Alvarez, I. & Jensen, R. T. P21-activated kinase 4 in pancreatic acinar cells is activated by numerous gastrointestinal hormones/neurotransmitters and growth factors by novel signaling, and its activation stimulates secretory/growth cascades. *Am J Physiol Gastrointest Liver Physiol* **315**, G302–G317 (2018).
406. Del Mar Maldonado, M. & Dharmawardhane, S. Targeting Rac and Cdc42 GTPases in Cancer. *Cancer Res* **78**, 3101–3111 (2018).
407. Gao, Y., Dickerson, J. B., Guo, F., Zheng, J. & Zheng, Y. Rational design and characterization of a Rac GTPase-specific small molecule inhibitor. *Proc Natl Acad Sci U S A* **101**, 7618–7623 (2004).
408. Montalvo-Ortiz, B. L. *et al.* Characterization of EHop-016, novel small molecule inhibitor of Rac GTPase. *J Biol Chem* **287**, 13228–13238 (2012).
409. Zins, K., Lucas, T., Reichl, P., Abraham, D. & Aharinejad, S. A Rac1/Cdc42 GTPase-Specific Small Molecule Inhibitor Suppresses Growth of Primary Human Prostate Cancer Xenografts and Prolongs Survival in Mice. *PLoS One* **8**, e74924 (2013).
410. Zins, K., Gunawardhana, S., Lucas, T., Abraham, D. & Aharinejad, S. Targeting Cdc42 with the small molecule drug AZA197 suppresses primary colon cancer growth and prolongs survival in a preclinical mouse xenograft model by downregulation of PAK1 activity. *J Transl Med* **11**, 295 (2013).

411. Friesland, A. *et al.* Small molecule targeting Cdc42-intersectin interaction disrupts Golgi organization and suppresses cell motility. *Proc Natl Acad Sci U S A* **110**, 1261–1266 (2013).
412. Pelish, H. E. *et al.* Secramine inhibits Cdc42-dependent functions in cells and Cdc42 activation in vitro. *Nat Chem Biol* **2**, 39–46 (2006).
413. Beausoleil, E. *et al.* Structure-activity relationship of isoform selective inhibitors of Rac1/1b GTPase nucleotide binding. *Bioorg Med Chem Lett* **19**, 5594–5598 (2009).
414. Surviladze, Z. *et al.* Identification of a small GTPase inhibitor using a high-throughput flow cytometry bead-based multiplex assay. *J Biomol Screen* **15**, 10–20 (2010).
415. Hong, L. *et al.* Characterization of a Cdc42 protein inhibitor and its use as a molecular probe. *J Biol Chem* **288**, 8531–8543 (2013).
416. Pleines, I. *et al.* Defective tubulin organization and proplatelet formation in murine megakaryocytes lacking Rac1 and Cdc42. *Blood* **122**, 3178–3187 (2013).
417. Dütting, S. *et al.* Critical off-target effects of the widely used Rac1 inhibitors NSC23766 and EHT1864 in mouse platelets. *J Thromb Haemost* **13**, 827–838 (2015).
418. Sawada, N., Salomone, S., Kim, H. H., Kwiatkowski, D. J. & Liao, J. K. Regulation of Endothelial Nitric Oxide Synthase and Postnatal Angiogenesis by Rac1. *Circ Res* **103**, 360 (2008).
419. Tan, W. *et al.* An essential role for Rac1 in endothelial cell function and vascular development. *FASEB J* **22**, 1829–1838 (2008).
420. Yasuda, S. *et al.* An essential role of Cdc42-like GTPases in mitosis of HeLa cells. *FEBS Lett* **580**, 3375–3380 (2006).
421. Ruiz, R. *et al.* The RhoJ-BAD signaling network: An Achilles' heel for BRAF mutant melanomas. *PLoS Genet* **13**, (2017).
422. Wang, H. *et al.* Prominent oncogenic roles of EVI1 in breast carcinoma. *Cancer Res* **77**, 2148–2160 (2017).
423. Kim, C. *et al.* Rho GTPase RhoJ is Associated with Gastric Cancer Progression and Metastasis. *J Cancer* **7**, 1550–1556 (2016).
424. Kim, C. *et al.* Vascular RhoJ is an effective and selective target for tumor angiogenesis and vascular disruption. *Cancer Cell* **25**, 102–117 (2014).
425. Wilson, E. *et al.* RhoJ interacts with the GIT-PIX complex and regulates focal adhesion disassembly. *J Cell Sci* **127**, 3039–3051 (2014).
426. Takase, H. *et al.* Genome-wide identification of endothelial cell-enriched genes in the mouse embryo. *Blood* **120**, 914–923 (2012).
427. Leszczynska, K., Kaur, S., Wilson, E., Bicknell, R. & Heath, V. L. The role of RhoJ in endothelial cell biology and angiogenesis. *Biochem Soc Trans* **39**, 1606–1611 (2011).
428. Bridges, E. *et al.* RHOQ is induced by DLL4 and regulates angiogenesis by determining the intracellular route of the Notch intracellular domain. *Angiogenesis* **23**, 493 (2020).
429. Ho, H. *et al.* RhoJ Regulates Melanoma Chemoresistance by Suppressing Pathways that Sense DNA Damage. *Cancer Res* **72**, 5516 (2012).
430. Han, S. W. *et al.* RNA editing in RHOQ promotes invasion potential in colorectal cancer. *J Exp Med* **211**, 613–621 (2014).
431. Tong, S., Liss, A. S., You, M. & Bose, H. R. The activation of TC10, a Rho small GTPase, contributes to v-Rel-mediated transformation. *Oncogene* **26**, 2318–2329 (2007).
432. Licciulli, S. *et al.* FRAX597, a Small Molecule Inhibitor of the p21-activated Kinases, Inhibits Tumorigenesis of Neurofibromatosis Type 2 (NF2)-associated Schwannomas. *J Biol Chem* **288**, 29105 (2013).
433. Murray, B. W. *et al.* Small-molecule p21-activated kinase inhibitor PF-3758309 is a potent inhibitor of oncogenic signaling and tumor growth. *Proc Natl Acad Sci U S A* **107**, 9446–9451 (2010).

434. Porchia, L. M. *et al.* 2-Amino-N-{4-[5-(2-phenanthrenyl)-3-(trifluoromethyl)-1H-pyrazol-1-yl]-phenyl} Acetamide (OSU-03012), a Celecoxib Derivative, Directly Targets p21-Activated Kinase. *Mol Pharmacol* **72**, 1124–1131 (2007).
435. Maksimoska, J. *et al.* Targeting large kinase active site with rigid, bulky octahedral ruthenium complexes. *J Am Chem Soc* **130**, 15764–15765 (2008).
436. Nheu, T. V. *et al.* The K252a derivatives, inhibitors for the PAK/MLK kinase family selectively block the growth of RAS transformants. *Cancer J* **8**, 328–336 (2002).
437. Bain, J. *et al.* The selectivity of protein kinase inhibitors: a further update. *Biochem J* **408**, 297–315 (2007).
438. Karaman, M. W. *et al.* A quantitative analysis of kinase inhibitor selectivity. *Nat Biotechnol* **26**, 127–132 (2008).
439. Yi, C., Maksimoska, J., Marmorstein, R. & Kissil, J. L. Development of small-molecule inhibitors of the group I p21-activated kinases, emerging therapeutic targets in cancer. *Biochem Pharmacol* **80**, 683–689 (2010).
440. Kim, D. J. *et al.* Small molecules that allosterically inhibit p21-activated kinase activity by binding to the regulatory p21-binding domain. *Experimental & Molecular Medicine* 2016 48:4 **48**, e229–e229 (2016).
441. Rosen, L. S. *et al.* Abstract A177: Phase 1, dose-escalation, safety, pharmacokinetic and pharmacodynamic study of single agent PF-03758309, an oral PAK inhibitor, in patients with advanced solid tumors. *Mol Cancer Ther* **10**, A177–A177 (2011).
442. Maroney, A. C. *et al.* Cep-1347 (KT7515), a semisynthetic inhibitor of the mixed lineage kinase family. *J Biol Chem* **276**, 25302–25308 (2001).
443. Deacon, S. W. *et al.* An isoform-selective, small-molecule inhibitor targets the autoregulatory mechanism of p21-activated kinase. *Chem Biol* **15**, 322–331 (2008).
444. Viaud, J. & Peterson, J. R. An allosteric kinase inhibitor binds the p21-activated kinase autoregulatory domain covalently. *Mol Cancer Ther* **8**, 2559–2565 (2009).
445. Rudolph, J., Crawford, J. J., Hoeflich, K. P. & Wang, W. Inhibitors of p21-activated kinases (PAKs). *J Med Chem* **58**, 111–129 (2015).
446. Dammann, K., Khare, V. & Gasche, C. Tracing PAKs from GI inflammation to cancer. *Gut* **63**, 1173–1184 (2014).
447. Eswaran, J., Li, D. Q., Shah, A. & Kumar, R. Molecular Pathways: Targeting P21-activated Kinase 1 Signaling in Cancer: Opportunities, Challenges and Limitations. *Clinical Cancer Research* **18**, 3743 (2012).
448. Aboud, O. A. *et al.* Dual and specific inhibition of NAMPT and PAK4 by KPT-9274 decreases kidney cancer growth. *Mol Cancer Ther* **15**, 2119 (2016).
449. Cordover, E. *et al.* KPT-9274, an Inhibitor of PAK4 and NAMPT, Leads to Downregulation of mTORC2 in Triple Negative Breast Cancer Cells. *Chem Res Toxicol* **33**, 482–491 (2020).
450. Liu, H., Liu, K. & Dong, Z. The Role of p21-Activated Kinases in Cancer and Beyond: Where Are We Heading? *Front Cell Dev Biol* **9**, 641381 (2021).
451. Li, N. *et al.* Dual PAK4-NAMPT Inhibition Impacts Growth and Survival, and Increases Sensitivity to DNA-Damaging Agents in Waldenström Macroglobulinemia. *Clin Cancer Res* **25**, 369–377 (2019).
452. Pawson, T. & Nash, P. Protein–protein interactions define specificity in signal transduction. *Genes Dev* **14**, 1027–1047 (2000).
453. Keskin, O., Gursoy, A., Ma, B. & Nussinov, R. Principles of Protein–Protein Interactions: What are the Preferred Ways For Proteins To Interact? (2008) doi:10.1021/cr040409x.
454. Ding, Z. & Kihara, D. Computational Methods for Predicting Protein-Protein Interactions Using Various Protein Features. *Curr Protoc Protein Sci* **93**, e62 (2018).

455. Pachov, G. V., Gabdoulline, R. R. & Wade, R. C. *Computational Protein-Protein Interactions - 1st Edition - Ruth Nussli. Computational Protein-Protein Interactions* (Taylor and Francis Group LLC, 2009).
456. Krapp, L. F., Abriata, L. A., Cortés Rodriguez, F. & Dal Peraro, M. PeSTo: parameter-free geometric deep learning for accurate prediction of protein binding interfaces. *Nature Communications* **2023** *14:1* **14**, 1–11 (2023).
457. Esquivel-Rodriguez, J., Filos-Gonzalez, V., Li, B. & Kihara, D. Pairwise and multimeric protein-protein docking using the LZerD program suite. *Methods Mol Biol* **1137**, 209–234 (2014).
458. Tovchigrechko, A. & Vakser, I. A. GRAMM-X public web server for protein–protein docking. *Nucleic Acids Res* **34**, W310–W314 (2006).
459. Pierce, B. G. *et al.* ZDOCK server: interactive docking prediction of protein-protein complexes and symmetric multimers. *Bioinformatics* **30**, 1771–1773 (2014).
460. Lyskov, S. & Gray, J. J. The RosettaDock server for local protein-protein docking. *Nucleic Acids Res* **36**, (2008).
461. Geng, C., Narasimhan, S., Rodrigues, J. P. G. L. M. & Bonvin, A. M. J. J. Information-Driven, Ensemble Flexible Peptide Docking Using HADDOCK. *Methods Mol Biol* **1561**, 109–138 (2017).
462. Torchala, M., Moal, I. H., Chaleil, R. A. G., Fernandez-Recio, J. & Bates, P. A. SwarmDock: a server for flexible protein-protein docking. *Bioinformatics* **29**, 807–809 (2013).
463. Ritchie, D. & Kemp, G. J. Protein docking using spherical polar Fourier correlations. *Proteins* **39**, 178–194 (2000).
464. Kozakov, D. *et al.* The ClusPro web server for protein-protein docking. *Nat Protoc* **12**, 255–278 (2017).
465. Gabb, H. A., Jackson, R. M. & Sternberg, M. J. E. Modelling protein docking using shape complementarity, electrostatics and biochemical information. *J Mol Biol* **272**, 106–120 (1997).
466. Shoichet, B. K. & Kuntz, I. D. Protein docking and complementarity. *J Mol Biol* **221**, 327–346 (1991).
467. Ritchie, D. Recent progress and future directions in protein-protein docking. *Curr Protein Pept Sci* **9**, 1–15 (2008).
468. Bonvin, A. M. Flexible protein-protein docking. *Curr Opin Struct Biol* **16**, 194–200 (2006).
469. Jorgensen, W. L. Efficient Drug Lead Discovery and Optimization. *Acc Chem Res* **42**, 724–733 (2009).
470. Lee, T. S. *et al.* Alchemical binding free energy calculations in AMBER20: Advances and best practices for drug discovery. *J Chem Inf Model* **60**, 5595–5623 (2020).
471. Wang, L. *et al.* Accurate and reliable prediction of relative ligand binding potency in prospective drug discovery by way of a modern free-energy calculation protocol and force field. *J Am Chem Soc* **137**, 2695–2703 (2015).
472. Schindler, C. E. M. *et al.* Large-scale assessment of binding free energy calculations in active drug discovery projects. *J Chem Inf Model* **60**, 5457–5474 (2020).
473. Gilson, M. K., Given, J. A., Bush, B. L. & McCammon, J. A. The statistical-thermodynamic basis for computation of binding affinities: a critical review. *Biophys J* **72**, 1047–1069 (1997).
474. Jorgensen, W. L. & Thomas, L. L. Perspective on Free-Energy Perturbation Calculations for Chemical Equilibria. *J Chem Theory Comput* **4**, 869 (2008).
475. Chipot, C. Frontiers in free-energy calculations of biological systems. *Wiley Interdiscip Rev Comput Mol Sci* **4**, 71–89 (2014).
476. Song, L. F. & Merz, K. M. Evolution of Alchemical Free Energy Methods in Drug Discovery. *J Chem Inf Model* **60**, 5308–5318 (2020).
477. Clark, A. J. *et al.* Free Energy Perturbation Calculation of Relative Binding Free Energy between Broadly Neutralizing Antibodies and the gp120 Glycoprotein of HIV-1. *J Mol Biol* **429**, 930–947 (2017).

478. Clark, A. J. *et al.* Relative Binding Affinity Prediction of Charge-Changing Sequence Mutations with FEP in Protein–Protein Interfaces. *J Mol Biol* **431**, 1481 (2019).
479. Kilburg, D. & Gallicchio, E. Assessment of a single decoupling alchemical approach for the calculation of the absolute binding free energies of protein-peptide complexes. *Front Mol Biosci* **5**, 22 (2018).
480. Panel, N., Villa, F., Fuentes, E. J. & Simonson, T. Accurate PDZ/Peptide Binding Specificity with Additive and Polarizable Free Energy Simulations. *Biophys J* **114**, 1091–1102 (2018).
481. Jorgensen, W. L. The many roles of computation in drug discovery. *Science* **303**, 1813–1818 (2004).
482. Kuntz, I. D., Blaney, J. M., Oatley, S. J., Langridge, R. & Ferrin, T. E. A geometric approach to macromolecule–ligand interactions. *J Mol Biol* **161**, 269–288 (1982).
483. Meng, X.-Y., Zhang, H.-X., Mezei, M. & Cui, M. Molecular docking: a powerful approach for structure-based drug discovery. *Curr Comput Aided Drug Des* **7**, 146–157 (2011).
484. Kitchen, D. B., Decornez, H., Furr, J. R. & Bajorath, J. Docking and scoring in virtual screening for drug discovery: methods and applications. *Nat Rev Drug Discov* **3**, 935–949 (2004).
485. Halperin, I., Ma, B., Wolfson, H. & Nussinov, R. Principles of docking: An overview of search algorithms and a guide to scoring functions. *Proteins* **47**, 409–443 (2002).
486. Fischer, D., Norel, R., Wolfson, H. & Nussinov, R. Surface motifs by a computer vision technique: searches, detection, and implications for protein–ligand recognition. *Proteins* **16**, 278–292 (1993).
487. Norel, R., Fischer, D., Wolfson, H. J. & Nussinov, R. Molecular surface recognition by a computer vision-based technique. *Protein Eng* **7**, 39–46 (1994).
488. Rarey, M., Kramer, B., Lengauer, T. & Klebe, G. A fast flexible docking method using an incremental construction algorithm. *J Mol Biol* **261**, 470–489 (1996).
489. DesJarlais, R. L., Kuntz, I. D., Sheridan, R. P., Venkataraghavan, R. & Dixon, J. S. Docking flexible ligands to macromolecular receptors by molecular shape. *J Med Chem* **29**, 2149–2153 (1986).
490. Miranker, A. & Karplus, M. Functionality maps of binding sites: a multiple copy simultaneous search method. *Proteins* **11**, 29–34 (1991).
491. Böhm, H. J. LUDI: rule-based automatic design of new substituents for enzyme inhibitor leads. *J Comput Aided Mol Des* **6**, 593–606 (1992).
492. Hart, T. N. & Read, R. J. A multiple-start Monte Carlo docking method. *Proteins* **13**, 206–222 (1992).
493. Jones, G., Willett, P., Glen, R. C., Leach, A. R. & Taylor, R. Development and validation of a genetic algorithm for flexible docking. *J Mol Biol* **267**, 727–748 (1997).
494. Oshiro, C. M., Kuntz, I. D. & Dixon, J. S. Flexible ligand docking using a genetic algorithm. *J Comput Aided Mol Des* **9**, 113–130 (1995).
495. Friesner, R. A. *et al.* Glide: A New Approach for Rapid, Accurate Docking and Scoring. 1. Method and Assessment of Docking Accuracy. *J Med Chem* **47**, 1739–1749 (2004).
496. De Vivo, M. & Cavalli, A. Recent advances in dynamic docking for drug discovery. *Wiley Interdiscip Rev Comput Mol Sci* **7**, e1320 (2017).
497. Gioia, D., Bertazzo, M., Recanatini, M., Masetti, M. & Cavalli, A. Dynamic Docking: A Paradigm Shift in Computational Drug Discovery. *Molecules* **22**, (2017).
498. Pissurlenkar, R. R. S., Shaikh, M. S., Iyer, R. P. & Coutinho, E. C. Molecular mechanics force fields and their applications in drug design. *Antiinfect Agents Med Chem* **8**, 128–150 (2009).
499. Kollman, P. Free Energy Calculations: Applications to Chemical and Biochemical Phenomena. *Chem Rev* **93**, 2395–2417 (1993).
500. Ewing, T. J. A., Makino, S., Skillman, A. G. & Kuntz, I. D. DOCK 4.0: search strategies for automated molecular docking of flexible molecule databases. *J Comput Aided Mol Des* **15**, 411–428 (2001).
501. Verdonk, M. L., Cole, J. C., Hartshorn, M. J., Murray, C. W. & Taylor, R. D. Improved protein–ligand docking using GOLD. *Proteins* **52**, 609–623 (2003).

502. Morris, G. M. *et al.* Automated Docking Using a Lamarckian Genetic Algorithm and an Empirical Binding Free Energy Function. *J Comput Chem* **19**, 16391662 (1639).
503. Böhm, H. J. Prediction of binding constants of protein ligands: a fast method for the prioritization of hits obtained from de novo design or 3D database search programs. *J Comput Aided Mol Des* **12**, 309 (1998).
504. Muegge, I. & Martin, Y. C. A general and fast scoring function for protein-ligand interactions: a simplified potential approach. *J Med Chem* **42**, 791–804 (1999).
505. Chen, F. *et al.* Assessing the performance of the MM/PBSA and MM/GBSA methods. 6. Capability to predict protein–protein binding free energies and re-rank binding poses generated by protein–protein docking. *Physical Chemistry Chemical Physics* **18**, 22129–22139 (2016).
506. MacArron, R. *et al.* Impact of high-throughput screening in biomedical research. *Nat Rev Drug Discov* **10**, 188–195 (2011).
507. Taylor, R. D., Jewsbury, P. J. & Essex, J. W. A review of protein-small molecule docking methods. *J Comput Aided Mol Des* **16**, 151–166 (2002).
508. Patrick Walters, W., Stahl, M. T. & Murcko, M. A. Virtual screening—an overview. *Drug Discov Today* **3**, 160–178 (1998).
509. Durrant, J. D. & McCammon, J. A. Molecular dynamics simulations and drug discovery. *BMC Biol* **9**, 71 (2011).
510. McCammon, J. A., Gelin, B. R. & Karplus, M. Dynamics of folded proteins. *Nature* 1977 267:5612 **267**, 585–590 (1977).
511. Levitt, M. & Warshel, A. Computer simulation of protein folding. *Nature* 1975 253:5494 **253**, 694–698 (1975).
512. Karplus, M. & McCammon, J. A. Molecular dynamics simulations of biomolecules. *Nature Structural Biology* 2002 9:9 **9**, 646–652 (2002).
513. Sborgi, L. *et al.* Interaction Networks in Protein Folding via Atomic-Resolution Experiments and Long-Time-Scale Molecular Dynamics Simulations. *J Am Chem Soc* **137**, 6506 (2015).
514. Karplus, M. & Kuriyan, J. Molecular dynamics and protein function. *Proc Natl Acad Sci U S A* **102**, 6679–6685 (2005).
515. De Vivo, M., Masetti, M., Bottegoni, G. & Cavalli, A. Role of Molecular Dynamics and Related Methods in Drug Discovery. *J Med Chem* **59**, 4035–4061 (2016).
516. Zheng, L., Alhossary, A. A., Kwoh, C. K. & Mu, Y. Molecular Dynamics and Simulation. *Encyclopedia of Bioinformatics and Computational Biology: ABC of Bioinformatics* **1–3**, 550–566 (2019).
517. Solomon, A. Molecular modelling and drug design. *Pharmacology & Therapeutics* (2000).
518. Leach, A. R. *Molecular Modelling: Principles and Applications*. (2001).
519. Mc Naught, a. D. & Wilkinson, a. *IUPAC - Compendium of Chemical Terminology - Gold Book*. Iupac (International Union of Pure and Applied Chemistry (IUPAC), 1997). doi:10.1351/goldbook.
520. Karplus, M. & Petsko, G. A. Molecular dynamics simulations in biology. *Nature* 1990 347:6294 **347**, 631–639 (1990).
521. Ponder, J. W. & Case, D. A. Force fields for protein simulations. *Adv Protein Chem* **66**, 27–85 (2003).
522. Jorgensen, W. L. & Tirado-Rives, J. The OPLS Potential Functions for Proteins. Energy Minimizations for Crystals of Cyclic Peptides and Crambin. *J Am Chem Soc* **110**, 1657–1666 (1988).
523. Gunsteren, W. F. van, Daura, X. & Mark, A. E. GROMOS Force Field. *Encyclopedia of Computational Chemistry* (1998) doi:10.1002/0470845015.CGA011.
524. Brooks, B. R. *et al.* CHARMM: A program for macromolecular energy, minimization, and dynamics calculations. *J Comput Chem* **4**, 187–217 (1983).
525. Schlick, T. *Molecular Modeling and Simulation: An Interdisciplinary Guide*. *Interdisciplinary Applied Mathematics* vol. 21 (Springer Nature, 2010).

526. Steinbach, P. J. & Brooks, B. R. New spherical-cutoff methods for long-range forces in macromolecular simulation. *J Comput Chem* **15**, 667–683 (1994).
527. Darden, T., York, D. & Pedersen, L. Particle mesh Ewald: An N·log(N) method for Ewald sums in large systems. *J Chem Phys* **98**, 10089–10092 (1993).
528. Essmann, U. *et al.* A smooth particle mesh Ewald method. *J Chem Phys* **103**, 8577–8593 (1995).
529. York, D. & Yang, W. The fast Fourier Poisson method for calculating Ewald sums. *J Chem Phys* **101**, 3298–3300 (1994).
530. Dunbar, R. C. Deriving the Maxwell distribution. *J Chem Educ* **59**, 22–23 (1982).
531. Cauchy, A. Méthode générale pour la résolution des systemes d'équations simultanées. *Comp. Rend. Sci.* (1847).
532. Nash, S. G. & Sofer, A.-. *Linear and Nonlinear Programming*. *cir.nii.ac.jp* (McGraw-Hill, 1996).
533. Meza, J. C. Steepest descent. *Wiley Interdiscip Rev Comput Stat* **2**, 719–722 (2010).
534. Hestenes, M. R. & Stiefel, E. Methods of conjugate gradients for solving linear systems. *J Res Natl Bur Stand (1934)* **49**, 409 (1952).
535. Nazareth, J. L. Conjugate gradient method. *Wiley Interdiscip Rev Comput Stat* **1**, 348–353 (2009).
536. Allen, M. P. & Tildesley, D. J. *Computer Simulation of Liquids*. (Oxford University Press, 1989).
537. Braun, E. *et al.* Best Practices for Foundations in Molecular Simulations [Article v1.0]. *Living J Comput Mol Sci* **1**, (2019).
538. Hünenberger, P. H. Thermostat algorithms for molecular dynamics simulations. *Advances in Polymer Science* **173**, 105–147 (2005).
539. Ryckaert, J. P., Ciccotti, G. & Berendsen, H. J. C. Numerical integration of the cartesian equations of motion of a system with constraints: molecular dynamics of n-alkanes. *J Comput Phys* **23**, 327–341 (1977).
540. Allen, M. P. & Tildesley, D. J. Computer simulation of liquids: Second edition. *Computer Simulation of Liquids: Second Edition* (2017) doi:10.1093/oso/9780198803195.001.0001.
541. Frenkel, D. & Smit, B. *Understanding Molecular Simulation: From Algorithms to Applications, Third Edition*. *Understanding Molecular Simulation: from Algorithms to Applications, Third Edition* (Elsevier, 2023). doi:10.1016/C2009-0-63921-0.
542. Decherchi, S. & Cavalli, A. Thermodynamics and Kinetics of Drug-Target Binding by Molecular Simulation. *Chem Rev* **120**, 12788–12833 (2020).
543. Jain, A. K., Murty, M. N. & Flynn, P. J. Data Clustering: A Review. (2000).
544. Rodriguez, A. & Laio, A. Clustering by fast search and find of density peaks. *Science (1979)* **344**, 1492–1496 (2014).
545. Li, H. M., Xie, Y. H., Liu, C. Q. & Liu, S. Q. Physicochemical bases for protein folding, dynamics, and protein-ligand binding. *Sci China Life Sci* **57**, 287–302 (2014).
546. Chodera, J. D. & Mobley, D. L. Entropy-enthalpy compensation: role and ramifications in biomolecular ligand recognition and design. *Annu Rev Biophys* **42**, 121–142 (2013).
547. Gilson, M. K. & Zhou, H. X. Calculation of protein-ligand binding affinities. *Annu Rev Biophys Biomol Struct* **36**, 21–42 (2007).
548. Srinivasan, J., Cheatham, T. E., Cieplak, P., Kollman, P. A. & Case, D. A. Continuum Solvent Studies of the Stability of DNA, RNA, and Phosphoramidate-DNA Helices. (1998) doi:10.1021/JA981844.
549. Wang, E. *et al.* End-Point Binding Free Energy Calculation with MM/PBSA and MM/GBSA: Strategies and Applications in Drug Design. *Chem Rev* **119**, 9478–9508 (2019).
550. Kollman, P. A. *et al.* Calculating structures and free energies of complex molecules: combining molecular mechanics and continuum models. *Acc Chem Res* **33**, 889–897 (2000).

551. Homeyer, N. & Gohlke, H. Free Energy Calculations by the Molecular Mechanics Poisson-Boltzmann Surface Area Method. *Mol Inform* **31**, 114–122 (2012).
552. Miller, B. R. *et al.* MMPBSA.py: An Efficient Program for End-State Free Energy Calculations. *J Chem Theory Comput* **8**, 3314–3321 (2012).
553. Mey, A. S. J. S. *et al.* Best Practices for Alchemical Free Energy Calculations [Article v1.0]. *Living J Comput Mol Sci* **2**, (2020).
554. Straatsma, T. P. & McCammon, J. A. Computational Alchemy. <https://doi.org/10.1146/annurev.pc.43.100192.002203> **43**, 407–435 (2003).
555. Beutler, T. C., Mark, A. E., van Schaik, R. C., Gerber, P. R. & van Gunsteren, W. F. Avoiding singularities and numerical instabilities in free energy calculations based on molecular simulations. *Chem Phys Lett* **222**, 529–539 (1994).
556. Lee, T. S. *et al.* Improved Alchemical Free Energy Calculations with Optimized Smoothstep Softcore Potentials. *J Chem Theory Comput* **16**, 5512 (2020).
557. Steinbrecher, T., Mobley, D. L. & Case, D. A. Nonlinear scaling schemes for Lennard-Jones interactions in free energy calculations. *J Chem Phys* **127**, 214108 (2007).
558. Kirkwood, J. G. Statistical Mechanics of Fluid Mixtures. *J Chem Phys* **3**, 300 (2004).
559. Wang, M. *et al.* RhoJ facilitates angiogenesis in glioblastoma via JNK/VEGFR2 mediated activation of PAK and ERK signaling pathways. *Int J Biol Sci* **18**, 942 (2022).
560. Ho, H. *et al.* RhoJ modulates melanoma invasion by altering actin cytoskeletal dynamics. *Pigment Cell Melanoma Res* **26**, 218–225 (2013).
561. Ostrem, J. M., Peters, U., Sos, M. L., Wells, J. A. & Shokat, K. M. K-Ras(G12C) inhibitors allosterically control GTP affinity and effector interactions. *Nature* **2013** 503:7477 **503**, 548–551 (2013).
562. Patricelli, M. P. *et al.* Selective Inhibition of Oncogenic KRAS Output with Small Molecules Targeting the Inactive State. *Cancer Discov* **6**, 316–329 (2016).
563. Janes, M. R. *et al.* Targeting KRAS Mutant Cancers with a Covalent G12C-Specific Inhibitor. *Cell* **172**, 578–589.e17 (2018).
564. Canon, J. *et al.* The clinical KRAS(G12C) inhibitor AMG 510 drives anti-tumour immunity. *Nature* **575**, 217–223 (2019).
565. Hallin, J. *et al.* The KRASG12C Inhibitor MRTX849 Provides Insight toward Therapeutic Susceptibility of KRAS-Mutant Cancers in Mouse Models and Patients. *Cancer Discov* **10**, 54–71 (2020).
566. Fell, J. B. *et al.* Identification of the Clinical Development Candidate MRTX849, a Covalent KRASG12C Inhibitor for the Treatment of Cancer. *J Med Chem* **63**, 6679–6693 (2020).
567. Maurer, T. *et al.* Small-molecule ligands bind to a distinct pocket in Ras and inhibit SOS-mediated nucleotide exchange activity. *Proc Natl Acad Sci U S A* **109**, 5299–5304 (2012).
568. Kessler, D. *et al.* Drugging an undruggable pocket on KRAS. *Proc Natl Acad Sci U S A* **116**, 15823–15829 (2019).
569. Sun, Q. *et al.* Discovery of small molecules that bind to K-Ras and inhibit Sos-mediated activation. *Angew Chem Int Ed Engl* **51**, 6140–6143 (2012).
570. Quevedo, C. E. *et al.* Small molecule inhibitors of RAS-effector protein interactions derived using an intracellular antibody fragment. *Nature Communications* **2018** 9:1 **9**, 1–12 (2018).
571. Cruz-Migoni, A. *et al.* Structure-based development of new RAS-effector inhibitors from a combination of active and inactive RAS-binding compounds. *Proc Natl Acad Sci U S A* **116**, 2545–2550 (2019).
572. Humphries-Bickley, T. *et al.* Characterization of a dual Rac/Cdc42 Inhibitor MBQ-167 in metastatic cancer. *Mol Cancer Ther* **16**, 805–818 (2017).

573. Hirshberg, M., Stockley, R. W., Dodson, G. & Webb, M. R. The crystal structure of human rac1, a member of the rho-family complexed with a GTP analogue. *Nature Structural Biology* 1997 4:2 **4**, 147–152 (1997).
574. Jacobson, M. P. *et al.* A hierarchical approach to all-atom protein loop prediction. *Proteins* **55**, 351–367 (2004).
575. Madhavi Sastry, G., Adzhigirey, M., Day, T., Annabhimoju, R. & Sherman, W. Protein and ligand preparation: parameters, protocols, and influence on virtual screening enrichments. *J Comput Aided Mol Des* **27**, 221–234 (2013).
576. Venkatesan, K. *et al.* An empirical framework for binary interactome mapping. *Nat Methods* **6**, 83–90 (2009).
577. Ryan, D. P. & Matthews, J. M. Protein-protein interactions in human disease. *Curr Opin Struct Biol* **15**, 441–446 (2005).
578. JA, G., CA, H. & MA, P. Inhibiting protein-protein interactions as an emerging paradigm for drug discovery. *Mini Rev Med Chem* **7**, 151–157 (2007).
579. Chène, P. Drugs targeting protein-protein interactions. *ChemMedChem* **1**, 400–411 (2006).
580. Fischer, P. M. Protein-protein interactions in drug discovery. *Drug Design Reviews Online* **2**, 179–207 (2005).
581. Lu, H. *et al.* Recent advances in the development of protein–protein interactions modulators: mechanisms and clinical trials. *Signal Transduction and Targeted Therapy* 2020 5:1 **5**, 1–23 (2020).
582. Duarte, D. P. *et al.* Btk SH2-kinase interface is critical for allosteric kinase activation and its targeting inhibits B-cell neoplasms. *Nature Communications* 2020 11:1 **11**, 1–15 (2020).
583. Morrow, K. J. Inhibiting protein–protein interactions. *Nature Reviews Drug Discovery* 2016 15:4 **15**, 234–234 (2016).
584. Crunkhorn, S. Inhibiting protein–protein interactions. *Nature Reviews Drug Discovery* 2016 15:4 **15**, 234–234 (2016).
585. Thompson, G., Owen, D., Chalk, P. A. & Lowe, P. N. Delineation of the Cdc42/Rac-Binding Domain of p21-Activated Kinase. (1998) doi:10.1021/BI980140.
586. Šali, A. & Blundell, T. L. Comparative protein modelling by satisfaction of spatial restraints. *J Mol Biol* **234**, 779–815 (1993).
587. Ha, B. H. & Boggon, T. J. CDC42 binds PAK4 via an extended GTPase-effector interface. *Proc Natl Acad Sci U S A* **115**, 531–536 (2018).
588. Owen, D., Mott, H. R., Laue, E. D. & Lowe, P. N. Residues in Cdc42 That Specify Binding to Individual CRIB Effector Proteins. *Biochemistry* **39**, 1243–1250 (2000).
589. Cunningham, B. C. & Wells, J. A. High-Resolution Epitope Mapping of hGH-Receptor Interactions by Alanine-Scanning Mutagenesis. *Science* (1979) **244**, 1081–1085 (1989).
590. He, X. *et al.* Fast, Accurate, and Reliable Protocols for Routine Calculations of Protein-Ligand Binding Affinities in Drug Design Projects Using AMBER GPU-TI with ff14SB/GAFF. *ACS Omega* **5**, 4611–4619 (2020).
591. Adams, P. D. & Oswald, R. E. Solution structure of an oncogenic mutant of Cdc42Hs. *Biochemistry* **45**, 2577–2583 (2006).
592. Hauser, K. *et al.* Predicting resistance of clinical Abl mutations to targeted kinase inhibitors using alchemical free-energy calculations. *Communications Biology* 2018 1:1 **1**, 1–14 (2018).
593. Cappel, D. *et al.* Relative Binding Free Energy Calculations Applied to Protein Homology Models. *J Chem Inf Model* **56**, 2388–2400 (2016).
594. Genheden, S. Are homology models sufficiently good for free-energy simulations? *J Chem Inf Model* **52**, 3013–3021 (2012).

595. Bhati, A. P., Wan, S., Wright, D. W. & Coveney, P. V. Rapid, accurate, precise, and reliable relative free energy prediction using ensemble based thermodynamic integration. *J Chem Theory Comput* **13**, 210–222 (2017).
596. Bhati, A. P., Wan, S., Hu, Y., Sherborne, B. & Coveney, P. V. Uncertainty Quantification in Alchemical Free Energy Methods. *J Chem Theory Comput* **14**, 2867–2880 (2018).
597. Massova, I. & Kollman, P. A. Computational alanine scanning to probe protein-protein interactions: A novel approach to evaluate binding free energies. *J Am Chem Soc* **121**, 8133–8143 (1999).
598. Case, D. A. *et al.* Amber 2021. Preprint at (2021).
599. Maier, J. A. *et al.* ff14SB: Improving the Accuracy of Protein Side Chain and Backbone Parameters from ff99SB. *J Chem Theory Comput* **11**, 3696–3713 (2015).
600. Meagher, K. L., Redman, L. T. & Carlson, H. A. Development of polyphosphate parameters for use with the AMBER force field. *J Comput Chem* **24**, 1016–1025 (2003).
601. Allnér, O., Nilsson, L. & Villa, A. Magnesium Ion–Water Coordination and Exchange in Biomolecular Simulations. *J Chem Theory Comput* **8**, 1493–1502 (2012).
602. Joung, I. S. & Cheatham, T. E. Determination of alkali and halide monovalent ion parameters for use in explicitly solvated biomolecular simulations. *Journal of Physical Chemistry B* **112**, 9020–9041 (2008).
603. Jorgensen, W. L., Chandrasekhar, J., Madura, J. D., Impey, R. W. & Klein, M. L. Comparison of simple potential functions for simulating liquid water. *J Chem Phys* **79**, 926 (1998).
604. Andrea, T. A., Swope, W. C. & Andersen, H. C. The role of long ranged forces in determining the structure and properties of liquid water. *J Chem Phys* **79**, 4576 (1998).
605. Wallace, J. A. & Shen, J. K. Charge-leveling and proper treatment of long-range electrostatics in all-atom molecular dynamics at constant pH. *J Chem Phys* **137**, (2012).
606. Chen, Y. & Roux, B. Constant-pH Hybrid Nonequilibrium Molecular Dynamics–Monte Carlo Simulation Method. *J Chem Theory Comput* **11**, 3919–3931 (2015).
607. Chodera, J. D. A Simple Method for Automated Equilibration Detection in Molecular Simulations. *J Chem Theory Comput* **12**, 1799–1805 (2016).
608. Klimovich, P. V., Shirts, M. R. & Mobley, D. L. Guidelines for the analysis of free energy calculations. *J Comput Aided Mol Des* **29**, 397–411 (2015).
609. Homeyer, N. & Gohlke, H. Free Energy Calculations by the Molecular Mechanics Poisson-Boltzmann Surface Area Method. *Mol Inform* **31**, 114–122 (2012).
610. Onufriev, A., Bashford, D. & Case, D. A. Modification of the Generalized Born Model Suitable for Macromolecules. *Journal of Physical Chemistry B* **104**, 3712–3720 (2000).
611. Weiser, J., Shenkin, P. S. & Clark Still, W. Approximate Atomic Surfaces from Linear Combinations of Pairwise () Overlaps LCPO–JORG. *J Comput Chem* **20**, 217230 (1999).
612. Ishizaki, T. *et al.* The small GTP-binding protein Rho binds to and activates a 160 kDa Ser/Thr protein kinase homologous to myotonic dystrophy kinase. *EMBO J* **15**, 1885 (1996).
613. Ishizaki, T. *et al.* p160ROCK, a Rho-associated coiled-coil forming protein kinase, works downstream of Rho and induces focal adhesions. *FEBS Lett* **404**, 118–124 (1997).
614. Amano, M. *et al.* The COOH terminus of Rho-kinase negatively regulates rho-kinase activity. *J Biol Chem* **274**, 32418–32424 (1999).
615. Kawano, Y. *et al.* Phosphorylation of Myosin-Binding Subunit (Mbs) of Myosin Phosphatase by Rho-Kinase in Vivo. *J Cell Biol* **147**, 1023 (1999).
616. Kimura, K. *et al.* Regulation of myosin phosphatase by Rho and Rho-associated kinase (Rho-kinase). *Science* **273**, 245–248 (1996).
617. Sumi, T., Matsumoto, K. & Nakamura, T. Specific activation of LIM kinase 2 via phosphorylation of threonine 505 by ROCK, a Rho-dependent protein kinase. *J Biol Chem* **276**, 670–676 (2001).

618. Yang, N. *et al.* Cofilin phosphorylation by LIM-kinase 1 and its role in Rac-mediated actin reorganization. *Nature* **393**, 809–812 (1998).
619. Ohashi, K. *et al.* Rho-associated kinase ROCK activates LIM-kinase 1 by phosphorylation at threonine 508 within the activation loop. *J Biol Chem* **275**, 3577–3582 (2000).
620. Amano, M. *et al.* Phosphorylation and activation of myosin by Rho-associated kinase (Rho-kinase). *J Biol Chem* **271**, 20246–20249 (1996).
621. Kureishi, Y. *et al.* Rho-associated kinase directly induces smooth muscle contraction through myosin light chain phosphorylation. *J Biol Chem* **272**, 12257–12260 (1997).
622. Amano, T., Tanabe, K., Eto, T., Narumiya, S. & Mizuno, K. LIM-kinase 2 induces formation of stress fibres, focal adhesions and membrane blebs, dependent on its activation by Rho-associated kinase-catalysed phosphorylation at threonine-505. *Biochemical Journal* **354**, 149 (2001).
623. Maekawa, M. *et al.* Signaling from Rho to the actin cytoskeleton through protein kinases ROCK and LIM-kinase. *Science* **285**, 895–898 (1999).
624. Arber, S. *et al.* Regulation of actin dynamics through phosphorylation of cofilin by LIM-kinase. *Nature* **393**, 805–809 (1998).
625. Matsui, T. *et al.* Rho-kinase phosphorylates COOH-terminal threonines of ezrin/radixin/moesin (ERM) proteins and regulates their head-to-tail association. *J Cell Biol* **140**, 647–657 (1998).
626. Ridley, A. J. Rho GTPases and cell migration. *J Cell Sci* **114**, 2713–2722 (2001).
627. Wehrle-Haller, B. Structure and function of focal adhesions. *Curr Opin Cell Biol* **24**, 116–124 (2012).
628. Petrie, R. J. & Yamada, K. M. At the leading edge of three-dimensional cell migration. *J Cell Sci* **125**, 5917–5926 (2012).
629. Charras, G. & Paluch, E. Blebs lead the way: how to migrate without lamellipodia. *Nat Rev Mol Cell Biol* **9**, 730–736 (2008).
630. Kureishi, Y. *et al.* Rho-associated kinase directly induces smooth muscle contraction through myosin light chain phosphorylation. *J Biol Chem* **272**, 12257–12260 (1997).
631. Matsumura, F. Regulation of myosin II during cytokinesis in higher eukaryotes. *Trends Cell Biol* **15**, 371–377 (2005).
632. Croft, D. R. & Olson, M. F. The Rho GTPase Effector ROCK Regulates Cyclin A, Cyclin D1, and p27Kip1 Levels by Distinct Mechanisms. *Mol Cell Biol* **26**, 4612 (2006).
633. Coleman, M. L. & Olson, M. F. Rho GTPase signalling pathways in the morphological changes associated with apoptosis. *Cell Death & Differentiation* **2002 9:5 9**, 493–504 (2002).
634. Coleman, M. L. *et al.* Membrane blebbing during apoptosis results from caspase-mediated activation of ROCK I. *Nat Cell Biol* **3**, 339–345 (2001).
635. Mills, J. C., Stone, N. L., Erhardt, J. & Pittman, R. N. Apoptotic membrane blebbing is regulated by myosin light chain phosphorylation. *J Cell Biol* **140**, 627–636 (1998).
636. Mills, J. C., Stone, N. L. & Pittman, R. N. Extranuclear apoptosis. The role of the cytoplasm in the execution phase. *J Cell Biol* **146**, 703–707 (1999).
637. Sebbagh, M. *et al.* Caspase-3-mediated cleavage of ROCK I induces MLC phosphorylation and apoptotic membrane blebbing. *Nat Cell Biol* **3**, 346–352 (2001).
638. Olazabal, I. M. *et al.* Rho-kinase and myosin-II control phagocytic cup formation during CR, but not FcγR, phagocytosis. *Curr Biol* **12**, 1413–1418 (2002).
639. Tang, L. *et al.* RhoA/ROCK signaling regulates smooth muscle phenotypic modulation and vascular remodeling via the JNK pathway and vimentin cytoskeleton. *Pharmacol Res* **133**, 201–212 (2018).
640. Noma, K., Oyama, N. & Liao, J. K. Physiological role of ROCKs in the cardiovascular system. *Am J Physiol Cell Physiol* **290**, (2006).
641. Swärd, K. *et al.* The role of RhoA and Rho-associated kinase in vascular smooth muscle contraction. *Curr Hypertens Rep* **5**, 66–72 (2003).

642. Heasman, S. J., Carlin, L. M., Cox, S., Ng, T. & Ridley, A. J. Coordinated RhoA signaling at the leading edge and uropod is required for T cell transendothelial migration. *J Cell Biol* **190**, 553 (2010).
643. Alblas, J., Ulfman, L., Hordijk, P. & Koenderman, L. Activation of RhoA and ROCK are essential for detachment of migrating leukocytes. *Mol Biol Cell* **12**, 2137–2145 (2001).
644. Millán, J. & Ridley, A. J. Rho GTPases and leucocyte-induced endothelial remodelling. *Biochemical Journal* **385**, 329 (2005).
645. Honing, H. *et al.* RhoA activation promotes transendothelial migration of monocytes via ROCK. *J Leukoc Biol* **75**, 523–528 (2004).
646. Yao, L. *et al.* The role of RhoA/Rho kinase pathway in endothelial dysfunction. *J Cardiovasc Dis Res* **1**, 165 (2010).
647. Lubos, E., Handy, D. E. & Loscalzo, J. Role of oxidative stress and nitric oxide in atherothrombosis. *Front Biosci* **13**, 5323 (2008).
648. Eckenstaler, R., Hauke, M. & Benndorf, R. A. A current overview of RhoA, RhoB, and RhoC functions in vascular biology and pathology. *Biochem Pharmacol* **206**, (2022).
649. Koch, J. C. *et al.* ROCK inhibition in models of neurodegeneration and its potential for clinical translation. *Pharmacol Ther* **189**, 1–21 (2018).
650. Bito, H. *et al.* A critical role for a Rho-associated kinase, p160ROCK, in determining axon outgrowth in mammalian CNS neurons. *Neuron* **26**, 431–441 (2000).
651. Fujita, Y. & Yamashita, T. Axon growth inhibition by RhoA/ROCK in the central nervous system. *Front Neurosci* **8**, (2014).
652. Koch, J. C. *et al.* ROCK inhibition in models of neurodegeneration and its potential for clinical translation. *Pharmacol Ther* **189**, 1–21 (2018).
653. Katoh, H., Aoki, J., Ichikawa, A. & Negishi, M. p160 RhoA-binding kinase ROK α induces neurite retraction. *J Biol Chem* **273**, 2489–2492 (1998).
654. Fujita, A., Hattori, Y., Takeuchi, T., Kamata, Y. & Hata, F. NGF induces neurite outgrowth via a decrease in phosphorylation of myosin light chain in PC12 cells. *Neuroreport* **12**, 3599–3602 (2001).
655. Amano, M. *et al.* Myosin II activation promotes neurite retraction during the action of Rho and Rho-kinase. *Genes Cells* **3**, 177–188 (1998).
656. Tönges, L., Koch, J.-C., Bähr, M. & Lingor, P. ROCKing Regeneration: Rho Kinase Inhibition as Molecular Target for Neurorestoration. *Front Mol Neurosci* **4**, (2011).
657. Koch, J. C. *et al.* ROCK inhibition in models of neurodegeneration and its potential for clinical translation. *Pharmacol Ther* **189**, 1–21 (2018).
658. Dergham, P. *et al.* Rho signaling pathway targeted to promote spinal cord repair. *J Neurosci* **22**, 6570–6577 (2002).
659. Morgan-Fisher, M., Wewer, U. M. & Yoneda, A. Regulation of ROCK Activity in Cancer. *Journal of Histochemistry and Cytochemistry* **61**, 185 (2013).
660. Lochhead, P. A., Wickman, G., Mezna, M. & Olson, M. F. Activating ROCK1 somatic mutations in human cancer. *Oncogene* **29**, 2591–2598 (2010).
661. Fritz, G., Just, I. & Kaina, B. Rho GTPases ARE OVER-EXPRESSED IN HUMAN TUMORS. *J. Cancer* **81**, 682–687 (1999).
662. Fritz, G., Brachetti, C., Bahlmann, F., Schmidt, M. & Kaina, B. Rho GTPases in human breast tumours: expression and mutation analyses and correlation with clinical parameters. *Br J Cancer* **87**, 635 (2002).
663. Burbelo, P., Wellstein, A. & Pestell, R. G. Altered Rho GTPase signaling pathways in breast cancer cells. *Breast Cancer Res Treat* **84**, 43–48 (2004).
664. Kamai, T., Arai, K., Tsujii, T., Honda, M. & Yoshida, K. Overexpression of RhoA mRNA is associated with advanced stage in testicular germ cell tumour. *BJU Int* **87**, 227–231 (2001).

665. Kamai, T. *et al.* RhoA is associated with invasion and lymph node metastasis in upper urinary tract cancer. *BJU Int* **91**, 234–238 (2003).
666. Wei, L., Surma, M., Shi, S., Lambert-Cheatham, N. & Shi, J. Novel Insights into the Roles of Rho Kinase in Cancer. *Arch Immunol Ther Exp (Warsz)* **64**, 259–278 (2016).
667. Sahai, E., Ishizaki, T., Narumiya, S. & Treisman, R. Transformation mediated by RhoA requires activity of ROCK kinases. *Curr Biol* **9**, 136–145 (1999).
668. Sahai, E., Alberts, A. S. & Treisman, R. RhoA effector mutants reveal distinct effector pathways for cytoskeletal reorganization, SRF activation and transformation. *EMBO J* **17**, 1350 (1998).
669. Abe, H. *et al.* The Rho-kinase inhibitor HA-1077 suppresses proliferation/migration and induces apoptosis of urothelial cancer cells. *BMC Cancer* **14**, (2014).
670. Clayton, N. S. & Ridley, A. J. Targeting Rho GTPase Signaling Networks in Cancer. *Front Cell Dev Biol* **8**, (2020).
671. Mardilovich, K., Olson, M. F. & Baugh, M. Targeting Rho GTPase signaling for cancer therapy. *Future Oncol* **8**, 165–177 (2012).
672. Doublier, S. *et al.* RhoA Silencing Reverts the Resistance to Doxorubicin in Human Colon Cancer Cells. *Molecular Cancer Research* **6**, 1607–1620 (2008).
673. Kim, S., Kim, S. A., Han, J. & Kim, I. S. Rho-Kinase as a Target for Cancer Therapy and Its Immunotherapeutic Potential. *Int J Mol Sci* **22**, (2021).
674. Schofield, A. V. & Bernard, O. Rho-associated coiled-coil kinase (ROCK) signaling and disease. *Crit Rev Biochem Mol Biol* **48**, 301–316 (2013).
675. Chang, Y.-W., Bean, R. & Jakobi, R. Targeting RhoA/Rho kinase and p21-activated kinase signaling to prevent cancer development and progression. *Recent Pat Anticancer Drug Discov* **4**, 110–124 (2009).
676. Wojciak-Stothard, B. & Ridley, A. J. Rho GTPases and the regulation of endothelial permeability. *Vascul Pharmacol* **39**, 187–199 (2002).
677. Itoh, K. *et al.* An essential part for Rho-associated kinase in the transcellular invasion of tumor cells. *Nat Med* **5**, 221–225 (1999).
678. Deng, B. *et al.* Biological role of matrix stiffness in tumor growth and treatment. *Journal of Translational Medicine* 2022 20:1 **20**, 1–15 (2022).
679. Jaalouk, D. E. & Lammerding, J. Mechanotransduction gone awry. *Nat Rev Mol Cell Biol* **10**, 63–73 (2009).
680. Wyckoff, J. B., Pinner, S. E., Gschmeissner, S., Condeelis, J. S. & Sahai, E. ROCK- and myosin-dependent matrix deformation enables protease-independent tumor-cell invasion in vivo. *Curr Biol* **16**, 1515–1523 (2006).
681. Peng, Y. *et al.* ROCK isoforms differentially modulate cancer cell motility by mechanosensing the substrate stiffness. *Acta Biomater* **88**, 86–101 (2019).
682. Zhao, D. *et al.* Substrate stiffness regulated migration and invasion ability of adenoid cystic carcinoma cells via RhoA/ROCK pathway. *Cell Prolif* **51**, (2018).
683. Kamai, T. *et al.* Significant association of Rho/ROCK pathway with invasion and metastasis of bladder cancer - PubMed. *Clin Cancer Res* **9**, 2632–2641 (2003).
684. Raviraj, V. *et al.* Regulation of ROCK1 via Notch1 during breast cancer cell migration into dense matrices. *BMC Cell Biol* **13**, (2012).
685. Liu, S., Goldstein, R. H., Scepanky, E. M. & Rosenblatt, M. Inhibition of Rho-associated kinase signaling prevents breast cancer metastasis to human bone. *Cancer Res* **69**, 8742–8751 (2009).
686. Bottino, J., Gelaleti, G. B., Maschio, L. B., Jardim-Perassi, B. V. & de Campos Zuccari, D. A. P. Immunoexpression of ROCK-1 and MMP-9 as prognostic markers in breast cancer. *Acta Histochem* **116**, 1367–1373 (2014).

687. Dyberg, C. *et al.* Rho-associated kinase is a therapeutic target in neuroblastoma. *Proc Natl Acad Sci U S A* **114**, E6603–E6612 (2017).
688. Dyberg, C. *et al.* Inhibition of Rho-Associated Kinase Suppresses Medulloblastoma Growth. *Cancers (Basel)* **12**, (2019).
689. Liu, X. *et al.* ROCK1 as a potential therapeutic target in osteosarcoma. *J Orthop Res* **29**, 1259–1266 (2011).
690. Chen, W., Mao, K., Liu, Z. & Dinh-Xuan, A. T. The role of the RhoA/Rho kinase pathway in angiogenesis and its potential value in prostate cancer (Review). *Oncol Lett* **8**, 1907 (2014).
691. Zakaria, M. A., Rajab, N. F., Chua, E. W., Selvarajah, G. T. & Masre, S. F. Roles of Rho-associated kinase in lung cancer (Review). *Int J Oncol* **58**, 185–198 (2021).
692. Cui, G. *et al.* MiR-186 targets ROCK1 to suppress the growth and metastasis of NSCLC cells. *Tumour Biol* **35**, 8933–8937 (2014).
693. Liu, D., Mei, X., Wang, L. & Yang, X. RhoA inhibits apoptosis and increases proliferation of cultured SPCA1 lung cancer cells. *Mol Med Rep* **15**, 3963–3968 (2017).
694. Yang, X. *et al.* The Rho-kinase inhibitor inhibits proliferation and metastasis of small cell lung cancer. *Biomed Pharmacother* **66**, 221–227 (2012).
695. Xin, T., Lv, W., Liu, D., Jing, Y. & Hu, F. ROCK1 knockdown inhibits non-small-cell lung cancer progression by activating the LATS2-JNK signaling pathway. *Aging (Albany NY)* **12**, 12160 (2020).
696. Wang, J. *et al.* DEK Depletion Negatively Regulates Rho/ROCK/MLC Pathway in Non–Small Cell Lung Cancer. *Journal of Histochemistry and Cytochemistry* **61**, 510 (2013).
697. Xu, N. *et al.* CHD4 mediates proliferation and migration of non-small cell lung cancer via the RhoA/ROCK pathway by regulating PHF5A. *BMC Cancer* **20**, (2020).
698. Hu, C. *et al.* ROCK1 promotes migration and invasion of non-small-cell lung cancer cells through the PTEN/PI3K/FAK pathway. *Int J Oncol* **55**, 833–844 (2019).
699. Zhu, F. *et al.* Rho kinase inhibitor fasudil suppresses migration and invasion through down-regulating the expression of VEGF in lung cancer cell line A549. *Med Oncol* **28**, 565–571 (2011).
700. Zhang, Z., Ren, J. H., Li, Z. Y., Nong, L. & Wu, G. Fasudil inhibits lung carcinoma-conditioned endothelial cell viability and migration. *Oncol Rep* **27**, 1561–1566 (2012).
701. Vennin, C., Rath, N., Pajic, M., Olson, M. F. & Timpson, P. Targeting ROCK activity to disrupt and prime pancreatic cancer for chemotherapy. *Small GTPases* **11**, 45 (2020).
702. Matsuoka, T. & Yashiro, M. Rho/ROCK signaling in motility and metastasis of gastric cancer. *World Journal of Gastroenterology : WJG* **20**, 13756 (2014).
703. Xu, X. T. *et al.* Inhibition of RhoA/ROCK signaling pathway promotes the apoptosis of gastric cancer cells. *Hepatogastroenterology* **59**, 2523–2526 (2012).
704. Lin, M. T. *et al.* IL-6 induces AGS gastric cancer cell invasion via activation of the c-Src/RhoA/ROCK signaling pathway. *Int J Cancer* **120**, 2600–2608 (2007).
705. Wong, C. C. L., Wong, C. M., Au, S. L. K. & Ng, I. O. L. RhoGTPases and Rho-effectors in hepatocellular carcinoma metastasis: ROCK N’Rho move it. *Liver Int* **30**, 642–656 (2010).
706. Cai, R. L. *et al.* Role of RhoA/ROCK signaling in Alzheimer’s disease. *Behavioural brain research* **414**, (2021).
707. Panza, F., Lozupone, M., Logroscino, G. & Imbimbo, B. P. A critical appraisal of amyloid- β -targeting therapies for Alzheimer disease. *Nat Rev Neurol* **15**, 73–88 (2019).
708. Zhou, Y. *et al.* Nonsteroidal anti-inflammatory drugs can lower amyloidogenic Abeta42 by inhibiting Rho. *Science* **302**, 1215–1217 (2003).
709. Pedrini, S. *et al.* Modulation of statin-activated shedding of Alzheimer APP ectodomain by ROCK. *PLoS Med* **2**, 0069–0078 (2005).

710. Henderson, B. W. *et al.* Rho-associated protein kinase 1 (ROCK1) is increased in Alzheimer's disease and ROCK1 depletion reduces amyloid- β levels in brain. *J Neurochem* **138**, 525–531 (2016).
711. Hu, Y. B. *et al.* Rho-associated coiled-coil kinase 1 activation mediates amyloid precursor protein site-specific Ser655 phosphorylation and triggers amyloid pathology. *Aging Cell* **18**, (2019).
712. Busche, M. A. & Hyman, B. T. Synergy between amyloid- β and tau in Alzheimer's disease. *Nat Neurosci* **23**, 1183–1193 (2020).
713. Al-Hilaly, Y. K. *et al.* Alzheimer's Disease-like Paired Helical Filament Assembly from Truncated Tau Protein Is Independent of Disulfide Crosslinking. *J Mol Biol* **429**, 3650–3665 (2017).
714. Goedert, M. Tau protein and the neurofibrillary pathology of Alzheimer's disease. *Ann N Y Acad Sci* **777**, 121–131 (1996).
715. Amano, M. *et al.* Identification of Tau and MAP2 as novel substrates of Rho-kinase and myosin phosphatase. *J Neurochem* **87**, 780–790 (2003).
716. Hamano, T. *et al.* Rho-kinase ROCK inhibitors reduce oligomeric tau protein. *Neurobiol Aging* **89**, 41 (2020).
717. Hamano, T., Yen, S. H., Gendron, T., Ko, L. wen & Kuriyama, M. Pitavastatin decreases tau levels via the inactivation of Rho/ROCK. *Neurobiol Aging* **33**, 2306–2320 (2012).
718. Castro-Alvarez, J. F., Gutierrez-Vargas, J., Darnaudéry, M. & Cardona-Gómez, G. P. ROCK inhibition prevents tau hyperphosphorylation and p25/CDK5 increase after global cerebral ischemia. *Behavioral neuroscience* **125**, 465–472 (2011).
719. Gu, Q. F. *et al.* Therapeutic effect of Rho kinase inhibitor FSD-C10 in a mouse model of Alzheimer's disease. *Exp Ther Med* **16**, 3929 (2018).
720. Lai, A. Y. & McLaurin, J. A. Rho-associated protein kinases as therapeutic targets for both vascular and parenchymal pathologies in Alzheimer's disease. *J Neurochem* **144**, 659–668 (2018).
721. Tönges, L. *et al.* Inhibition of rho kinase enhances survival of dopaminergic neurons and attenuates axonal loss in a mouse model of Parkinson's disease. *Brain* **135**, 3355–3370 (2012).
722. Li, M., Huang, Y., Ma, A. A. K., Lin, E. & Diamond, M. I. Y-27632 improves rotarod performance and reduces huntingtin levels in R6/2 mice. *Neurobiol Dis* **36**, 413–420 (2009).
723. Takata, M. *et al.* Fasudil, a rho kinase inhibitor, limits motor neuron loss in experimental models of amyotrophic lateral sclerosis. *Br J Pharmacol* **170**, 341–351 (2013).
724. Paintlia, A. S., Paintlia, M. K., Hollis, B. W., Singh, A. K. & Singh, I. Interference with RhoA–ROCK Signaling Mechanism in Autoreactive CD4+ T Cells Enhances the Bioavailability of 1,25-Dihydroxyvitamin D3 in Experimental Autoimmune Encephalomyelitis. *Am J Pathol* **181**, 993 (2012).
725. Koch, J. C. *et al.* ROCK inhibition in models of neurodegeneration and its potential for clinical translation. *Pharmacol Ther* **189**, 1–21 (2018).
726. Mulherkar, S. & Tolia, K. F. RhoA-ROCK Signaling as a Therapeutic Target in Traumatic Brain Injury. *Cells* **9**, (2020).
727. Bye, N., Christie, K. J., Turbic, A., Basrai, H. S. & Turnley, A. M. Rho kinase inhibition following traumatic brain injury in mice promotes functional improvement and acute neuron survival but has little effect on neurogenesis, glial responses or neuroinflammation. *Exp Neurol* **279**, 86–95 (2016).
728. Watzlawick, R. *et al.* Effect and reporting bias of RhoA/ROCK-blockade intervention on locomotor recovery after spinal cord injury: a systematic review and meta-analysis. *JAMA Neurol* **71**, 91–99 (2014).
729. Tönges, L., Koch, J.-C., Bähr, M. & Lingor, P. ROCKing Regeneration: Rho Kinase Inhibition as Molecular Target for Neurorestoration. *Front Mol Neurosci* **4**, (2011).
730. Saha, B. C., Kumari, R., Kushumesh, R., Ambasta, A. & Sinha, B. P. Status of Rho kinase inhibitors in glaucoma therapeutics-an overview. *Int Ophthalmol* **42**, 281–294 (2022).
731. Shimokawa, H. Rho-kinase as a novel therapeutic target in treatment of cardiovascular diseases. *J Cardiovasc Pharmacol* **39**, 319–327 (2002).

732. Loirand, G. Rho Kinases in Health and Disease: From Basic Science to Translational Research. *Pharmacol Rev* **67**, 1074–1095 (2015).
733. Rao, P. V., Pattabiraman, P. P. & Kocpozynski, C. Role of the Rho GTPase/Rho kinase signaling pathway in pathogenesis and treatment of glaucoma: Bench to bedside research. *Exp Eye Res* **158**, 23–32 (2017).
734. Shimokawa, H., Sunamura, S. & Satoh, K. RhoA/Rho-Kinase in the Cardiovascular System. *Circ Res* **118**, 352–366 (2016).
735. Ming, X.-F. *et al.* Rho GTPase/Rho kinase negatively regulates endothelial nitric oxide synthase phosphorylation through the inhibition of protein kinase B/Akt in human endothelial cells. *Mol Cell Biol* **22**, 8467–8477 (2002).
736. Laufs, U. *et al.* Neuroprotection mediated by changes in the endothelial actin cytoskeleton. *J Clin Invest* **106**, 15–24 (2000).
737. Laufs, U. & Liao, J. K. Post-transcriptional regulation of endothelial nitric oxide synthase mRNA stability by Rho GTPase. *J Biol Chem* **273**, 24266–24271 (1998).
738. Takemoto, M., Sun, J., Hiroki, J., Shimokawa, H. & Liao, J. K. Rho-Kinase Mediates Hypoxia-Induced Downregulation of Endothelial Nitric Oxide Synthase. *Circulation* **106**, 57–62 (2002).
739. Kishi, T. *et al.* Rho-kinase inhibitor improves increased vascular resistance and impaired vasodilation of the forearm in patients with heart failure. *Circulation* **111**, 2741–2747 (2005).
740. Kandabashi, T. *et al.* Evidence for Protein Kinase C-Mediated Activation of Rho-Kinase in a Porcine Model of Coronary Artery Spasm. *Arterioscler Thromb Vasc Biol* **23**, 2209–2214 (2003).
741. Kandabashi, T. *et al.* Involvement of rho-kinase in agonists-induced contractions of arteriosclerotic human arteries. *Arterioscler Thromb Vasc Biol* **22**, 243–248 (2002).
742. Sawada, N. & Liao, J. K. Rho/Rho-Associated Coiled-Coil Forming Kinase Pathway as Therapeutic Targets for Statins in Atherosclerosis. *Antioxid Redox Signal* **20**, 1251 (2014).
743. Wolfrum, S. *et al.* Inhibition of Rho-kinase leads to rapid activation of phosphatidylinositol 3-kinase/protein kinase Akt and cardiovascular protection. *Arterioscler Thromb Vasc Biol* **24**, 1842–1847 (2004).
744. Masumoto, A. *et al.* Possible involvement of Rho-kinase in the pathogenesis of hypertension in humans. *Hypertension* **38**, 1307–1310 (2001).
745. Ross, R. The pathogenesis of atherosclerosis: a perspective for the 1990s. *Nature* **362**, 801–809 (1993).
746. Van Nieuw Amerongen, G. P., Delft, S. Van, Vermeer, M. A., Collard, J. G. & Van Hinsbergh, V. W. M. Activation of RhoA by thrombin in endothelial hyperpermeability: role of Rho kinase and protein tyrosine kinases. *Circ Res* **87**, 335–340 (2000).
747. Yao, L. *et al.* The role of RhoA/Rho kinase pathway in endothelial dysfunction. *J Cardiovasc Dis Res* **1**, 165 (2010).
748. Miyazaki, T., Honda, K. & Ohata, H. m-Calpain antagonizes RhoA overactivation and endothelial barrier dysfunction under disturbed shear conditions. *Cardiovasc Res* **85**, 530–541 (2010).
749. Satoh, K., Fukumoto, Y. & Shimokawa, H. Rho-kinase: important new therapeutic target in cardiovascular diseases. *Am J Physiol Heart Circ Physiol* **301**, (2011).
750. Nakakuki, T. *et al.* Rho/Rho-kinase pathway contributes to C-reactive protein-induced plasminogen activator inhibitor-1 expression in endothelial cells. *Arterioscler Thromb Vasc Biol* **25**, 2088–2093 (2005).
751. Eto, M., Kozai, T., Cosentino, F., Joch, H. & Lüscher, T. F. Statin prevents tissue factor expression in human endothelial cells: role of Rho/Rho-kinase and Akt pathways. *Circulation* **105**, 1756–1759 (2002).
752. Shimizu, T. & Liao, J. K. Rho Kinases and Cardiac Remodeling. *Circ J* **80**, 1491–1498 (2016).
753. Gabrielli, L. *et al.* Increased rho-kinase activity in hypertensive patients with left ventricular hypertrophy. *Am J Hypertens* **27**, 838–845 (2014).

754. Kobayashi, N. *et al.* Critical role of Rho-kinase pathway for cardiac performance and remodeling in failing rat hearts. *Cardiovasc Res* **55**, 757–767 (2002).
755. Yang, X. *et al.* Mechanism of fibrotic cardiomyopathy in mice expressing truncated Rho-associated coiled-coil protein kinase 1. *The FASEB Journal* **26**, 2105 (2012).
756. Shi, J., Zhang, Y. W., Yang, Y., Zhang, L. & Wei, L. ROCK1 plays an essential role in the transition from cardiac hypertrophy to failure in mice. *J Mol Cell Cardiol* **49**, 819 (2010).
757. Chang, J. *et al.* Activation of Rho-associated coiled-coil protein kinase 1 (ROCK-1) by caspase-3 cleavage plays an essential role in cardiac myocyte apoptosis. *Proc Natl Acad Sci U S A* **103**, 14495–14500 (2006).
758. Higashi, M. *et al.* Long-term inhibition of Rho-kinase suppresses angiotensin II-induced cardiovascular hypertrophy in rats in vivo: effect on endothelial NAD(P)H oxidase system. *Circ Res* **93**, 767–775 (2003).
759. Wang, Y. X. *et al.* Inhibition of Rho-kinase by fasudil attenuated angiotensin II-induced cardiac hypertrophy in apolipoprotein E deficient mice. *Eur J Pharmacol* **512**, 215–222 (2005).
760. Rajapurohitam, V., Izaddoustdar, F., Martinez-Abundis, E. & Karmazyn, M. Leptin-induced cardiomyocyte hypertrophy reveals both calcium-dependent and calcium-independent/RhoA-dependent calcineurin activation and NFAT nuclear translocation. *Cell Signal* **24**, 2283–2290 (2012).
761. Hoshijima, M., Sah, V. P., Wang, Y., Chien, K. R. & Brown, J. H. The low molecular weight GTPase Rho regulates myofibril formation and organization in neonatal rat ventricular myocytes. Involvement of Rho kinase. *J Biol Chem* **273**, 7725–7730 (1998).
762. Li, Q., Xu, Y., Li, X., Guo, Y. & Liu, G. Inhibition of Rho-kinase ameliorates myocardial remodeling and fibrosis in pressure overload and myocardial infarction: role of TGF- β 1-TAK1. *Toxicol Lett* **211**, 91–97 (2012).
763. Loirand, G. & Pacaud, P. The role of Rho protein signaling in hypertension. *Nat Rev Cardiol* **7**, 637–647 (2010).
764. Zhang, Y. *et al.* Targeted deletion of ROCK1 protects the heart against pressure overload by inhibiting reactive fibrosis. *FASEB J* **20**, 916–925 (2006).
765. Oka, M., Fagan, K. A., Jones, P. L. & McMurtry, I. F. Therapeutic potential of RhoA/Rho kinase inhibitors in pulmonary hypertension. *Br J Pharmacol* **155**, 444–454 (2008).
766. Abe, K. *et al.* Long-Term Treatment With a Rho-Kinase Inhibitor Improves Monocrotaline-Induced Fatal Pulmonary Hypertension in Rats. *Circ Res* **94**, 385–393 (2004).
767. Fagan, K. A. *et al.* Attenuation of acute hypoxic pulmonary vasoconstriction and hypoxic pulmonary hypertension in mice by inhibition of Rho-kinase. *Am J Physiol Lung Cell Mol Physiol* **287**, (2004).
768. Nagaoka, T. *et al.* Inhaled Rho kinase inhibitors are potent and selective vasodilators in rat pulmonary hypertension. *Am J Respir Crit Care Med* **171**, 494–499 (2005).
769. Nagaoka, T. *et al.* Rho/Rho kinase signaling mediates increased basal pulmonary vascular tone in chronically hypoxic rats. *Am J Physiol Lung Cell Mol Physiol* **287**, (2004).
770. Do.e, Z. *et al.* Evidence for Rho-kinase activation in patients with pulmonary arterial hypertension. *Circ J* **73**, 1731–1739 (2009).
771. Cordle, A., Koenigsnecht-Talboo, J., Wilkinson, B., Limpert, A. & Landreth, G. Mechanisms of statin-mediated inhibition of small G-protein function. *J Biol Chem* **280**, 34202–34209 (2005).
772. Rikitake, Y. & Liao, J. K. Rho GTPases, statins, and nitric oxide. *Circ Res* **97**, 1232–1235 (2005).
773. Guilluy, C. *et al.* Inhibition of RhoA/Rho kinase pathway is involved in the beneficial effect of sildenafil on pulmonary hypertension. *Br J Pharmacol* **146**, 1010–1018 (2005).
774. Hemnes, A. R., Zaiman, A. & Champion, H. C. PDE5A inhibition attenuates bleomycin-induced pulmonary fibrosis and pulmonary hypertension through inhibition of ROS generation and RhoA/Rho kinase activation. *Am J Physiol Lung Cell Mol Physiol* **294**, (2008).
775. Pernis, A. B., Ricker, E., Weng, C. H., Roza, C. & Yi, W. Rho Kinases in Autoimmune Diseases. *Annu Rev Med* **67**, 355–374 (2016).

776. Ricker, E., Chowdhury, L., Yi, W. & Pernis, A. B. The RhoA-ROCK pathway in the regulation of T and B cell responses. *F1000Res* **5**, (2016).
777. Zhu, M. *et al.* Role of Rho kinase isoforms in murine allergic airway responses. *Eur Respir J* **38**, 841–850 (2011).
778. Schaafsma, D., Bos, I. S. T., Zuidhof, A. B., Zaagsma, J. & Meurs, H. The inhaled Rho kinase inhibitor Y-27632 protects against allergen-induced acute bronchoconstriction, airway hyperresponsiveness, and inflammation. *Am J Physiol Lung Cell Mol Physiol* **295**, (2008).
779. Schaafsma, D., Bos, I. S. T., Zuidhof, A. B., Zaagsma, J. & Meurs, H. Inhalation of the Rho-kinase inhibitor Y-27632 reverses allergen-induced airway hyperresponsiveness after the early and late asthmatic reaction. *Respir Res* **7**, 121 (2006).
780. Mali, R. S., Kapur, S. & Kapur, R. Role of Rho kinases in abnormal and normal hematopoiesis. *Curr Opin Hematol* **21**, 271 (2014).
781. Komers, R. Rho kinase inhibition in diabetic nephropathy. *Curr Opin Nephrol Hypertens* **20**, 77–83 (2011).
782. Matoba, K. *et al.* Rho-kinase inhibition prevents the progression of diabetic nephropathy by downregulating hypoxia-inducible factor 1 α . *Kidney Int* **84**, 545–554 (2013).
783. Manning, G., Whyte, D. B., Martinez, R., Hunter, T. & Sudarsanam, S. The protein kinase complement of the human genome. *Science* **298**, 1912–1934 (2002).
784. Singh, R. K. & Singh, R. K. Protein Kinases - Promising Targets for Anticancer Drug Research. **24**, (2021).
785. Feng, Y., Lograsso, P. V., Defert, O. & Li, R. Rho Kinase (ROCK) Inhibitors and Their Therapeutic Potential. *J Med Chem* **59**, 2269–2300 (2016).
786. Barcelo, J., Samain, R. & Sanz-Moreno, V. Preclinical to clinical utility of ROCK inhibitors in cancer. *Trends Cancer* **9**, 250–263 (2023).
787. Hidaka, H. *et al.* A novel vascular relaxing agent, N-(6--aminohexyl)-5-chloro-1-naphthalensulfonamide which affects vascular smooth muscle actomyosin. *Journal of Pharmacology and Experimental Therapeutics* **1**, 8–15 (1978).
788. Ono-Saito, N., Niki, I. & Hidaka, H. H-series protein kinase inhibitors and potential clinical applications. *Pharmacol Ther* **82**, 123–131 (1999).
789. Takayasu, M. *et al.* The effects of HA compound calcium antagonists on delayed cerebral vasospasm in dogs. *J Neurosurg* **65**, 80–85 (1986).
790. Asano, T. *et al.* Mechanism of action of a novel antivasospasm drug, HA1077. *Journal of Pharmacology and Experimental Therapeutics* **241**, 1033–1040 (1987).
791. Asano, T. *et al.* Vasodilator actions of HA1077 in vitro and in vivo putatively mediated by the inhibition of protein kinase. *Br J Pharmacol* **98**, 1091–1100 (1989).
792. Asano, T. *et al.* Endothelin: a potential modulator of cerebral vasospasm. *Eur J Pharmacol* **190**, 365–372 (1990).
793. Asano, T. *et al.* Blockade of intracellular actions of calcium may protect against ischaemic damage to the gerbil brain. *Br J Pharmacol* **103**, 1935–1938 (1991).
794. Satoh, S. *et al.* The effects of HA1077 on the cerebral circulation after subarachnoid haemorrhage in dogs. *Acta Neurochir (Wien)* **110**, 185–188 (1991).
795. Jacobs, M. *et al.* The structure of dimeric ROCK I reveals the mechanism for ligand selectivity. *J Biol Chem* **281**, 260–268 (2006).
796. Yamaguchi, H., Kasa, M., Amano, M., Kaibuchi, K. & Hakoshima, T. Molecular mechanism for the regulation of rho-kinase by dimerization and its inhibition by fasudil. *Structure* **14**, 589–600 (2006).
797. Misek, S. A. *et al.* Rho-mediated signaling promotes BRAF inhibitor resistance in de-differentiated melanoma cells. *Oncogene* **2019** 39:7 **39**, 1466–1483 (2019).

798. Vennin, C. *et al.* Transient tissue priming via ROCK inhibition uncouples pancreatic cancer progression, sensitivity to chemotherapy, and metastasis. *Sci Transl Med* **9**, (2017).
799. Heikkila, T. *et al.* Co-crystal structures of inhibitors with MRCK β , a key regulator of tumor cell invasion. *PLoS One* **6**, (2011).
800. Zhang, E. Y., Ha, B. H. & Boggon, T. J. PAK4 crystal structures suggest unusual kinase conformational movements. *Biochim Biophys Acta* **1866**, 356 (2018).
801. Breitenlechner, C. *et al.* Protein Kinase a in Complex with Rho-Kinase Inhibitors Y-27632, Fasudil, and H-1152P: Structural Basis of Selectivity. *Structure* **11**, 1595–1607 (2003).
802. Wiene-Schmidt, B., Oebbeke, M., Ngo, K., Heine, A. & Klebe, G. Two Methods, One Goal: Structural Differences between Cocrystallization and Crystal Soaking to Discover Ligand Binding Poses. *ChemMedChem* **16**, 292 (2021).
803. Garnock-Jones, K. P. Ripasudil: first global approval. *Drugs* **74**, 2211–2215 (2014).
804. Yamamoto, K. *et al.* The novel Rho kinase (ROCK) inhibitor K-115: a new candidate drug for neuroprotective treatment in glaucoma. *Invest Ophthalmol Vis Sci* **55**, 7126–7136 (2014).
805. Sumi, K., Yoshida, Y. & Hidaka, H. Isoquinoline sulfonamides such as fasudil, H-1152, ripasudil and H-1129 produce IOP-lowering and neuroprotective effects through Rho kinase inhibition. *Invest Ophthalmol Vis Sci* **59**, 1781–1781 (2018).
806. Tanihara, H. *et al.* Intra-ocular pressure-lowering effects of a Rho kinase inhibitor, ripasudil (K-115), over 24 hours in primary open-angle glaucoma and ocular hypertension: a randomized, open-label, crossover study. *Acta Ophthalmol* **93**, e254–e260 (2015).
807. Batra, M. *et al.* Netarsudil: A new ophthalmic drug in the treatment of chronic primary open angle glaucoma and ocular hypertension. *Eur J Ophthalmol* **31**, 2237–2244 (2021).
808. Serle, J. B. *et al.* Two Phase 3 Clinical Trials Comparing the Safety and Efficacy of Netarsudil to Timolol in Patients With Elevated Intraocular Pressure: Rho Kinase Elevated IOP Treatment Trial 1 and 2 (ROCKET-1 and ROCKET-2). *Am J Ophthalmol* **186**, 116–127 (2018).
809. Sturdivant, J. M. *et al.* Discovery of the ROCK inhibitor netarsudil for the treatment of open-angle glaucoma. *Bioorg Med Chem Lett* **26**, 2475–2480 (2016).
810. Mehran, N. A., Sinha, S. & Razeghinejad, R. New glaucoma medications: latanoprostene bunod, netarsudil, and fixed combination netarsudil-latanoprost. *Eye* **2019 34:1** **34**, 72–88 (2019).
811. Jagasia, M. *et al.* ROCK2 Inhibition With Belumosudil (KD025) for the Treatment of Chronic Graft-Versus-Host Disease. *J Clin Oncol* **39**, 1888–1898 (2021).
812. Cutler, C. *et al.* Belumosudil for chronic graft-versus-host disease after 2 or more prior lines of therapy: the ROCKstar Study. *Blood* **138**, 2278–2289 (2021).
813. Blair, H. A. Belumosudil: First Approval. *Drugs* **81**, 1677–1682 (2021).
814. Zanin-Zhorov, A. *et al.* Selective oral ROCK2 inhibitor down-regulates IL-21 and IL-17 secretion in human T cells via STAT3-dependent mechanism. *Proc Natl Acad Sci U S A* **111**, 16814–16819 (2014).
815. Flynn, R. *et al.* Targeted Rho-associated kinase 2 inhibition suppresses murine and human chronic GVHD through a Stat3-dependent mechanism. *Blood* **127**, 2144–2154 (2016).
816. Lai, A. & Frishman, W. H. Rho-kinase inhibition in the therapy of cardiovascular disease. *Cardiol Rev* **13**, 285–292 (2005).
817. Rikitake, Y. & Liao, J. K. ROCKs as therapeutic targets in cardiovascular diseases. *Expert Rev Cardiovasc Ther* **3**, 441–451 (2005).
818. Chou, H. C., Huang, L. T., Yeh, T. F. & Chen, C. M. Rho-kinase inhibitor Y-27632 attenuates pulmonary hypertension in hyperoxia-exposed newborn rats. *Acta Pharmacologica Sinica* **2013 34:10** **34**, 1310–1316 (2013).
819. Mueller, B. K., Mack, H. & Teusch, N. Rho kinase, a promising drug target for neurological disorders. *Nature Reviews Drug Discovery* **2005 4:5** **4**, 387–398 (2005).

820. Martín-Cámara, O., Cores, Á., López-Alvarado, P. & Menéndez, J. C. Emerging targets in drug discovery against neurodegenerative diseases: Control of synapsis dysfunction by the RhoA/ROCK pathway. *Eur J Med Chem* **225**, 113742 (2021).
821. Honjo, M. *et al.* Potential role of Rho-associated protein kinase inhibitor Y-27632 in glaucoma filtration surgery. *Invest Ophthalmol Vis Sci* **48**, 5549–5557 (2007).
822. Ibrahim, D. G., Ko, J.-A., Iwata, W., Okumichi, H. & Kiuchi, Y. Inhibitory effects of Y-27632, Rho-associated protein kinase inhibitor, on scarring formation following glaucoma filtration surgery. *Invest Ophthalmol Vis Sci* **59**, 478–478 (2018).
823. Wang, L., Xue, L., Yan, H., Li, J. & Lu, Y. Effects of ROCK inhibitor, Y-27632, on adhesion and mobility in esophageal squamous cell cancer cells. *Mol Biol Rep* **37**, 1971–1977 (2010).
824. Jiang, L., Wen, J. & Luo, W. Rho-associated kinase inhibitor, Y-27632, inhibits the invasion and proliferation of T24 and 5367 bladder cancer cells. *Mol Med Rep* **12**, 7526–7530 (2015).
825. Wang, Z. M. *et al.* ROCK inhibitor Y-27632 inhibits the growth, migration, and invasion of Tca8113 and CAL-27 cells in tongue squamous cell carcinoma. *Tumor Biology* **37**, 3757–3764 (2016).
826. Routhier, A. *et al.* Pharmacological inhibition of Rho-kinase signaling with Y-27632 blocks melanoma tumor growth. *Oncol Rep* **23**, 861–867 (2010).
827. McLeod, R. *et al.* First-in-Human Study of AT13148, a Dual ROCK-AKT Inhibitor in Patients with Solid Tumors. *Clin Cancer Res* **26**, 4777–4784 (2020).
828. Bellizzi, A. *et al.* RhoA protein expression in primary breast cancers and matched lymphocytes is associated with progression of the disease. *Int J Mol Med* **22**, 25–31 (2008).
829. Faried, A., Faried, L. S., Usman, N., Kato, H. & Kuwano, H. Clinical and prognostic significance of RhoA and RhoC gene expression in esophageal squamous cell carcinoma. *Ann Surg Oncol* **14**, 3593–3601 (2007).
830. Horiuchi, A. *et al.* Up-Regulation of Small GTPases, RhoA and RhoC, Is Associated with Tumor Progression in Ovarian Carcinoma. *Laboratory Investigation* **2003** 83:6 **83**, 861–870 (2003).
831. Li, B. *et al.* Involvement of Rho/ROCK signalling in small cell lung cancer migration through human brain microvascular endothelial cells. *FEBS Lett* **580**, 4252–4260 (2006).
832. Denoyelle, C. *et al.* Molecular mechanism of the anti-cancer activity of cerivastatin, an inhibitor of HMG-CoA reductase, on aggressive human breast cancer cells. *Cell Signal* **15**, 327–338 (2003).
833. Shang, X. *et al.* Rational design of small molecule inhibitors targeting RhoA subfamily Rho GTPases. *Chem Biol* **19**, 699–710 (2012).
834. Kristelly, R., Gao, G. & Tesmer, J. J. G. Structural determinants of RhoA binding and nucleotide exchange in leukemia-associated Rho guanine-nucleotide exchange factor. *J Biol Chem* **279**, 47352–47362 (2004).
835. Shang, X. *et al.* Small-molecule inhibitors targeting G-protein-coupled Rho guanine nucleotide exchange factors. *Proc Natl Acad Sci U S A* **110**, 3155–3160 (2013).
836. Tsubaki, M. *et al.* Rhosin Suppressed Tumor Cell Metastasis through Inhibition of Rho/YAP Pathway and Expression of RHAMM and CXCR4 in Melanoma and Breast Cancer Cells. *Biomedicines* **9**, 1–17 (2021).
837. Boquet, P. The cytotoxic necrotizing factor 1 (CNF1) from Escherichia coli. *Toxicon* **39**, 1673–1680 (2001).
838. Fabbri, A., Travaglione, S. & Fiorentini, C. Escherichia coli cytotoxic necrotizing factor 1 (CNF1): toxin biology, in vivo applications and therapeutic potential. *Toxins (Basel)* **2**, 283–296 (2010).
839. Wilde, C., Genth, H., Aktories, K. & Just, I. Recognition of RhoA by Clostridium botulinum C3 exoenzyme. *J Biol Chem* **275**, 16478–16483 (2000).
840. Akiyuki, T., Toshiharu, T., Toru, Y., Yayoi, T. & Tsuge, H. Rho GTPase Recognition by C3 Exoenzyme Based on C3-RhoA Complex Structure. *J Biol Chem* **290**, 19423–19432 (2015).
841. Solski, P. A., Helms, W., Keely, P. J., Su, L. & Der, C. J. RhoA Biological Activity Is Dependent on Prenylation but Independent of Specific Isoprenoid Modification. *Cell Growth Differ* **13**, 363 (2002).

842. Allal, C. *et al.* RhoA prenylation is required for promotion of cell growth and transformation and cytoskeleton organization but not for induction of serum response element transcription. *J Biol Chem* **275**, 31001–31008 (2000).
843. Kamel, W. A. *et al.* Simvastatin-Induced Apoptosis in Osteosarcoma Cells: A Key Role of RhoA-AMPK/p38 MAPK Signaling in Antitumor Activity. *Mol Cancer Ther* **16**, 182–192 (2017).
844. Fromigué, O. *et al.* RhoA GTPase inactivation by statins induces osteosarcoma cell apoptosis by inhibiting p42/p44-MAPKs-Bcl-2 signaling independently of BMP-2 and cell differentiation. *Cell Death Differ* **13**, 1845–1856 (2006).
845. Lee, Y. C. G. *et al.* Tumoricidal Activity of Simvastatin in Synergy with RhoA Inactivation in Antimigration of Clear Cell Renal Cell Carcinoma Cells. *Int J Mol Sci* **24**, (2023).
846. Qiu, Y. *et al.* Simvastatin Attenuates Neuropathic Pain by Inhibiting the RhoA/LIMK/Cofilin Pathway. *Neurochem Res* **41**, 2457–2469 (2016).
847. Dvorsky, R., Blumenstein, L., Vetter, I. R. & Ahmadian, M. R. Structural insights into the interaction of ROCK1 with the switch regions of RhoA. *J Biol Chem* **279**, 7098–7104 (2004).
848. Shimizu, T. *et al.* Parallel coiled-coil association of the RhoA-binding domain in Rho-kinase. *J Biol Chem* **278**, 46046–46051 (2003).
849. Tu, D. *et al.* Crystal structure of a coiled-coil domain from human ROCK I. *PLoS One* **6**, (2011).
850. Longenecker, K. *et al.* Structure of a constitutively activated RhoA mutant (Q63L) at 1.55 Å resolution. *Acta Crystallogr D Biol Crystallogr* **59**, 876–880 (2003).
851. Brückner, A., Polge, C., Lentze, N., Auerbach, D. & Schlattner, U. Yeast Two-Hybrid, a Powerful Tool for Systems Biology. *Int J Mol Sci* **10**, 2763 (2009).
852. Fields, S. & Song, O. K. A novel genetic system to detect protein–protein interactions. *Nature* **1989** 340:6230 **340**, 245–246 (1989).
853. Feilotter, H. E., Harmon, G. J., Ruddell, C. J. & Beach, D. Construction of an improved host strain for two hybrid screening. *Nucleic Acids Res* **22**, 1502 (1994).
854. Fuxman Bass, J. I., Reece-Hoyes, J. S. & Walhout, A. J. M. Colony Lift Colorimetric Assay for β -Galactosidase Activity. *Cold Spring Harb Protoc* **2016**, 1110–1112 (2016).
855. Hilpert, K. *et al.* Anti-c-myc antibody 9E10: epitope key positions and variability characterized using peptide spot synthesis on cellulose. *Protein Engineering, Design and Selection* **14**, 803–806 (2001).